

Sheffield Hallam University

Dislocation related defects in silicon and gallium nitride.

EMIROGLU, Deniz.

Available from the Sheffield Hallam University Research Archive (SHURA) at:

<http://shura.shu.ac.uk/19626/>

A Sheffield Hallam University thesis

This thesis is protected by copyright which belongs to the author.

The content must not be changed in any way or sold commercially in any format or medium without the formal permission of the author.

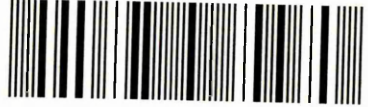
When referring to this work, full bibliographic details including the author, title, awarding institution and date of the thesis must be given.

Please visit <http://shura.shu.ac.uk/19626/> and <http://shura.shu.ac.uk/information.html> for further details about copyright and re-use permissions.

Adsetts Centre City Campus
Sheffield S1 1WB

23343

101 897 974 3



Sheffield Hallam University
Learning and IT Services
Adsetts Centre City Campus
Sheffield S1 1WB

REFERENCE

Return to

ProQuest Number: 10694507

All rights reserved

INFORMATION TO ALL USERS

The quality of this reproduction is dependent upon the quality of the copy submitted.

In the unlikely event that the author did not send a complete manuscript and there are missing pages, these will be noted. Also, if material had to be removed, a note will indicate the deletion.



ProQuest 10694507

Published by ProQuest LLC (2017). Copyright of the Dissertation is held by the Author.

All rights reserved.

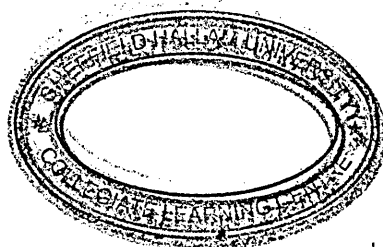
This work is protected against unauthorized copying under Title 17, United States Code
Microform Edition © ProQuest LLC.

ProQuest LLC.
789 East Eisenhower Parkway
P.O. Box 1346
Ann Arbor, MI 48106 – 1346

Dislocation Related Defects in Silicon and Gallium Nitride

Deniz Emiroglu

A thesis submitted in partial fulfilment of the requirements of
Sheffield Hallam University for the degree of Doctor of Philosophy



October 2007

Abstract

This thesis examines the kinetics of carrier capture and emission from dislocations in silicon (Si) and gallium nitride (GaN) using deep level transient spectroscopy (DLTS) and Laplace DLTS (LDLTS).

Laplace DLTS is a powerful tool in characterising point defect related emission, but until now it has not been used extensively for investigating emission from extended defects. Using LDLTS, broad DLTS peaks arising from dislocations in Si containing oxidation-induced stacking faults (OISF) were resolved into multiple emission rates. For the first time, the change in emission rates from deep levels due to the band edge modification at dislocations was evidenced by LDLTS.

Silicon can be grown virtually defect free, but dislocations may be introduced in very-large scale integration (VLSI) to act as impurity gettering centres. Additionally, the interstitial oxygen inherent in Czochralski (Cz) silicon can be made to segregate to dislocation cores by specific bending and annealing conditions to increase the mechanical hardness of wafers. This process is termed dislocation locking. In this work, Cz-Si with different amounts of oxygen at dislocation cores were characterised by DLTS and LDLTS. Results show the presence of a deep level with complex capture properties. A direct correlation is observed between the DLTS peak height of this level and the amount of oxygen at the dislocation core. Laplace DLTS was used to resolve broad DLTS peaks into numerous emission rates. The fill pulse dependency tests revealed that certain emission rates are not affected by the long range Coulomb forces due to neighbouring states. This suggests that certain emission rates contained in the broad DLTS peaks may be associated with point defects which are not in the vicinity of dislocations.

In comparison to silicon, the deep level characterisation of GaN using DLTS and Laplace DLTS is still in its infancy. In this work, the application of DLTS to *n*-type hexagonal GaN Schottky diodes has revealed a shallow donor level, a series of deep electron traps and a thermally activated metastable hole trap. The dominant deep electron level is shown to emit around room temperature. DLTS and Laplace DLTS results indicate that this level exhibits local band-bending and is likely to arise from dislocations. Laplace DLTS of electron traps has shown that the broad DLTS emission is made up of numerous emission rates. Some of these emission rates do not exhibit fill pulse dependency and could arise from point defects in the strain field of dislocations. If the sample is heated to 600K and cooled down, the subsequent DLTS spectrum displays a dominant negative peak due to hole emission. The spectrum recovers to its original state showing only electron traps if the sample is not electrically characterised for a period of several days or a week, depending on the sample. The formation of this level results in a significant drop in carrier density. It is discussed with reference to the gallium vacancy and its complexes with oxygen donors.

Declaration

This thesis is the outcome of the work undertaken at the Centre for Electronic Materials at the University of Manchester Institute of Science and Technology (UMIST) during October 2003 and August 2004, and at the Centre for Electronic Materials and Devices at Sheffield Hallam University during August 2004 and October 2006.

This thesis is the result of my own work and no portion of this work has been submitted for any other degree or qualification at another university or institute of learning.

Acknowledgements

I would like to heartily thank my supervisor Professor Jan Evans-Freeman for providing me with the opportunity to undertake this research and her incessant support, guidance and advice throughout this work. I would also like to thank her for reading individual chapters and a draft version of this thesis.

I would also like to thank Dr John Gorman for proof reading individual chapters and for useful corrections.

I would like to acknowledge Mr Mal McGowan for his assistance in the fabrication of silicon Schottky diodes and Dr Ian Hawkins for teaching of the operation of lab equipment.

Discussions with Professor R. Jones and Professor Dannie Auret were beneficial and I wish to thank them for their time and interest in this project.

Numerous members of the University of Manchester and Sheffield Hallam University were extremely helpful, including Dr Rosemary Booth, Dr K. D. Vernon-Parry, Dr Angeliki Bouloukou, Dr Boumedienne Boudjelida and I acknowledge their assistance.

Publications

High resolution laplace deep level transient spectroscopy studies of electron and hole traps in n-type GaN, D. Emiroglu, J. H. Evans-Freeman, M. J. Kappers, C. McAleese, C. J. Humphreys, submitted for publication in *Phys. Stat. Sol., Proceedings of the 7th International Conference of Nitride Semiconductors*.

Deep electronic states associated with a meta-stable hole trap in n-type GaN, D. Emiroglu, J. H. Evans-Freeman, M. J. Kappers, C. McAleese, C. J. Humphreys, accepted for publication in *Physica B, Proceedings of the 17th International Conference on Defects in Semiconductors*.

Deep electronic states in ion implanted Si, J. H. Evans-Freeman, D. Emiroglu, M. A. Gad, N. Mitromara, K. D. Vernon-Parry, *J. Mater. Sci.* **41**, 1007 (2006).

High resolution deep level transient spectroscopy applied to extended defects in silicon, J. H. Evans-Freeman, D. Emiroglu, K. D. Vernon-Parry, J. D. Murphy, P.R. Wilshaw, *J. Phys.: Condens. Matter* **17**, 2219 (2005).

High resolution deep level transient spectroscopy and process-induced defects in silicon, J. H. Evans-Freeman, D. Emiroglu, K. D. Vernon-Parry, *Mat. Sci. Eng B* **114**, 307 (2004).

Abbreviations and Acronyms

σ_n	Electron capture cross-section (cm^2)
σ_p	Hole capture cross-section (cm^2)
c_n	Electron capture coefficient
Cz growth	Czochralski growth method of silicon
DLTS	Deep Level Transient Spectroscopy
E_c	Conduction band
EELS	Electron energy-loss spectroscopy
E_F	Fermi level within the bandgap (eV)
E_g	Semiconductor bandgap (eV)
e_n	Electron emission rate (s^{-1})
e_p	Hole emission rate (s^{-1})
f.c.c.	Face-centred cubic
f_{nt}	Fraction of traps occupied by electrons
f_{pt}	Fraction of traps occupied by holes
G-R centre	Generation-recombination centre
HT	High temperature
k_B	Boltzmann constant ($k_B = 8.6174 \times 10^{-5} \text{ eVK}^{-1}$)
\mathbf{k}_n	Wave vector, where n is an integer
LD	Laser diode
LDLTS	Laplace Deep Level Transient Spectroscopy
LED	Light emitting diode
MOCVD	Metal organic chemical vapour deposition
n	Electron concentration in the conduction band (cm^{-3})
N_A^-	Ionised acceptor concentration (cm^{-3})
N_c	Effective density of states in the conduction band
N_D^+	Ionised donor concentration (cm^{-3})
$n\text{-GaN}$	n -type gallium nitride
NL	Nucleation layer

N_t	Trap concentration (cm^{-3})
N_v	Effective density of states in the valence band
OMVPE	Organometallic vapour phase epitaxy
p	Hole concentration in the valence band (cm^{-3})
SCR	Space-charge region
TD	Threading dislocation
TEM	Transmission electron microscopy
TSCAP	Thermally stimulated capacitance spectroscopy
VLSI	Very-large scale integration
v_n	Thermal velocity of electrons (cms^{-1})
v_p	Thermal velocity of holes (cms^{-1})
VPE	Vapour phase epitaxy

Table of Contents

Chapter 1: Introduction	1
Chapter 2: Point and extended defects in semiconductors	4
2.1 Crystal structure and band theory, 4	
2.2 Deep level occupation statistics, 7	
2.2.1 Capture at deep levels, 9	
2.2.2 Emission from deep levels, 11	
2.2.3 The emission-capture relationship at deep levels, 12	
2.3 Dislocation structures, 14	
2.4 Electrical properties of extended defects, 16	
2.5 Summary, 18	
2.6 References, 19	
Chapter 3: Defects in silicon and gallium nitride	20
3.1 Structure of dislocations in silicon, 20	
3.1.1 Oxidation-induced stacking faults (OISF), 23	
3.1.2 Dislocation-locking by oxygen in Czochralski silicon, 23	
3.2 Growth of GaN and formation of threading dislocations, 26	
3.2.1 Crystal structure, 26	
3.2.2 Threading dislocations in GaN, 27	
3.2.3 Metal organic chemical vapour deposition, 29	
3.3 Point defects in GaN, 31	
3.3.1 Hydrogen, 31	
3.3.2 The nitrogen vacancy (V_N), 31	
3.3.3 Silicon at a gallium site (Si_{Ga}), 32	
3.3.4 Oxygen at a nitrogen site, 32	
3.4 The gallium vacancy and associated complexes, 32	
3.4.1 $V_{Ga} - (O_N)_x$ complexes, 35	
3.5 Summary, 39	
3.6 References, 40	

Chapter 4: Characterisation techniques..... 44

- 4.1 The Schottky Barrier Diode, 44
 - 4.1.1 Energy band structure, 44
 - 4.1.2 The depletion region, 45
- 4.2 Capacitance – voltage measurements, 47
- 4.3 Deep Level Transient Spectroscopy, 49
 - 4.3.1 Trap activation energy, 56
 - 4.3.2 Trap density, 58
 - 4.3.3 Deep level spatial profiling, 59
- 4.4 Laplace deep level transient spectroscopy, 60
- 4.5 System setup, 62
- 4.6 Summary, 63
- 4.7 References, 64

Chapter 5: Review of deep level transient spectroscopy of extended defects in silicon and gallium nitride 65

- 5.1 Deep level transient spectroscopy of extended defects, 65
- 5.2 DLTS of dislocations in silicon, 68
 - 5.2.1 OISF related deep levels in *n*-type silicon, 72
 - 5.2.2 Oxygen and dislocations in *p*-type Si, 74
- 5.3 Deep Level Transient Spectroscopy of *n*-type hexagonal GaN, 75
 - 5.3.1 Bias dependency and hydrogen passivation of the E₁ level, 77
 - 5.3.2 Emission from minority carrier traps, 79
- 5.4 Summary, 82
- 5.5 References, 83

Chapter 6: Deep level emission from extended defects in silicon ... 86

- 6.1 Sample specifications and fabrication methods, 86
 - 6.1.1 Schottky diode fabrication, 86
 - 6.1.2 *n*-type OISF sample, 88
 - 6.1.1 *p*-type O-LD sample, 89
- 6.2 Results: OISF sample, 90
- 6.3 Results: Oxygen-locked dislocations, 98
 - 6.3.1 Capacitance-temperature characteristics, 108
- 6.4 Summary, 109
- 6.5 References, 110

Chapter 7: Emission from point and extended defects in gallium nitride	111
7.1 Sample details, 111	
7.2 Carrier density and device characteristics, 112	
7.2.1 Carrier concentration, 112	
7.2.2 Current-voltage measurements, 114	
7.3 Deep level transient spectroscopy of gallium nitride, 116	
7.4 Shallow levels, 118	
7.5 Deep levels, 122	
7.5.1 Level E_1 , 122	
7.5.2 Level E_2 (100 – 200K), 132	
7.5.3 Near-midgap states, 134	
7.6 Minority carrier emission, 138	
7.6.1 Changes to carrier density, 142	
7.6.2 Formation temperature of E_h , 145	
7.6.3 Bias dependency, 147	
7.6.4 Effect of thermal stress on deep level stability, 148	
7.6.5 Fill pulse dependency, 153	
7.6.6 Activation energy measurements of the E_h level, 159	
7.7 Discussion, 161	
7.7.1 Electron traps and dislocation related emission, 161	
7.7.2 Minority carrier emission, 162	
7.7.3 Capture properties of the E_h level, 168	
7.7.4 Dependency of emission on the trap position in the lattice, 171	
7.8 Summary, 173	
7.9 References, 174	
Chapter 8: Conclusions and future work	177
8.1 Silicon, 177	
8.1.1 Future work, 178	
8.2 Gallium nitride, 178	
8.2.1 Future work, 180	
8.3 Laplace DLTS and extended defects, 181	
8.4 References, 183	

Chapter 1

Introduction

This thesis addresses issues concerning characterisation of extended defects in two very different materials, silicon (Si) and gallium nitride (GaN). Commercial Si is currently structurally perfect, yet intentionally introduced dislocations do have a role to play in improving device performance. On the other hand, GaN has a very high concentration of grown-in dislocations which are unavoidable. However, GaN based optical devices are a commercial success. Nevertheless, it is essential to understand the electrical effects of extended defects in Si and GaN in order to progress device performance enhancement.

Extended defects possess strain fields which can trap impurities and other point defects. Dislocations have been associated with high leakage currents in reverse biased junctions and can provide non-radiative recombination centres. To this day, there is no clear answer to whether 'clean' (i.e. undecorated) dislocations would introduce deep levels in the semiconductor bandgap. There is substantial work which indicates that deep levels at dislocations arise from regions in the vicinity of the dislocation line, where tensile and compressive strains are at their maxima. This, combined with enhanced electrical activity observed after impurity in-diffusion and segregation to dislocation cores by annealing, is a strong indication that electrical activity at dislocations is due to impurities and defects which have segregated to dislocation cores.

At a first glance, the semiconductors silicon (Si) and gallium nitride (GaN) may appear vastly different from one another when considering their properties, such as their bandgap, crystal structure and applications. However, when considering the presence of extended defects resulting in deep levels in the bandgap, the two differ only slightly.

Deep level transient spectroscopy (DLTS) is commonly used to characterise deep levels in semiconductors and will be used in this study to investigate deep levels in *n*-type GaN and in silicon containing oxygen locked dislocations. Laplace DLTS (LDLTS) has been shown to have enhanced resolution and can, in some cases, provide additional information regarding the capture and emission properties of deep levels. It will be shown in Chapter 6 that the application of LDLTS to extended defects can be used to

resolve broad DLTS spectra and to distinguish between point and extended defects. The principles behind DLTS and Laplace DLTS are discussed in Chapter 4.

The capture and emission statistics at deep levels is discussed in Chapter 2. Carrier capture at extended defects is modified by the initial occupation of deep levels at extended defects, resulting in the formation of a capture barrier for incoming charge carriers. Such behaviour can be detected readily by the use of DLTS and this is discussed in Chapter 5.

Silicon can be grown virtually defect free, but dislocations are often introduced as gettering centres to allow impurities to segregate away from active areas of devices. Additionally, it has been shown that oxygen can improve the mechanical hardness of silicon by diffusing to dislocation cores and inhibiting dislocation movement¹. However, the effects on electrical properties of intentional extended defect incorporation should be characterised. Oxford Materials at Oxford University are the leading group in dislocation locking processes to improve the mechanical hardness of silicon. Samples prepared by Oxford Materials were characterised in this study to investigate the electrical properties of oxygen-locked dislocations in silicon.

In contrast, extended defects in gallium nitride (GaN) are currently unavoidable due to the lattice mismatch of substrates available. This mismatch between the substrate and the material results in a high level of strain in the lattice and dislocations (typically in the form of threading edge dislocations) are created during growth to minimise strain. Gallium vacancies were reported to be dominant defects in *n*-type GaN^{2,3} and are thought to exist as triple acceptors, which form complexes with the abundant ionised oxygen donor impurities in the material^{4,5}. The deep acceptors at dislocation cores result in negatively charged dislocations and were reported to act as carrier scattering centres, reducing mobility⁶. This has significant implications on GaN-based devices at a time when the industry is pushing for wide bandgap materials for higher power and higher frequency applications. The Cambridge Centre for GaN at Cambridge University is at the forefront of GaN growth by metal organic chemical vapour deposition (MOCVD) and have provided *n*-type GaN samples to be characterised in this study.

Chapter 3 provides an overview of structural properties of extended defects in Si and also of GaN growth and related defects. A review of DLTS on extended defects in Si and GaN are discussed in Chapter 5. The results on silicon are presented in Chapter 6, which also includes the application of Laplace DLTS to study the carrier capture at extended defects. The electrical characterisation results on *n*-GaN are presented in

Chapter 7. Emphasis is placed on a metastable minority carrier level, which has previously been associated with the gallium vacancy.

Chapter 8 of this thesis summarises the results achieved in this study and provides suggestions for future work.

References

- ¹ S. M. Hu, *Appl. Phys. Lett.* **31**, 53 (1977).
- ² J. Neugebauer and C. G. Van de Walle, *Phys. Rev. B* **50**, 8067 (1994).
- ³ J. Oila, J. Kivioja, V. Ranki, K. Saarinen, D. C. Look, R. J. Molnar, S. S. Park, S. K. Lee, J. Y. Han, *Appl. Phys. Lett.* **82**, 3433 (2003).
- ⁴ T. Mattila and R. M. Nieminen. *Phys. Rev. B* **55**, 9571 (1997).
- ⁵ J. Elsner, R. Jones, M. I. Heggie, P. K. Stitch, M. Haugk, Th. Frauenheim, S. Öberg, P. R. Briddon, *Phys. Rev. B* **58**, 12571 (1998).
- ⁶ N. G. Weimann, L. Eastman, D. Doppalapudi, H. M. Ng, T. D. Moustakas, *J. Appl. Phys.* **83**, 3656 (1998).

Chapter 2

Point and extended defects in semiconductors

This chapter examines the influence of deep levels on the electrical properties of semiconductors. An outline of semiconductor band theory relevant to this work is presented. This is followed by a discussion of deep level statistics, which governs the interaction of deep levels with the conduction and valence bands. Finally, the structural and line charge properties of extended defects are considered.

2.1 Crystal structure and band theory

This section is an overview of the fundamental semiconductor principles based on the discussions provided by Sze¹, Streetman and Banerjee², Lannoo³, and Kittel⁴.

Atoms in semiconductors are arranged in a periodic lattice where every two nearest neighbours are bonded covalently by two electrons with opposite spins. The electron energy states in an isolated atom can be obtained through quantum mechanical analysis. The most common method uses Schrödinger's wave equation in which the atom is represented by a potential well. The equations are analytically solved only for the hydrogen atom. For more complex atoms and systems, a solution to Schrödinger's wave equation can be obtained using approximations. The solution provides the electron energy states as continuous functions $\varepsilon_n(\mathbf{k}_n)$. The wave function, ψ_n , of the electron is assumed to be a plane wave, with a wave vector \mathbf{k}_n , where n is an integer labelled the quantum number².

As two atoms are brought together, the attractive and repulsive forces acting between them are balanced at a specific inter-atomic distance. At such separations, the electron wave functions of the electrons belonging to the two atoms begin to overlap³. The discrete energy levels of the two atoms split and the resulting levels belong to the new system and not to individual atoms. As many atoms (N) are brought together, such as in a solid, the splitting of N energy levels results in a band of energies (the conduction

band and the valence band) separated by an energy gap, E_g . In a perfect crystal, there would be no allowable electron energy levels within the band gap.

It is possible to plot the allowed energies against the wave vector k . This plot is commonly known as the band structure of a crystal lattice⁴. Figure 2.1 shows direct (a) and (b) and indirect (c) electron transitions from the conduction band energy minimum to the valence band maximum. It is worth mentioning the difference between direct and indirect semiconductors, as the two materials studied in this work, namely gallium nitride and silicon, are of the former and latter type, respectively. For a direct semiconductor, such as gallium nitride, an electron transition between the conduction band minimum and the valence band maximum occurs at the same value of k , as shown by (a) Figure 2.1. Therefore, the transition from the conduction band to the valence band does not result in a change of electron momentum. For an indirect semiconductor, such as silicon, the conduction band minimum and the valence band maximum do not occur at the same value of k . Therefore, a transition from the conduction band minimum to the valence band maximum as indicated by (c) would involve a change in the electron momentum.

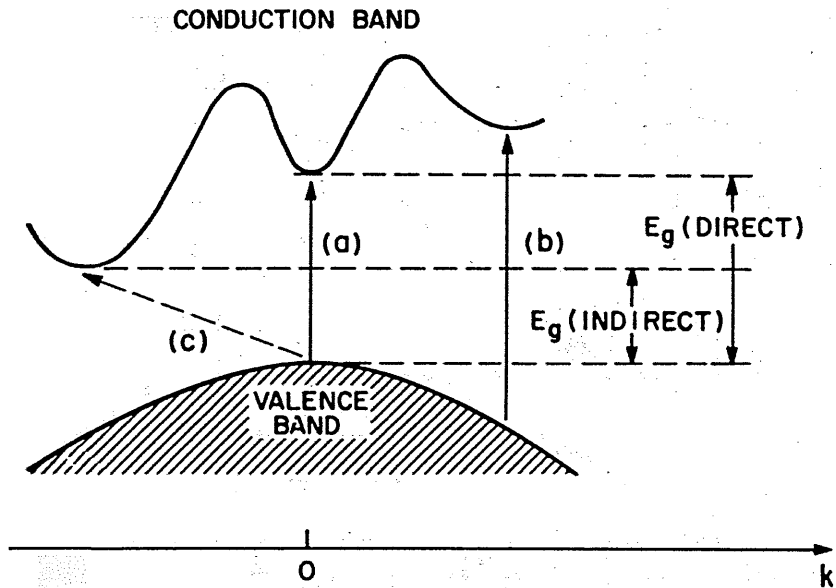


Figure 2.1: Illustrations of electron transitions from the conduction to the valence band: (a) and (b) represent direct transitions and (c) an indirect transition. After Sze¹.

The electrons in a crystal lattice are not completely free and atomic values of parameters do not apply³. Therefore, the effect of the lattice is taken into account by using the effective mass theory. The effective mass of an electron is determined by the second derivative, or the curvature of the energy-momentum ($E - k$) relationship

$$m^* = \frac{\hbar^2}{d^2 E/d\mathbf{k}^2} \quad 2.1$$

Equation 2.1 suggests that bands with stronger curvature and hence a greater $d^2 E/d\mathbf{k}^2$, result in a smaller electron (or hole) effective mass².

In an intrinsic semiconductor at absolute temperature (0K), the valence band is filled with electrons and the conduction band is empty. For conduction to occur, electrons must be thermally or optically excited to the conduction band, which results in electron-hole pairs (EHP)². The electron concentration in the conduction band is universally known as n (electrons/cm³) and the hole concentration in the valence band as p (holes/cm³). However, in an intrinsic material, the existence of one without the other is not possible and hence each intrinsic carrier concentration is referred to as n_i . Therefore, $n_i = n = p$. At steady state, the carrier concentration is fixed and the temperature dependent EHP generation rate is equal to the temperature dependent EHP recombination rate.

It follows from the above discussion that the electrical properties of a semiconductor are determined by the density of electrons in the conduction band and density of holes in the valence band. These values, in turn, are determined by the effective density of states N_c and N_v in the conduction and valence bands respectively, together with the probability of their occupancy. The electron concentration in the conduction band, E_c , can be expressed mathematically as

$$n = N_c f(E_c) \quad 2.2$$

The probability of occupancy involves Fermi-Dirac statistics, which states that the electron distribution at equilibrium over allowed energy levels is given by

$$f(E_c) = \left[1 + e^{(E_c - E_F)/kT} \right]^{-1} \approx e^{-(E_c - E_F)/kT} \quad 2.3$$

provided that the semiconductor is non-degenerate¹. E_F is referred to as the Fermi level. The probability of a state at the Fermi level being occupied is $1/2$. Substituting equation 2.3 into 2.2 gives the expression for the electron concentration in the conduction band at equilibrium to be

$$n = N_c e^{-(E_c - E_F)/kT} \quad 2.4$$

The argument is similar for the concentration of holes in the valence band, E_v , at equilibrium. The effective density of states in the valence band is denoted N_v and the probability of occupancy now becomes

$$1 - f(E_v) = 1 - \left[1 + e^{(E_v - E_F)/kT} \right]^{-1} \approx e^{-(E_F - E_v)/kT} \quad 2.5$$

Equation 2.5 also assumes that the semiconductor is not degenerate and therefore that the Fermi level lies at least several kT above the valence band.

The above equations apply to both undoped (intrinsic) and doped semiconductors, but for the former type, the Fermi level lies approximately at the middle of the bandgap.

2.2 Deep level occupation statistics

Defects in semiconductors cover a wide range of lattice imperfections and can be subdivided into point and extended defects. Point defects include substitutional impurities, vacancies, foreign interstitials and self-interstitials. Extended defects include edge and screw dislocations, stacking faults, grain boundaries, clusters and precipitates. Defects often introduce deep levels (traps) within the bandgap, which can influence the electrical properties of semiconductors. The free carrier concentration at room temperature ($n = N_D^+ - N_A^-$ or $p = N_A^- - N_D^+$, where N_A^- and N_D^+ are the ionised acceptor and donor concentrations, respectively) can easily be affected by compensation from deep levels, provided that the shallow background doping and the deep donor (or acceptor) concentrations are comparable. Furthermore, deep levels can act as generation or recombination centres and can hinder device performance, such as increasing reverse bias leakage currents. Therefore, it is imperative that the deep level impurity concentration and crystal lattice defects are controlled.

The statistical analysis of the recombination of electrons and holes was first initiated by Shockley and was later developed into the Shockley-Read-Hall (SRH) theory that is now widely used to study the occupation of deep level defects. In this section, carrier emission and capture processes at deep levels are examined and the effects of deep levels on carrier density are considered. The following discussions are based on the studies by Shockley and Read⁵, Sah *et al*⁶, Feichtinger⁷ and Schroder⁸.

The mathematical study of deep levels differs from that of shallow levels, because in the latter the carriers (i.e. electrons or holes) are weakly bound to the host atom and can be

described by effective mass theory. This approach utilises two assumptions. Firstly, the binding energy is assumed to be weak and that it varies slowly between the closest lattice points to the defect. Secondly, the wavefunction of the particle (electron or hole) is assumed to be localised in k -space. For trap levels lying deeper in the bandgap (i.e. closer to midgap), the short-range potential increases and the carrier wavefunction becomes confined around the defect and is delocalised in k -space⁷.

Figure 2.3 illustrates the four possible interactions of carriers with the deep level and the conduction or valence bands. The level of the trap within the bandgap is denoted by E_t , with a concentration of N_t traps per cubic centimetre.

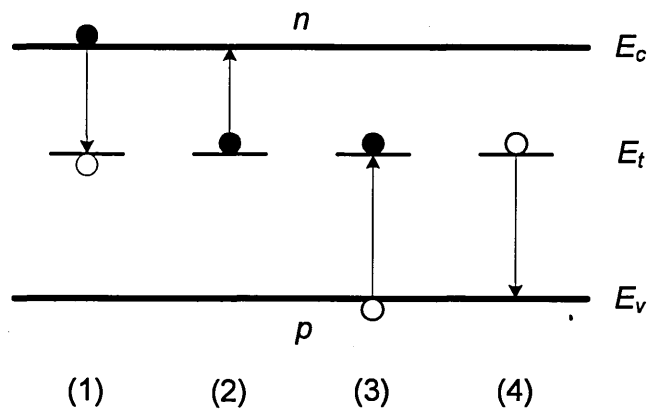


Figure 2.3: Possible interactions of the trap level with the energy bands, showing (1) electron capture, (2) electron emission, (3) hole capture and (4) hole emission. The electron density in the conduction band and the hole density in the valence band are denoted by n and p respectively. After Schroder⁸.

In process (1) the trap, at E_t , is initially occupied by a hole and captures an electron from the conduction band. The captured electron can either be emitted back to the conduction band by process (2), or the trap can capture a hole from the valence band (3). If the deep level captures a hole from the valence band, (3), the hole can be emitted back to the valence band by step (4) or it can capture an electron from the conduction band, (1). If step (1) is followed by (3), or if (3) is preceded by (1), the deep level acts as a *recombination* centre.

On the other hand, if the emission of a hole (electron) is followed by the emission of an electron (hole), the deep level would be termed a *generation* centre. In Figure 2.3, such a level would be described by either step (2) followed by (4), or (4) followed by (2). For generation-recombination (G-R) centres, both the conduction and valence bands are involved in the capture and emission processes. However, a trap only interacts with

either the conduction or valence bands. The capture and emission rates determine whether the deep level acts as a trap or a G-R centre and these are discussed in the following sections.

The carrier capture and emission processes are governed by Fermi-Dirac statistics, which were introduced in section 2.1, where the probability that a quantum state is occupied by an electron is given by equation 2.2. In this section the symbols f_n and f_p will be used to denote the probabilities of a quantum state being occupied by an electron or a hole, respectively. The statistical analysis assumes that a state occupied by hole is equivalent to an empty state⁶. However, this is not always true. Certain deep levels can have multiple charge states and can be occupied by more than one electron, such as the divacancy in silicon⁹.

In the following analysis, the equations for electron capture will be discussed and those for holes will be stated. The subscripts n and p will be used for electrons and holes respectively. The capture at deep levels will be considered first, followed by emission from deep levels. The mathematical terms for the capture and emission rates will then be used to obtain the steady state electron and hole densities in the conduction and valence bands, respectively.

2.2.1 Capture at deep levels

In order to determine the capture rate of a deep level, it is essential that the initial quantum state of the system is known. It is assumed that the trap must be empty (hole occupied) for electron capture to occur. However, as mentioned, this is not strictly true, as deep levels can have multiple charge states. The fraction of traps occupied by holes or electrons is denoted by f_{pt} and f_{nt} , respectively. Since a given state can only be occupied by an electron *or* a hole, the following relationship of fractional occupancy can be derived⁶

$$f_{pt} = 1 - f_{nt} \quad 2.6$$

For capture to occur, carriers must be available in the conduction or valence bands. In the case of electron capture, the free electron density in the conduction band is governed by the number of quantum states $N(E_c)$ in the energy range dE , and the fraction of those states occupied by electrons, $f_n(E)$ ⁵. The expression for $f(E)$ is determined by Fermi-Dirac statistics and is provided by equation 2.3.

The ability of a level to capture an electron is greatly determined by its capture cross section (σ_n) and the thermal velocity of the electrons (v_n)⁸. The former term is defined as the area a deep level presents to a passing electron. The capture coefficient, $c_n(E)$, is the volume of electrons it is capable of capturing per unit time and is given by

$$c_n(E) = \sigma_n v_n \quad 2.7$$

Using the above terms, the electron capture rate, dC/dt , for N_t number of trapping centres per unit volume is defined as⁵

$$\left. \frac{dC}{dt} \right|_n = f_{pt} c_n(E) N_t f_n(E) N(E) dE \quad 2.8$$

A similar expression is obtained for the hole capture rate

$$\left. \frac{dC}{dt} \right|_p = f_{mt} c_p(E) N_t f_p(E) N(E) dE \quad 2.9$$

where c_p is the capture coefficient for holes and $f_p(E)$ is the fraction of states of energy E that are occupied by holes. Hole capture from the valence band can be visualised as electron emission from the trap level to the valence band. Therefore, the trap must initially be occupied by an electron, unless doubly charged.

Equations 2. 8 and 2. 9 can be reduced to

$$\left. \frac{dC}{dt} \right|_n = (1 - f_{mt}) c_n n \quad 2.10$$

for electron capture, and

$$\left. \frac{dC}{dt} \right|_p = f_{mt} c_p p \quad 2.11$$

for hole capture, respectively.

If the electron capture rate exceeds the hole capture rate, the deep level is likely to behave as an electron trap and will be closer to the conduction band. Equations 2.10 and 2.11 show that for a deep level to behave as an electron trap, the electron capture coefficient and/or the electron carrier density in the conduction band must exceed the hole capture coefficient and the hole density in the valence band. However, if both the electron and hole capture rates are comparable, then the deep level is likely to exist near

the middle of the gap and behave as a recombination centre. It must be noted that the carrier densities, n and p , are temperature dependent and are governed by the position of the Fermi level within the bandgap, as described by equations 2.4a and 2.4b, respectively.

2.2.2 Emission from deep levels

For electron emission to occur from a deep level, the level must initially be occupied by at least one electron. This implies that the fractional occupancy of the deep level by electrons, f_{nt} , must be greater than zero. The electron emission rate, from a deep level is given by the emission time constant, e_n , together with the fraction of deep levels occupied by electrons and the density of traps. The electron emission rate, $d\mathcal{E}/dt$, can be written as

$$\left. \frac{d\mathcal{E}}{dt} \right|_n = f_{nt} e_n N_t \quad 2.12$$

For hole emission to occur, the deep level must initially be occupied by a hole. Using the relationship in equation 2.6 between the hole and electron occupancy, the hole emission rate from deep levels can be expressed as

$$\left. \frac{d\mathcal{E}}{dt} \right|_p = (1 - f_{nt}) e_p N_t \quad 2.13$$

Similar to the expressions for carrier capture, equations 2.12 and 2.13 can be simplified to give

$$\left. \frac{d\mathcal{E}}{dt} \right|_n = f_{nt} e_n \quad 2.14$$

for electron emission and

$$\left. \frac{d\mathcal{E}}{dt} \right|_p = (1 - f_{nt}) e_p \quad 2.15$$

for hole emission.

If the electron and hole emission rates are comparable, the deep level is likely to behave as a generation centre. Similarly, the deep level is likely to be closer to the valence band and act as a hole trap if the hole emission rate exceeds the electron emission rate.

2.2.3 The emission-capture relationship at deep levels

A relationship between carrier capture and emission can be obtained by making use of the mathematical relationships provided in sections 2.2.1 and 2.2.2 and the assumption that the electrons are in thermal equilibrium. The net electron capture rate at a deep level is equal to the difference between the electron capture rate (equation 2. 8) and the electron emission rate (equation 2. 12). This can be written as

$$\left. \frac{dC_{net}}{dt} \right|_n = \left[(1-f_{nt})f_n(E)N_c - f_{nt} \frac{e_n}{c_n} \right] N_t c_n \quad 2.16$$

Under the principle of detailed balance, the electron capture rate must be equal to the electron emission rate¹⁰. To satisfy this condition, the terms within the square brackets must equate to zero. This gives the following expression for the emission-capture relationship:

$$(1-f_{nt})f_n(E)N_c = f_{nt} \frac{e_n}{c_n} \quad 2.17$$

where the fractional occupancy of the deep level, $f_{nt}(E)$, is also governed by Fermi-Dirac statistics, with the term E replaced by E_t .

Substituting the relevant terms into equation 2. 17, the emission-capture relationship can be written in the form

$$e_n = \sigma_n v_n N_c \exp[-(E_c - E_t)/kT], \quad 2.18$$

where $\sigma_n v_n = c_n$. A similar expression can be obtained for holes

$$e_p = \sigma_p v_p N_v \exp[-(E_t - E_v)/kT], \quad 2.19$$

where σ_p and v_p are the hole capture cross-section and hole thermal velocity respectively, and $\sigma_p v_p = c_p$.

Deep levels can have a strong influence on the free carrier density, depending on their position within the bandgap and their trap concentration. The rate of change of the electron density due to deep levels must be equal to the emission minus the capture process and is given by

$$\frac{dn}{dt} = f_{nt} e_n - (1-f_{nt}) n c_n. \quad 2.20$$

Similarly for holes, the rate of change of the free hole density in the valence band must be equal to the hole emission minus the hole capture process, which can be written as

$$\frac{dp}{dt} = (1 - f_m)e_p - f_m pc_p \quad 2.21$$

Using equations 2.20 and 2.21, it is possible to express the overall deep level occupancy as

$$\frac{d(f_t)}{dt} = \frac{dp}{dt} - \frac{dn}{dt} = (1 - f_m)(e_p + nc_n) - f_m(pc_p + e_n). \quad 2.22$$

In deep level characterisation, which is discussed in Chapter 4, the trap occupancy is perturbed periodically. The expressions for the initial and final trap occupation, $f_t(0)$ and $f_t(\infty)$ are essential to the deep level measurements in this work and will be mentioned here. The time-dependant trap occupancy is given by⁸

$$f_t(t) = f_t(0) \exp\left(\frac{-t}{\tau}\right) + \frac{(e_p + nc_n)N_t}{e_n + nc_n + e_p + pc_p} \left[1 - \exp\left(\frac{-t}{\tau}\right)\right], \quad 2.23$$

where

$$\tau = \frac{e_p + nc_n}{e_n + nc_n + e_p + pc_p} N_t, \quad 2.24$$

and $f_t(0)$ is the fractional occupation of the deep level at $t = 0$. As $t \rightarrow \infty$, the steady-state deep level density is given by

$$f_t = \frac{e_p + nc_n}{e_n + nc_n + e_p + pc_p} N_t, \quad 2.25$$

where N_t represents the total trap density.

It is apparent from the above discussion that the trap occupancy is strongly time dependent. Furthermore, it is governed by the trap concentration and the competing emission and capture processes⁸.

2.3 Dislocation structures

Extended defects can have a strong influence on electrical and mechanical properties of crystalline materials. These types of defects include dislocations, grain boundaries and precipitates. Dislocations fall into the category of line defects, which keep the lattice translational symmetry along the dislocation line, but not in a radial direction¹¹. Due to the different crystal structure of silicon and gallium nitride, the types of dislocations in these samples are discussed in further detail in chapters 3 and 4 respectively. This section aims to give a brief overview of the structural nature of dislocations in order to aid in the discussion of the electrical properties of dislocations.

An edge dislocation is created by inserting a half-plane of atoms, PQ, in a crystal structure, as shown in Figure 2.4. The row of atoms at the bottom of the inserted half-plane is referred to as the ‘dislocation line’, which is shown at point ‘Q’ in Figure 2.4, and exists along the y -axis in the diagram.

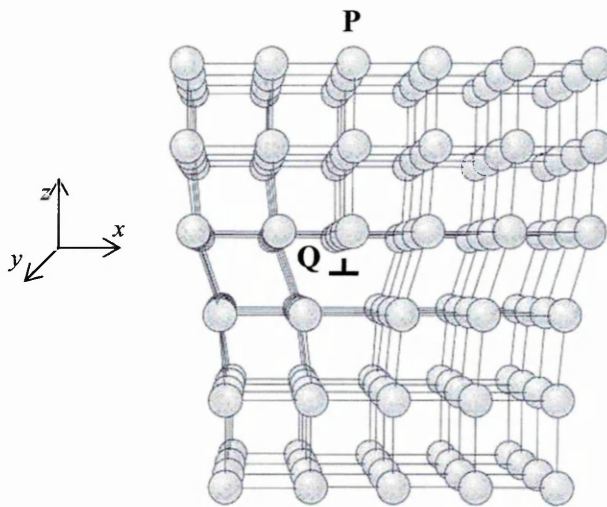


Figure 2.4: An edge dislocation in a crystal lattice, showing the insertion of a half-plane of atoms into the otherwise perfect crystal lattice. After Kittel⁴.

Line defects such as dislocations are one dimensional (1D) defects. Atoms sufficiently far away from the dislocation core are less perturbed and the crystal lattice retains its structure. However, the regions above and below the dislocation line are under compressive and tensile strain respectively¹². Compressive and tensile strains have an effect on the bandgap of semiconductors^{4,13} and this is illustrated in Figure 2.5. Point defects situated at or near a dislocation core should therefore have a distribution of activation energies¹³.

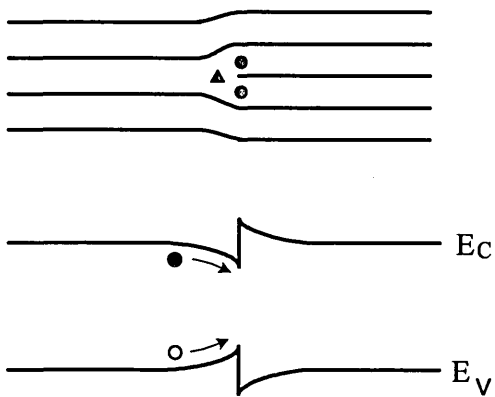


Figure 2.5: The effects of compressive (●) and tensile (▲) strain on the band structure due to an edge dislocation. After Pankove¹⁴

Point defects which are larger in size than the host atom, such as certain transition metals, will segregate to regions under tensile strain, whereas those that are smaller will move towards regions under compressive strain.

Dislocations in crystals are commonly described by their Burgers vector, b , which is the vector required to close the circuit around a dislocation. The Burgers vectors in edge and screw dislocations are shown in Figures 2.6 (a) and (b), respectively.

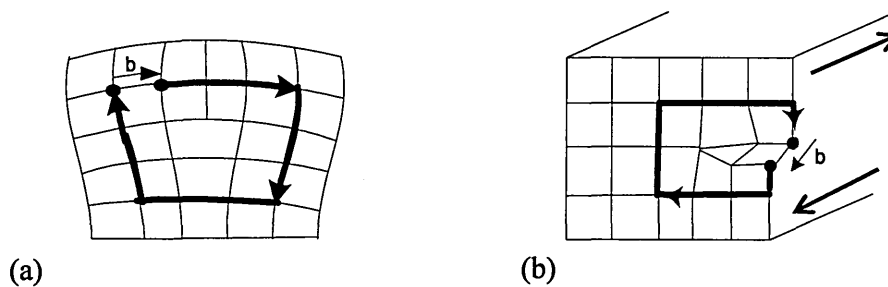


Figure 2.6: The Burgers vector, b , associated with (a) edge and (b) screw dislocations. The start and end points of a circuit around a dislocation are not at the same position, due to the imperfection of the lattice. The circuit around a dislocation is completed with the addition of the Burgers vector.

In screw dislocations, bonds in the lattice are strongly deformed, but not broken. However, the strain fields of the deformed bonds can lead to impurity trapping at the dislocation cores¹². The dislocation structures relevant to silicon and gallium nitride will be discussed in chapter 3.

2.4 Electrical properties of extended defects

Dislocations act as carrier trapping centres and can have a strong influence on the recombination mechanism of excess charge carriers. It has been shown in a number of semiconductors that an increase in dislocation density leads to decrease in carrier lifetime, which is an important parameter in transistor operation¹⁵. Since the 1950s, much effort has been spent on understanding the nature of the electrical activity associated with dislocations. In edge dislocations, there is an atom missing directly below (or above in the case of negative edge dislocations) the dislocation line and hence a dangling bond is present, if the bonds are assumed not to reconstruct. In 1953, Shockley described the 60° -shuffle-dislocation core as a row of dangling bonds and proposed that an edge dislocation in covalently bonded crystals could be represented by a half-filled one-dimensional (1D) band of states. This is because for a neutral dislocation, none of the states at the line are filled and each dangling bond contains one electron¹¹. This model is only applicable to edge dislocations or similar structures where bonds have been broken and does not apply to screw dislocations, where bonds are deformed, but not actually broken. However, the first model of the electrical properties of dislocations was developed in 1954 by Read, who was the first to take into consideration the line charge and long-range screening associated with dislocations¹⁶. He modelled the dislocation core as a row of closely spaced discrete acceptor-like states, at a level $(E_V + E_d)$, distributed evenly along the dislocation line, with spacing a between each acceptor state. The subscript d denotes dislocation. Hence there are $1/a$ states present per unit length of dislocation line. The distance between actual charged states is determined by the occupation ratio, f_d , which is equal to the fraction of occupied sites at the dislocation line, as illustrated in Figure 2.7.

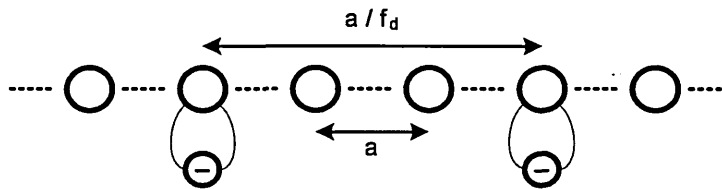


Figure 2.7: Schematic of negatively charged localised states at a dislocation core. Spacing between states is denoted by a . After Schroter and Cerva¹¹.

Generally, the separation between extrinsic point defects in dislocation-free material is large enough to avoid Coulomb forces acting between them. However, due to the small

separation between states in extended defects, a Coulomb interaction exists. To explain this effect, Read assumed that once these states are charged, the dislocation line develops a *line charge*, which is given by

$$q_d = \frac{ef_d}{a} \quad 2.26$$

and is extended over a cylinder of radius r_d , which is comparable to a in magnitude and it is determined by the extent of the wavefunction in the direction normal to the dislocation line¹⁷. Read described this cylinder as containing charged shallow impurities, with an associated charge density for values $r < r_d$ and zero charge density for $r > r_d$. It has been shown that this model can be applied to germanium (Ge), as the states are non-localised and distributed homogeneously along the dislocation line¹⁷. However, the model has been shown to be inadequate for Si, as the states are localised along the dislocation (such as impurities, kinks, or jogs)¹⁷. The line charge and its associated screening significantly influence the occupation statistics at dislocations. Due to the electrostatic interaction, the energy of an additional electron or hole that is added to the core is governed by the amount of charge already present (i.e. the number of occupied states). Güth and Haist reported that the interaction potential of an incoming carrier is perpendicular to the dislocation line and its magnitude varies logarithmically as a function of the distance from the core¹⁸. The authors derived the interaction potential to be significant until 10-20Å, after which the Coulombic interaction no longer has a strong influence on carriers in the vicinity of the core. The line charge of a dislocation is responsible for carrier scattering in various semiconductors. In 1960, Figielski found that the steady-state concentration of photocarriers was proportional to the logarithm of the light intensity, by photoconductivity experiments on plastically deformed germanium¹⁵. It was subsequently shown that a logarithmic capture law results in a Coulombic repulsion of carriers due to the line charge of the dislocation¹⁹. This principle is currently widely used in deep level transient spectroscopy (DLTS) to distinguish between extended and point defects in semiconductors. The DLTS technique is presented in Chapter 4 and DLTS of extended defects is discussed in Chapter 5.

2.5 Summary

This chapter has presented the occupation statistics at deep levels. It was shown that the capture and emission processes are dynamic, time-dependent systems. The trap occupancy of a deep level is governed by the free carrier densities within the material, as well as the capture and emission coefficients. The line charge properties of dislocations were discussed. A review of deep levels associated with dislocations in silicon and gallium nitride is presented in Chapter 5.

2.6 References

- ¹ S. M. Sze, *Physics of Semiconductor Devices*, John Wiley & Sons: New York (1981).
- ² B. Streetman and S. Banerjee, *Solid State Electronic Devices*, Prentice Hall: New Jersey, 2000.
- ³ M. Lannoo, *Band Theory Applied to Semiconductors* in *Handbook of Semiconductor Technology*, Edited by K. A. Jackson and W. Schöter, Vol. 1, Wiley-VCH: New York (2000).
- ⁴ C. Kittel, *Introduction to Solid State Physics*, John Wiley & Sons, New York (2005).
- ⁵ W. Shockley and W. T. Read, *Phys. Rev.* **87**, 835 (1952).
- ⁶ C. T. Sah, L. Forbes, L. L. Rosier, A. F. Tasch Jr, *Sol. State Electron.* **13**, 759 (1970).
- ⁷ H. Feichtinger, *Deep Centres in Semiconductors* in *Handbook of Semiconductor Technology*, Edited by K. A. Jackson and W. Schöter, Vol. 1, Wiley-VCH: New York (2000).
- ⁸ D. K. Shroder, *Semiconductor Material and Device Characterisation*, Wiley-Interscience: New York (1998).
- ⁹ I. Kovačević, V. P. Markevich, I. D. Hawkins, B. Pivac, A. R. Peaker, *J. Phys.: Condens. Matter* **17** S2229 (2005).
- ¹⁰ M. J. Klein, *Phys. Rev.* **97**, 1446 (1955).
- ¹¹ W. Schröter, H. Cerva, *Solid State Phenomena* **85-86**, 67 (2002).
- ¹² J. Friedel, *Dislocations*, Pergamon Press: Oxford (1964).
- ¹³ W. Schröter, I. Queisser, J. Kronewitz, *Inst. Phys. Conf. Ser.* **104**, 75 (1989).
- ¹⁴ J. I. Pankove, *Optical Processes in Semiconductors*, Dover Publications Inc.: New York (1971).
- ¹⁵ T. Figielski, *J. Phys.: Condens Matter* **14**, 12665 (2002).
- ¹⁶ W. T. Read, *Phil. Mag.* **45**, 775 or 1119 (1954).
- ¹⁷ R. Labusch, *J. Phys.: Condens. Matter* **14**, 12801 (2002).
- ¹⁸ W. Güth, W. Haist, *Phys. Stat. Sol.* **17**, 691 (1966).
- ¹⁹ T. Figielski, *Sol. State Electron* **21**, 1403 (1978).

Chapter 3

Defects in silicon and gallium nitride

This chapter considers defect structures in silicon and gallium nitride, which are of relevance to the results presented in chapters 6 and 7. Extended defects in silicon, including dislocations and oxidation-induced stacking faults are discussed in section 3.1. This is followed by an overview of threading dislocation formation in gallium nitride (GaN) due to growth on lattice mismatched substrates. The final sections of this chapter present a review of point defects and complexes inherent in *n*-type GaN.

3.1 Structure of dislocations in silicon

Dislocations in silicon can be detrimental to device performance by increasing leakage currents when present in active areas of devices. However, current fabrication techniques enable virtually defect-free silicon processes and dislocations are commonly introduced as gettering centres to remove impurities from active regions in very-large scale integration (VLSI) devices¹. The structural properties of dislocations and oxygen-induced-stacking faults and their associated levels in the silicon bandgap are discussed. The mechanism of dislocation-locking by oxygen is reviewed and oxygen related electrical levels are presented.

Silicon has the diamond crystal structure, as shown in Figure 3.1, where each atom is bonded covalently to four nearest neighbouring atoms in a tetrahedron configuration.

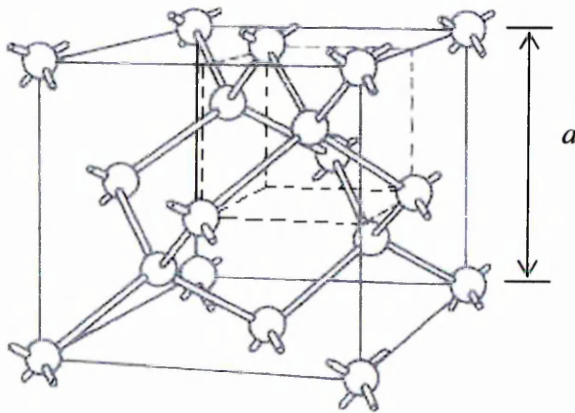


Figure 3.1: The diamond crystal structure. The lattice constant is denoted by 'a' and is equal to 5.43 Å at 300K in silicon. After Sze².

Dislocations in silicon can be generated due to a local defect (or flaw) resulting from mechanical stimulation, such as a scratch or indentation, at the surface. This forms an amorphous region, which transforms into dislocated Si at temperatures higher than about 500°C. In high-purity silicon, dislocations are generated even if the stress applied is very low. However, in Si containing particular impurities, the dislocations are only generated once the stress applied is greater than a certain critical value³.

Dislocations in silicon are energetically favourable when they lie along the [111] planes and are parallel to one of the close packed $\langle 110 \rangle$ directions^{4,5}. The common types of dislocations in Si are the '60°' and the 'screw' dislocations, where the Burgers vectorⁱ makes a 60° angle with the dislocation line for the former type and 0 degree angle for the latter³. Perfect dislocations in face-centred cubic (f.c.c.) crystals have a Burgers vector of $a/2 \langle 110 \rangle$ ⁵. However, the diamond crystal structure has two sublattices due to the interpenetrating body centred cubic structure in the f.c.c. lattice. Therefore, silicon has two different planes in which dislocation movement can occur. These are the closely packed (*glide*) or widely spaced (*shuffle*) planes, as shown in Figure 3.2.

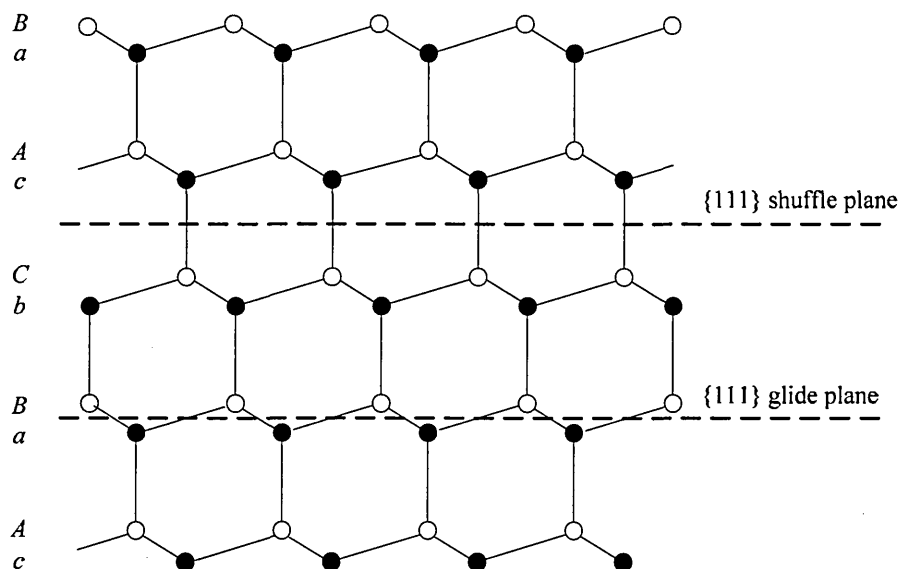


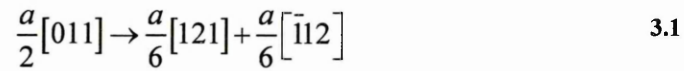
Figure 3.2: $\langle 110 \rangle$ projection of the silicon lattice, showing the stacking sequence and the glide and shuffle planes. The open and filled circles represent the different sublattices in the diamond crystal structure. After Duesbery and Joós⁶.

In Figure 3.2, the separation between the atomic layers in the shuffle plane, such as *A* and *a*, is equal to a covalent bond length. In contrast, the separation between atoms in the glide plane, such as *a* and *B* is equal to one third of a bond length⁷.

ⁱ The Burgers vector is described in Chapter 2, section 2.3.

Theoretical calculations suggest that dislocation movement in the shuffle plane should require less energy compared to the glide plane⁸. For a dislocation to move in the shuffle plane, only one bond must be broken, in comparison to the glide plane, where dislocation movement requires three bonds to be broken for the same distance of movement⁵.

The 60 degree dislocation in the glide plane dissociates into 90 degree and 30 degree Shockley partials separated by an intrinsic stacking fault of approximately 50\AA ⁹, as shown in Figure 3.3, with the following dissociation reaction^{5,10}:



This dissociation is only possible in the closely packed glide plane. This can be explained by taking into consideration that the formation of a Shockley partial requires a displacement of $a/6$. If such a displacement were to occur in the shuffle plane, the broken bonds of the Si atoms concerned would not be able to reconstruct in the tetrahedral structure. However, by considering an equal displacement in the glide plane, the broken bonds are able to reconstruct, which is energetically more favourable for the system as a whole. Furthermore, due to the closely-spaced structure of the glide plane, the orbitals exhibit a greater overlap in the glide set than in the core of the shuffle set dislocation. This suggests that reconstruction is more likely in the glide set dislocations than in the shuffle set⁵.

The intrinsic stacking fault resulting from the dissociation of the 60 degree dislocation is illustrated in Figure 3.3. The stacking sequence at the stacking fault in Figure 3.3 is “*Cc Aa Cc Aa B*”, in contrast to the stacking sequence of “*c Aa Bb Cc Aa B*” in the undisturbed structure illustrated in Figure 3.2.

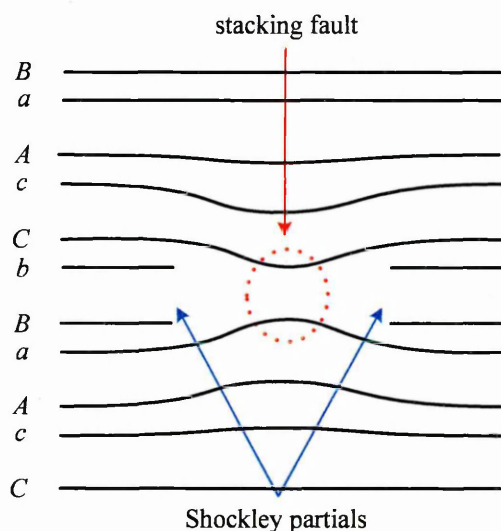


Figure 3.3: Two Shockley partials separated by an intrinsic stacking fault, due to the dissociation of the 60 degree dislocation in the glide plane.

Dislocation motion is considered to occur through certain points along the dislocation line, which are referred to as *kinks* and is governed by the kink formation and migration energies, which are denoted by F_k and W_m , respectively¹¹.

3.1.1 Oxidation-induced stacking faults (OISF)

During thermal oxidation of silicon, oxygen atoms diffuse through the growing silicon oxide (SiO_2) into the $\text{SiO}_2 - \text{Si}$ interface¹². However, not all silicon atoms at the oxide-silicon interface are oxidised to form SiO_2 and an excess of silicon atoms exist near the interface, forming silicon self-interstitials^{13,14}. The concentration of the interstitial Si atoms was found to decrease with an increasing oxidation rate¹⁵. The nucleation of OISF was observed to occur at sites of mechanical damage or impurity in inhomogeneities¹². Unlike the structure in Figure 3.3, OISFs consist of an *extrinsic* stacking fault surrounded by $a/3 \langle 111 \rangle$ Frank partial dislocations. This is illustrated in Figure 3.4, where the stacking sequence at the fault is “*c Aa Bb Aa Cc Aa B*”.

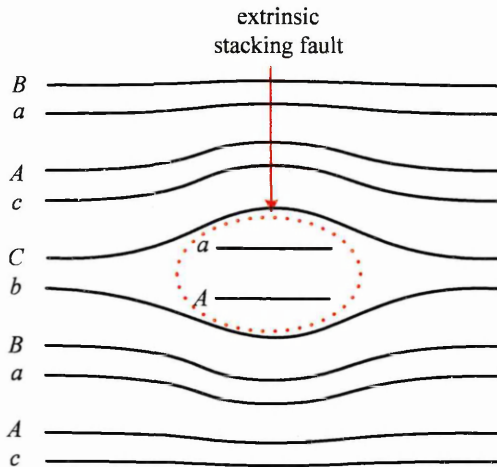


Figure 3. 4: An extrinsic stacking fault due to a plane of aA atoms inserted into an otherwise undisturbed structure. The stacking fault is bound by Frank partial dislocations with a Burgers vector of $a/3 \langle 111 \rangle$.

3.1.2 Dislocation-locking by oxygen in Czochralski silicon

Impurities tend to segregate to dislocations by diffusion processes, resulting in the accumulation of impurities at the dislocation, which is often referred to as a *Cottrell atmosphere*¹⁶, which can aid in suppressing dislocation generation in silicon³. The distribution of impurities around a dislocation are governed by Fermi-Dirac statistics, whereby the probability of an impurity occupying a site at the dislocation is given by

$$p = [1 + (1/C_0) \exp(-E_i/k_B T)]^{-1} \quad 3.2$$

where E_i is the energy of interaction between the impurity atom and the dislocation, C_0 is the average impurity concentration in the crystal, k_B is the Boltzmann constant and T is the temperature¹⁷. It can be seen from equation 3.2 that the probability of an impurity existing at the dislocation is reduced at higher temperatures and increased at lower temperatures. However, for any given impurity concentration, impurities are more likely to be trapped at dislocations at higher interaction energies, E_i . The interaction energy is governed by the elastic strain field of both the dislocation and the impurity atom¹⁷.

The oxygen impurity will be considered in this section, as the samples used in this study have been grown by the Czochralski (Cz) method, which has a typical interstitial oxygen concentration of 10^{17} - 10^{18} cm⁻³. At temperatures common to device processing (<1200°C) the interstitial oxygen exists as a super-saturated solution, leading to the formation of oxide precipitates^{18,19}.

Dislocations behave as nucleation sites for precipitates, which leads to the accumulation of super-saturated oxygen atoms at the dislocation. The nucleation step is the initial stage in precipitation and the models to describe nucleation are more complex than those for precipitate growth²⁰. Below ~650°C, oxygen precipitates lie homogeneously along the dislocation line, but at higher temperatures (above ~900°C), they have been observed by TEM studies to exist at discrete points along the dislocation line³. The size and the separation of the precipitates have been observed to increase with temperature and the anneal time²¹.

Oxygen precipitates at the dislocation core inhibit the movement of dislocations under stress, a phenomenon commonly known as *dislocation-locking*²². Dislocation motion occurs when the applied stress is above a critical stress, referred to as the *unlocking stress*. This property of oxygen precipitates in Cz-Si is highly beneficial, as it prevents plastic deformation during processing, which is why Cz-Si is the preferred starting material for very-large scale integration (VLSI)²³.

Yonenaga and Sumino have reported that the unlocking stress has been observed to increase with increasing oxygen content at the dislocation core, in samples with different dislocation densities²⁴. Investigations by Senkader *et al.* have shown that the unlocking stress also depends on the anneal time and temperature, as well as the oxygen concentration²⁵. Furthermore, Jurkschat *et al.* have reported that the unlocking stress is also determined by the mean precipitate diameter²⁶.

It has been shown experimentally that the dependency of the unlocking stress on annealing time of samples annealed between 700 and 850°C exhibit five different regimes, which is illustrated in Figure 3.5. The regimes are explained by Senkader *et al.*

as follows: In regime 1, the oxygen concentration at the dislocation core is low and increases with annealing time as the oxygen segregates to the core, resulting in an increase in the unlocking stress. This process is also temperature dependent and the probability of an oxygen atom occupying a site at the dislocation core will be increased at higher temperatures, as described by equation 3.2. As the oxygen concentration reaches a certain level, it enters into equilibrium with the background oxygen concentration, where the rate of oxygen capture and emission at the dislocation become matched. Any increase in temperature results in a decrease in the oxygen concentration at the core, as the O-atoms ‘boil off’ the dislocation. This is referred to as regime 2.

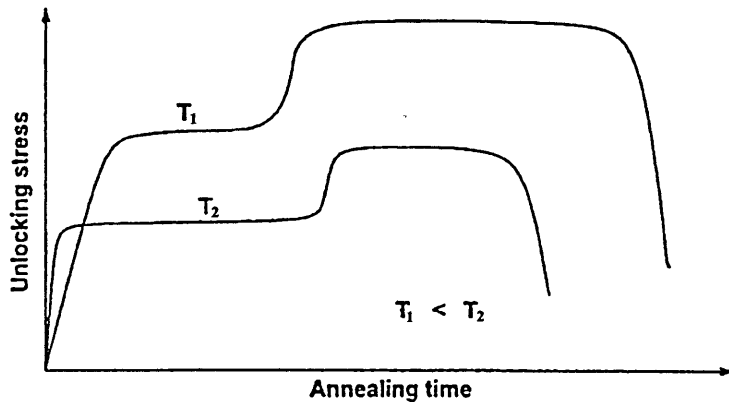


Figure 3.5: Illustration of the unlocking stress as a function of annealing time for two temperatures, T_1 and T_2 , where $T_1 < T_2$. After Senkader *et al.*¹⁸

In the third regime, oxygen precipitation occurs, resulting in a sudden increase in the unlocking stress. This is followed by another saturation phase (regime 4). In the final phase (regime 5), a decrease in the unlocking stress occurs, for which the authors have not yet provided an explanation. At lower annealing temperatures (350 – 700°C), regime 1 was observed, but the regime 2 and 3 behaviour was ambiguous. In some samples annealed at a lower temperature of 650°C, regimes 2 and 3 were observed after very long annealing times, resulting in very high unlocking stresses. On the other hand, samples annealed at higher temperatures shattered before any signs of regime 2 or 3 type behaviour were observed.

3.2 Growth of GaN and formation of threading dislocations

Despite many unanswered questions regarding the role of defects in gallium nitride (GaN), there has been considerable advancement in GaN based technologies, particularly for laser diodes (LDs) and short wavelength light emitting diodes (LEDs)^{27,28,29}. The properties of GaN show great potential for high power, high temperature, high frequency devices as well as optical devices³⁰. However, device performance is often limited by material quality and GaN suffers greatly from the presence of dislocations within the material, due to growth on lattice mismatched substrates³¹. Threading dislocations in GaN have been shown to provide pathways for leakage currents^{32,33} and to affect laser lifetimes³⁴.

In the following sections, the crystal structure of GaN is reviewed, followed by a discussion of growth induced threading edge dislocations. An overview of common point defects in GaN is provided in section 3.3 and and specific emphasis is placed on the gallium vacancy in section 3.4. To aid in the analysis of results in chapter 7, the focus of this chapter is primarily on *n*-type wurtzite GaN.

The material used for this study was grown by metal organic chemical vapour deposition (MOCVD). There are numerous techniques for growing gallium nitride and although this section will focus on the MOCVD technique, other leading methods will also be outlined to provide a comparison in material quality.

3.2.1 Crystal structure

Group III nitrides, such as GaN, InN and AlN, can crystallise in either the *zincblende* or the *wurtzite* structure, depending on growth conditions. The material studied in this work is hexagonal wurtzite GaN, which will be considered in this section.

The wurtzite structure resembles two interpenetrating hexagonal close-packed lattices. Each nitrogen (N) atom is tetrahedrally bonded to four neighbouring gallium (Ga) atoms. Similarly, each Ga atom is bonded to four N atoms. The crystal structure of wurtzite GaN is illustrated in Figure 3.6.

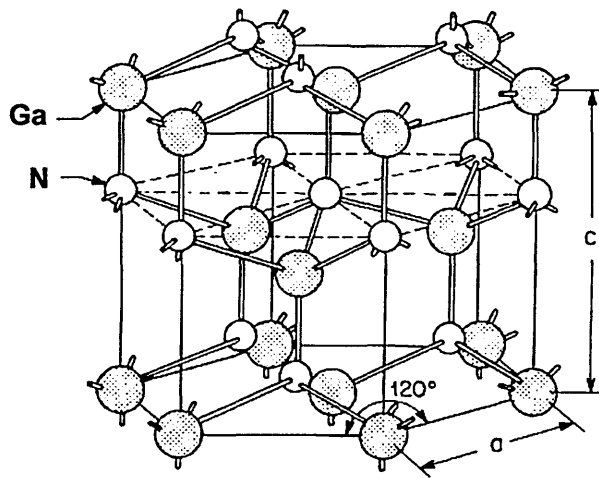


Figure 3.6: The wurtzite crystal structure of gallium nitride. The distance between Ga atoms (or N atoms) on the same hexagonal plane is denoted by the lattice constant a . The inter-plane spacing is denoted by the lattice constant c . After Sze².

The lattice constants a and c are in the range $5.75 - 6.03 \text{ \AA}$ and $9.39 - 9.861 \text{ \AA}$, respectively, giving a c/a ratio of $1.625 - 1.653$ ³⁵.

3.2.2 Threading dislocations in GaN

The theoretical melting point of gallium nitride is reported to be at a temperature of $\sim 2800\text{K}$ and at a pressure of 45kbar ^{36,37}. This results in a high nitrogen partial pressure near the melting point, where the dissociation of the nitrogen atom from the gallium atom becomes more favourable and prevents the growth of GaN from a melt³¹. The commercially viable method of GaN growth currently makes use of a substrate material. Common substrates are silicon carbide (SiC) and sapphire (Al_2O_3). The latter substrate material will be considered in this chapter, as the samples characterised in this work have been grown on sapphire.

The lattice parameters of Al_2O_3 and GaN are 4.76\AA and 3.18\AA , respectively. In theory, this should lead to a lattice mismatch of $\sim 50\%$. However, the actual lattice mismatch between Al_2O_3 and GaN is $\sim 14.6\%$, due to a 30° rotation of the GaN film about the $[0001]$ axis³⁸.

GaN grown on sapphire typically contains dislocation densities in the order of $10^6 - 10^8 \text{ cm}^{-2}$. The predominant dislocation types in MOCVD grown GaN are pure edge and mixed type dislocations. These dislocations are generated at the substrate-material interface and thread towards the surface, hence the term *threading dislocations* (TDs). Figure 3.7 (a) and (b) shows the dislocation line and the Burgers vector associated with pure edge and mixed type dislocations, respectively. In threading edge dislocations, Figure 3.7(a), the dislocation line is perpendicular to the sapphire-GaN interface.

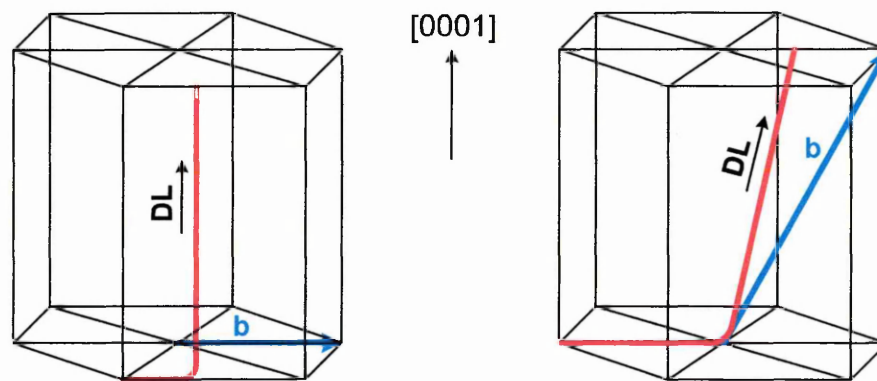


Figure 3.7 : The Burgers vector, b , associated with (a) pure edge and (b) mixed-type dislocations in GaN. DL indicates the dislocation line direction. After Mathis³⁹.

GaN growth typically involves a two step process. The initial step involves the growth of a $\sim 200\text{\AA}$ nucleation layer (NL) at $500 - 600^\circ\text{C}$ ³⁹. The NL is predominantly cubic³⁹ and associated with a stacking disorder⁴⁰. The second growth step is carried out at $\sim 1050^\circ\text{C}$ ^{38,39,41} where the NL partially transforms to hexagonal GaN³⁹. During the high temperature (HT) growth, islands of GaN (HT islands) are deposited on the NL layer, which grow laterally over the NL. It was suggested that the formation of threading edge dislocations is due to the coalescence of isolated HT islands during growth^{38,42}. More recent cross sectional TEM studies by Narayanan *et al.*⁴¹ indicated that TDs stem from the NL layer, which contains stacking faults.

It is not fully understood whether the dislocations themselves introduce deep levels into the bandgap, or whether the levels observed are solely due to point defects and clusters trapped at the dislocation cores. Theoretical calculations indicate that edge dislocations in GaN should have no deep states within the bandgap due to the relaxation of the lattice^{43,44}. However, the stretched bonds (Figure 3.8) result in stress fields, which may trap impurities and complexes and result in electrical activity^{44,45,46}.

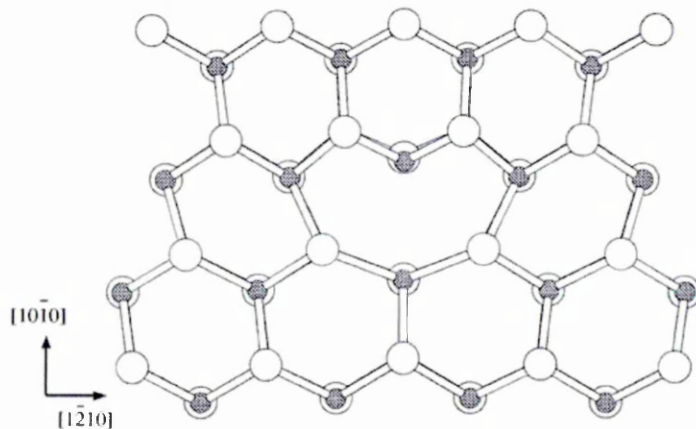


Figure 3.8: Top view (from the $[0001]$ direction) of the relaxed edge dislocation location core in GaN. The bond angles are widened and bond lengths are extended in the core region, resulting in a stress field. After Blumenau⁴⁴.

Impurity segregation to dislocations was confirmed using high resolution electron energy-loss spectroscopy (EELS)⁴⁷. Common defects situated at dislocations are gallium vacancies (V_{Ga}) and their complexes with oxygen atoms sitting at a nitrogen site (O_{N})⁴⁸. These types of defects will be discussed in more detail in section 3.4.

3.2.3 Metal organic chemical vapour deposition (MOCVD)

MOCVD is also referred to as metal organic vapour phase epitaxy (MOVPE) or organometallic VPE (OMVPE)³¹. This method is currently the leading technique for growing thin films of gallium nitride within the lighting industry, where the production of bright blue LEDs and other advanced GaN-based devices has been realised^{27,28}. MOCVD is currently preferred for large-scale manufacturing, because of well controlled *n*- and *p*-type doping³¹. Furthermore, it offers the possibility of depositing other elements such as aluminium (Al) and indium (In) and is regarded as the leading method for growing heterostructures^{27,28,31}. Multiple wafers that are typically 2" in diameter can be loaded into the reactor^{27,49}, with better than 2% thickness uniformities⁴⁹. In MOCVD, the sources of gallium and nitrogen are trimethylgallium (TMGa) and ammonia (NH_3) respectively.

Before the introduction of the two-flow reactor by Nakamura *et al.*⁵⁰ in 1990, high quality growth of GaN was problematic. The higher density and lower thermal conductivity of ammonia in comparison to hydrogen resulted in turbulent gas flows and reduced material quality⁵¹. The schematic of the two-flow reactor is shown in Figure 3.9(a). The reactor makes use of a subflow of nitrogen (N_2) and hydrogen (H_2) to bring the main flow (TMGa, NH_3 , H_2) into contact with the substrate, as illustrated in Figure 3.9(b).

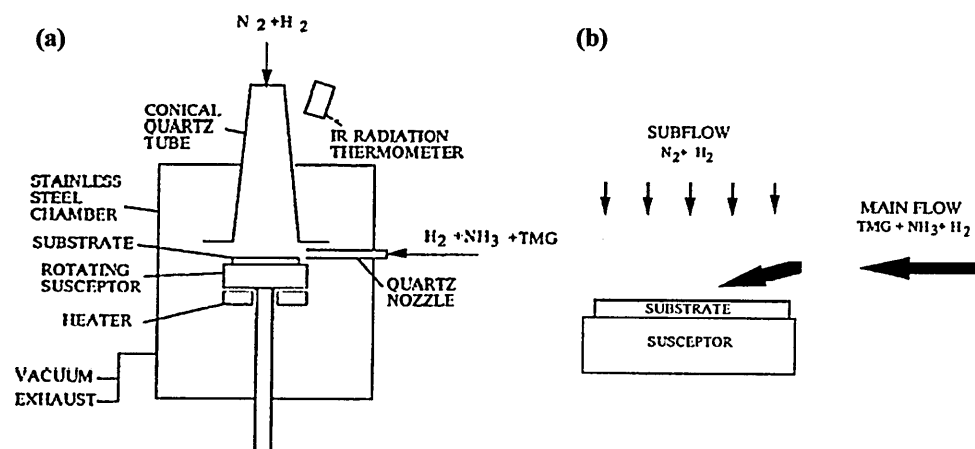


Figure 3.9: (a) Schematic of the two-flow MOCVD reactor and (b) illustration of the subflow of nitrogen and hydrogen used to bring the main flow into contact with the substrate. After Nakamura *et al.*⁵⁰

Other leading growth techniques include molecular beam epitaxy (MBE) and hydride vapour phase epitaxy (HVPE). The dislocation densities in GaN layers grown by MBE are typically in the order of 10^8 cm^{-2} , depending on growth conditions, buffer layer and the substrate used^{52,53}. Figure 3.10 illustrates the reduction in threading edge dislocations in the $1.4\mu\text{m}$ MBE grown layer in comparison to the $1.6\mu\text{m}$ MOCVD grown buffer layer.

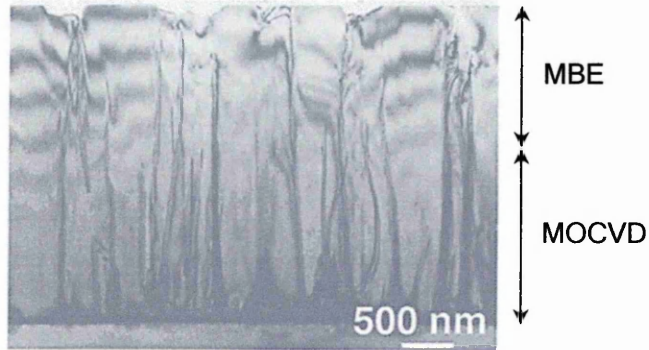


Figure 3.10: Cross-section TEM micrograph of GaN consisting of a $1.4 \mu\text{m}$ layer grown by MBE on top of a $1.6 \mu\text{m}$ MOCVD grown buffer layer. After Mathis *et al.*³⁹

Higher growth rates of $100\mu\text{m/h}$ are achievable through hydride vapour phase epitaxial (HVPE) growth of gallium nitride⁵⁴. By using this method, material quality is sacrificed for speed. Thick layers can be grown relatively quickly to provide templates for further thin film deposition using techniques resulting in higher quality films, such as MOCVD or MBE. Thick, free-standing GaN samples grown by HVPE with a dislocation density of 10^6 cm^{-2} at the upper surface have been reported⁵⁵.

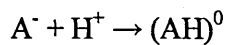
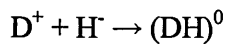
In this technique, the nitrogen source is ammonia (NH_3) gas, whilst the gallium is supplied by gallium monochloride (GaCl) gas, which is produced by the reaction of gallium with hydrogen chloride (HCl) at around 850°C ⁵⁶. Typically, thick layers (around $100\mu\text{m}$) are required for strain-free layers. Although the optical quality of GaN grown by this method is unexpectedly high, the possibility of device fabrication from such layers is limited due to the high amount of stress incorporated in the layers, which results in wafer bending.

3.3 Point defects in GaN

In this section the common defects in *n*-GaN are examined to provide a basis for the discussion of the electrically active deep levels in Chapter 5. The defects considered are hydrogen, silicon, oxygen, nitrogen vacancies and carbon. The gallium vacancy related defects are discussed separately in section 3.4 due to their dominance of the electrical activity associated with *n*-GaN.

3.3.1 Hydrogen

Hydrogen is present in most GaN growth processes such as MOCVD, ammonia-based MBE and HVPE⁵⁷. Atomic hydrogen can exist as H^0 , H^+ and H^- and the theoretical formation energies for these defects are dependent on the position of the Fermi level in the bandgap⁵⁸. In *p*-type GaN, it is able to compensate carriers by forming complexes with dopant atoms, resulting in the increase of material resistivity²⁷. This effect is generally more evident near the surface due to in-diffusion as a result of device processing. Neutral complexes with dopants form as outlined below³⁰. The ionised donor and acceptor is denoted by D^+ and A^- respectively.



Hydrogen is particularly found to be problematic in *p*-type material, where it forms neutral complexes with magnesium (Mg) acceptors and results in an increase in the material resistivity. Post-growth annealing at 400-500°C can be employed to activate the acceptors^{59,60}.

3.3.2 The nitrogen vacancy (V_N)

The nitrogen vacancy has been a topic of debate over the past decade, with opposing theoretical and experimental results on the electrical behaviour of the V_N . Due to the high vapour pressure of nitrogen during growth, the resulting GaN crystal was assumed to be nitrogen deficient. Based on an ionic model, the nitrogen vacancy should result in *n*-type conductivity, due to the spare electron in the outer shell of the gallium atom. Nominally undoped GaN is generally observed to be *n*-type and this behaviour was commonly assigned to the presence of V_N , which was thought to be the dominating native donor in GaN⁶¹. However, this model was found to have some flaws. Firstly, the theoretical formation energies of V_N do not agree with the high electron concentrations observed and the formation of nitrogen vacancies is energetically unfavourable. Additionally, secondary ion mass spectroscopy (SIMS) measurements have shown that

the concentrations of silicon and oxygen in nominally undoped GaN are high enough to correspond to the observed n -type conductivity⁶². Although nitrogen vacancies are no longer assumed to be the dominant donors in n -type gallium nitride, they are believed to act as compensating centres in p -type GaN⁶³.

3.3.3 Silicon at a gallium site (Si_{Ga})

Hall effect measurements indicate that the substitutional silicon atom at a gallium site (Si_{Ga}) is a single donor with an activation energy of $\sim 28\text{meV}$ ⁶⁴. However, values reported are believed to have a large inaccuracy due to the assumption that the prefactor used in the Arrhenius analysis is temperature independent⁶⁵. Further variable temperature Hall effect measurements in conjunction with photoluminescence studies by Götz *et al.*⁶⁵ have revealed lower activation energies between 12 and 17meV. The activation energy was found to be lower with increasing donor concentration and silane flow. Results also show that increasing donor concentration leads to a decrease in the donor activation energy. SIMS measurements have revealed that silicon concentrations can be in the order of 10^{17}cm^{-2} in nominally undoped GaN⁶⁶. Silicon is now the most common dopant used for n -type GaN.

3.3.4 Oxygen at a nitrogen site (O_{N})

The substrate-material interface is commonly highly defective, but also highly conductive⁶⁷. SIMS results indicate that oxygen is the main impurity in GaN grown on a sapphire substrate⁶⁸ and that the oxygen concentration can be twice that of silicon⁶⁹. Oxygen incorporation into GaN layers during growth is observed to increase the carrier concentration in the material by an order of magnitude⁷⁰. Theoretical calculations derive formation energy of less than 2eV for the O_{N} defect⁶², which is suggested to act as a shallow donor in GaN⁶⁹.

3.4 The gallium vacancy (V_{Ga}) and associated complexes

There is experimental evidence that dislocations in gallium nitride are negatively charged, suggesting that acceptor-type defects are present at dislocation cores. The negative charge associated with dislocations has been reported using scanning capacitance microscopy⁷¹ and electron holography in the transmission electron microscope (EH-TEM)⁴⁷. EH-TEM studies revealed a dislocation core charge of 4×10^7 electrons cm^{-1} in n -type GaN grown by MOCVD⁷². Initial observation of gallium

vacancies were reported by Saarinen *et al.*, who carried out substantial quantitative analysis using positron annihilation studies on MOCVD grown n -GaN⁷³. Positron annihilation is particularly useful in characterising vacancy-type defects, as the vacancies, which are missing a positive ion core, behave as trapping sites for positrons⁷⁴. Gallium vacancy (V_{Ga}) concentrations in the range of 10^{17} - 10^{18} cm^{-3} were reported⁷³.

There is good agreement between experimental and theoretical work on the nature and behaviour of the V_{Ga} . Theoretical calculations indicate that the gallium vacancy is the dominant point defect species in n -type GaN grown under nitrogen rich conditions^{63,75}. This is supported by positron annihilation studies, which have shown that V_{Ga} is the dominant acceptor in n -type GaN grown by MOCVD⁷³ and HVPE⁷⁶. The Ga vacancy is reported to be a triple acceptor, with a level deep in the bandgap^{43,77}. The transition energies associated with the V_{Ga} will be discussed later in this section.

Positron annihilation studies by Oila *et al.*⁷⁶ revealed that the V_{Ga} concentration decreases from $\sim 10^{19}$ to 10^{16} cm^{-3} , moving further away from the substrate-material interface (from 1 to 300 μm). This further confirms that there is a direct relationship between the Ga vacancy concentration and the dislocation density in the material, because the dislocation density increases towards the material-substrate interface. These deep acceptors at the dislocation sites will act as carrier trapping centres, reducing the free carrier concentration within the material⁷⁸.

Figure 3.11 shows the reported relationship between doping and free carrier (electron) concentrations in samples with different dislocation densities. The model is based on the calculated fraction of filled acceptor traps at dislocations⁷⁸.

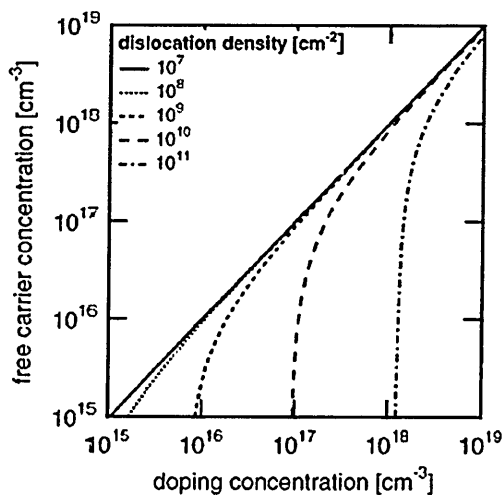


Figure 3.11: Free carrier (electron) density as a function of doping concentration with dislocation densities varying from 10^7 – 10^{11} cm^{-2} . After Weiman⁷⁸.

Figure 3.11 shows that a greater doping concentration is required to achieve a specific electron concentration for higher dislocation densities within the sample. Gallium vacancies were reported by Saarinen *et al.*⁷⁹ to be more abundant under nitrogen-rich conditions. An increase in the V/III molar ratio from 1000 to 10000 resulted in an increase in the V_{Ga} concentration from 10^{16} to 10^{19} cm^{-3} and a subsequent decrease in carrier concentration from 10^{20} to 10^{16} cm^{-3} . The carriers trapped at deep acceptors along dislocations results in negatively charged threading dislocations⁴⁷, which act as Coulomb scattering centres, consequently reducing transverse carrier mobility⁷⁸.

Theoretical calculations reveal the gallium vacancy to have the lowest formation energy in comparison to other native defects in n -GaN^{62,63}. The formation energy of V_{Ga} is reported to be dependent on the position of the Fermi level (E_{F}) within the bandgap^{62,63}. The theoretical formation energies of native defectsⁱⁱ in GaN are presented in Figure 3.12.

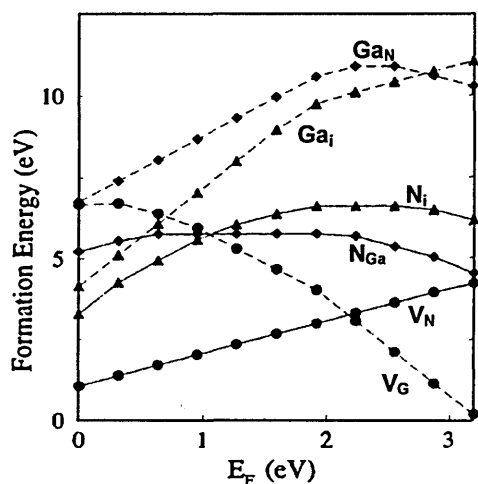


Figure 3.12: Theoretical formation energies of defects in gallium nitride as a function of the Fermi level position in the bandgap. After Neugebauer and Van de Walle⁶³.

Figure 3.12 shows that the formation energy of V_{Ga} should decrease as the Fermi level is raised. The gallium vacancy should readily form for heavily n -type samples with the Fermi level at the conduction band edge. Similarly, high V_{Ga} formation energies are expected for heavily p -type samples. This is supported by the absence of gallium vacancies in p -type GaN⁸⁰.

It was mentioned that the formation of Ga vacancies is more favourable under N-rich conditions, as reported by Saarinen *et al.* This was explained by considering that Ga sites may be left empty as a result of excess nitrogen during growth⁷⁹. Figure 3.13 presents the formation energies of defects and complexes common to GaN under Ga-

ⁱⁱ The term *native defects* describe defects which are associated with gallium and nitrogen atoms only and does not include defects due to impurities.

rich conditions. It is evident that the formation energy of V_{Ga} is greater under Ga-rich conditions than for N-rich conditions (Figure 3.12) for the same position of the Fermi level. This is in agreement with the above positron annihilation studies reported by Saarinen *et al.*⁷⁹. Gallium vacancy formation energies were also reported to depend on positions in the vicinity of dislocation cores. This will be discussed in section 3.4.1.

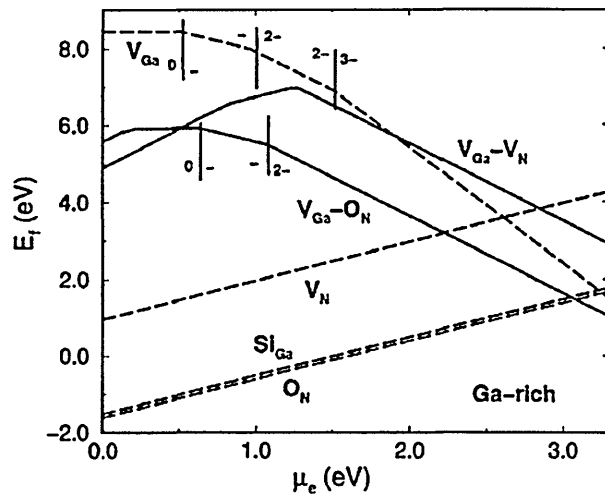


Figure 3.13: Theoretical formation energies of defects and complexes in GaN under gallium-rich conditions. After Mattila and Nieminen⁶².

Gallium vacancies created by electron irradiation with energies greater than 1MeV were observed to be stable up to 500 – 600 K using positron annihilation studies⁸¹. At such temperatures, they recover in long-range migration processes with a migration energy of ~ 1.5 eV⁸¹. This is in agreement with a theoretical migration barrier of 1.9 eV⁷⁷ and V_{Ga} is expected to be mobile at typical growth and annealing temperatures⁵⁷.

3.4.1 $V_{\text{Ga}} - (\text{O}_\text{N})_x$ complexes

Although the gallium vacancy is reported to have a low formation energy, experimental and theoretical work suggests that they form complexes with other impurities^{48,81}. The strongest candidate to form a complex with the V_{Ga} is the oxygen atom sitting at a nitrogen site (O_N)⁴³. This is based on several observations. Firstly, positron annihilation studies by Saarinen *et al.* indicate that Ga vacancies formed during growth (native V_{Ga}) are stable to much higher temperatures (1300 – 1500K) in comparison to those formed by electron irradiation, which recover at 500-600K⁸¹. This result suggests that native Ga vacancies are not isolated point defects, but are part of stable defect complexes, most likely with the highly abundant oxygen impurities⁸¹. Secondly, Oila *et al.* observed the

depth profile of V_{Ga} to be comparable to that of oxygen, which is greater towards the material-substrate interface. This indicates that O impurities may complex with Ga vacancies at dislocation cores⁷⁶.

Given that the concentration of gallium vacancies is typically in the range of 10^{17} - 10^{18} cm^{-3} , it would be reasonable to expect a high level of free carrier compensation, resulting in low carrier concentration levels. However, this is often not the case in n -type GaN, where free carrier density is not below the doping concentration. This suggests that the gallium vacancy is likely to complex with a shallow donor in GaN, resulting in negatively charged dislocations. It was mentioned in section 3.3.4 that oxygen at a nitrogen site is accepted to be a shallow donor and that SIMS measurements reveal the background oxygen concentration to be high enough to account for the carrier concentrations observed. Therefore, a reasonable assumption would be the formation of complexes between gallium vacancies and one or more oxygen atoms at a nitrogen site, which would account for carrier concentrations comparable to or higher than doping levels. This is supported by calculations which suggest that the formation of the $V_{\text{Ga}} - \text{O}_{\text{N}}$ complex is more energetically favourable than the isolated V_{Ga} ⁸². Figure 3.14 illustrates the structure of the $V_{\text{Ga}} - \text{O}_{\text{N}}$ complex. The V_{Ga}^{3-} is suggested to complex with up to three positively charged O_{N} donors^{48,62}. This results in the $V_{\text{Ga}} - (\text{O}_{\text{N}})_x^{(x-3)-}$ complex, where the value of 'x' can be 1, 2 or 3^[43]. For example, a Ga vacancy that has complexed with two oxygen donors results in the $V_{\text{Ga}} - (\text{O}_{2\text{N}})^-$ complex, which is a single acceptor. The binding energy of a single O_{N}^+ atom to the V_{Ga}^{3-} defect is calculated to be 2.2 eV⁴⁸.

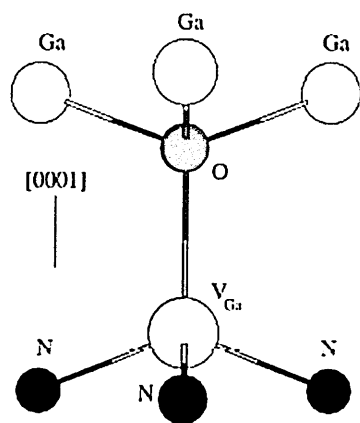


Figure 3.14: Schematic of the $V_{\text{Ga}} - \text{O}_{\text{N}}$ complex in GaN. The $V_{\text{Ga}} - (\text{O}_{\text{N}})_2$ and $V_{\text{Ga}} - (\text{O}_{\text{N}})_3$ complexes are formed by substituting additional threefold-coordinated nitrogen atoms by oxygen atoms. After Elsner *et al.*⁴⁸.

The negatively charged dislocations observed by positron annihilation⁷⁶, scanning capacitance spectroscopy⁷¹ and electron holography^{47,72} studies strongly suggest that acceptor centres, such as the V_{Ga} defects and $V_{\text{Ga}} - (\text{O}_{\text{N}})_x$ complexes, segregate to

dislocation cores. This is highly plausible due to the strain fields associated with dislocations, which act as impurity/defect trapping sites⁷⁵.

Extensive theoretical studies were carried out by Elsner *et al.* to investigate the formation and transition energies of the $V_{\text{Ga}} - (\text{O}_{\text{N}})_x$ complex at bulk and dislocation sites in GaN⁴⁸. The formation energies and transition levels are of significance to this work and will be mentioned here. Figure 3.15 shows three different positions (0, 1, 2 and 3) in a GaN supercell of 312 atoms. The positions are described in the figure caption.

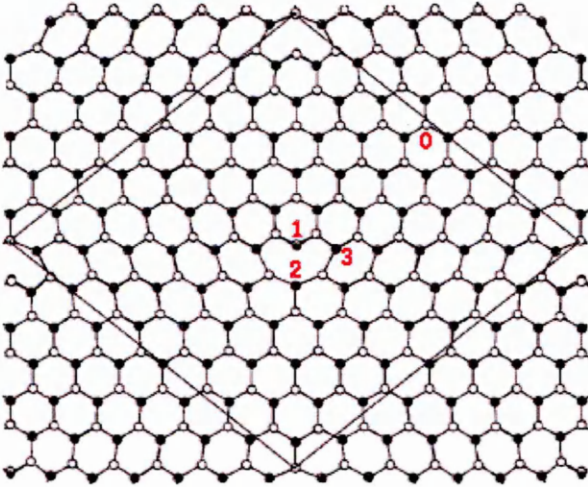


Figure 3.15: Different positions at an edge dislocation in a wurtzite supercell. The dislocations line (core) is labelled as position 1. Two additional positions, 2 and 3, are in the strain field of the dislocation. Position 0 represents a bulklike position, where the strain field of the dislocation is minimal in comparison to the core. After Elsner *et al.*⁴⁸.

The theoretical formation energies at positions 0, 1, 2 and 3, as obtained by Elsner *et al.*⁴⁸, are presented in Table 4.1. The calculations assume *n*-type doping where the Fermi level is pinned close to the conduction band edge.

Position	$E_f(V_{\text{Ga}}^{3-})$	$E_f(\text{O}_{\text{N}}^+)$	$E_f(V_{\text{Ga}}-\text{O}_{\text{N}})^{2-}$	$E_f(V_{\text{Ga}}-\text{O}_{2\text{N}}^-)$	$E_f(V_{\text{Ga}}-\text{O}_{3\text{N}})$
0 (bulk)	1.7	1.5	1.0	0.9	0.7
1 (core)	-0.2	0.2	-2.3	-2.5	-3.0
2	-0.3	1.3	-0.6	-0.3	-0.3
3	0.3	1.0	-1.0	-1.0	-0.8

Table 4.1: Formation energies of the triply charged Ga vacancy (V_{Ga}^{3-}), the positive oxygen donor (O_{N}^+) and their complexes $V_{\text{Ga}}-(\text{O}_{\text{N}})_x$ at the core of a dislocations and in the bulk of the crystal. The values are presented in electron volts (eV). After Elsner *et al.*⁴⁸.

The formation energies in Table 4.1 have several implications for the defect/impurity complexes. The formation energies associated with the oxygen donor suggest that it is

more stable at dislocation cores by 1.3 eV than in the bulk. It was reported by Oila *et al.* that the concentration of vacancies detected is greater by an order of magnitude in samples where *n*-type conductivity is achieved by oxygen doping than for Si doping⁸⁰. The above results are in support of $V_{\text{Ga}} - (\text{O}_{\text{N}})_x$ formation.

Similarly, the formation energy V_{Ga}^{3-} and its complexes with oxygen donor(s) is reported to be negative at the dislocation core in comparison to bulk positions. There is a strong agreement in theoretical calculations for the formation energy of the $V_{\text{Ga}} - (\text{O}_{\text{N}})^{2-}$ defect at bulk positions. Mattila and Nieminen report lower values of $\sim 0.9\text{eV}$ ⁶², whereas Neugebauer and Van de Walle also report a formation energy of $\sim 1.1\text{eV}$ ⁸².

The theoretical transition energies of the V_{Ga} and of $V_{\text{Ga}} - (\text{O}_{\text{N}})_x$ complexes from the valence band edge, in relation to their positions in the material are shown in Table 4.2.

Position	$E(V_{\text{Ga}})^{2-/3-}$	$E(V_{\text{Ga}}-\text{O}_{\text{N}})^{1-/2-}$	$E(V_{\text{Ga}}-\text{O}_{2\text{N}})^{0/-}$	$E(V_{\text{Ga}}-\text{O}_{3\text{N}})^{+/0}$
0 (bulk)	1.4	1.0	0.7	0.9
1 (core)	0.8	1.0	0.7	0.4
2	0.4	0.3	0.6	0.8
3	0.8	1.4	1.0	0.9

Table 4.2: The levels of the triple negatively charged Ga vacancy and of the $V_{\text{Ga}} - (\text{O}_{\text{N}})_x$ complexes within the bandgap. The values are measured in electron volts (eV) and are measured from the valence band edge.

The calculated energies are an indication of the energy separation between the valence band edge and the $V_{\text{Ga}} - (\text{O}_{\text{N}})_x$ complex. For example, the transition of a $V_{\text{Ga}} - (\text{O}_{\text{N}})$ complex from 1- to 2- requires the emission of a hole to the valence band (VB), which is the equivalent of capturing an electron from the VB.

The bonds in position 2 (Figure 3.8) are strongly strained and it is apparent from Table 4.2 that the theoretical transition energies are consistently low for the V_{Ga} defects and complexes at this position. Mattila and Nieminen⁶² report ~ 1.5 eV for the 2-/3- transition energy of the V_{Ga} defect, whereas Limpijumngong and Van de Walle⁷⁷ derive a lower transition energy of ~ 1.1 eV.

In summary, the stress field of threading-edge dislocations is expected to trap Ga vacancies, oxygen and their complexes. The gallium vacancies are expected to be

mobile at typical growth and processing temperatures. It can be concluded that the theoretical formation and transition energies for the V_{Ga}^{3-} are in good agreement. However, it is suggested that Ga vacancies are unstable and are expected to form stable complexes with other impurities. The oxygen impurity has been of significant consideration in the literature and is reported to be a strong contender to form a complex with the gallium vacancy. The $V_{\text{Ga}} - (\text{O}_{\text{N}})_x$ complexes are suggested to be most stable at dislocation cores. The presence of trapped charge at dislocations was evidenced by positron annihilation studies, scanning capacitance spectroscopy and electron holography. Moreover, the formation and transition energies are reported to be dependent on the position of the defect or complex within the material. This is due to the strongly deformed bonds at dislocations, resulting in strain fields.

3.5 Summary

Structural properties of dislocations and oxygen-induced stacking faults in silicon have been discussed. The properties of oxygen in silicon were considered in terms of their ability to inhibit dislocation motion, thereby improving the mechanical hardness of the crystal.

The key issues regarding GaN growth and related defects were highlighted. The gallium vacancy appears to be a dominant acceptor type defect in *n*-GaN and is associated with carrier compensation. Although the carrier compensation may appear minimal compared to doping levels due to the high shallow donor concentrations resulting from the oxygen impurities incorporated during growth, the carrier mobility is affected by the negatively charged dislocations. A strong relationship between V_{Ga} concentration and sample thickness has been provided through positron annihilation studies. Furthermore, theoretical studies suggests that the formation and ionisation energies of the $V_{\text{Ga}} - (\text{O}_{\text{N}})_x$ complexes are dependent on bulk positions.

3.6 References

- ¹ A. Giannattasio, S. Senkader, R. J. Falster, P. R. Wilshaw, *J. Phys. C* **14** 12981 (2002).
- ² S. M. Sze, *Physics of Semiconductor Devices*, John Wiley & Sons: New York (1981).
- ³ K. Sumino, *Metal. & Mat. Transactions A* **30A** 1465 (1999).
- ⁴ M. I. Heggie, R. Jones, G. M. S. Lister, A. Umerski, *Inst. Phys. Conf. Ser.* **104** 43 (1989).
- ⁵ H. Alexander and H. Teichler, *Dislocations in Handbook of Semiconductor Technology*, Edited by K. A. Jackson and W. Schöter, Vol. 1, Wiley-VCH: New York (2000).
- ⁶ M. S. Duesbery and B. Joós, *Phil. Mag. Lett.* **74**, 253 (1996).
- ⁷ M. Y. Chou, M. L. Cohen, S. G. Louie, *Phys. Rev. B* **32**, 7979 (1985).
- ⁸ W. Shockley, *Phys. Rev.* **91** 228 (1953).
- ⁹ P. B. Hirsch, *Mat. Sci. Tech.* **1** 666 (1985).
- ¹⁰ D. Hull, D. J. Bacon, *Introduction to Dislocations*, Butterworth-Heinemann: Oxford (1995).
- ¹¹ S. Scarle, C. P. Ewels, M. Heggie, N. Martsinovich, *Phys. Rev. B* **69**, 075209 (2004).
- ¹² K. V. Ravi, C. J. Varker, *J. Appl. Phys.* **45**, 263 (1974).
- ¹³ S. M. Hu, *J. Appl. Phys.* **45** 1567 (1974).
- ¹⁴ A. M-R Lin, R. W. Dutton, D. A. Antoniadis, W. A. Tiller, *J. Electrochem. Soc.* **128**, 1121 (1981).
- ¹⁵ S. P. Murarka, *J. Appl. Phys.* **48**, 5020 (1977).
- ¹⁶ R. Bullough, R. C. Newman, *Rep. Prog. Phys.* **33** 101 (1970).
- ¹⁷ K. Sumino, *Phys. Stat. Sol. (a)* **171** 111 (1999).
- ¹⁸ S. Senkader, P.R. Wilshaw, R. J. Falster, *J. Appl. Phys.* **89** 4803 (2001).
- ¹⁹ C. Claeys, E. Simoen, J. Vanhellefont, *J. Phys. III France* **7** 1469 (1997).
- ²⁰ K. F. Kelton, R. Falster, D. Gambaro, M. Olmo, M. Cornara, P. F. Wei, *J. Appl. Phys.* **85** 8097 (1999).
- ²¹ I. Yonenaga and K. Sumino, *J. Appl. Phys.* **80** 734 (1966).
- ²² S. M. Hu, *Appl. Phys. Lett.* **31** 53 (1977).
- ²³ S. Senkader, K. Jurkshat, D. Gambaro, R. J. Falster, P. R. Wilshaw, *Phil. Mag. A* **81**, 759 (2001).

- ²⁴ I. Yonenaga, K. Sumino, *J. Appl. Phys.* **56** 2346 (1984).
- ²⁵ S. Senkader, P. R. Wilshaw, R. J. Falster, *J. Appl. Phys.* **89**, 4803 (2001).
- ²⁶ K. Jurkschat, S. Senkader, P. R. Wilshaw, D. Gambaro, R. J. Falster, *J. Appl. Phys.* **90** 3219 (2001).
- ²⁷ R. Szweda, *Gallium Nitride & Related Wide Bandgap Materials & Devices*, Elsevier Science Ltd: Oxford (2000).
- ²⁸ S. J. Pearton, F. Ren, A. P. Zhang, K. P. Lee, *Mat. Sci. Eng.* **250**, 1 (2000).
- ²⁹ S. D. Lester, F. A. Ponce, M. G. Craford, D. A. Steigerwald, *Appl. Phys. Lett.* **66**, 1249 (1995).
- ³⁰ S. J. Pearton, J. C. Zolper, R. J. Shul, F. Ren, *J. Appl. Phys.* **86**, 1 (1999).
- ³¹ E. R. Weber and J. Krüger, *New Materials: Gallium Nitride* in *Handbook of Semiconductor Technology*, Edited by K. A. Jackson and W. Schöter, Vol. 1, Wiley-VCH: New York (2000).
- ³² P. Kozodoy, J. P. Ibbetson, H. Marchand, P. T. Fini, S. Keller, J. S. Speck, S. P. DenBaars, U. K. Mishra, *Appl. Phys. Lett.* **73**, 975 (1998).
- ³³ E. J. Miller, E. T. Yu, P. Waltereit, J. S. Speck, *Appl. Phys. Lett.* **84**, 535 (2004).
- ³⁴ M. Hansen, P. Fini, L. Zhao, A. C. Abare, L. A. Coldren, J. S. Speck, S. P. DenBaars, *Appl. Phys. Lett.* **76**, 529 (2000).
- ³⁵ B. J. Min, C. T. Chan, K. M. Ho, *Phys. Rev. B* **45**, 1159 (1992).
- ³⁶ S. Krukowski, *Cryst. Res. Technol.* **34**, 785 (1999).
- ³⁷ I. Grzegory, *J. Phys.: Condens. Matter* **13**, 6875 (2001).
- ³⁸ X. H. Wu, L. M. Brown, D. Kapolnek, S. Keller, B. Keller, S. P. DenBaars, J. S. Speck, *J. Appl. Phys.* **80**, 3228 (1996).
- ³⁹ S. K. Mathis, A. E. Romanov, L. F. Chen, G. E. Beltz, W. Pompe, J. S. Speck, *Phys. Stat. Sol. (a)* **179**, 125 (2000).
- ⁴⁰ J. S. Speck, S. J. Rosner, *Physica B* **273**, 24 (1999).
- ⁴¹ V. Narayanan, K. Lorenz, Wook Kim, S. Mahajan, *Appl. Phys. Lett.* **78**, 1544 (2001).
- ⁴² X. J. Ning, F. R. Chien, P. Pirouz, J. W. Yang, M. Asif Khan, *J. Mater. Res.* **11**, 580 (1996).
- ⁴³ R. Jones, J. Elsner, M. Haugk, R. Gutierrez, Th. Frauenheim, M. I. Heggie, S. Öberg, P. R. Briddon, *Phys. Stat. Sol. (a)* **171**, 167 (1999).
- ⁴⁴ A. T. Blumenau, J. Elsner, R. Jones, M. I. Heggie, S. Öberg, Th. Frauenheim, P. R. Briddon, *J. Phys. C* **12**, 10223 (2000).

- ⁴⁵ J. Elsner, R. Jones, P. K. Stitch, V. D. Porezag, M. Elstner, Th. Frauenheim, M. I. Heggie, S. Öberg, P. R. Briddon, *Phys. Rev. Lett.* **79** 3672 (1997).
- ⁴⁶ I. Arslan and N. D. Browning, *Phys. Rev. B* **65**, 075310-1 (2002).
- ⁴⁷ D. Cherns, M. E. Hawkrigde, *J. Mater. Sci.* **41** 2685 (2006).
- ⁴⁸ J. Elsner, R. Jones, M. I. Heggie, P. K. Stitch, M. Haugk, Th. Frauenheim, S. Öberg, P. R. Briddon, *Phys. Rev. B* **58**, 12571 (1998).
- ⁴⁹ B. Wachtendorf, R. Beccard, H. Jürgensen, O. Schön, M. Heuken, E. Woelk, *Mat. Res. Soc. Symp. Proc.* **468**, 7 (1997).
- ⁵⁰ S. Nakamura, Y. Harada, M. Seno, *Appl. Phys. Lett.* **58**, 2021 (1991).
- ⁵¹ D. Steigerwald, S. Rudaz, H. Liu, R. S. Kern, W. Götz, R. Fletcher, *J. Miner. Met. & Mat. Soc.* **49**, 18 (1997).
- ⁵² B. Heying, I. Smorchkova, C. Poblentz, C. Elsass, P. Fini, S. Den Baars, U. Mishra, J. S. Speck, *Appl. Phys. Lett.* **77**, 2885 (2000).
- ⁵³ H. M. Ng, D. Doppalapudi, T. D. Moustakas, N. G. Weimann, L. F. Eastman, *Appl. Phys. Lett.* **73**, 821, (1998).
- ⁵⁴ B. N. Feigelson and R. L. Henry, *J. Cryst. Growth* **281**, 5 (2005).
- ⁵⁵ J. Jasinski, W. Swider, Z. Litiental-Weber, P. Visconti, K. M. Jones, M. A. Reshchikov, F. Yun, H. Morkoç, S. S. Park, K. Y. Lee, *Appl. Phys. Lett.* **68**, 2297 (2001).
- ⁵⁶ S. T. Kim, Y. J. Lee, D. C. Moon, C. H. Hong, T. K. Yoo, *J. Cryst. Growth*, **194**, 37 (1998).
- ⁵⁷ M. A. Reshchikov, H. Morkoç, *J. Appl. Phys.* **97**, 061301-1 (2005).
- ⁵⁸ J. Neugebauer, C. G. Van de Walle, *Phys. Rev. Lett.* **75**, 4452 (1995).
- ⁵⁹ C. G. Van de Walle, *Phys. Rev. B* **56**, 10020 (1997).
- ⁶⁰ S. J. Pearton, C. R. Abernathy, C. B. Vartuli, J. W. Lee, J. D. MacKenzie, R. G. Wilson, R. J. Shul, F. Ren, J. M. Zavada, *J. Vac. Sci. Technol. A* **14**, 831 (1996).
- ⁶¹ P. Boguslawski, E. L. Briggs, J. Bernholc, *Phys. Rev. B* **51**, 17225 (1995).
- ⁶² T. Mattila, R. M. Nieminen, *Phys. Rev. B* **55**, 9571 (1997).
- ⁶³ J. Neugebauer, C. G. Van de Walle, *Phys. Rev. B* **50**, 8067 (1994).
- ⁶⁴ P. Hacke, A. Maekawa, N. Koide, K. Hiramatsu, N. Sawaki, *Jpn. J. Appl. Phys.* **33**, 6443 (1994).
- ⁶⁵ W. Götz, N. M. Johnson, C. Chen, H. Liu, C. Kuo, W. Imler, *Appl. Phys. Lett.* **68**, 3144 (1996).
- ⁶⁶ D. C. Look, C. E. Stutz, R. J. Molnar, K. Saarinen, Z. Liliental-Weber, *Sol. State Commun.* **117**, 571 (2001).

- ⁶⁷ C. Mavroidis, J. J. Harris, M. J. Kappers, N. Sharma, C. J. Humphreys, E. J. Thrush, *Appl. Phys. Lett.* **79**, 1121 (2001).
- ⁶⁸ G. Popovici, W. Kim, A. Botchkarev, H. Tang, J. Solomon, H. Morkoç, *Mat. Res. Soc. Symp. Proc.* **468**, 3 (1997).
- ⁶⁹ D. Meister, M. Böhm, M. Topf, W. Kriegseis, W. Burkhardt, I. Dirnstorfer, S. Rösel, B. Farangis, B. K. Meyer, A. Hoffmann, H. Siegle, C. Thomsen, J. Christen, F. Bertram, *J. Appl. Phys.* **88**, 1811 (2000).
- ⁷⁰ B. C. Chung, M. Gershenson, *J. Appl. Phys.* **72**, 651 (1992).
- ⁷¹ P. J. Hansen, Y. E. Strausser, A. N. Erickson, E. J. Tarsa, P. Kozodoy, E. G. Brazel, J. P. Ibbetson, U. Mishra, V. Narayanamurti, S. P. Den Baars, J. S. Speck, *Appl. Phys. Lett.* **72**, 2247 (1998).
- ⁷² D. Cherns, C. G. Jiao, *Phys. Rev. Lett.* **87**, 205504-1 (2001).
- ⁷³ K. Saarinen, T. Laine, S. Kuisma, J. Nissilä, P. Hautojärvi, L. Dobrzynski, J. M. Baranowski, K. Pakula, R. Stepniewski, M. Wojdak, A. Wyszomolek, T. Suski, M. Leszczynski, I. Grzegory, S. Porowski, *Phys. Rev. Lett.* **79**, 3030 (1997).
- ⁷⁴ D. K. Schroder, *Semiconductor Material and Device Characterisation*, John Wiley & Sons: New York (1998).
- ⁷⁵ A. F. Wright, U. Grossner, *Appl. Phys. Lett.* **73**, 2751 (1998).
- ⁷⁶ J. Oila, J. Kivioja, V. Ranki, K. Saarinen, D. C. Look, R. J. Molnar, S. S. Park, S. K. Lee, J. Y. Han, *Appl. Phys. Lett.* **82**, 3433 (2003).
- ⁷⁷ S. Limpijumnong, C. G. Van de Walle, *Phys. Rev. B* **69**, 035207 (2004).
- ⁷⁸ N. G. Weimann, L. F. Eastman, D. Doppalapudi, H. M. Ng, T. D. Moustakas, *J. Appl. Phys.* **83**, 3656 (1998).
- ⁷⁹ K. Saarinen, P. Seppälä, J. Oila, P. Hautojärvi, C. Corbel, O. Briot, R. L. Aulombard, *Appl. Phys. Lett.* **73**, 3253 (1998).
- ⁸⁰ J. Oila, V. Ranki, J. Kivioja, K. Saarinen, P. Hautojärvi, J. Likonen, J. M. Baranowski, K. Pakula, T. Suski, M. Leszczynski, I. Grzegory, *Phys. Rev. B* **63**, 045205-1 (2001).
- ⁸¹ K. Saarinen, T. Suski, I. Grzegory, D. C. Look, *Phys. Rev. B* **64**, 233201 (2001).
- ⁸² J. Neugebauer and C. Van de Walle, *Appl. Phys. Lett.* **69**, 503 (1996).

Chapter 4

Characterisation techniques

This chapter presents the experimental techniques and theoretical concepts which are used in the characterisation of defects in semiconductors studied in this work. The first section describes the principles of the Schottky Barrier Diode (SBD), to establish the foundations for the characterisation techniques used in this study. The following sections describe the deep level transient spectroscopy (DLTS) and Laplace DLTS (LDLTS) techniques.

4.1 The Schottky Barrier Diode

The space-charge region (SCR) in a Schottky diode is fundamental to the principles of DLTS and Laplace DLTS. Therefore, the principles of the Schottky diode are examined in this section. Numerous manuscripts cover the theoretical concepts of the Schottky barrier diode, including Sze¹, Schroder² and Rhoderick and Williams³, which have been referenced in the following summary.

4.1.1 Energy band structure

Figure 4.1(a) shows the band diagrams of a metal and n -type semiconductor, which are sufficiently far apart and electrically neutral. The workfunctions of the metal and semiconductor are denoted by $q\phi_m$ and $q\phi_s$, respectively. The workfunction of a solid is the energy required to excite an electron from the Fermi level to the vacuum level¹. For a semiconductor this is equal to $q\phi_s = q(\chi_s + V_n)$. The electron affinity at the surface, $q\chi_s$, is equal to the energy difference between the vacuum level and the conduction band edge¹. The difference between the Fermi level and the conduction band edge is denoted by qV_n .

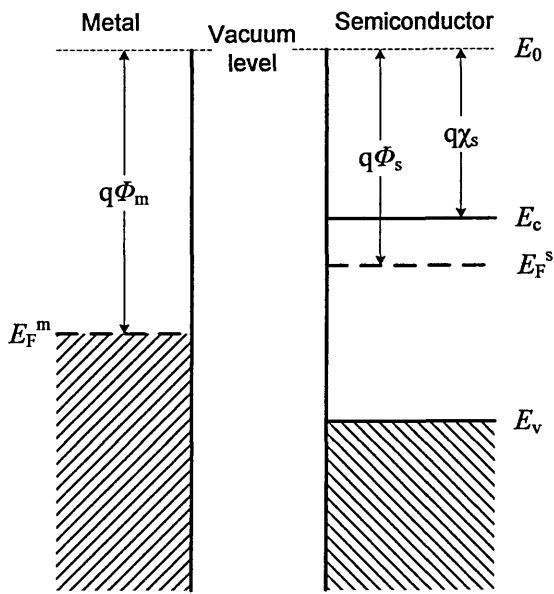


Figure 4.1(a): Energy band diagram of a metal and *n*-type semiconductor placed apart and electrically neutral.

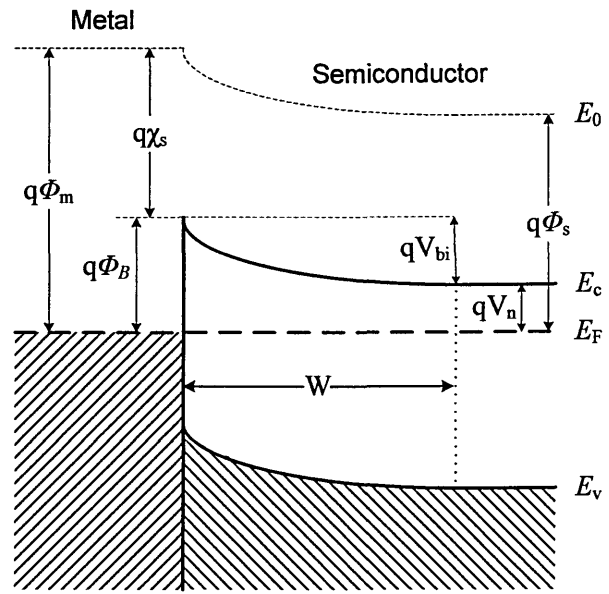


Figure 4.1(b): Energy band diagram of a metal and semiconductor in perfect contact and thermal equilibrium.

Upon contact, the electrons from the semiconductor flow into the metal and the Fermi levels become aligned at thermal equilibrium³. This is illustrated in Figure 4.1(b). The electrons passing from the metal to the semiconductor face a potential barrier, $q\phi_B = q(\phi_m - \chi_s)$. Similarly, the electrons flowing from the semiconductor into the metal face a potential barrier, $V_{bi} = \phi_m - \phi_s$, which is referred to as the built-in potential^{1,3}. For a Schottky barrier diode the workfunction of the metal must be greater than that of the semiconductor, in order for the diode to have electrical current rectification properties required for Scottky device operation.

4.1.2 The depletion region

The electron flow from the semiconductor to the metal under thermal equilibrium leaves behind uncompensated donor ions close to the metal-semiconductor interface. This region is referred to as the space-charge region (or depletion region), as it is depleted of free carriers³. The space-charge region exists from the metal-semiconductor interface ($x = 0$) until the point where the semiconductor energy bands become flat ($x = W$), as denoted by ' W ' in Figure 4.1(b).

For an *n*-type semiconductor with no external bias applied, the charge density within the depletion region is equal to qN_D . However beyond $x = W$, the semiconductor is neutral¹.

Using Gauss's theorem, the electric field in the SCR can be related to the charge density by³

$$\frac{\partial \mathcal{E}}{\partial x} = \frac{qN_D}{\epsilon_s} \quad 4.1$$

Integrating equation 4.1 with respect to x , with one boundary condition of $x = W$ at the edge of the SCR gives

$$\mathcal{E}(x) = -\frac{qN_D(W-x)}{\epsilon_s} \quad 4.2$$

The electric field, $\mathcal{E}(x)$ increases linearly from the edge of the depletion region (at $x = W$), where it is equal to zero, to a maximum at the metal-semiconductor interface (at $x = 0$)². The magnitude of $\mathcal{E}(x)$ is therefore negative, as it increases in the negative x direction.

The potential distribution within the SCR is obtained by integrating equation 4.2 using the previous boundary conditions

$$V(x) = -\frac{qN_D}{\epsilon_s} \int_x^W (W-x) dx = -\frac{qN_D}{2\epsilon_s} (W-x)^2 \quad 4.3$$

The potential rises quadratically towards the metal-semiconductor interface, where it is equal to diffusion potential (or built-in potential)

$$V_{bi} = \frac{qN_D W^2}{2\epsilon_s} \quad 4.4$$

which gives the depletion region width as

$$W = \sqrt{\frac{2\epsilon_s V_{bi}}{qN_D}} \quad 4.5$$

It must be noted that equation 4.5 is obtained through the abrupt approximation, which assumes that the transition between the space-charge region and the neutral semiconductor is abrupt¹. This is not the case in real semiconductors and the depletion region width can be represented more accurately by replacing the term V_{bi} by $(V_{bi} - kT/q)$ as a correction factor for the majority carrier distribution tails¹. For a pn-junction, this correction value would be doubled, to account for the holes on the p side. This transition length is referred to as the Debye length, L_D , and is given by

$$L_D = \sqrt{\frac{\epsilon_s kT}{q^2 N_D}} \quad 4.6$$

Figure 4.2(a) and (b) illustrate the effect of external bias on the width of the SCR region for an n -type semiconductor under two different reverse bias conditions. In Figure 4.2(a) a reverse bias of V_R is applied, resulting in a space-charge region of W_R . The reverse bias V_P in (b) is more positive than V_R and results in a smaller SCR width, denoted by W_P .

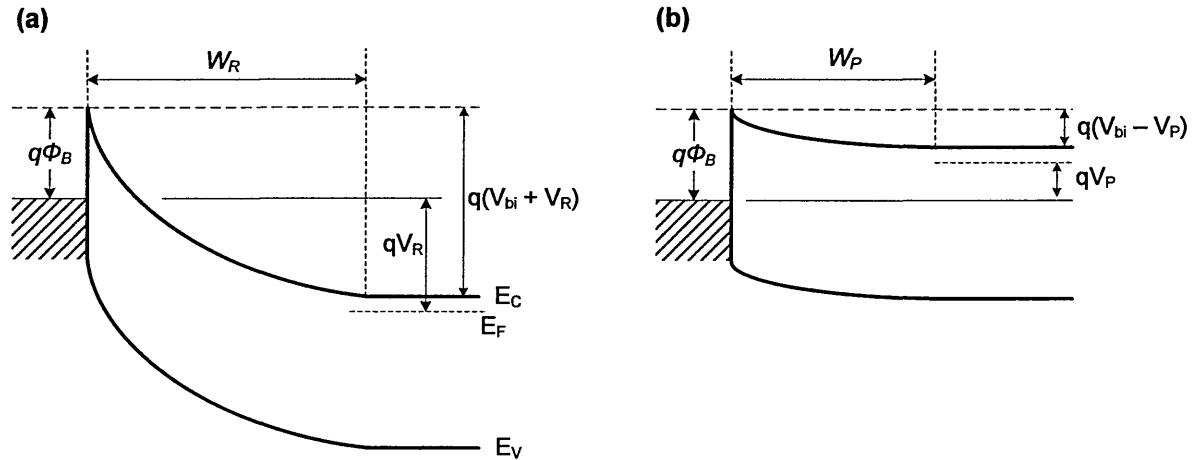


Figure 4.2: The energy band diagrams for a Schottky barrier diode under (a) a reverse bias of V_R and (b) a bias $V_R < V_P < 0V$, typically used in DLTS as a filling pulse.

4.2 Capacitance – voltage measurements

Referring to the band diagram in Figure 4.2(b) of a reverse biased diode with a depletion region of W , a further increase in the reverse bias will result in an increase in the SCR width. Therefore, the total charge in the depletion region will change, resulting in a change in capacitance.

From equation 4.4, which defines the built-in voltage, V_{bi} , an expression for the maximum field strength, $|\mathcal{E}_{max}|$ can be obtained

$$|\mathcal{E}_{max}| = \frac{qN_D W}{\epsilon_s} = \frac{Q_D}{\epsilon_s} \quad 4.7$$

where Q_D is the total charge per unit area in the depletion region. Rearranging equation 4.7 to solve for W in terms of Q_D and substituting this into equation 4.4 gives

$$V_{bi} = \frac{Q_D^2}{2\epsilon_s q N_D} \quad 4.8$$

The capacitance per unit area, C , is obtained by differentiating equation 4.8 with respect to V_{bi} and substituting for V_{bi} using equation 4.8, and for Q_D using equation 4.7

$$C \equiv \frac{\partial Q_D}{\partial V_{bi}} = \sqrt{\frac{\epsilon_s q N_D}{2V_{bi}}} = \frac{\epsilon_s}{W} \quad 4.9$$

Equation 4.8 shows that under the depletion approximation the resulting capacitance per unit area due to the space-charge region of a Schottky diode is represented in the same way as that of a parallel-plate capacitor with a dielectric constant of ϵ_s and width W^1 . However, some significant differences do exist. Equation 4.9 is derived using the abrupt approximation and does not take into account the Debye tail, as discussed in section 4.1.2 and represented by equation 4.5. The width of the depletion region, W , is not static and is a function of the reverse bias applied. Furthermore, the charge on a parallel-plate capacitor exists on the two surfaces of the metal plates on either side of the dielectric. By contrast, the charge in a Schottky diode consists of the charge in the metal and at the edge of the depletion region, which is balanced by the uncompensated donors and acceptors in the depletion region³.

Solving for $1/C^2$ in equation 4.9 gives $1/C^2 = 2V_{bi}/\epsilon_s q N_D$ and differentiating this with respect to V results in the following expression for $\partial(1/C^2)/\partial V$

$$\frac{\partial(1/C^2)}{\partial V} = \frac{2}{\epsilon_s q N_D} \quad 4.10$$

The capacitance of a diode is measured as a function of the applied reverse bias, V . The ionised donor concentration in the substrate can be determined from the slope of a $1/C^2$ versus V curve².

4.3 Deep Level Transient Spectroscopy

Deep level transient spectroscopy (DLTS) was introduced by Lang in 1974⁴ and is now a commonly used technique for characterising deep levels in semiconductors. The sensitivity of DLTS is outstanding and electrically active trap concentrations of $\sim 10^{10}$ - 10^{11} cm^{-3} can be detected. Typically, DLTS can detect concentrations as low as 10^{-6} times the background carrier concentration, if the background carrier concentration is of the order of 10^{16} cm^{-3} .

The principle of DLTS relies on changing the trap occupancy in the space-charge region, in order to produce a depletion capacitance transient, from which the temperature-dependent emission behaviour of traps can be investigated. It is based on the thermally stimulated capacitance (TSCAP) method, which has been covered extensively by Sah *et al.*⁵ and Miller *et al.*⁶. However, DLTS offers greater sensitivity and measurements are much more rapid using DLTS than other methods. This is primarily because Lang introduced the 'rate window' concept, which allows the measurement to be carried out continuously over a temperature range, rather than collecting data over a range of fixed temperatures.

In order to describe the DLTS method, an *n*-type Schottky diode will be considered. DLTS involves applying a quiescent reverse bias V_R to a diode and periodically applying a bias pulse V_P , which is commonly referred to as the fill pulse. The fill pulse must be relatively more positive than V_R (i.e. $V_P > V_R$, although $|V_P| < |V_R|$), in order to fill the empty traps in the space-charge region. A typical DLTS pulse train is illustrated in Figure 4.3.

As described in the previous section, each reverse bias results in a specific space-charge width and capacitance. The capacitance at the quiescent reverse bias (or steady-state capacitance) is denoted by C_0 and occurs at $V = V_R$.

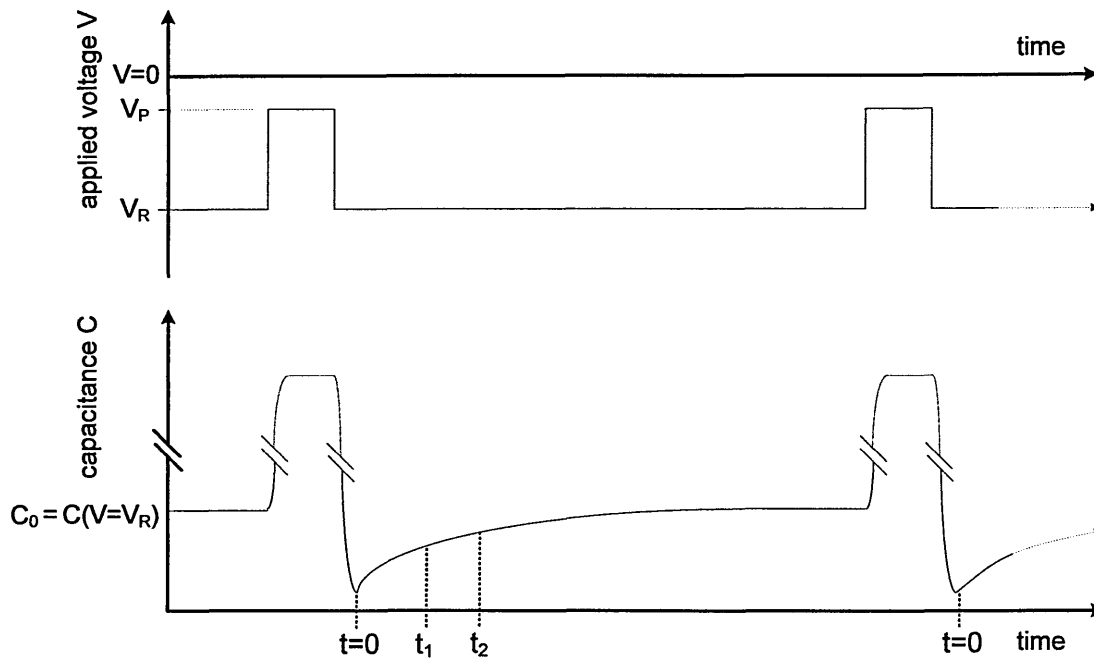


Figure 4.3: Illustration of the DLTS pulse train sequence (top) and the resulting diode capacitance (bottom). The diode is kept at a steady-state reverse bias (V_R) and periodically pulsed to a relatively more positive value (V_P). In DLTS, the capacitance transient during return to steady-state (C_0) is sampled at two points in time, t_1 and t_2 .

In order to explain the changes in the diode capacitance, the depletion region must be considered. Figure 4.4 illustrates the effects on the SCR at three stages during the biasing sequence. Initially, the diode is under a quiescent reverse bias, (a), and the resulting depletion width is denoted by W_R . However, the width of the region directly beneath the metal/semiconductor interface containing empty traps is not necessarily equal to the width of the space-charge region. In reality, the states below the Fermi level are full and those that lie above are empty, which suggests that there could be deep levels within the depletion region which are occupied by electrons, depending on the position of the trap level and the Fermi level within the bandgap⁷. This is illustrated in Figure 4.5 and the region within the SCR containing levels occupied by electrons is denoted by λ .

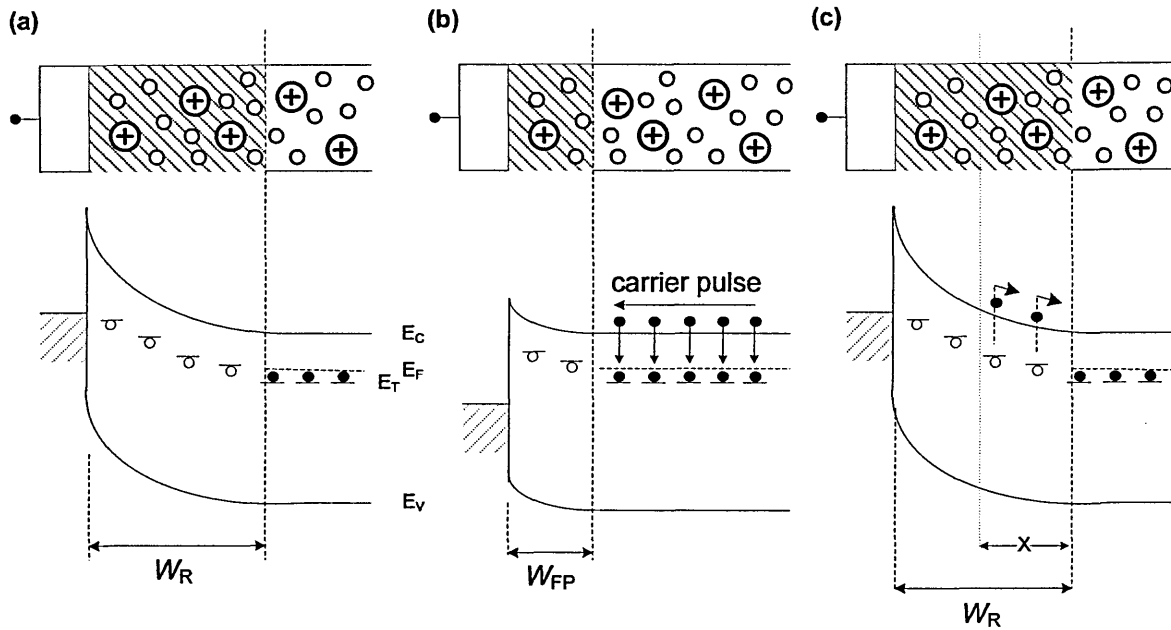


Figure 4.4: Energy-band diagram and schematic of a Schottky diode showing the depletion region and filled/empty traps under (a) quiescent reverse bias V_R ($t > 0$) (b) a carrier injection (fill) pulse of V_p and (c) return to original quiescent reverse bias V_R . The region probed during the DLTS experiment is indicated by 'X'. The dark and open circles represent occupied and vacant states, respectively. The carrier pulse indicates the movement of electrons.

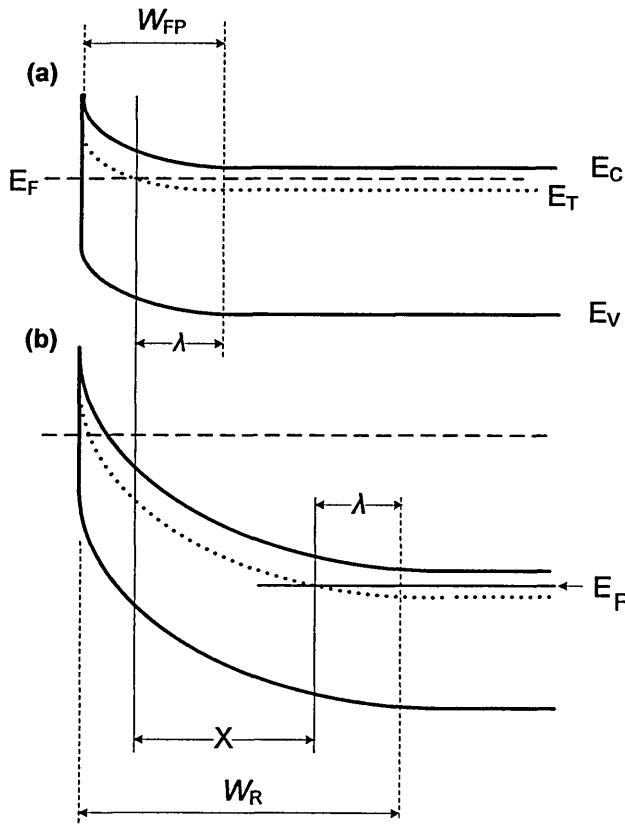


Figure 4.5: Energy-band diagram of an n -type Schottky diode showing the region within the depletion region containing occupied states, as denoted by λ , under (a) a filling pulse of $V_R < V_{FP} < 0$, such as in Figure 4.2(b) and (b) a reverse bias of V_R , with a Fermi level of E_{Fn} . It can be seen that in both cases, the region λ is the same, as it is independent of the bias applied. The region probed during the DLTS experiment is denoted by X.

The region of occupied levels, λ , is independent of the applied bias⁷ and is given by

$$\lambda = \sqrt{\frac{2\varepsilon_s(E_F - E_T)}{q^2(N_D - N_A)}} \approx \sqrt{\frac{2\varepsilon_s(E_F - E_T)}{q^2N_D}} \quad \text{for } N_D \gg N_A \quad 4.11$$

The application of a forward bias pulse (V_P) allows majority carriers, in this case electrons, to be introduced into the scr, where they are captured, as shown in Figure 4.4 (b). Returning the bias back to V_R momentarily reduces the depletion capacitance to below the steady-state value of C_0 . The deep levels are no longer in thermal equilibrium and the electrons are thermally emitted back to the conduction band over time, which is displayed in Figure 4.4 (c). During this process, the diode capacitance returns to its steady-state value C_0 , as represented by the capacitance transient in Figure 4.3. The transient displayed in Figure 4.3 is a result of majority carrier emission. The transient for minority carrier emission is the opposite of the one in Figure 4.3. This is because during the return to equilibrium, the minority carrier traps emit their carriers, similar to the situation for majority carrier traps. For an n -type semiconductor, the minority carriers are holes. By emitting a hole to the valence band, the charge state of a minority carrier trap changes from being neutral, to being negatively charged. The time-dependant exponential transient for a minority carrier emission process is displayed in Figure 4.6. Transient A is similar to that in Figure 4.3 and is a result of emission from majority carrier traps. The steady-state capacitance is denoted by C_0 , where the traps have emitted their carriers and the total charge in the depletion region is equal to the ionised donor concentration. Transient B is representative of minority carrier emission, where the minority carrier traps emit their carriers and the depletion region gradually becomes more negative. The total charge in the depletion region at steady-state is equal to $N_D - N_T$ and the capacitance falls to C_Z . It is also apparent from Figure 4.6 that at $t = 0$, the capacitance for transient A is equal to C_Z , because at this point, the majority carrier traps are occupied by electrons.

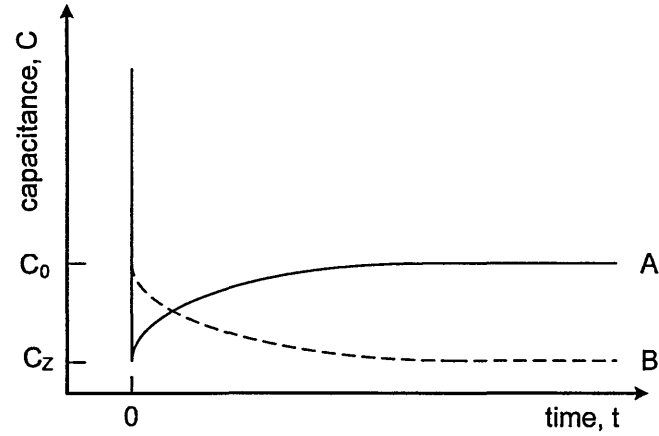


Figure 4.6: The time dependant capacitance transients following a carrier injection pulse for majority carrier emission (A) and minority carrier emission (B).

The capacitance transients considered are the essence of TSCAP and DLTS. This section will build on the emission and capture kinetics from defects, which have been considered in Chapter 2 in order to describe the principles behind DLTS.

The capacitance of a Schottky diode with an area A is given by

$$C = A \sqrt{\frac{q\epsilon_s N_w}{2(V_{bi} - V)}} = A \sqrt{\frac{q\epsilon_s}{2}} \sqrt{\frac{N_w}{(V_{bi} - V)}} \quad 4.12$$

Where N_w is the ionised impurity density in the space-charge region. For an n -type Schottky diode, the ionised donor atoms are positively charged and the deep levels occupied by electrons are negatively charged. Therefore, the total ionised impurity density is given by $N_w = N_D^- - n_T^+$, where n_T is the steady state trap densityⁱ. Substituting this into equation 4.12 gives

$$C = A \sqrt{\frac{q\epsilon_s}{2(V_{bi} - V)}} \sqrt{N_D - n_T(t)} = A \sqrt{\frac{q\epsilon_s N_D}{2(V_{bi} - V)}} \sqrt{1 - \frac{n_T(t)}{N_D}} = C_0 \sqrt{1 - \frac{n_T(t)}{N_D}} \quad 4.13$$

This can be approximated using the first-order expansion to give

$$C \approx C_0 \left(1 - \frac{n_T(t)}{2N_D} \right) \quad 4.14$$

ⁱ The steady state trap density was discussed in chapter 2, section 2.2.3, where it was denoted by f_t for clarity and to avoid confusion between the terms n (electron density) and n_T (trap density).

Substituting equation 2.25 in Chapter 2, which provides the time-dependency of $n_T(t)$ for emission, into equation 4.14 results in an exponential time-dependent equation for the diode capacitance transient

$$C(t) = C_0 \left[1 - \left(\frac{n_T(0)}{2N_D} \right) \exp\left(\frac{-t}{\tau_e}\right) \right] \quad 4.15$$

where τ_e is the emission time constant, as discussed in Chapter 2. Equation 4.15 represents the capacitance transient from $t = 0$, but just before any emission takes place, until steady-state capacitance (C_0) is reached, as displayed in Figure 4.3.

In DLTS, the capacitance transient represented by equation 4.15 is sampled at two points in time, $t = t_1$ and $t = t_2$. The DLTS signal, at any one temperature is equal to the difference between the capacitance at t_1 and at t_2

$$\delta C = C(t_1) - C(t_2) \quad 4.16$$

In a DLTS measurement, the sample is periodically pulsed between V_R and V_P as discussed previously and illustrated in Figure 4.3, whilst the sample temperature is increased or decreased over a given range. The resulting DLTS peak is dependent upon the nature of the capacitance transient at any given temperature, as illustrated in Figure 4.7.

The expression for the DLTS signal can be obtained by substituting the expression for capacitance at t_1 and t_2 using equation 4.15 into equation 4.16

$$\delta C = C(t_1) - C(t_2) = \frac{C_0 n_T(0)}{2N_D} \left[\exp\left(\frac{-t_2}{\tau_e}\right) - \exp\left(\frac{-t_1}{\tau_e}\right) \right] \quad 4.17$$

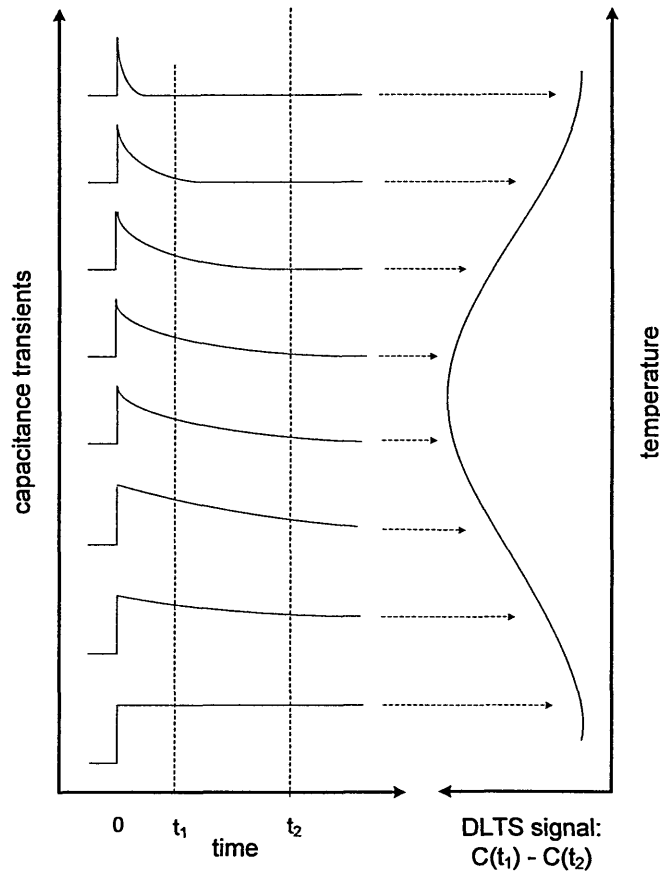


Figure 4.7: Representation of how a DLTS signal is formed as the sample is scanned up or down in temperature. The capacitance transients shown on the left hand side are representative of minority carrier emission from traps in the space charge region sampled as the capacitance returns to its quiescent value. The difference between the capacitance at time t_1 and t_2 form the DLTS signal, as shown on the right hand side. After Lang⁴.

The maximum point in the DLTS curve, or δC_{\max} , can be obtained by differentiating equation 4.17 with respect to the emission time constant τ_e and setting $d(\delta C)/d\tau_e$ to equal zero. The maximum value of the time constant $\tau_{e(\max)}$ is then given by

$$\tau_{e(\max)} = \frac{t_2 - t_1}{\ln(t_2/t_1)} \quad 4.18$$

Therefore, the maximum emission rate, $e_{n(\max)}$ is given by

$$e_{n(\max)} = \tau_{e(\max)}^{-1} = \frac{\ln(t_2/t_1)}{t_2 - t_1} \quad 4.19$$

A DLTS system is designed such that it only responds when a transient occurs within a certain rate window. This is achieved by passing the transient signal through a double boxcar and setting the gates t_1 and t_2 so that the system can respond to trap emission rates which occur within a set rate window. The signal to noise ratio is proportional to the square root of the gate width. Therefore, in practice the gate width must be wide enough in order to maximise the signal to noise ratio. For correct notation, t_1 and t_2 must

be written as $(t_1 + \Delta t)$ and $(t_2 + \Delta t)$ respectively. However, setting the gate width too wide can decrease the accuracy of the measurement. Typically in DLTS, the gates are set so that (t_2 / t_1) is a constant. Not only does this allow for easier data processing, but it also results in peaks which are of similar shapes, when alternate rate windows are employed.

In reality the capacitance transient is distorted by noise and the hardware is designed to extract the transient. The capacitance transient $C(t)$ is multiplied by a weighting function $w(t)$ and the resulting product is averaged using a filter. Investigations by several groups indicate that the double boxcar method with relatively narrow gate widths and sufficient periods between consecutive pulses must be used for optimum resolution in DLTS measurements².

4.3.1 Trap activation energy

To obtain the level of a trap within the bandgap, the DLTS experiment is repeated with different rate windows, as shown in Figure 4.8. For each new spectrum, the temperature of the peak position is obtained. This corresponds to the temperature at which $e_{n(\max)}$ occurs. Using the emission rates and the corresponding temperatures, an Arrhenius plot is constructed by plotting $\ln(e/T^2)$ on the y-axis and $1000/T$ on the x-axis.

The difference in energy between the trap level and the conduction or valence band ($E_c - E_t$, or $E_t - E_v$) is typically referred to as the trap activation energy, E_A . It is obtained from the slope of the $\ln(e/T^2)$ vs $1000/T$ plot. However, the value derived from the slope is not strictly equal to $E_c - E_t$ or $E_t - E_v$. During DLTS measurements a change in Gibbs free energy, $\Delta G_{n,p}$, occurs for the thermally activated process in exciting an electron (hole) from the deep level to the conduction (valence) band.

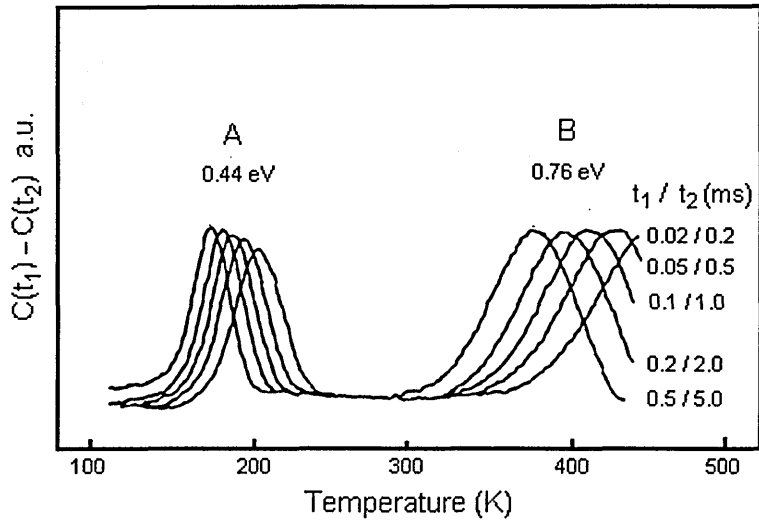


Figure 4.8: DLTS spectra recorded using different settings of t_1 and t_2 , resulting in different rate windows. In each case t_1/t_2 is the same value. The peak positions are used together with the emission rates to construct an Arrhenius plot. The gradient is equal to the enthalpy change involved in carrier emission from a trap to the conduction or valence band. After Lang⁴.

The electron (hole) emission rate from a deep level is related to its capture cross section by equation 2.18 (2.19). This relationship is repeated here for electrons

$$e_n = \sigma_n \nu_n N_c \exp\left[\frac{-(E_c - E_t)}{kT}\right] \quad 4.20$$

Substituting $E_c - E_t$ for the Gibbs free energy gives

$$e_n = \sigma_n \nu_n N_c \exp\left[\frac{-\Delta G_n}{kT}\right] \quad 4.21$$

From thermodynamics, the Gibbs free energy is related to enthalpy, H , and entropy, S , by the equation

$$\Delta G = \Delta H - T\Delta S \quad 4.22$$

Substituting equation 4.22 into 4.21 gives the following relationship for the electron emission rate

$$e_n = \sigma_n \nu_n N_c e^{\frac{\Delta S}{k}} e^{-\frac{\Delta H}{kT}} \quad 4.23$$

The slope of the $\ln(e/T^2)$ vs $1000/T$ Arrhenius plot is equal to $(-\Delta H/k)$, which is globally referred to as the trap activation energy and values are typically quoted as

$E_c - E_t$ or $E_t - E_v$. However, ΔH is not strictly equal to the energy spacing between the trap level and the conduction or valence band edge.

It is possible to derive the capture cross section of the trap from the intercept on the $\ln(e/T^2)$ axis. However, cross sections obtained by this method can be incorrect by a factor of 50. For accurate values, the capture cross sections must be measured experimentally. This is because the entropy term, ΔS , is based on the degeneracy of the trap when occupied and unoccupied by an electron and is not well known for deep levels. Furthermore, the capture cross section can be temperature dependent, which is not accounted for by values derived using the intercept on the $\ln(e/T^2)$ axis.

4.3.2 Trap density

DLTS is commonly used to obtain the trap concentration within the region probed during the measurement.

At $t = 0$, $n_T(t) \approx N_T$, using equation 2.25 in Chapter 2. Substituting this into equation 4.16, gives an expression for the DLTS signal in terms of the total trap density

$$\delta C_{\max} = \frac{C_0 N_T}{2N_D} \left[\exp\left(\frac{-t_2}{\tau_{e_{\max}}}\right) - \exp\left(\frac{-t_1}{\tau_{e_{\max}}}\right) \right] \quad 4.24$$

Equation 4.24 can be rearranged to obtain N_T

$$N_T = 2N_D \frac{\delta C_{\max}}{C_0} \left[\exp\left(\frac{-t_2}{\tau_{e_{\max}}}\right) - \exp\left(\frac{-t_1}{\tau_{e_{\max}}}\right) \right]^{-1} \quad 4.25$$

A more accurate representation of the trap density can be achieved by including the effect of λ in the equations^{7,8}. This level of accuracy is not required in the analysis and equation 4.21 is sufficient for this work. The effect of λ should be considered when the region probed is comparable to the Debye length, such as during depth profiling measurements (section 4.3.3).

In order to determine the trap density from a given DLTS peak, the steady-state capacitance C_0 and the ionised donor impurity density must be obtained from the $C-V$ characteristics. These values are typically obtained from the $C-V$ characteristics recorded at room temperature.

4.3.3 Deep level spatial profiling

It can be seen from Figures 4.4 and 4.5 that it is possible to measure the trap density within a specific region of the semiconductor beneath the metal/semiconductor interface, by selecting appropriate values of reverse bias and fill pulse using the C - V characteristics of the diode together with the depth vs voltage characteristics.

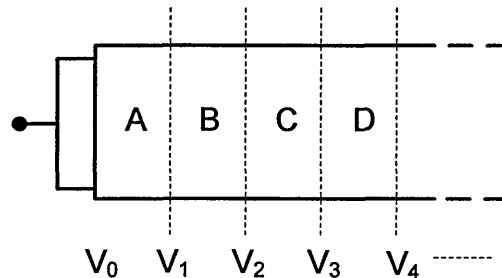


Figure 4.9: Schematic representation of the deep level spatial profiling method. Predetermined values of reverse bias and fill pulse are chosen to probe specific regions within the semiconductor.

For example, to determine the trap density in the region labelled 'B' in Figure 4.8, the reverse bias and fill pulse applied would have to be V_2 and V_1 , respectively. From the depth vs voltage characteristics, it is possible to determine the value of reverse bias required to create a depletion region that would extend to the B/C interface in Figure 4.8. Similarly, an appropriate fill pulse can be determined, which would bring the depletion region to the A/B interface.

In order to obtain the trap density in a given region of semiconductor, the ionised donor impurity density and the steady-state capacitance values must be entered into equation 4.25, together with the maximum value of the DLTS signal, δC_{\max} .

By measuring the trap density in several regions of the semiconductor, it is possible to determine whether the trap density is increasing or decreasing into the bulk. The accuracy of the measurement can be enhanced by ensuring that region probed in any one measurement is far greater than the Debye length, which was discussed in Section 4.1.2. Another potential drawback to this method is the fact that the potential difference between the reverse bias and fill pulse are, in reality, not the same for each region. In other words, it is likely that some emitted carriers will experience a far greater acceleration towards the surface than others, depending on the required biases for the experiment.

If the quasi neutral region effects are significant, a more accurate method of spatial profiling of the $(V_2 - V_1)$ region is by subtracting the trap concentration in the region $(V_1 - V_0)$ from $(V_2 - V_0)$. This method is referred to as Double DLTS (DDLTS)⁹.

4.4 Laplace deep level transient spectroscopy

Different weighting functions have been employed by several groups in order to improve the time constant resolution of DLTS. However, DLTS inherently results in broad peaks due to the nature of how the peak is obtained. Even a perfect defect state with a single time constant will result in a relatively broad spectrum. The problem is intensified when the technique is applied to more complex defect structures, with multiple closely spaced exponentials. Until now, no significant improvements have been made to the resolution of DLTS in extracting transient time constants.

Digital methods and mathematical algorithms have been employed by several groups in order to improve the time-constant resolution of the DLTS technique. These methods include a method of moments and a numerical inverse Laplace transform. In digital methods, the baseline must be subtracted from the measured transient to eliminate any dc drift and to avoid large contributions to the integrals used¹⁰. The baseline is the value of the signal at $t = 0$. In other words, to obtain accurate solutions from the algorithms employed, it is vital that only the transient is considered in its entirety, from $t = 0$, until it becomes sufficiently level. This is also essential in Laplace DLTS.

Digital schemes are typically based on the assumption that the DLTS signal is made up of a sum of exponential decays

$$\delta C(t) = \sum_i^n C_i e^{-t/\tau_i} \quad 4.26$$

where τ_i are the temperature dependent emission time-constants. It must be noted that the actual correlator output is the DLTS signal multiplied by a weighting function, as discussed previously. However, for simplicity, the DLTS signal will be denoted by $\delta C(t)$.

The inverse Laplace transform of equation 4.26 can be represented by

$$C(t) = \int_0^\infty F(s) e^{-st} ds \quad 4.27$$

where $C(t)$ is the time-dependent transient and $F(s)$ is the spectral density function. Equation 4.27 states that the Laplace transform of $F(s)$ is equal to the recorded

capacitance transient. Therefore, the spectral density function must be obtained by performing an inverse Laplace transform.

However, for a problem to be *well-posed* mathematically, it must have certain properties, as defined by Hadamard; (i) a solution must exist, (ii) the solution must be unique and (iii) the solution must continually depend on the data, in some reasonable topology^{11,12}. The process of extracting multiple closely spaced exponentials can yield infinite solutions and is not a well-posed problem. Furthermore, the transients studied are typically corrupted by noise and have an unknown base line, as discussed previously. Such ill-posed problems are approached by using *regularisation methods* and possibly the most common scheme is the Tikhonov regularisation method^{13,14}. For this reason, the Laplace DLTS (LDLTS) technique is often referred to as high resolution DLTS (HR-DLTS), as the result is not derived by an inverse Laplace transform only. However, the initial methods used a Laplace transform and the term LDLTS is currently used to describe the technique.

Figure 4.10 illustrates the application of Laplace DLTS to separate closely spaced exponentials. The broad DLTS spectrum centred at 260K in the inset was associated with the gold-hydrogen and the gold acceptor levels in silicon. The LDLTS measurements carried out at 260K show that two separate emissions are present at this temperature. This supports the previous discussion that the resolution of conventional DLTS is not sensitive enough for closely separated exponentials.

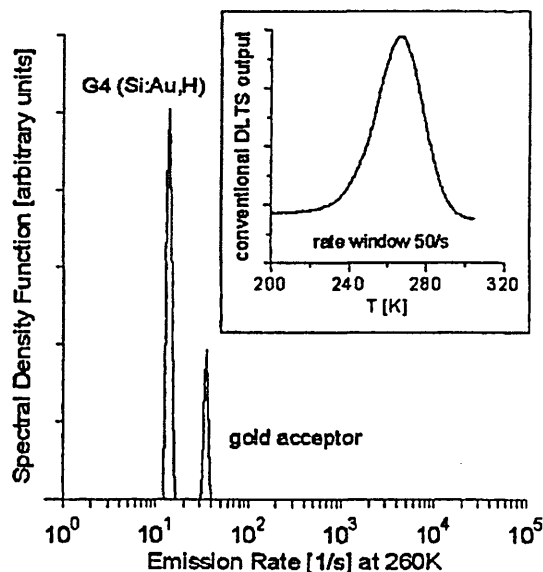


Figure 4.10: The broad DLTS spectrum in the inset was associated with the gold acceptor and the gold-hydrogen level. The Laplace DLTS recorded at 260K shows two separate emissions, which shows that the original DLTS spectrum consists of more than one emission. After Deixler *et al*¹⁵.

In Laplace DLTS, the sample is held at a fixed temperature and several thousand transients are typically recorded to minimise noise and generally the signal to noise ratio should ideally be in the order of 10^3 for reliable results. The sampling rate and the total number of samples per scan must be selected prior to the measurement. In practice, the sampling rate used must be relatively low to avoid distorting the signal due to the slower response time of the capacitance meter, which acts as a low-pass filter. Once the transients are recorded and averaged, the software employs three mathematical algorithms which are based on the Tikhonov regularisation method to extract the time-constants and hence the emission rates. These algorithms are called CONTIN, FTIKREG and FLOG. In practice, it is beneficial to use all three and compare the results to ensure that the emission rates observed are reliable.

It is also possible to use LDLTS to obtain the activation energy of a trap. In this case, the measurement temperature must be incremented in small steps of about 2K and the LDLTS measurement is then carried out at each new temperature. As the carrier emission from traps is temperature dependent, the emission rates are observed to increase with temperature, from which an Arrhenius plot can be constructed to obtain the trap activation energy, as discussed in section 4.3.1. This method tends to be more accurate than DLTS, which has an error of 50 meV.

4.5 System setup

The setup of the DLTS and LDLTS equipment is shown in Figure 4.11. The sample is mounted inside a vertical-mount high temperature (700K) cryostat. The measurements are performed under vacuum ($\sim 10^{-4}$ mbar) and the cryostat is cooled by a constant-flow helium compressor. The temperature inside the cryostat is controlled using a temperature controller. The capacitance of the diode is measured by the Boonton capacitance meter.

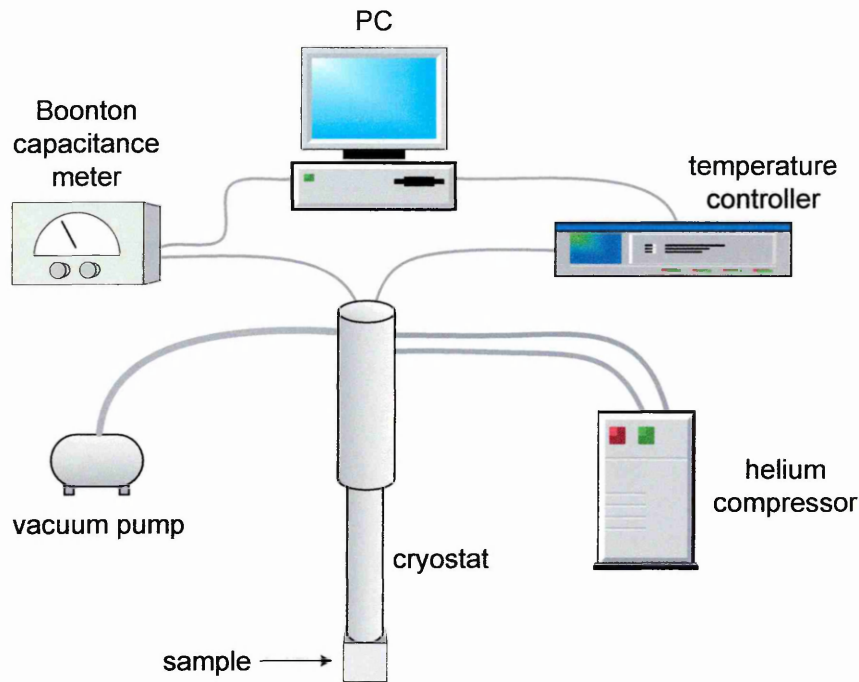


Figure 4.11: Typical system setup required for DLTS and Laplace DLTS measurements.

4.6 Summary

The DLTS measurement probes the space-charge region of a Schottky or p-n junction diode under reverse bias. The capacitance transient due to emission from deep levels is monitored at two instances in time, whilst the sample temperature is ramped or cooled. The difference between the two capacitance values gives rise to the DLTS signal.

In contrast, the sample is held at a fixed temperature during Laplace DLTS and several thousand transients are recorded. The emission rates are extracted through complex algorithms and the time constant resolution is enhanced.

4.7 References

- ¹ S. M. Sze, *Physics of Semiconductor Devices*, John Wiley & Sons: New York (1981).
- ² D. K. Schroder, *Semiconductor Material and Device Characterisation*, John Wiley & Sons, New York (1998).
- ³ E. H. Rhoderick and R. H. Williams, *Metal-Semiconductor Contacts*, Clarendon Press: Oxford (1988).
- ⁴ D. V. Lang, *J. Appl. Phys.* **45**, 3023 (1974).
- ⁵ C. T. Sah, L. Forbes, L. L. Rosier, A. F. Tasch Jr., *Sol. Stat. Electron.* **13**, 759 (1970).
- ⁶ G. L. Miller, D. V. Lang, L. C. Kimmerling, *Ann. Rev. Mater. Sci.*, 377-448 (1977).
- ⁷ Y. Zohta and M. O. Watanabe, *J. Appl. Phys.* **53**, 1809 (1983).
- ⁸ E. Meijer, H. G. Grimmeiss, L-Å. Ledebø, *J. Appl. Phys.* **55**, 4266 (1984).
- ⁹ H. Lefèvre and M. Schulz, *Appl. Phys.* **12**, 45 (1977).
- ¹⁰ K. Ikossi-Anastasiou, K. P. Roenker, *J. Appl. Phys.* **61**, 182 (1986).
- ¹¹ T. Poggio, C. Koch, *Proc. R. Soc. Lond. B* **226**, 303 (1985).
- ¹² M. Bertero, T. A. Poggio, V. Torre, *Proc. of the IEEE* **76**(8), 869 (1988).
- ¹³ H. W. Engl, K. Kunisch, A. Neubauer, *Inverse Problems* **5**, 523 (1989).
- ¹⁴ J. Honerkamp and J. Weese, *Continuum Mech. Thermodyn.* **2**, 17 (1990).
- ¹⁵ P. Deixler, J. Terry, I. D. Hawkins, J. H. Evans-Freeman, A. R. Peaker, L. Rubaldo, D. K. Maude, J. -C. Portal, L. Dobaczewski, K. Bonde Nielsen, A. Nylandsted Larsen, A. Mesli, *Appl. Phys. Lett.* **73**, 3126 (1998).

Chapter 5

Review of deep level transient spectroscopy of extended defects in silicon and gallium nitride

In this chapter deep level transient spectroscopy (DLTS) of extended defects in silicon and gallium nitride are considered. A general overview of band edge modification associated with extended defects and the resulting capture and emission kinetics are presented. The structural properties of point and extended defects in gallium nitride and silicon were discussed in Chapter 3. This chapter provides a summary of relevant DLTS results from silicon containing dislocations and from *n*-type gallium nitride.

5.1 Deep level transient spectroscopy of extended defects

In this section, the general characteristics of DLTS spectra that arise from the presence of extended defects are discussed.

At dislocations, the electrical activity is often due to the atomic structure of the dislocation (such as kinks), which are referred to as *bandlike states*, in addition to the localised states of impurities decoratingⁱ the dislocation. The total density of deep states $N(E)$ is given by the sum of the localised and bandlike states¹. Therefore, it is of importance that the point defect densities are well-controlled. In a DLTS measurement the signal amplitude is determined by the trap concentration within the region probed. This is described in chapter 4. It was shown in sections 2.2.1 and 2.2.2 of Chapter 2 that the capture and emission from ideal point defects obey a linear relationship with the trap occupancy, f_n or f_p . However, for extended defects, the Coulomb repulsion due to the charged dislocation has an effect on the capture and emission kinetics. The line charge at a dislocation has an associated local band-bending, which results in a barrier for subsequent capture, as illustrated in Figure 5.1. The deep level of a neutral dislocation is denoted by $E_d^{(0)}$ and lies slightly below midgap. Once the bandlike states become

ⁱ The term ‘decoration’ refers to impurities which have segregated to the dislocation core.

occupied by charge-carriers (electrons in Figure 5. 1), the deep level associated with the dislocation is shifted to $E_d^{(n)}$, where n denotes the number of occupied states. The conduction band is raised by δE_c , which is expressed as

$$\delta E_c = \frac{Q}{2\pi\epsilon_s} \left[\ln \left(\frac{\lambda_D Q}{q} \right) - 0.5 \right] \quad 5.1$$

where Q is the uniform line charge of the dislocation per unit length, ϵ_s is the semiconductor permittivity, and λ_D is the Debye length². Equation 5.1 shows that the amount of band-bending has a strong dependence on the amount of charge present at the dislocation.

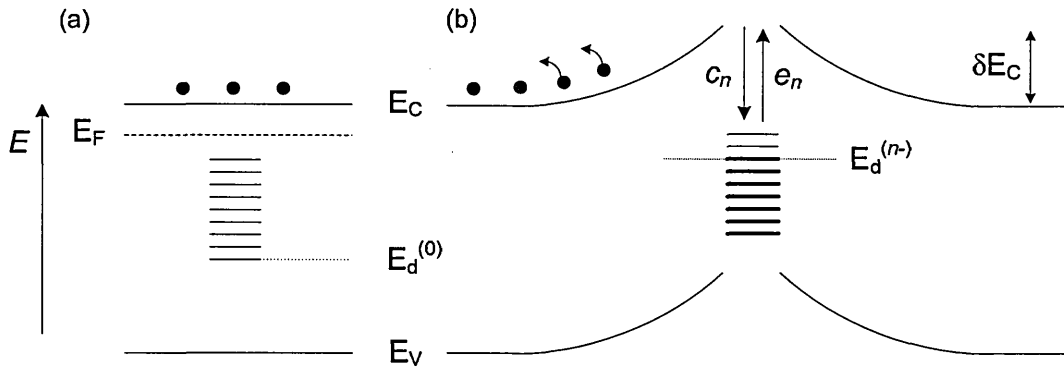


Figure 5. 1: Band diagrams associated with (a) a neutral (i.e. unoccupied) and (b) charged dislocation in an n -type semiconductor. The line charge of the dislocation results in local band-bending and a barrier for subsequent electron capture.

The band-bending, δE_c , can be approximated to $\delta E_c = \alpha f$, where α is a constant and f is the fractional occupancy of the bandlike states. The following expressions for the capture and emission rates at dislocations are those outlined by Schröter *et al.*^{1,3,4}.

The capture rate, r_c , at extended defects in n -type material is given by

$$r_c = \sigma_n v_{th} n (1-f) \exp \left[\frac{-\delta E_c}{kT} \right] \quad 5.2$$

The emission rate, r_e , at extended defects is dependent on the quasi-Fermi level, E_{qF} , the density of point defects, N_d , the total density of deep states, $N(E)$ and the emission time constant, e_n in the following relationship

$$r_e(E_{qF}) = \int_0^{\infty} e_n(E) \frac{N(E)}{N_d} dE \times \frac{1}{1 + \exp\left[\frac{E + \alpha F_T - E_{qF}}{kT}\right]} \quad 5.3$$

where F_T is the total occupation of deep levels.

It was shown by Grillot *et al.*⁵ that the trap concentration, which is determined by the DLTS signal amplitude, is proportional to the logarithm of the fill pulse duration, t_p and is given by

$$n_T(t_p) = \sigma v_{th} n \tau N_T \ln(t_p / \tau) \quad 5.4$$

where n_T is the trap occupancy, σ is the trap capture cross-section, v_{th} is the thermal velocity of the carriers, and τ is the time required for the Coulombic barrier to evolve.

This relationship can be detected by plotting $\ln[(dC_{\infty} - dC(t_p)) / C_{\infty}]$ as a function of t_p , where dC_{∞} is the maximum DLTS signal when the deep levels are saturated and $C(t_p)$ is the DLTS signal height at a given fill pulse duration, which is below the value required to saturate the deep levels. If the emission detected is from *point* defects, then the plot will result in a linear relationship. Therefore, any deviation from a linear relationship is an indication that emission is occurring from extended defect structures. The logarithmic filling law is considered to be the only feature which is accepted as a fingerprint of an extended defect⁶.

Schröter *et al.* have developed computer simulations to model the behaviour of the DLTS spectra from extended defects with variations in the fill pulse duration during the measurement^{1,3}. It was discussed above that a variation in fill pulse length affects the amount of local band-bending at the dislocation, leading to modified capture and emission rates. Experimental results and simulations indicate that DLTS of extended defects often exhibit line broadening with increasing fill pulse duration during a deep level measurement. This is typically more exaggerated on the lower temperature side of the peak detected, whereas the high temperature sides of the peaks are observed to overlap^{1,3}. The line broadening coincides with a shift of the peak position to lower temperatures.

5.2 DLTS of dislocations in silicon

The materials characterised in this work are both *n*-type samples containing OISFs and *p*-type silicon containing oxygen-locked dislocations (O-LD). Therefore, it is of significance to discuss extended defect related levels in the literature. The first part of this section will provide an overview of dislocation-related DLTS results from *n*- and *p*-type Si. This is followed by electrical activity specific to OISFs. The last section considers oxygen related levels in *p*-type Si.

It has been widely reported that plastic deformation of semiconductor crystals results in deep levels within the bandgap⁷⁻¹⁸. Extensive research has been carried out in order to determine whether the deep levels observed are due to the dislocations themselves, or due to point defects such as impurities at the core of dislocations. The DLTS spectra of both *n*- and *p*-type Si containing dislocations are complex and result in numerous peaks, some of which are broad in nature and are likely to consist of more than one level.

Kimerling and Patel were one of the first to report deep levels related to dislocations in *p*-type and *n*-type silicon using capacitance transient spectroscopy (CTS)⁷. This was followed by the study of carrier capture dynamics at dislocations using DLTS, carried out by Kveder *et al.*⁸. In both studies, Schottky diodes fabricated on *n*- and *p*-type Si were characterised after plastic deformation at 750-770°C⁷ and 680-700°C⁸. The CTS⁷ and DLTS⁸ measurements were carried out before and after the plastically deformed samples were annealed. The spectra reported by Kveder *et al.* and Kimerling and Patel for *n*-type Si are displayed in Figure 3.6. The figure aims to portray the effects of annealing on dislocation related levels. The amplitudes are not exact and the peak positions are an indication only. The peaks displayed are due to majority carrier (electron) traps.

Spectra *A* and *B* (solid lines) are those reported by Kveder *et al.* of plastically deformed *n*-Si before and after a 20 min anneal at 780°C, respectively. Spectrum *C* (dashed) corresponds to the CTS results obtained by Kimerling and Patel after a 1hr anneal at 700°C. The effects of a further 1hr anneal at 800°C and an additional 1hr anneal at 900°C are represented by spectrum *D* (dashed). According to Kimerling and Patel, no further change to the spectrum was observed after a subsequent 1hr anneal at 1000°C.

The CTS spectrum of the deformed sample before annealing (not displayed) shows a broad peak due to an electron trap 0.68 eV below the conduction band edge⁷. This level was found to move closer to the conduction band (to $E_c - 0.63$ eV), upon an increase in the amount of *n*-type doping from $5 \times 10^{13} \text{ cm}^{-3}$ to $\sim 10^{15} \text{ cm}^{-3}$.

It can be seen in Figure 5.2 that the four electron traps shown in spectrum *C* at 0.28, 0.41, 0.48 and 0.63 eV below the conduction band edge disappear after an additional 1hr anneal at 900°C. The resulting spectrum, as shown in *D*, reveals one dominant peak, with a corresponding level at $E_c - 0.38$ eV. Kimerling and Patel suggest that the deformation of silicon introduces deep levels into the Si bandgap, possibly due to acceptor-like “dangling bonds”. The disappearance of most levels is proposed to be due to the reconstruction of these bonds.

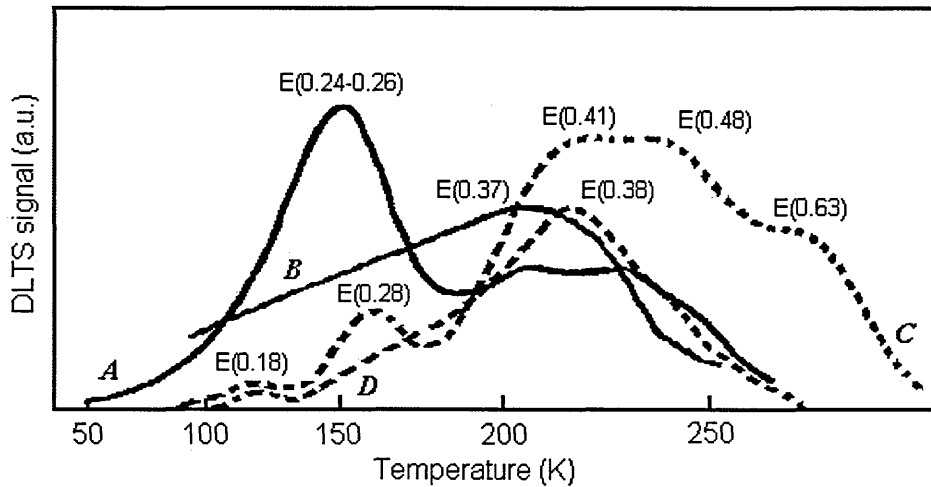


Figure 5.2: DLTS of plastically deformed *n*-type silicon before (spectra *A* and *C*) and after (spectra *B* and *D*) annealing. After Kveder *et al.*⁸ and Kimerling and Patel⁷.

The broad peak in the $\sim 170 - 280$ K region of spectrum *A* was reportedly made up of three levels, $E(0.33-0.36$ eV), $E(0.48-0.51$ eV) and $E(0.58-0.60$ eV). The range of activation energies for each level was discussed by Kveder *et al.* in terms of the logarithmic time dependence for the capture process. This is also applicable to the $E(0.24 - 0.26$ eV) level, emitting at ~ 150 K in spectrum *A*. The fill pulse dependency of the deep level occupation in extended defects was discussed in section 5.1. The broadening of the DLTS spectra are explained by considering the Coulomb potential, Φ , which builds up around the dislocations due to additional electrons (or holes in the case of *p*-type samples) in a multi-state system, containing many closely-spaced electron states. The authors argue that the potential Φ at the dislocation varies during the emission process, which may result in multiple exponentials within a single capacitance transient.

Following the notation of Omling *et al.*⁹, the dominant peak in *n*-type plastically deformed silicon which remains after annealing is commonly referred to as the *C*-line.

Following this notation, the E(0.18-0.19 eV), E(0.28-0.29 eV) and E(0.54 eV) levels are labelled the *A*, *B* and *D* lines, respectively. Unlike Kveder *et al*, Omling *et al*. did not observe fill pulse dependency of the activation energy for the *A*, *B* and *D* lines. These levels were reportedly associated with point defects in the vicinity of dislocations, because of their dependence on the amount of deformation. In particular, the *D*-line was reported to be in low concentration for low dislocation densities, especially for straight type dislocations.

Studies by Knobloch *et al*. on silicon containing clean 60 degree dislocations revealed only one electron trap E(0.28 eV), which the authors associated with the *B*-line. The silicon used for this work was grown on silicon germanium ($\text{Si}_{0.98}\text{Ge}_{0.02}$) by chemical vapour deposition (CVD)¹⁰. In contrast to results provided by Omling *et al*, Knobloch *et al*. have shown that the trap density of the *B*-line does not increase with increasing dislocation density. This is further supported by the work of Cavalcoli *et al*¹¹.

Omling *et al* showed that the *C*-line, E(0.37 – 0.39 eV) in Figure 5.2, is made up of two levels, labelled C_1 and C_2 . These levels are reported to be dependent on the annealing and deformation methods, but stable up to 900°C⁹. However, the C_1 level was not observed in *n*-type silicon containing clean 60 degree dislocations studied by Knobloch *et al*.¹⁰

Two other samples investigated by Knobloch *et al*. were contaminated by gold implantation and subjected to rapid thermal annealing (RTA). The impurity densities were reported to be 10^4 - 10^5 cm⁻¹ in one sample and $>10^6$ in another, and two additional electron traps were observed in these samples, labelled MF-E2 and MF-E3. The level of MF-E3 was found to be in the range 0.39 and 0.52 eV below the conduction band edge, and displayed line-broadening on the lower temperature side of the spectrum with increasing fill pulse length. The authors associate this level (MF-E3) with the C_1 level observed previously by other groups. The trap density of this level was observed to increase deeper into the sample, which follows the profile of the dislocation density in the Si epilayer, with a maximum at the Si - $\text{Si}_{0.98}\text{Ge}_{0.02}$ interface. Furthermore, it was shown by electron-beam-induced current (EBIC) measurements that the DLTS peak height (and hence the trap density) of the *C*-line is much larger in the regions which were observed to have a higher dislocation density. This supports the notion that the *C*-line is dislocation related.

Certain similarities exist in the results reported by Kveder *et al*. and Kimmerling and Patel on *p*-type Si. Both groups report more levels in *p*-type silicon than in *n*-type material. Kveder *et al*. have observed five levels due to hole traps, H_1 (0.25 eV), H_2 (0.39

eV), H₃(0.40 eV), H₄(0.47 eV) and H₅(0.67 eV). Furthermore, in both studies, DLTS of the *p*-type material after annealing produces a broad peak, also centred at around H (~0.35 eV), which is commonly referred to as the F-line. Kveder *et al.* suggest that the levels observed may be due to the dislocations themselves (arising from localised levels at the dislocation core), or possibly due to point defect clouds surrounding the dislocation. The annealing effects are difficult to compare to the previous work of Kimmerling and Patel, as the annealing temperatures and durations were different in the two studies.

The thermal stability of the broad peak centred at H (~0.35 eV), the F-line, in plastically deformed *p*-type silicon was investigated by Ono and Sumino¹². This level was observed upon deformation at 750°C in samples with different dislocation densities of $7.6 \times 10^6 \text{ cm}^{-2}$, $4 \times 10^7 \text{ cm}^{-2}$ and $1.4 \times 10^8 \text{ cm}^{-2}$. The peak height was found to be proportional to the dislocation density, whilst two other levels H(0.24 eV) and H(0.56 eV) only displayed a slight increase with larger amount of dislocations. Upon annealing at 900°C, the peak heights (and hence the trap density) of all three levels appeared to decrease. In an earlier study, Lemke detected the F-line as a result of deformation at 1000°C¹³. This suggests that the F-line could be reduced upon annealing if it is formed by deformation at lower temperatures. These results suggest that the F-line is strongly dependent on deformation and annealing methods.

Dislocation-impurity interactions give rise to an inhomogeneous distribution of impurities, which result in the spatial variation of the electrical properties of materials. The electrical properties often follow the dislocation distribution in the crystal¹⁴. The DLTS of plastically deformed *n*-type and *p*-type silicon is complex, but a general trend is visible. In both *n*-Si and *p*-Si, multiple peaks are detected in the initial DLTS spectra. Upon high temperature annealing, the DLTS spectrum displays a broad peak, which is centred around $\sim E_C - (0.37 - 0.38) \text{ eV}$ (the C-line) and around $\sim E_V + 0.35 \text{ eV}$ (the F-line) for *n*-type and *p*-type silicon, respectively.

It is possible to distinguish between point and extended defect related emission by observing the capture properties of the deep levels as a function of the fill pulse duration, as reported by Kveder *et al.*⁸

It is evident that DLTS results on silicon containing dislocations vary significantly. Considerable work was carried out in the late 80s and 90s by various groups, including Lahiji *et al.*¹⁵, Peaker *et al.*¹⁶, Kaniewska *et al.*¹⁷ and Qian *et al.*¹⁸ to determine the effects of contamination on dislocation related deep levels. The findings suggest that the impurity decoration of extended defects is the main cause for electrical activity and

account for the variation observed in the literature. This is discussed in more detail in the following section, because the work was carried out primarily on oxidation-induced stacking faults (OISF). However, OISFs are a type of dislocation and the results are equally applicable to plastically deformed silicon.

5.2.1 OISF related deep levels in *n*-type silicon

Before commercial fabrication methods had been improved to successfully produce defect-free devices, the presence of dislocations and stacking faults were detrimental to device performance. It has been reported by Varker and Ravi that oxidation-induced stacking faults in p-n junction diodes lead to excess leakage currents¹⁹. Kolbesen *et al.* showed a correlation between stacking fault density and leakage currents in MOS power devices²⁰.

Kawado²¹ reported EBIC studies of silicon containing oxygen-induced stacking faults. The OISF samples were fabricated by thermal oxidation at 1150°C between 1 and 5 hours in a dry oxygen atmosphere, after which the oxide was removed in order to deposit the Schottky contacts. The EBIC images reveal dark spots, which have been shown to correspond to the ends of line etch grooves. The author concludes that the Frank partial dislocations act as recombination centres, resulting in a decrease in the EBIC signal. The earlier work of Kimmerling *et al.* showed that the stacking fault plane itself also exhibits EBIC contrast²². Castaldini *et al.* reported through infrared beam induced current (IRBIC) that electrical activity occurs along the stacking fault, as well as at the Frank partials²³.

The effect of gold and platinum on the electrical behaviour of OISF's in *n*-type silicon has been reported by Peaker *et al.*¹⁶. The authors studied clean (not intentionally contaminated), platinum diffused and gold diffused samples, all of which were damaged at the surface and oxidized at 1050°C to form OISF's, with concentrations ranging from 2×10^6 to 5×10^7 cm⁻², with average stacking fault lengths of 4 μm. The diffusions were carried out in a nitrogen atmosphere at 700°C and 750°C for platinum and at 700°C, 750°C and 800°C for gold, with diffusion times varying between 5 and 30 minutes to create low levels of metal contamination. The sample containing clean OISF's produced a broad peak with an activation energy of 415 meV. The amplitude of this level was found to increase with stacking fault density. The authors note that this behaviour is similar to that of the C-line as reported by Omling *et al.* (section 3.1.2). The platinum and gold diffused samples produce deep acceptor levels at 227 meV and 560 meV below the conduction band, respectively. The clean (undecorated) stacking faults

displayed point defect like behaviour with a large capture cross-section of $1.7 \times 10^{-14} \text{ cm}^2$, whereas the capture process for decorated stacking faults displayed a logarithmic dependence on the filling time. At low decoration levels (samples with lower diffusion temperatures) the activation energy was found to increase with the level of metal contamination. The authors proposed that the metal impurities decorate the Frank partial dislocations and give rise to electrical activity. In samples which have undergone metal diffusion at higher temperatures to produce a larger metal concentration, the activation energies related to the metal contamination were reported to decrease with increasing impurity concentration. The authors note that the logarithmic capture behaviour of dislocations in silicon, as previously reported by other groups, may have been due to unintentional contamination, since their clean OISF samples displayed exponential capture properties that are characteristic of point defects.

The behaviour of the gold acceptor level in silicon is intriguing, as it was reported to have a different electrically active state depending on whether the diffusion is carried out at low-temperature (below 850°C) or at high-temperature (above 850°C). The level related to low temperature diffusion was found to anneal out at low temperatures, whereas the level due to high temperature gold diffusion is difficult to anneal^{24,25}. However, Kaniewska *et al.* have shown that the presence of OISFs stabilise the Au-level, whereby gold diffused at 800°C (in the lower diffusion temperature range) produces a level which is characteristic of Au diffused above 850°C ¹⁷.

The increase in activation energy upon metal contamination was also observed by Qian *et al.*¹⁸. The DLTS spectra of nominally clean, Au- and Cu-decorated stacking fault samples show that the effect of metal decoration results in a shift of the DLTS spectrum towards higher temperatures. The capture properties of the decorated levels were also observed to be dependent on the fill pulse length. The activation energies for both the Au- and Cu-decorated levels were observed to decrease steadily when the fill pulse was increased from 0.01 to 15 seconds. The reported levels were 480-570 meV and 465-573 meV for the levels due to Cu- and Au-decorated stacking faults, respectively. This is in support of the finding that the capture properties of levels due to decorated stacking faults have a logarithmic dependency on the fill pulse duration, as reported by Peaker *et al.*¹⁶. The diffusions were carried out in a nitrogen atmosphere for 30 minutes at 750°C . The observed shift of the levels towards midgap due to Cu- and Au-decoration agree with the results presented by Peaker *et al.*¹⁶ in the lower diffusion temperature range.

Significant properties of OISF-related levels have been presented by Kaniewski *et al.*²⁶. By applying the technique of spatial profiling by DLTSⁱⁱ, they showed that the broad peak occurring in the region of ~130-250K, which is initially observed upon using a reverse bias of -6V, can actually be resolved into much narrower peaks. Three peaks were reported in this region; E(~160K), E(~215K) and E(~230K). Trap concentration measurements as a function of depth have indicated that the E(~160K) level is associated with the Frank partials bounding the stacking fault, as the trap concentration for this level is observed to follow the depth profile of the Frank partial dislocation density. It is proposed that the electrical activity associated with the E(~160K) level is not due to the stacking fault itself. Furthermore, a point defect-like peak is reported to occur at ~290K, for which the trap concentration increases deeper into the sample from the surface. A shallow level emitting at ~110K also has a similar depth profile in comparison to the stacking fault density, but is detectable beyond the depth at which the Frank partials are present, as determined by TEM studies.

5.2.2 Oxygen and dislocations in *p*-type Si

It is widely accepted that oxygen in silicon is stable and electrically inactive in an interstitial position (O_i) as an isolated oxygen atom covalently bonded to two neighbouring silicon atoms²⁷. This has been shown in the 1950s by Kaiser *et al.* by infrared (IR) measurements²⁸ on oxygen-doped silicon, which was later confirmed using X-ray diffraction measurements by Bond and Kaiser²⁹. The interstitial oxygen content has been shown to greatly influence the recombination activity of dislocations measured by electron-beam induced current³⁰.

Oxygen in silicon can lead to the formation various types of thermal donor defects when annealed in the temperature range of 350-550°C³¹. These levels can be annealed out at higher temperatures, but too high an annealing temperature can lead to the formation of other defects. The observed electrical activity has been associated with the diffusion of oxygen atoms to form stable clusters of four atoms³². The level of the shallow thermal donor (STD) lies ~37 meV below the conduction band edge. The neutral (TD^0) and the singly ionised (TD^+) thermal donors have levels ~53–69 meV and ~11–119 meV, respectively. However, in *p*-type Si with a high oxygen content, Claeys *et al.*³³ and

ⁱⁱ Spatial profiling by DLTS is described in chapter 4.

Chan *et al.*³⁴ have detected a minority carrier (electron) trap in samples which have not undergone any heat treatments.

It has been shown by Feklisova *et al.*³⁵ that the DLTS signal amplitude in dislocated *p*-type Si is dependent on the duration of deformation. Their results show that the trap concentration determined by DLTS is significantly reduced when the deformation duration, carried out at 700°C, is increased from 15 minutes to 1 hour. A further, but less significant decrease is observed when the deformation time is increased to 2 hours.

Castaldini *et al.*³⁶ have associated the F-line H (~0.33 – 0.35 eV) in *p*-type Si, which survives upon annealing, with an impurity localised in the strain field of extended defects, such as dislocations or oxygen precipitates. The authors studied various samples with different deformation methods at either 670 or 800°C, some of which were subjected to high temperature annealing at either 800 or 1000°C. Numerous levels above the valence band edge are reported and labelled as T1 (0.27 – 0.28 eV), T2 (0.42 – 0.45 eV), T3 (0.4 eV) and T4 (0.38 eV). The level T3 has been associated with iron and oxygen related defects or complexes. One level of particular interest to this work is the appearance of a shallow level, $\sim E_v + 70$ meV, at ~ 50 K in samples which have been subjected to bending along the [110] direction at 670°C for 1hr and subsequently been annealed at 800°C for 24 hours. The amplitude of this peak is extremely small and therefore is presumed to have a very low trap concentration.

5.3 Deep level transient spectroscopy of *n*-type hexagonal GaN

This section will discuss the deep levels detected by deep level transient spectroscopy (DLTS) in *n*-type hexagonal GaN. Figure 5.3 shows DLTS spectra obtained from *n*-GaN samples grown by MBE and HVPE, as described in the caption. The levels presented were obtained by Fang *et al.*³⁷ and are representative of levels typically reported in the literature. A universal numbering scheme of levels does not exist in the literature (e.g. references 37 to 42). In Figure 5.3, the peaks are labelled with specific reference to Chapter 7, which presents the electrical characterisation results from hexagonal *n*-GaN. The magnitudes of the DLTS peaks are inconsequential and should not be viewed as absolute. Moreover, the peak positions are an indication of the levels observed and are not the same throughout the literature. This is because the peak position can be influenced by the rate window, reverse bias, the fill pulse magnitude and duration used in the measurement, and also whether the emission is from extended defects. However, it is of importance to display typical DLTS spectra of *n*-GaN in order

to familiarise the reader with the deep levels commonly observed and to discuss their capture properties. The DLTS technique is described in Chapter 4.

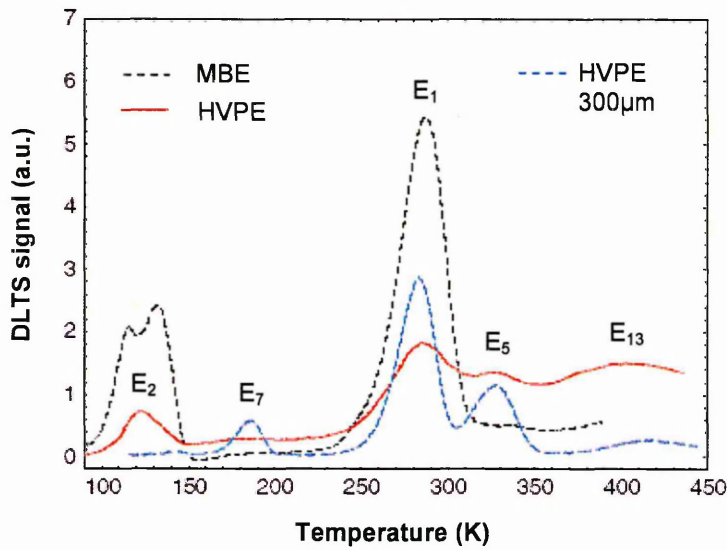


Figure 5.3: Typical DLTS spectra of hexagonal n -GaN. The MBE grown sample (---) was $1.6\mu\text{m}$ thick. The thickness of the HVPE grown samples were $5\mu\text{m}$ (—) and $300\mu\text{m}$ (- - -). Reproduced using results by Fang *et al.*³⁷.

In the following discussion, the levels presented are examined in relation to the *range* of activation energies reported in the literature.

Level	$E_C - E_T$ (eV)
E_1	$\sim 0.53 - 0.61$
E_2	$\sim 0.22 - 0.27$
E_5	$\sim 0.65 - 0.67$
E_7	$\sim 0.35 - 0.4$
E_{13}	$\sim 1 \text{ eV}$

Table 5.1: Approximate positions in the bandgap of common defect levels detected by DLTS in hexagonal n -GaN.

The levels shown in Figure 5.3 were also reported in GaN grown by MOCVD^{38,39}, MBE⁴⁰ and HVPE^{38,41}. The DLTS spectra reported have significant implications for device performance. The dominant emission around room temperature arising from level E_1 may be associated with leakage currents detected in reverse biased junctions^{42,43}.

It was mentioned in section 3.2 of Chapter 3 that the HVPE growth technique compromises material quality for speed and that MBE compromises speed for material

quality. The red and blue lines in Figure 5.3 were reported from 5 μm and 300 μm HVPE grown GaN, respectively. The dislocations density decreases with increasing thickness and it is apparent from Figure 5.3 that the spectra from the 300 μm thick sample (shown in blue) is more defined and the levels observed are more representative of point defect related emission. Furthermore, the emission from level E_2 does not appear to be present in the 300 μm thick sample. Similarly, in the 1.6 μm thick MBE grown sample, only levels E_1 and E_2 are dominant. The spectra suggest a correlation between dislocation density and deep level emission.

Hacke *et al.* investigated GaN grown by HVPE on two different substrate materials⁴¹. The substrate materials used were zinc oxide (ZnO) and MOCVD grown GaN. Levels E_2 , E_1 and E_5 were detected by isothermal capacitance transient spectroscopy (ICTS). The levels did not display a conclusive dependence on the substrate material. Slight variations in the activation energies were associated with the different amounts of strain at dislocations.

Soh *et al.*⁴⁴ have carried out DLTS studies on GaN grown by MOCVD on crack-free and cracked templates in order reduce the screw dislocation density by an order of magnitude through rapid thermal annealing (RTA). By obtaining DLTS spectra before and after the RTA treatment, was possible to determine the levels associated with edge and screw dislocations. The results indicate that the level E_1 is still present after subsequent RTA treatments at 750, 850 and 950°C. However, carrier capture at E_1 displayed a logarithmic dependence on fill pulse duration, which is indicative of extended defect related emission. Therefore, the level E_1 was associated with threading edge dislocations, which were unaffected by the RTA treatments.

In contrast, the trap concentration of level E_2 is reported to decrease with the RTA treatments, suggesting that the level is due to screw and/or mixed type dislocations. This inference was based on the logarithmic capture dependence on the fill pulse duration, suggesting emission from extended defects.

5.3.1 Bias dependency and hydrogen passivation of the E_1 level

Annealing studies were carried out by Wu *et al.* on HVPE grown n -GaN^{45,46}. Levels E_1 (0.27eV), E_2 (0.61eV) and E_5 (0.65eV) were detected using DLTS. Upon reverse biased annealing (RBA) of 30min at 370K prior to the DLTS measurement, the trap concentration of all three levels were observed to increase. In contrast, zero biased annealing (ZBA) for 15min at 370K resulted in a decrease in the E_1 peak height.

However, a prolonged anneal (>12 hrs) was not found to decrease the peak height further⁴⁶.

The increase in trap concentration due to the RBA treatment was observed to be sensitive to the RBA temperature. Results show that the lower the RBA temperature, the smaller the increase in trap concentration relative to the concentration obtained after the ZBA treatment⁴⁵. From the three traps, the E_1 level appears to be most sensitive to the RBA treatment and this is illustrated in Figure 5.4. The reactivation energy for the E_1 level is derived to be $E_{\text{reac}} = 0.96\text{eV}$ ⁴⁶.

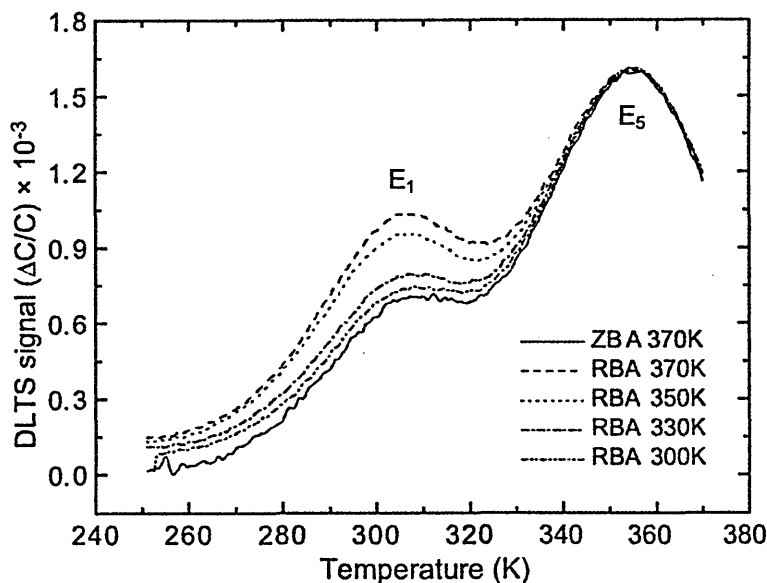


Figure 5.4: The peak height dependence of the E_1 level on RBA temperature. The RBA was carried out for 30 min at each temperature. After Wu *et al.*⁴⁵.

By investigating four samples with different thicknesses, Wu *et al.* obtained a direct correlation between dislocation density and the amount of increase in trap concentration due to RBA. It is shown that a greater change in trap concentration is observed for samples with a larger dislocation density⁴⁵.

The reduction in peak height due to RBA treatment is explained by the presence of a mobile defect or ion, which is able to drift under an electric field and elevated temperatures⁴⁵. The negatively charged hydrogen atom, H^- , is suggested as a probable candidate⁴⁶.

Hydrogen is a common by-product of most growth methods^{47,48}. The hydrogenation of GaN for 30min at 200°C was shown to reduce the E_1 peak height by a factor of 30⁴⁹.

Initial theoretical studies based on zincblende GaN suggested that H^- is very stable in GaN, with a migration barrier of $\sim 3.4\text{eV}$ ⁵⁰. However, theoretical studies by Wright showed that H^- is expected to have a higher mobility in wurtzite GaN⁵¹. Both studies agree that H^- prefers the Ga antibonding site^{50,51}. Wright notes that the mobility of H^- is

blocked by a pair of Ga and N atoms at intervals of 7.8Å in the zincblende structure, which is not the case in hexagonal GaN⁵¹.

The above theoretical and experimental studies suggest that hydrogen passivation of deep levels in *n*-GaN is highly probable.

5.3.2 Emission from minority carrier traps

There is recent experimental evidence of a minority carrier (hole) trap in *n*-GaN grown by MOCVD^{52,53,54} and HVPE⁵⁵. An acceptor level E_h , $\sim 0.7 - 0.9$ eV above the valence band edge was detected by DLTS^{52,54,56} on $p^+ - n$ junction diodes, and by optical DLTS (ODLTS)⁵⁵ and minority carrier transient spectroscopy (MCTS)⁵³ on Schottky diodes. The trap concentration of the E_h level is typically reported to be in the region of $10^{15} - 10^{16} \text{ cm}^{-3}$ and the level observed is typically associated with the gallium vacancy^[58-61].

Figure 5.5 shows minority carrier emission detected by DLTS using $p^+ - n$ junction diodes as in (a) and by MCTS using Schottky diodes, as shown in (b). In both (a) and (b) the E_h level is not apparent in Schottky diodes investigated by DLTS.

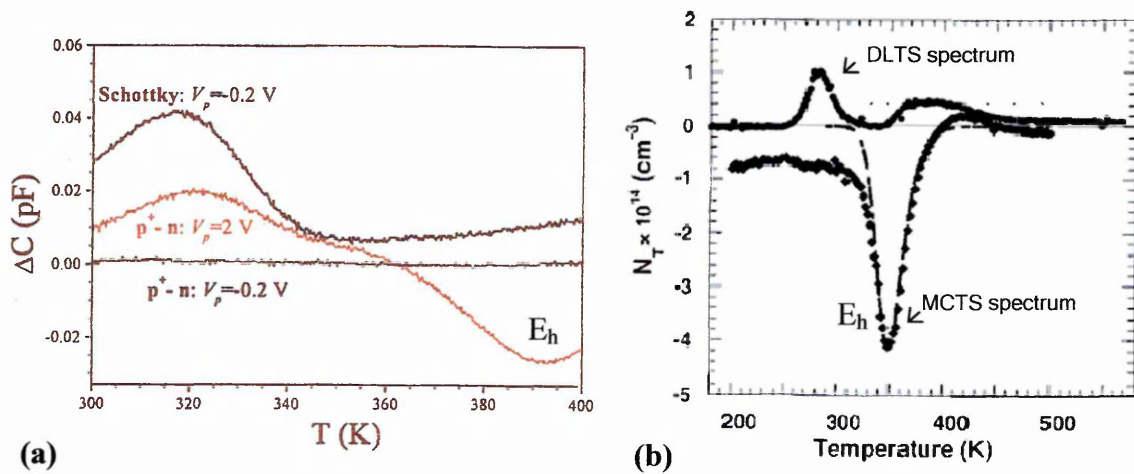


Figure 5.5: (a) Electron emission in Schottky diodes showing only electron emission. The E_h level in $p^+ - n$ junction diodes is detected using a forward bias pulse of 2V. After Hierro *et al.*⁵² (b) The positive spectra show electron emission obtained by DLTS on Schottky diodes. The presence of the E_h level is detected by MCTS. After Muret *et al.*⁵³.

In $p^+ - n$ junction diodes, the space charge region on the *p*-type region of the junction is negligible and DLTS is used to study deep levels in the *n*-type region. The detection of the E_h level by DLTS using $p^+ - n$ junction diodes is reported to require biasing parameters to ensure significant minority carrier injection. Hierro *et al.*⁵² note that no deep levels were observed in the $p^+ - n$ junction diodes investigated when the fill pulse amplitude was -0.2V. Furthermore, Asghar *et al.*⁵⁴ only observed minority carrier

emission by applying an injection pulse of 0.5V prior to the DLTS sequence, with an extended fill pulse duration from 0.1 to 1s to achieve sufficient minority carrier injection.

The MCTS studies carried out by Muret *et al.* made use of samples grown by conventional MOCVD and by the epitaxial lateral overgrowth (ELOG) method in different reactors⁵³. The dislocation density in the ELOG samples was $\sim 10^7 \text{ cm}^{-2}$, which is noted to be at least two orders of magnitude less than in samples grown by conventional MOCVD⁵³. During the MCTS measurements, a light source with a photon energy larger than the bandgap was used and the MCTS data was obtained through the Fourier transform of capacitance transients. The advantage of using this technique is that the Arrhenius plot is made up of many data points, hence increasing the accuracy of the derived acceptor level. The activation energy of the E_h level was reported to be $E_v + 0.81 \text{ eV}$, with a concentration of $\sim 10^{14} \text{ cm}^{-3}$ and a hole capture cross section of $2 \times 10^{-14} \text{ cm}^{-2}$. Muret *et al.* note that the E_h level was independent of the dislocation density, concentration or the reactor used⁵³.

In contrast, Ployakov *et al.* showed that the trap concentration of the E_h level increased with higher dislocation densities^{55,57}. The E_h level at $\sim E_v + 0.9 \text{ eV}$ was detected by the application of optical deep level transient spectroscopy (ODLTS) to both the N- and Ga-sides of the sample. The N-side of the sample was closer to the material-substrate interface and was reported to have a higher dislocation density⁵⁵. The hole trap concentration was seen to be larger on the N-side than for the Ga-side, which suggests that the traps giving rise to hole emission may exist at dislocations sites. Polyakov *et al.* studied HVPE grown GaN layers with varying thickness from 2.6 to 68 μm , again with the application of optical DLTS⁵⁷. A direct correlation between the concentration of the E_h level and the sample thickness was observed. The 2.6 to 68 μm thick samples displayed acceptor trap concentrations in the range of 10^{15} to 10^{16} cm^{-3} . In the thick, free standing layer the acceptor concentration was found to be in the range of 10^{12} to 10^{13} cm^{-3} . These results coincide with the work of Oila *et al.* who have shown using positron annihilation studies that a direct correlation exists between dislocation density and acceptor states in the material⁵⁸.

Hierro *et al.*⁵⁹ showed that the trap occupation of the E_h level has a logarithmic dependence on the filling pulse. This indicates that the trapping behaviour of neighbouring defects is affected by the Coulombic repulsion resulting from adjacent occupied states. Schröter's model suggests that the emission from dislocation cores is due to a *band of states* and is signified by three characteristics. Firstly, the DLTS peak

temperature is observed to be strongly dependent on the filling pulse duration, t_p . Secondly, the low temperature side of the DLTS peak is expected to be linearly dependent on t_p . Finally, the high temperature side of the peak due to emission from a dislocation core is seen to overlap for all values of filling pulse used. Hierro *et al.* note that these characteristics are not observed for the E_h level and suggest that the emission observed may not arise from dislocation cores.

Muret *et al.* investigated the electron-hole recombination properties the E_h level by MCTS⁵³. The measured electron capture cross section is reported to be temperature independent and a single time constant is derived from the capture cross section measurements. Muret *et al.* suggest the presence of a point defect at dislocation cores, based on the properties of Ga vacancy reported in the literature. Furthermore, capture cross-section measurements indicate that the centre is still negatively charged after the process of hole capture. This result indicates that the defect has multiple charge states, A^-/A^{2-} or A^{2-}/A^{3-} , which is in support of previous theoretical work by Elsner *et al.*⁶⁰ and Mattila and Nieminen⁶¹.

Multiple minority carrier levels were reported in the literature including those by Auret *et al.*⁶² and Asghar *et al.*⁵⁴. An additional level at $\sim E_v + 0.25$ eV, with a trap concentration of $\sim 5 \times 10^{14}$ cm⁻³, was detected by Auret *et al.* in samples grown by ELOG-MOCVD⁶².

On the other hand, Asghar *et al.* observed a dominant emission at ~ 230 K due to a level at $\sim E_v + 0.5$ eV, with a trap concentration of 8.0×10^{15} cm⁻³. Furthermore, a broad emission is detected in the 300K to 400K region, which is resolved into three peaks with levels $E_v + 0.7$ eV, $E_v + 0.75$ eV and $E_v + 0.86$ eV. Using the basic energy-wavelength relationship $E = hc/\lambda$, Asghar *et al.* relate the levels to the 427 (violet-blue), 457 (blue), 467 (blue) and 488nm (blue-green) spectral lines respectively. This is in support of previous work by Nakamura *et al.*, who have reported a broadband luminescence around 430nm, involving a deep centre at $E_c - 2.8$ eV. The results of Ashgar *et al.* would suggest that the level H1(0.5eV) is a candidate for violet-blue emission⁵⁴.

It was shown by Auret *et al.*⁶² that 1.8 MeV proton bombardment of *n*-GaN with a dose of 4.4×10^{13} protons cm⁻² is observed to reduce the trap concentration of the E_h level (~ 0.87 eV) from 2×10^{15} cm⁻³ to 4×10^{14} cm⁻³. The authors controversially conclude that the E_h level typically observed in the literature cannot be due to the gallium vacancy, as previously thought by other groups. Auret *et al.* argue that vacancies and interstitials are primary radiation-induced defects in semiconductors, and the

concentration of the gallium vacancy should therefore increase upon proton bombardment⁶².

It is widely accepted that the hole trap is linked to the gallium vacancy and its complexes with oxygen at threading edge dislocations. However, there appears to be a controversy regarding the capture properties of the E_h level. Hierro *et al.* suggest extended defect related emission⁵⁹, whereas Muret *et al.* derive a single recombination time constant, indicating that the defect level concerned is not of a complex nature⁵³. It is also not clear whether the defect behaves only as a trapping centre or whether it is a path for recombination. Polyakov *et al.* have stated that this level is observed to capture electrons during the discharge period as a result of the forward bias pulse applied⁵⁵.

5.4 Summary

The modified carrier capture and emission at extended defects was discussed. The presence of a *band of states* at extended defects results in a potential barrier for subsequent electron capture due to occupied states at the dislocation core. This is the basis of the logarithmic capture law used in DLTS to verify emission from extended defects. Furthermore, emission from extended defects typically results in line broadening when longer fill pulses are applied and the peak position is observed to shift to a lower temperature.

The dominant DLTS lines in plastically deformed *n*- and *p*-type Si are the *C* and *F* lines, respectively. These are reported to survive high annealing temperatures. DLTS results indicate that the electrical activity at dislocations is strongly dependent on the level of decoration.

DLTS of *n*-GaN reveals dislocation related emission at around room temperature. This suggests that threading dislocations in GaN may pose significant problems for GaN based junction devices. Results indicate the presence of a hole trap in GaN grown by various methods. This level has been associated with the gallium vacancy. However, there is still some disagreement in terms of the capture properties of this defect. The negative charge associated with dislocations and the existence of gallium vacancies at dislocation cores in GaN were discussed in Chapter 3. Dislocations have been shown to be negatively charged and existence of vacancies at the dislocation core has been evidenced through positron annihilation studies, as discussed in Chapter 3. Therefore, the capture properties of the E_h level should resemble extended defect related emission. However, DLTS results do not fully support this argument, although fill pulse dependency was reported by Hierro *et al.*

5.5 References

- ¹ W. Schröter, J. Kronewitz, U. Gnauert, F. Riedel, M. Seibt, *Phys. Rev. B* **52**, 13726 (1995).
- ² P. R. Wilshaw, T. S. Fell, *Inst. Phys. Conf. Ser.* **104**, 85 (1989).
- ³ W. Schröter, I. Queisser, J. Kronewitz, *Inst. Phys. Conf. Ser.* **104**, 75 (1989).
- ⁴ W. Schröter, H. Cerva, *Solid State Phenomena* **85-86**, 67 (2002).
- ⁵ P. N. Grillo, S. A. Ringel, E. A. Fitzgerald, G. P. Watson, Y. H. Xie, *J. Appl. Phys.* **77**, 3248 (1995).
- ⁶ T. Figielski, *Phys. Stat. Sol. (a)* **121**, 187 (1990).
- ⁷ L. C. Kimmerling, J. R. Patel, *Appl. Phys. Lett.* **34** 73 (1979).
- ⁸ V. V. Kveder, Yu. A. Osipyan, W. Schröter, G. Zoth, *Phys. Stat. Sol. (a)* **72** 701 (1982).
- ⁹ P. Omling, E. R. Weber, L. Montelius, H. Alexander, J. Michel, *Phys. Rev. B* **32** 6571 (1985).
- ¹⁰ K. Knobloch, M. Kittler, W. Seifert, *J. Appl. Phys.* **93** 1069 (2003).
- ¹¹ D. Cavalcoli, A. Cavellini, E. Gombia, *Phys. Rev. B* **56** 10208 (1997).
- ¹² H. Ono, K. Sumino, *J. Appl. Phys.* **57** 287 (1985).
- ¹³ H. Lemke, *Phys. Stat. Sol. (a)* **65** 389 (1981).
- ¹⁴ K. Sumino, *Phys. Stat. Sol. (a)* **171**, 111 (1999).
- ¹⁵ G. R. Lahiji, B. Hamilton, A. R. Peaker, *Electron. Lett.* **24**, 1340 (1988).
- ¹⁶ A. R. Peaker, B. Hamilton, G. R. Lahiji, I. E. Ture, G. Lorimer, *Mat. Sci. Eng. B* **4** 123 (1989).
- ¹⁷ M. Kaniewska, J. Kaniewski, A. R. Peaker, *Materials Science Forum* **143-147**, 1722 (1993).
- ¹⁸ Y. Qian, J. H. Evans, A. R. Peaker, *Inst. Phys. Conf. Ser.* **134** 121 (1993).
- ¹⁹ C. J. Varker, K. V. Ravi, *J. Appl. Phys.* **45** 272 (1974).
- ²⁰ B. O. Kolbesen, W. Bergholz, H. Cerva, F. Gelsdorf, H. Wendt, G. Soth, *Proc. 6th Int. Symp. on the Structure and Properties of Dislocations*, *Inst. Phys. Conf. Ser.* **104**, 421 (1990).
- ²¹ S. Kawado, *Japanese J. Appl. Phys.* **19** 1591 (1980).
- ²² L. C. Kimmerling, H. J. Leamy, J. R. Patel, *J. Appl. Phys.* **30** 217 (1977).
- ²³ A. Castaldini, A. Cavellini, A. Poggi, E. Susi, *Appl. Phys. A* **48** 431 (1989).

- ²⁴ M. Morooka, H. Tomokage, H. Kitagawa, M. Yoshida, *Jpn. J. Appl. Phys.* **24** 133 (1985).
- ²⁵ M. Morooka, H. Tomokage, M. Yoshida, *Jpn. J. Appl. Phys.* **24** 1778 (1988).
- ²⁶ J. Kaniewski, M. Kaniewska, A. R. Peaker, *Appl. Phys. Lett.* **60** 359 (1992).
- ²⁷ A. Borghesi, B. Pivac, A. Sassella, A. Stella, *J. Appl. Phys.* **77** 4169 (1995).
- ²⁸ W. Kaiser, P. H. Keck, C. F. Lange, *Phys. Rev.* **101** 1264 (1956).
- ²⁹ W. L. Bond and W. Kaiser, *J. Phys. Chem. Solids* **16** 44 (1960).
- ³⁰ I. E. Bondarenko and E. B. Yakimov, *Phys. Stat. Sol. (a)* **122** 121 (1990).
- ³¹ L. Murin, J. L. Lindström, V. P. Markevich, A. Misiuk, C. A. Londos, *J. Phys. C* **17**, 2237 (2005).
- ³² R. C. Newman, *Rep. Prog. Phys.* **45** 1163 (1982).
- ³³ C. Claeys, E. Simoen, J. Vanhellefont, *J. Phys. III France* **7** 1469 (1997).
- ³⁴ S. S. Chan, C. J. Varker, J. D. Whitfield, R. W. Carpenter, *Mat. Res. Soc. Symp. Proc.* **46** 281 (1985).
- ³⁵ O. V. Feliksova, G. Mariani-Regula, B. Pichaud, E. B. Yakimov, *Phys. Stat. Sol. (a)* **171** 341 (1999).
- ³⁶ A. Castaldini, D. Cavalcoli, A. Cavallini, S. Pizzini, *Phys. Stat. Sol. (a)* **202**, 889 (2005).
- ³⁷ Z. Q. Fang, D. C. Look, L. Polenta, *J. Phys. C* **14**, 13061 (2002).
- ³⁸ F. D. Auret, S. A. Goodman, G. Myburg, W. E. Meyer, J.-M. Spaeth, P. Gibart, B. Beaumont, *Radiation Effects & Defects in Solids* **156**, 255 (2001).
- ³⁹ C. B. Soh, D. Z. Chi, A. Ramam, H. F. Lim, S. J. Chua, *Mat. Sci. Sem. Process.* **4**, 595 (2001).
- ⁴⁰ C. D. Wang, L. S. Yu, S. S. Lau, E. T. Yu, W. Kim, A. E. Botchkarev, H. Morkoç, *Appl. Phys. Lett.* **72**, 1211 (1998).
- ⁴¹ P. Hacke, T. Detchprohm, K. Hiramatsu, N. Sawaki, *J. Appl. Phys.* **76** 304 (1994).
- ⁴² P. Kozodoy, J. P. Ibbetson, H. Marchand, P. T. Fini, S. Keller, J. S. Speck, S. P. DenBaars, U. K. Mishra, *Appl. Phys. Lett.* **73**, 975 (1998).
- ⁴³ E. J. Miller, E. T. Yu, P. Waltereit, J. S. Speck, *Appl. Phys. Lett.* **84**, 535 (2004).
- ⁴⁴ C. Soh, S. Chua, H. Lim, D. Chi, W. Liu, S. Tripathy, *J. Phys.: Condens. Matter* **16**, 6305 (2004).
- ⁴⁵ L. Wu, W. E. Meyer, F. D. Auret, M. Hayes, *Physica B* **340-342**, 475 (2003).
- ⁴⁶ L. Wu, W. E. Meyer, F. D. Auret, *Phys. Stat. Sol. (a)* **201**, 2277 (2004).

- ⁴⁷ E. R. Weber and J. Krüger, *New Materials: Gallium Nitride* in *Handbook of Semiconductor Technology*, Edited by K. A. Jackson and W. Schröter, Vol. 1, Wiley-VCH, New York (2000).
- ⁴⁸ M. A. Reschikov and H. Morkoç, *J. Appl. Phys.* **97**, 061301-1 (2005).
- ⁴⁹ A. Hierro, S. A. Ringel, M. Hansen, J. S. Speck, U. K. Mishra, S. P. DenBaars, *Appl. Phys. Lett.* **77**, 1499 (2000).
- ⁵⁰ J. Neugebauer and C. G. Van de Walle, *Phys. Rev. Lett.* **75**, 4452 (1995).
- ⁵¹ A. F. Wright, *Phys. Rev. B* **60**, R5101 (1999).
- ⁵² A. Hierro, D. Kwon, S. A. Ringel, M. Hansen, J. S. Speck, U. K. Mishra, S. P. DenBaars, *Appl. Phys. Lett.* **76**, 3064 (2000).
- ⁵³ P. Muret, A. Philippe, E. Monroy, E. Muñoz, B. Beaumont, F. Omnès, P. Gibart, *J. Appl. Phys.* **91**, 2998 (2002).
- ⁵⁴ M. Asghar, P. Muret, I. Hussain, B. Beaumont, P. Gibart, M. Shahid, *Mat. Sci. Eng. B* **130**, 173 (2006).
- ⁵⁵ A. Y. Polyakov, N. B. Smirnov, A. V. Govorkov, Z. -Q. Fang, D. C. Look, S. S. Park, J. H. Han, *J. Appl. Phys.* **92**, 5241 (2002).
- ⁵⁶ C. B. Soh, D. Z. Chi, A. Ramam, H. F. Lim, S. J. Chua, *Mat. Sci. Sem. Proc.* **4**, 595 (2001).
- ⁵⁷ A. Y. Polyakov, N. B. Smirnov, A. V. Govorkov, Z. -Q. Fang, D. C. Look, R. J. Molnar, A. V. Osinsky, *J. Appl. Phys.* **91**, 6580 (2002).
- ⁵⁸ J. Oila, V. Ranki, J. Kivioja, K. Saarinen, P. Hautojärvi, J. Likonen, J. M. Baranowski, K. Pakula, T. Suski, M. Leszczynski, I. Grzegory, *Phys. Rev. B* **63**, 045205-1 (2001).
- ⁵⁹ A. Hierro, M. Hansen, J. J. Boeckl, L. Zhao, J. S. Speck, U. K. Mishra, S. P. DenBaars, S. A. Ringel, *Phys. Stat. Sol. (b)* **228**, 937 (2001).
- ⁶⁰ J. Elsner, R. Jones, M. I. Heggie, P. K. Stitch, M. Haugk, Th. Frauenheim, S. Öberg, P. R. Briddon, *Phys. Rev. B* **58**, 12571 (1998).
- ⁶¹ T. Mattila and R. M. Nieminen, *Phys. Rev. B* **55**, 9571 (1997).
- ⁶² F. D. Auret, W. E. Meyer, L. Wu, M. Hayes, M. J. Legodi, B. Beaumont, P. Gibart, *Phys. Stat. Sol. (a)* **201** 2271 (2004).

Chapter 6

Deep level emission from extended defects in silicon

In this chapter, results are presented from the electrical characterisation of both *n*-type and *p*-type silicon containing extended defects. In the *n*-type silicon samples, the main interest of the work was the application of Laplace deep level transient spectroscopy (LDLTS) to study the carrier capture behaviour of active defects associated with extended defect structures consisting of oxidation-induced stacking faults (OISF). The understanding gained from this work enabled the interpretation of LDLTS results when applied to *p*-type samples containing oxygen-locked dislocations (O-LD). A review of OISFs and dislocation locking by oxygen was presented in chapter 3 and the characterisation methods used for this study were described in chapter 4.

6.1 Sample specifications and fabrication methods

The Schottky barrier diode fabrication process is outlined, followed by details of the *n*-type samples containing OISFs and *p*-type samples with oxygen-locked dislocations.

The steps taken in the fabrication of Schottky barrier diodes are listed, followed by an outline of sample details. The formation of the stacking faults and the locking of dislocations by oxygen were performed prior to this work by the Oxford Materials group at Oxford University. However, the fabrication was carried out during and solely for this study.

6.1.1 Schottky diode fabrication

For both the OISF (*n*-type) samples and those containing O-LDs (*p*-type), the steps taken in fabricating Schottky diodes are listed below and are the same for both materials, unless stated otherwise.

I. Sample cleaning

1. Degreasing:

Samples are placed in a beaker containing one of the following chemicals at a time for 10 minutes in an ultrasonic bath in the listed order:

- a) Trichloroethylene,
- b) Acetone,
- c) Methanol.

After the final methanol stage, a rinse in deionised (DI) water is required. Samples are then placed in a mixture of sulphuric acid (H₂SO₄) and hydrogen peroxide (H₂O₂) at a ratio of 2:1 for 10 min, followed by a DI water rinse.

2. Oxide removal:

Samples are dipped in 10% HF solution for 5 minutes and then rinsed with DI water.

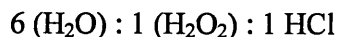
3. Organic contaminants removal (RCA1):

Samples are left for 10 minutes at an elevated temperature of 75-85°C in the following solution, with a subsequent DI water rinse:



4. Metallic contaminants removal (RCA2):

Samples are left for 10 minutes at an elevated temperature of 75-85°C in the following solution, with a subsequent DI water rinse:



5. Oxide removal prior to metal deposition:

A dip in concentrated HF for 10 seconds is necessary in order to remove any oxide before the metal contacts are sputtered/evaporated. This is again followed by a DI water rinse.

II. Schottky Barrier deposition

a) n-type OISF samples:

For these samples, 1mm diameter gold dots are evaporated on the front surface of the silicon through a mask at a base pressure of $\sim 2 \times 10^{-5}$ Torr.

b) *p*-type O-LD samples:

To ensure that the Schottky barriers were directly above the dislocations, the 1mm dots were aligned using a mask aligner. This was possible with the aid of a map for each sample showing the positions of the dislocations, which was provided by Oxford University.

The mask aligner step involves spinning on positive photoresist at 5000 rpm for 30 seconds followed by a prebake at 90°C. After the prebake step, the samples are left in chlorobenzene for 5 min. The purpose of this step is to enhance the perpendicular features of the pattern to be exposed rather than resulting in slanted walls of resist. This is important in DLTS, as the area of the diode must be determined as accurately as possible for the determination of the trap concentration. Once the mask is aligned to the sample, it is exposed to ultraviolet (U.V.) light for 50 seconds and developed for 2 minutes. Immediately prior to the Schottky barrier deposition, the samples are dipped in concentrated HF to remove surface oxide.

The Schottky barrier used for *p*-type silicon is Titanium (Ti), which is sputtered to a thickness of ~50 nm. Subsequently, a thicker layer (~300 nm) of aluminium (Al) is sputtered without bringing the chamber to atmosphere to avoid the oxidation of the Ti layer.

III. Ohmic contact deposition

For both types of samples, a layer of Al is evaporated on the back surface. The thickness is not a critical parameter and is not measured.

IV. Sample bonding

This step is the same for all samples and involves mounting the samples on a ceramic bonding package using conductive silver paint, which also acts as the contact to the back (ohmic contact). The Schottky barriers are subsequently bonded to the gold pads on the ceramic package using gold wire. The use of a ceramic package is not necessary, but protects the Schottky contact from becoming scratched by the contact pins inside the cryostat.

6.1.2 *n*-type OISF sample

The starting material for these samples was *n*-type Czochralski (CZ) silicon, with a resistivity of 1-2 Ωcm. The stacking faults in the sample were created by oxidising for 1 hour at 1100°C. The average length of each stacking fault was ~1μm.

6.1.1 *p*-type O-LD sample

This work was undertaken in collaboration with researchers at Oxford Materials, Oxford University. A topic of research at Oxford, in conjunction with MEMC, is the effect of dislocation locking by impurities in order to improve the mechanical hardness of silicon wafers. Three samples (A, B and C) have been prepared at Oxford University, containing dislocations which have been locked by oxygen. The principles of dislocation locking by impurities are discussed in chapter 3. The amount of unlocking stress required for dislocation movement is different for each sample and is determined by the annealing time.

Bars measuring approximately 20 mm × 3.5 mm × 0.7 mm were cleaved from a *p*-type CZ-silicon wafer, with an interstitial oxygen concentration of $1.05 \times 10^{18} \text{ cm}^{-3}$. The cleaved edges were mechanically polished. The samples were indented at three regions along the bar at 40 μm intervals with a Vickers indent, which had a 10g load and was applied for 5s at a time. This created dislocation half-loops, situated on the {111} set of planes and were identified to be either of screw or 60° type. A schematic of this configuration is shown in Figure 6.1.

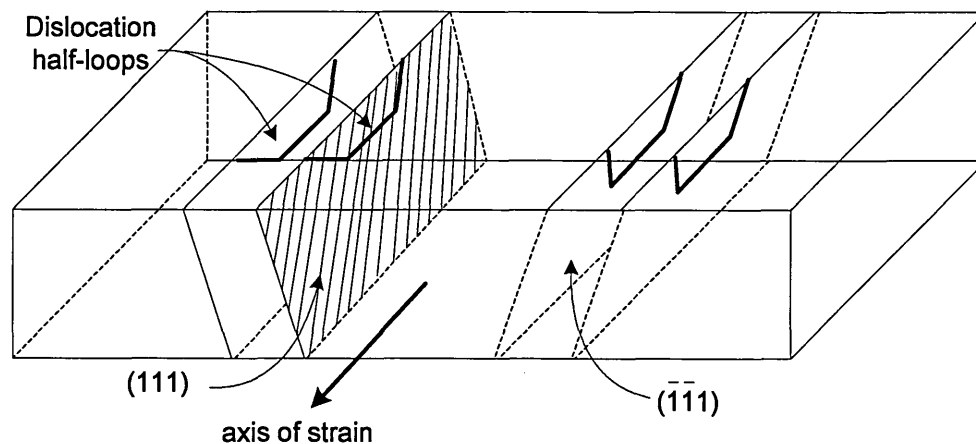


Figure 6.1: Schematic of sample containing dislocation loops

The dislocation half-loops were allowed to grow into the sample by four-point bending at approximately 570°C. The three samples were subsequently annealed at 500°C for different lengths of time in order to allow different amounts of oxygen to segregate to the dislocation cores, resulting in different amounts of unlocking stress for each sample. The amount of unlocking stress required for dislocation motion and the approximate number of oxygen atoms per unit length of dislocation was estimated using previous data^{1,2}. The details for each sample are displayed in table 6.1.

<i>Sample</i>	<i>Anneal time (hrs)</i>	<i>Approximate unlocking stress (MPa)</i>	<i>Approximate number of oxygen atoms per unit length of dislocation (cm^{-1})</i>
A	35	150	2×10^7
B	15	75	1×10^7
C	<i>Not annealed</i>	<10	$\sim 1 \times 10^6$

Table 6.1: List of annealing times for each sample, together with the stress required to start dislocation motion

The position of the dislocations within the samples were determined by Nomarski microscopy so that the Schottky barrier diodes could be placed directly on top of the dislocations, as described in section 6.1.1 (II). Approximately 50 μm of material was removed from the surface in order to eliminate the effects of oxygen out-diffusion and to remove the indents. To prepare the surface for electrical measurements, the sample surfaces were then polished by mechanical and chemomechanical methods.

6.2 Results: OISF sample

Figure 6.2 shows the DLTS spectrum of the OISF sample, at a reverse bias of -2V and a forward bias pulse of 0.1V . This value of reverse bias has been chosen with the aid of I-V and C-V characteristics, to ensure that the carrier concentration is uniform and that the reverse leakage current is negligible within the region probed. The pairs of rate windows employed are 1000 s^{-1} and 400 s^{-1} , 200 s^{-1} and 80 s^{-1} , 50 s^{-1} and 20 s^{-1} . The spectra reveal two peaks, which are labelled as SF1 ($\sim 40 - 240\text{K}$) and SF2 ($\sim 240 - 300\text{K}$). A broad DLTS peak ($\sim 130 - 240\text{K}$) associated with nominally ‘clean’ OISFs in n -type Si has previously been reported^{3,4}, as described in chapter 3.

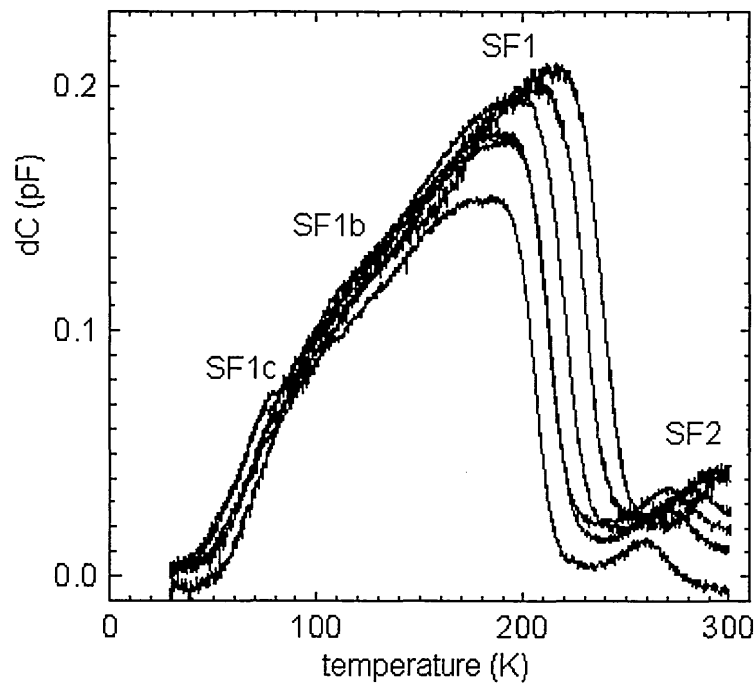


Figure 6.2: DLTS of sample OISF. The quiescent reverse bias was -2V , with a fill pulse voltage of 0.1V and a duration of 1ms .

It can be seen that SF1 consists of more than one level. There are at least two ‘shoulders’ present to the left of SF1, which are labelled SF1b and SF1c. Although the main objective of this study is the application of Laplace deep level transient spectroscopy (LDLTS) to study the emission behaviour of extended defects, it is still of interest to understand the nature of the levels observed in DLTS. It has been shown by Kaniewski *et al.* that these peaks can be resolved into individual peaks by implementing the technique of spatial profiling⁴ (as described in chapter 5) and that the depth profile of one of the resolved peaks follows that of the stacking faults. Interestingly, the samples used in reference 4 were prepared under similar conditions and in the same cleanroom as those used for this current study. The main difference in the processing methods is the length of annealing time. Those investigated by Kaniewski *et al.* have been annealed for double the time (2 hours). Assuming that the levels can be related on this basis, the level they associated with the stacking faults could possibly be level SF1c in Figure 6.2.

The small peak above 240K , SF2, is likely to be due to a point defect, judging by the symmetry of the peak, and it appears to have a low concentration in comparison to SF1. The activation energy of this peak has not been obtained, as the main focus of the work involved the level associated with the OISF. However, results of Kaniewski *et al.* on *n*-type Si containing OISFs have also revealed a smaller point-defect-like peak in the

same temperature range as that of SF2. If SF2 is in any way related to the level labelled 6 in reference 4, it could be expected to have an increasing trap concentration deeper into the sample, in which case it is not likely to be associated with the OISFs.

It was discussed in Chapter 5 that the capture properties of extended defects in silicon (and other semiconductors) are strongly influenced by the number of traps already occupied within the extended defect configuration due to the long range Coulomb potential associated with closely-spaced, many-electron (or hole) systems. This phenomenon is discussed in chapter 2 and some points are summarised here. The capture properties of extended defects have been extensively characterised using DLTS and it has been reported that the capture of the (next) incoming electron is greatly influenced by the states that are already filled in the extended defect configuration. This is observed as a change in the activation energy of the deep level as a result of a change in the fill pulse applied. The result is often a decrease in the activation energy and capture cross-section with increasing fill pulse. The states that are already filled provide a repulsive force for an incoming electron and a local band-bending exists at the extended defect.

To investigate this principle, the DLTS measurements were repeated using different fill pulses and the resulting activation energies of level SF1 were obtained. All other parameters were kept the same. Figure 6.3 shows the Arrhenius plots with three different fill pulse durations of 0.1ms, 1ms and 5ms. The derivation of the activation energy from an Arrhenius plot was described in Chapter 5.

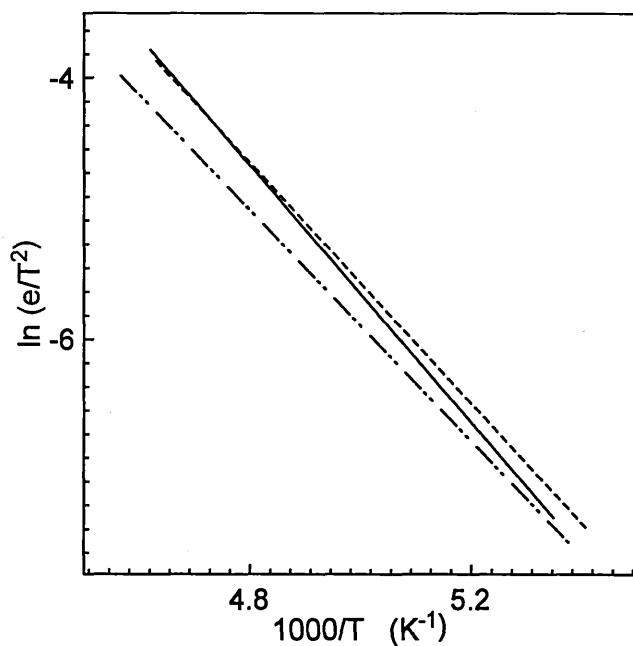


Figure 6.3: Arrhenius plots of OISF sample at fill pulse lengths of 0.1ms(—), 1ms(- -) and 5ms(—-).

There is a clear difference in the gradients of the plots. The derived values of activation energies for each fill pulse length used are listed in Table 3.2. The value reported in each case is the difference between the deep level and the conduction band edge.

<i>Fill pulse length (ms)</i>	<i>Activation energy (meV)</i>
0.1	420
1	395
5	350

Table 3.2: List of activation energies derived as a result of a change in fill pulse length.

Results show that as the carriers flow over the states for a longer period of time, the activation energy of the defect level decreases, as previously reported^{5,6}. This effect is due to the band-edge modification at the dislocation core due to local charge build-up, as described in Chapter 2, section 2.4.1. The fill pulse in DLTS brings carriers into the depletion region where some are trapped by close-packed states at the dislocation core, resulting in a line charge. Increasing the duration of this filling process allows the trapping of electrons by states that are physically farther away from the dislocation core. This increases the charge at the dislocation line, resulting in an increase in the electrostatic potential of the system, which further increases the amount of band-bending. As the diode is brought back to its quiescent state, the activation energy of emission from traps is reduced by the repulsive electrostatic charge which builds up along the dislocation line. This is because these states are affected by the long-range Coulomb potential of the line charge at the dislocation core. This phenomenon is illustrated in Figure 6.4

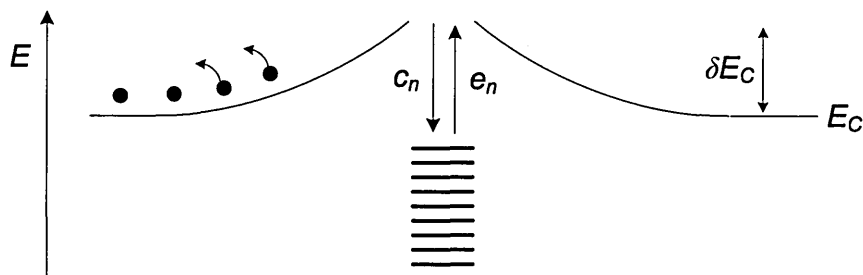


Figure 6.4: Band bending due to the fill-pulse dependent dislocation line-charge.

LDLTS measurements for this sample have been carried out at 220K, at the peak of SF1, with fill pulses of 1 and 5ms. The resulting spectra are presented in Figure 6.5. The same biasing parameters have been used as the DLTS measurement. There are a number of observations to be made about the differences between the emission rates due to the 1 ms and the 5 ms fill pulses. Firstly, four emission rates are detected and a clear shift towards higher emission rates are observed for all emissions as a result of an increase in fill pulse length. This is a direct observation of the effect of the filling pulse length on the emission rate from extended defects. This is due to the build-up of charge along the dislocation line, resulting in local band-edge modification, as illustrated in Figure 6.4.

The amplitudes of three of the four emission rates decrease as a result of increasing fill pulse. This effect was not expected, as an increase in fill pulse duration should, result in an increase in the signal amplitude, due to more levels emptying at a given time. That is, if more levels are filled, then more should also empty during the measurement phase. The level of band-bending together with the Coulombic repulsion at the dislocation could be large enough to inhibit electron capture at certain levels in the band gap. In other words, these incoming electrons could experience a weaker binding energy to the deep level for a fill pulse of 5 ms than for a 1 ms fill pulse.

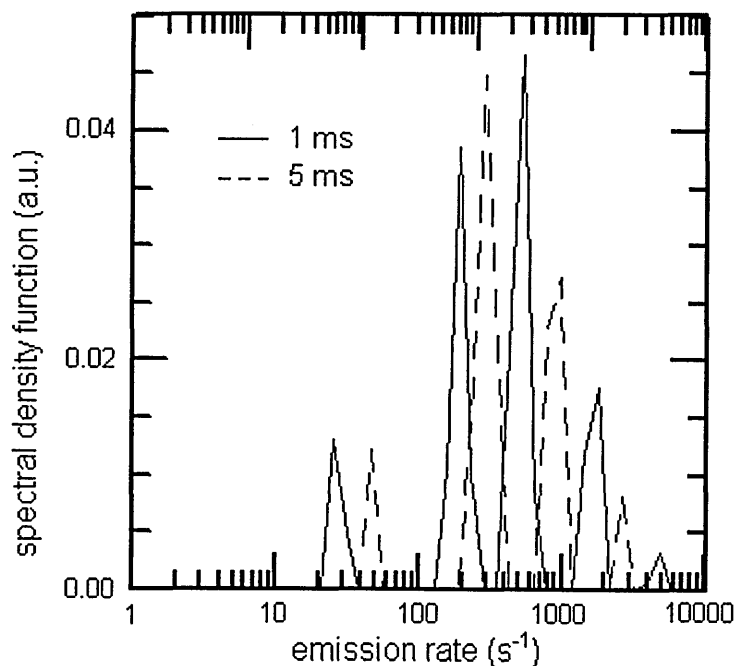


Figure 6.5: Laplace DLTS of OISF sample at 220K

If it can be assumed that the levels are saturated at some time between 1 and 5 ms, then the following model is proposed, to suggest an explanation for the decrease in amplitude

observed. It must be emphasised that the following is merely a model of the capacitance transients which *could* explain the decrease in the amplitude of some of the LDLTS emissions observed.

Figure 6.6 illustrates the possible capacitance transients during the above LDLTS measurement. Transient A would be representative of a transient arising from defects very close to (or at) saturation, such as the 1 ms fill pulse in the above case. The principles behind the capacitance transient in DLTS were described in chapter 5 and are briefly summarised here. After the fill pulse, the diode is brought back to a quiescent reverse bias, which reduces the diode capacitance to a value below its quiescent value, due to filled traps. The point in time at which the capacitance transient begins is set as $t = 0$. This is when the traps emit their carriers and the diode capacitance begins to return to its quiescent value. The transient arises due to the emission of electrons from deep levels. The trap occupancy is governed by an exponential dependency on time. In LDLTS, the data points before $t = 0$ are discarded, in order to analyse the transient only.

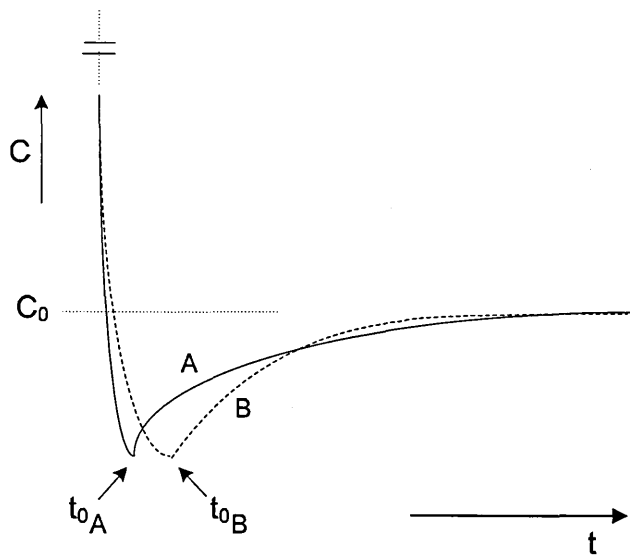


Figure 6.6: Possible capacitance transients of saturated levels at extended defects.

A further increase in the fill pulse duration would induce greater band-bending at the dislocation, which results in a larger barrier for electron capture. At the instance that the diode is brought back to the reverse bias, a build-up of uncaptured charge may exist between dislocations. This is illustrated in Figure 6.7.

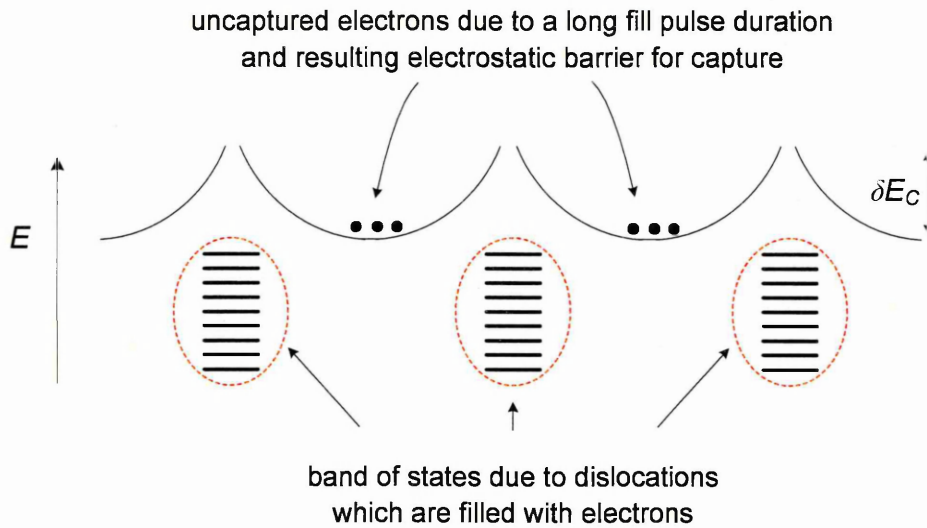


Figure 6.7: The presence of uncaptured electrons between dislocations due to long fill pulse durations giving rise to a dislocation line charge and local band-bending at dislocations.

This will affect the time it takes from when the diode is returned to the reverse bias, to when the deep levels start to emit their carriers. This resulting transient process is represented by B in Figure 6.6, where the time difference between $A(t_0)$ and $B(t_0)$ is greatly exaggerated. The transient itself solely consists of the emission of carriers from deep levels, which will appear to emit faster due to the increase in fill pulse and resulting electrostatic potential. However, the time taken for the transient to reach equilibrium will not take much longer, as the levels will now emit faster than they would for a shorter fill pulse, due to electrostatic repulsion at the band of states.

The superposition of transients A and B from $t = 0$ is illustrated in Figure 6.8. Capacitance transients due to emission from extended defects are not exponential with time, due to the Coulomb interaction between closely-spaced levels⁷. Three regions are of interest in Figure 6.8, labelled 1, 2 and 3. It can be seen from the transients in Figure 6.8 that superposition of transients made up of different emission rates may lead to changes in amplitude.

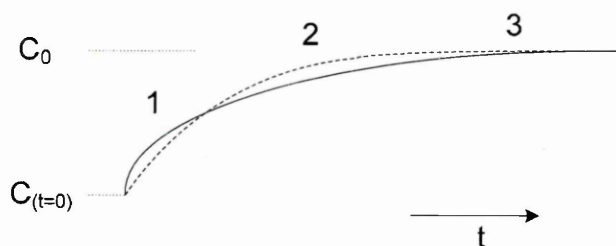


Figure 6.8: Superposition of capacitance transients A (solid) and B (dashed) which have been introduced in figure 6.6.

Another observation worthy of note is that additional emission rates have not been observed after the fill pulse has been increased to 5 ms. An increase in fill pulse is a spatial extension. This is illustrated in Figure 6.9. A cross-section of a reverse biased n -type silicon is considered, such as in a typical DLTS experiment. The quasi-neutral region and the presence of dislocations are ignored for simplicity. The pathway of the incoming electrons during a fill pulse is indicated by the arrow. For shorter fill pulses, the filling of states obeys Fermi-Dirac statistics, as described in Chapter 2. Due to the potential difference between the two terminals, the states in the path of the electron movement are likely to fill first. However, with longer fill pulse durations, states which exist further away from the electron pathway will begin to fill. This process is referred to as a spatial extension of the filling of empty states. Such a spatial extension occurs in two dimensions, but not deeper into the bulk. This is because the states outside the depletion region (further into the bulk) are already full and the empty states should only exist within the space-charge region.

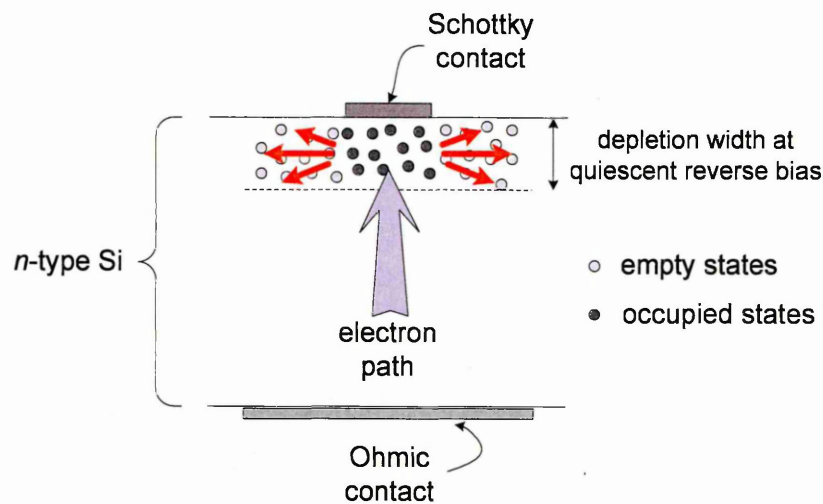


Figure 6.9: Illustration of the spatial extension effect of the increase in fill pulse duration during a DLTS or LDITS experiment. The electron path indicated corresponds to the fill pulse phase during measurements.

By the spatial extension process described above, one could expect the appearance of additional levels as a result of a longer fill pulse. For example, other defect states such as the Frank partials at the end of stacking faults, could be sufficiently further away not to be filled by an increase from 1 to 5ms of the filling pulse. However, filling of additional states may be possible by applying a much longer fill pulse, such as 50 ms.

It must be emphasised that the phenomena considered above are only possible models to describe the fill pulse dependence of the peak heights in the Laplace DLTS results observed. Limitations to the models exist and should be discussed. Firstly, the uncaptured charge between dislocations is only likely if the dislocations are very close to one another. Secondly, it is not possible to measure the time taken between when the reverse bias is applied to the diode (after the fill pulse) to when the deep levels begin to emit their carriers. Therefore, the above must only be viewed as a possible reason to why the peak heights are reduced upon an increase in the fill pulse length.

The use of Laplace DLTS has shown in this instance that the broad OISF-related level between 130 – 240K in fact is made up of multiple levels, with at least four emission rates. Furthermore, a direct effect on the emission rates from deep levels has been observed as a result of an increasing fill pulse length. It is widely known that capture properties at extended defects can be modified by changing the fill pulse length during a DLTS measurement⁸, but the effect on the actual emission rates have not been reported. LDLTS has been previously applied to ion implanted silicon, in which multiple levels have been detected⁹, but a direct observation of the change in emission rate as a result of the filling process is not known to be reported previously.

6.3 Results: Oxygen-locked dislocations

The biasing parameters used and the corresponding region probed during the DLTS measurements for samples A, B and C are presented in table 6.3. The depth probed during the DLTS experiment was obtained from the C-V plots using equation 5.8 in chapter 5.

<i>Sample</i>	<i>Quiescent reverse bias (V)</i>	<i>Forward bias pulse (V)</i>	<i>Depth probed during DLTS (μm)</i>
A	-4	0.1	~1.2
B	-1.5	0.1	~2.2
C	-2	0.1	~3.3

Table 6.3: Biasing parameters used for samples A, B and C during DLTS measurements.

The parameters selected for each sample have been determined through C-V and I-V measurements (as for the OISF sample) to ensure that the leakage current is negligible during the measurement, whilst maintaining constant carrier concentration within the region probed. It is interesting to note that the depth probed in sample A below the

surface is almost half that of B, whilst the reverse bias used is more than double the reverse bias used for B. This will be significant when examining the DLTS results obtained.

Figure 6.10 presents the DLTS spectra obtained for samples A, B and C, at a rate window of 200s^{-1} . The first noticeable result is the presence of a low temperature peak in the spectra for samples A and B, which is not present for sample C. The stress required to start the movement of dislocations in this sample is negligible ($\sim 10\text{MPa}$) in comparison to samples A and B, which have an unlocking stress of 75MPa and 150MPa respectively. Oxygen atoms have not intentionally been allowed to segregate to the dislocation cores in sample C. Furthermore, it can be seen that the magnitude of this level is greater for sample A than it is for B, although the depth probed during A is half that of B. Recalling that sample A has the highest amount of oxygen at the dislocation cores, whilst C has the least amount, it is reasonable to conclude that this level is directly linked to the oxygen segregated to the dislocation cores.

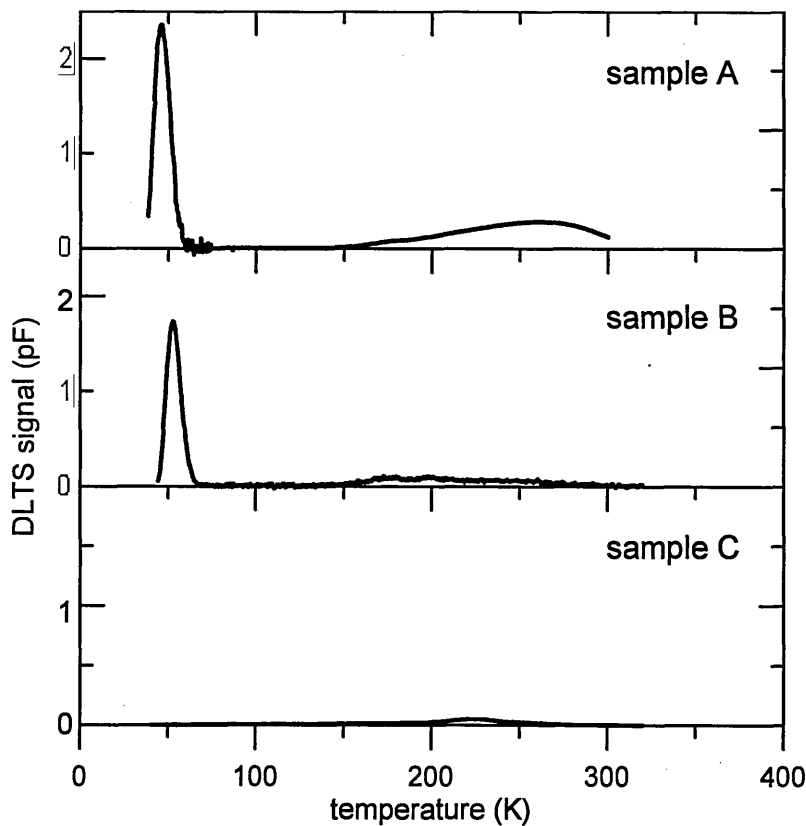


Figure 6.10: DLTS spectra of samples A, B and C at a rate window 200s^{-1} and a fill pulse of 1ms .

Although the shapes of the low temperature DLTS peaks (samples A and B) are point-defect-like, further electrical characterisation reveals that their capture properties are complex. As with the oxygen-induced stacking fault sample, the variation of activation

energy with fill pulse length has been investigated for the low temperature peaks in samples A and B, which are listed in Table 6.4. The activation energy values in Table 6.4 correspond to the difference between the valence band edge and the deep level. In both samples, there is a clear decrease in the activation energy as the fill pulse length is increased. This further supports the notion that the low temperature peak is arising from the dislocation core, where there is a build-up of charge.

<i>Sample</i>	<i>Fill pulse length (ms)</i>	<i>Activation energy (meV)</i>
A	1	250
	10	220
B	1	280
	10	260

Table 6.4: Variation of activation energy with fill pulse length for the low temperature peaks observed in the DLTS spectra of samples A and B.

It is noticeable that the derived activation energies are extremely high considering that the emission occurs at temperatures of about 50-60K. This could be explained by considering that the defect states detected are in the strain-field of the dislocation core, with unusually large capture cross-sections, which may mean that the capture rate is faster than the emission rate. In this case, the calculated activation energy is not likely to be a meaningful representation of the emission process.

Figure 6.11 shows the Arrhenius plots of sample B with fill pulses of 1 and 10ms, which is also representative of sample A. Although the data resulted in good linear fit, the capture cross-section (σ_p) obtained by extrapolation to the intercept on the $\ln(e/T^2)$ axis was a value of greater than 1cm^2 , which is physically impossible. Typical values of σ_p for neutral traps are in the region of 10^{-15}cm^2 [10]. Again, these complex capture and emission processes are an indication that the defects detected are at dislocation cores.

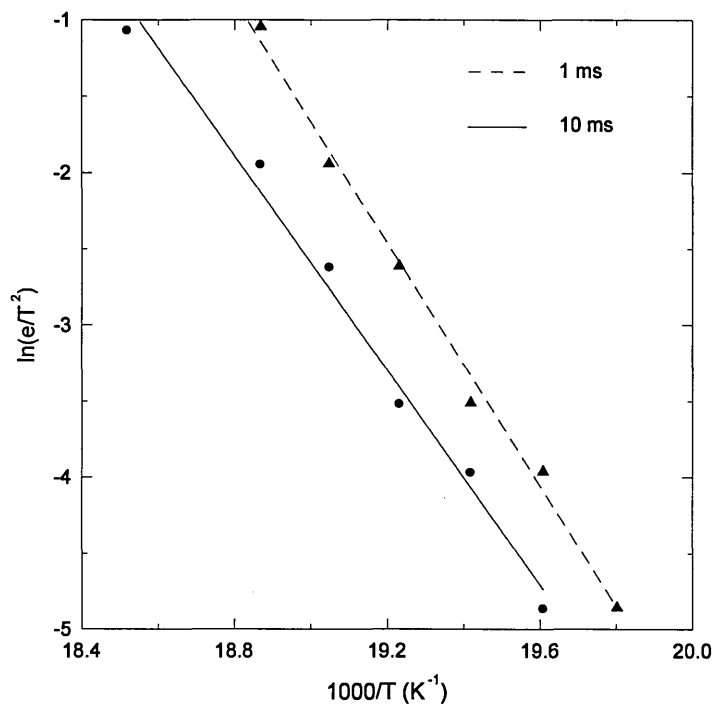


Figure 6.11: Arrhenius plots of the level occurring at $\sim 50\text{-}60\text{K}$ with fill pulses of 10 ms (---) and 1 ms (---).

A similar level emitting at $\sim 50\text{K}$ was observed by Castaldini *et al.* in *p*-type Cz-Si samples which have been subjected to bending and annealing conditions¹¹. The level they observed is very small in magnitude ($<0.01\text{pF}$) and is dominated by other peaks at higher temperatures. This particular level is reported to be $\sim 70\text{ meV}$ above the valence band edge. There may be several reasons why the peak they observed is not dominating the spectrum, as it is in this work (Figure 6.10). It is not specified in the reference whether or not the bending was performed by a four-point method. Furthermore, the authors have annealed the samples at 800°C for 1 hr. A detailed study by Senkader *et al* was carried out, who have measured the unlocking stresses of samples annealed for different times at various temperatures¹. The results suggest that a 1hr anneal at 800°C should result in an unlocking stress of $\sim 40\text{MPa}$ and $\sim 70\text{MPa}$ for low and high oxygen concentrations within the samples, respectively. The O concentrations were not provided by Castaldini *et al.* However, it is possible that the concentration of oxygen in the samples were low. This could explain the small peak height reported in reference 11, in contrast to the dominant peaks observed in this work, where the unlocking stresses were $\sim 75\text{MPa}$ and $\sim 150\text{MPa}$ for samples B and A, respectively.

Further investigation into the capture properties of the low temperature level has been carried out using Laplace DLTS and the results for sample B taken at 50K, with the same biasing parameters, are presented in figure 6.12.

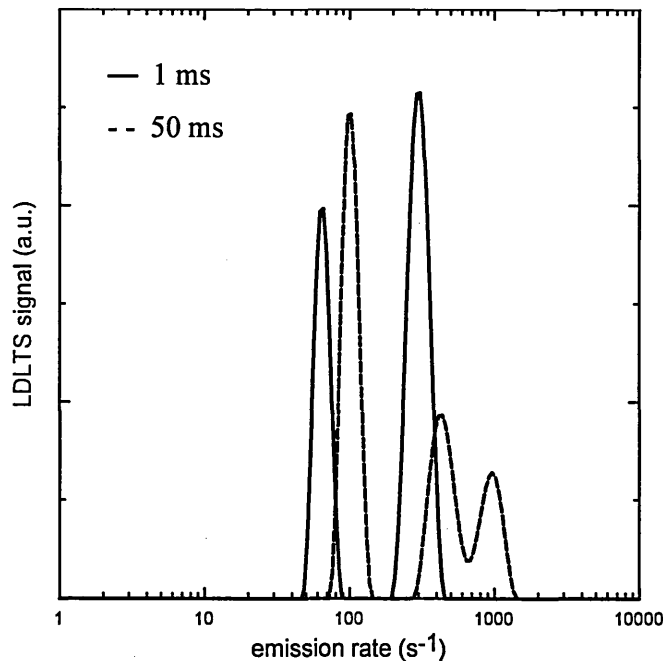


Figure 6.12: LDLTS of sample B at 50K, with fill pulses of 1ms (—) and 50ms (---).

The LDLTS shows a clear increase in the emission rates, agreeing with the decreasing activation energies obtained and revealing extended defect behaviour. Similar spectra were obtained for sample A, with slightly higher amplitudes, but the emissions detected were also around the 100 s⁻¹ and 500 s⁻¹ regions. Upon increasing the fill pulse to 50 ms, two faster emission rates of smaller amplitudes are detected, instead of the emission at 500 s⁻¹. Again, increasing the fill pulse does not allow states to be filled which are deeper into the sample, but it is a lateral spatial process as illustrated in Figure 6.8. This suggests that an additional level is possibly being filled when the fill pulse length is increased to 50 ms.

Several weeks later, this particular level (~60K) in sample A displayed a shift towards lower temperature, possibly as a result of repeated heating and cooling during the DLTS experiments. This shift was not observed in sample B, but it should be noted that sample A was used more often than B in the initial phase of the study. The Arrhenius plots before and after the shift are presented in figure 6.13. The activation energy of this level was reduced to about half the original value, but the peak shifted by only about 10-15K to the left. This could suggest that possibly some other impurity had originally formed a complex with oxygen atoms at the core, but this level could be mobile or may have changed its charge state.

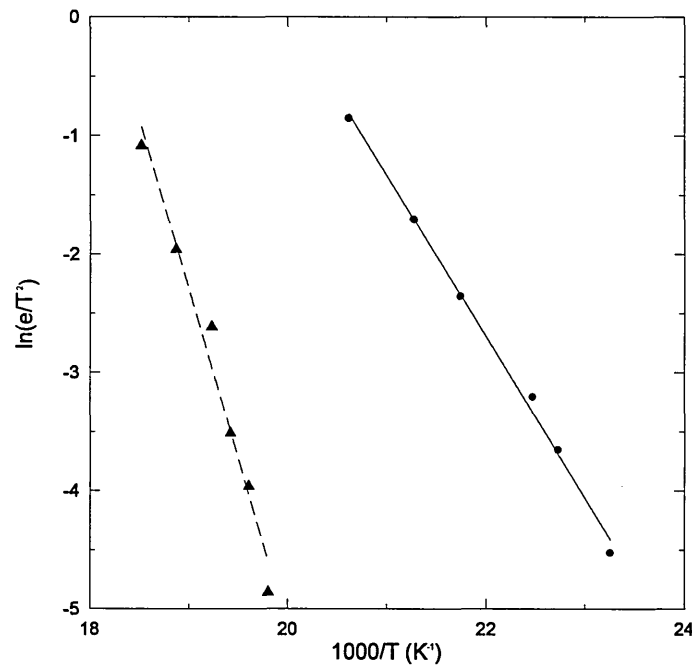


Figure 6.13: Arrhenius plots of the level occurring at ~40-60K, before (---) and after (—) a shift by ~15K to lower temperature.

Alternatively, the bonding configuration with the oxygen atom may have changed. However, no other impurities have been incorporated intentionally during fabrication, and the thermal stress applied during fabrication was minimal (maximum temperature of 90°C, for 25 minutes) and is therefore unlikely that impurities could have diffused far into the sample. Furthermore, any additional decoration at the dislocation is likely to result in a broader DLTS peak.

The new value of activation energy ($\sim E_v + 110$ meV) is far more reasonable in the temperature range detected. Additionally, the extrapolated capture cross-section from the Arrhenius plot is now $\sim 10^{-10}$ cm²s⁻¹, which is still high. Capture cross-section measurements should ideally always be measured experimentally, as the values obtained through an Arrhenius plot tend to give much higher values, where the error can be as much as fifty times the measured value¹⁰. This measurement was attempted, but fill pulses in the range 10-100 μ s were not short enough and the plots obtained were as a result of the slow capture from carrier tails extending into the space-charge region. The pulse generator in the Boonton capacitance meter was not suitable at the nanosecond fill pulse range. However, capture cross-section measurements before and after the thermal shift would have provided more information about the capture properties of this level.

Given the fact that this level is not surface related (as it was detected deeper into the sample), and that the amplitude of the peak follows the oxygen content at the dislocation core, the level is most probably linked in some way to oxygen. However,

LDLTS shows complex behaviour, which also suggests that the level observed is not due to isolated point defects.

The high temperature peaks have also been investigated with DLTS and Laplace DLTS. Figure 6.14 shows the DLTS spectrum of sample C, with minimal oxygen at the dislocation cores. The spectrum was recorded between 100 and 300K, at a rate window of 200s^{-1} .

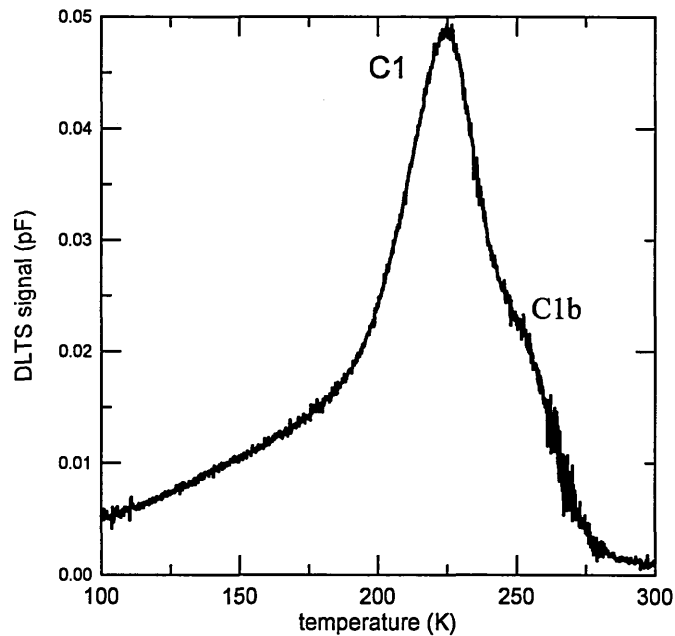


Figure 6.14: DLTS of sample C between 100 – 300K, at a rate window of 200s^{-1} .

The peak labelled C1 appears to be characteristic of a point-defect, as it is relatively narrow and symmetric. A broad background emission is present to the left of C1 in addition to a 'shoulder' to the right, labelled C1b. The activation energy of C1 has been determined through DLTS at fill pulse lengths of 1 and 10 ms. The corresponding Arrhenius plots in figure 6.15 show that the capture properties of this level are not affected by an increase in fill pulse length, as the differences in the Arrhenius plots are minimal and within the error limit of DLTS measurements. This indicates that no band-bending exists at this level, which in turn suggests that the defect giving rise to C1 is likely to be a point-defect and is sufficiently far away from neighbouring defects not to be influenced by any long-range Coulomb potential which may be present. The profile of C1b is not clear, but it is possible that this level is also arising from a point-defect.

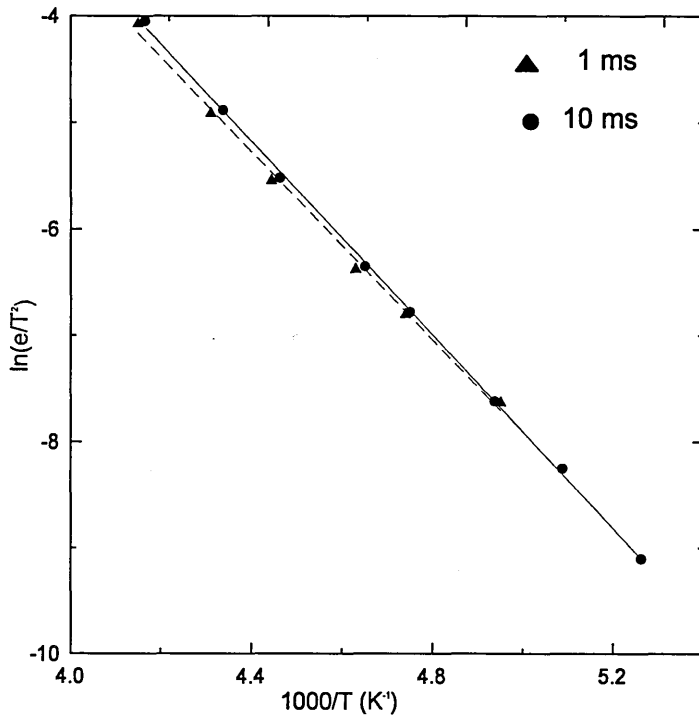


Figure 6.15: Arrhenius plots of the C1 level at fill pulse lengths of 1 and 10 ms

Laplace DLTS has been carried out at 225K (at the peak of C1) using fill pulse lengths of 1 and 10 ms in order to obtain further information about its capture properties and the results are shown in figure 6.16. Upon initial observation, the spectra look complex and more typical to be arising from an extended defect-type structure, with multiple levels, or 'band-like states'. However, closer inspection reveals that the emissions with a rate of less than $100s^{-1}$ do not shift with increasing fill pulse.

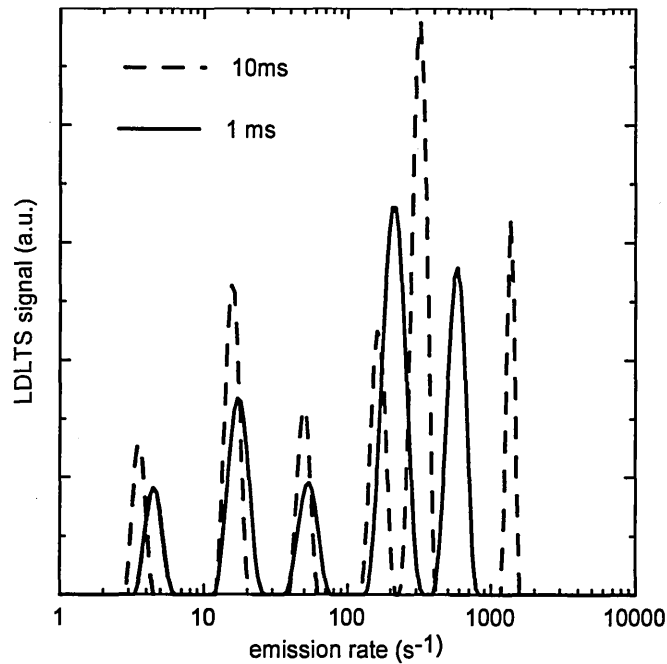


Figure 6.16: LDLTS of sample C at 225K, with fill pulse lengths of 1 and 10ms.

On the other hand, the emissions above 100s^{-1} display a shift towards higher emission rates and an additional level is also detected.

It must be noted that figure 6.16 is a logarithmic plot and the results become more apparent when plotted on a linear axis, as shown in figure 6.17. It can be seen that the shifts observed for the slower emission rates ($<100\text{ s}^{-1}$) are minimal and within error limits of Laplace DLTS. It is also visible that the faster emission rates ($>100\text{ s}^{-1}$) exhibit a much more significant shift with increasing fill pulse. This result agrees with the observation that the DLTS line of sample C is due to a combination of point and extended defects.

Furthermore, an additional level is detected when the fill pulse is increased to 10 ms. Again, this could be attributed to the 'spatial extension effect' of a longer fill pulse, allowing levels to be filled which could be physically further away.

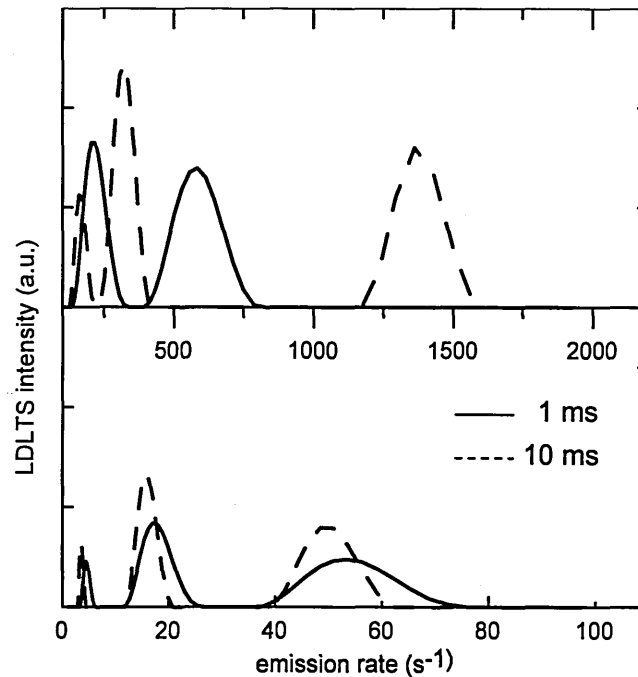


Figure 6.17: Linear plot of Figure 6.11 to show the relative changes in emission rates with an increase in fill pulse.

The LDLTS results of sample C show that conventional DLTS is not always sensitive enough to detect the interaction between levels. The Arrhenius plots in figure 6.15 showed no extended defect-like behaviour, but closer examination with Laplace DLTS has revealed that certain levels are physically close enough to one another, giving rise to an electrostatic potential and local band-bending. It is apparent from the LDLTS results

that there is a combination of point and extended defect activity contained within the simple DLTS peak in Figure 6.14.

LDLTS has also been applied to samples A and B in the high temperature region of $\sim 150 - 300\text{K}$. The results obtained were similar for both samples. The LDLTS spectra of sample B at 225K are shown in Figure 6.18. This is the same temperature as for sample C, for which the results were displayed in Figures 6.16 and 6.17.

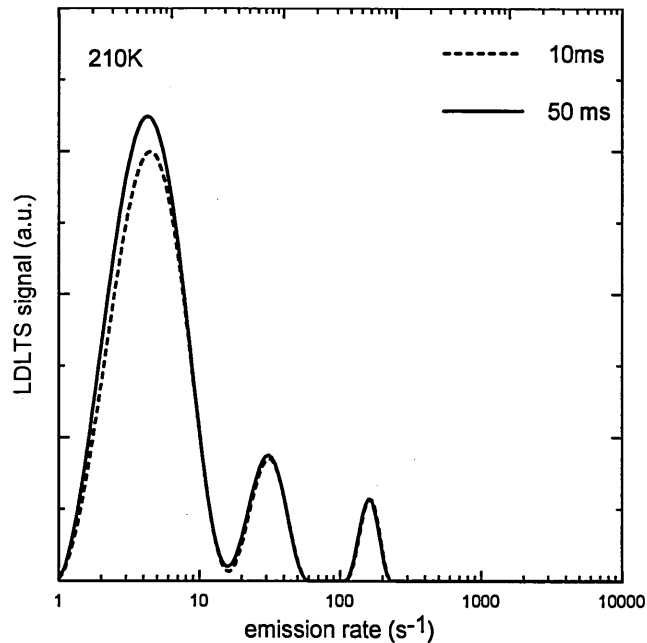


Figure 6.18: LDLTS of sample B at 225K with fill pulse lengths of 10 and 50 ms.

A comparison of figures 6.16 and 6.18 reveals that the LDLTS spectra of samples B and C at 225K are considerably different. However, closer examination of the emission rates present shows that the emission rates visible in the spectra of sample B (figure 6.18) are also present in the LDLTS results of sample C (figures 6.16 and 6.17). On the other hand, sample C exhibits three additional peaks in the spectra taken at a fill pulse of 10 ms. This could be due to a number of factors. One possible reason for this result is that annealing removes deformation-induced defects^{5,12} and whilst sample C has not been annealed at all, sample B has been annealed for 15 hours at 500°C. This could explain the fewer emissions observed for sample B in comparison to sample C. It is also possible that certain defects do not possess a homogeneous depth profile and may exist in clusters. These additional levels may possibly not be present in the region probed in sample B during the LDLTS experiment. Furthermore, it must be noted that the regions probed during LDLTS were 2.2 and 3.3 μm for samples B and C, respectively.

6.3.1 Capacitance-temperature characteristics

Figure 6.19 shows the zero voltage capacitances (i.e. $C_{V=0}$) of samples A, B and C as a function of temperature. It has been previously reported that an increase in capacitance is an indication that deformation-induced states are being removed⁵. It is evident in Figure 6.19 that the annealing time has a strong effect on the open-circuit capacitance of the diodes, with sample A (annealed for 35 hours) having the highest capacitance and sample C (not annealed) having the lowest. A higher capacitance in the same material is indicative of more carriers.

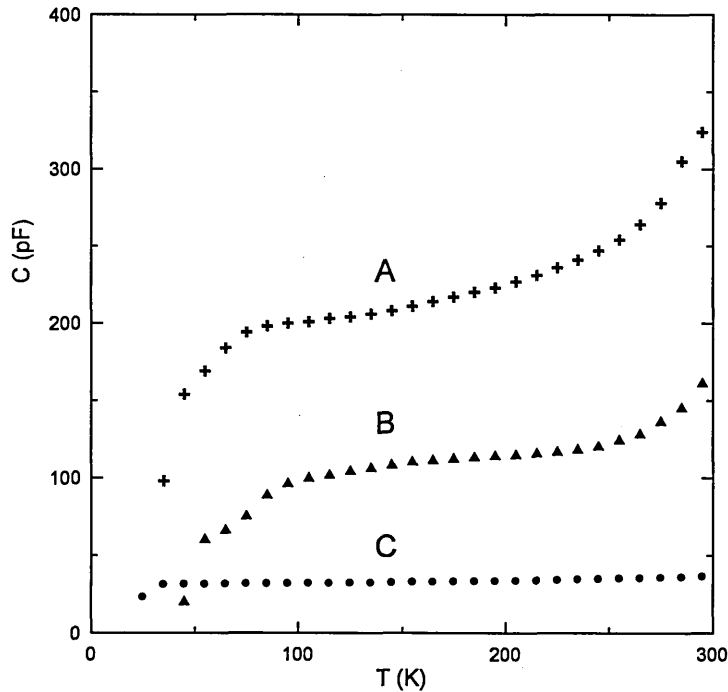


Figure 6.19: Zero voltage capacitances of samples A, B and C as a function of temperature.

Another feature worth mentioning is that the capacitance of sample A shows a much larger dependency on temperature. Sample C hardly displays any C-T dependency, whilst the dependency of B resembles that of A, but is less steep in the 50-100K and the 250-300K regions. It is interesting to note that the C-T relationship observed for a particular sample follows the DLTS spectrum of that sample to a certain extent. It can be seen from Figure 6.10 that above ~ 200 K and ~ 250 K for samples B and A respectively, the DLTS signal and hence the trap concentration is greatly reduced. In other words, the hole traps above these temperatures are no longer occupied and the effective acceptor concentration in the samples are now given by $(N_A + N_T)$, where N_T is the trap density.

The zero voltage capacitance of a Schottky diode is caused by the depletion region at thermal equilibrium. This is discussed in chapter 5, but the equation is repeated here:

$$C \equiv \frac{\partial Q_D}{\partial V_{bi}} = \sqrt{\frac{\epsilon_s q N_A}{2(V_{bi} - V - kT/q)}} \quad 6.1$$

where ϵ_s is the semiconductor permittivity, V_{bi} is the built-in voltage, V is the applied voltage (in this case $V = 0V$). The only variable between the samples that could give rise to the differences observed in the C - T relationships in this case is the value of N_A , which can be substituted by $(N_A + N_T)$.

The length of anneal time during the four-point bend conditions could have had an effect on the depth profiles of the related traps in each of the samples. The number of acceptor states in the depletion width at thermal equilibrium is different in each of the samples, resulting in different capacitances.

6.4 Summary

Historically, Laplace DLTS has generally been applied to point defects. However, results from this work have shown that it is a valuable tool for the deep level characterisation of extended defects, revealing results not directly obtainable with conventional DLTS. Using LDLTS, a direct influence of the fill pulse duration on trap emission rates has been observed in both the OISF and O-LD samples. The DLTS and LDLTS results of the O-LD samples have shown that a level emitting at low temperatures is present, with complex capture properties. Results suggest that this level is most likely due to the presence of oxygen at the dislocation core. Furthermore, broad DLTS spectra in the temperature range of 130 – 300K have been resolved with LDLTS revealing capture properties which could not be obtained through conventional DLTS. Additionally, it has been shown that the annealing time of the sample has had an effect on the acceptor profiles within the samples.

6.5 References

- ¹ S. Senkader, K. Jurkschat, D. Gambaro, R. J. Falster, P. R. Wilshaw, *Phil. Mag. A* **81** 759 (2001).
- ² S. Senkader, R. J. Falster, P. R. Wilshaw, *J. Appl. Phys.* **89** 4803 (2001).
- ³ M. Saritas, A. R. Peaker, *Solid State Electron.* **38** 1025 (1995).
- ⁴ J. Kaniewski, M. Kaniewska, A. R. Peaker, *Appl. Phys. Lett.* **60** 359 (1992).
- ⁵ V. V. Kveder, Yu. A. Osipyanyan, W. Schröter, G. Zoth, *Phys. Stat. Sol. (a)* **72**, 701 (1982).
- ⁶ Y. Qian, J. H. Evans, A. R. Peaker, *Inst. Phys. Conf. Ser.* **134**, 121 (1993).
- ⁷ T. Figielski, *Phys. Stat. Sol. (a)* **121**, 187 (1990).
- ⁸ W. Schröter, H. Cerva, *Solid State Phenomena* **85-86**, 67 (2002).
- ⁹ J. H. Evans-Freeman, N. Abdelgader, P. Y. Y. Kan, A. R. Peaker, *Nucl. Instr. and Meth. in Phys. Res. B* **186** 41 (2002).
- ¹⁰ D. K. Schroder, *Semiconductor Material and Device Characterisation, 2nd Ed.*, John Wiley & Sons: New York (1998).
- ¹¹ A. Castaldini, D. Cavalcoli, A. Cavallini, S. Pizzini, *Phys. Stat. Sol. (a)* **202**, 889 (2005).
- ¹² L. C. Kimerling, J. R. Patel, *Appl. Phys. Lett.* **34**, 73 (1979).

Chapter 7

Emission from point and extended defects in *n*-type gallium nitride

In comparison to silicon, gallium nitride (GaN) is a relatively new material for electronic devices. With a bandgap of 3.34 eV at room temperature, GaN is highly suited for high temperature, high power and high frequency applications¹. The emission from the most common deep level found in *n*-GaN occurs around room temperature. The complex nature of deep levels in *n*-type hexagonal GaN was discussed in Chapter 5. This chapter presents electrical characterisation of hexagonal *n*-GaN provided by Cambridge University. Deep level transient spectroscopy (DLTS) and Laplace DLTS (LDLTS) were used to investigate emission from deep levels and to detect extended-defect related emission. Particular emphasis is placed on the effects of thermal stress on device characteristics and emission from deep levels.

7.1 Sample details

The growth of the material and Schottky diode fabrication were carried out at the Cambridge Centre for GaN at Cambridge University, headed by Professor Colin Humphreys.

The gallium nitride wafer was grown by metal-organic chemical vapour deposition (MOCVD) on a *c*-plane sapphire substrate. A 1 μm thick layer of nominally undoped GaN was grown directly on the sapphire to serve as a buffer layer between the substrate and the active *n*-type layer. The Si doped *n*-GaN layer was grown on top of the buffer layer around 1020°C in an atmosphere of hydrogen and ammonia. The gallium source was trimethyl gallium (TMGa) and silane (SiH_4) was used as the Si source. Sufficient Si was introduced during growth to produce an electron density of at least $\sim 2.6 \times 10^{18} \text{ cm}^{-3}$ at 300K. The sample was subsequently cooled to room temperature in a flow of ammonia and hydrogen. No annealing step was used in the growth process. Three

samples ($\sim 1 \times 1 \text{ cm}^{-2}$) were cleaved from the same wafer for Schottky diode fabrication. Four diodes on these samples were used for electrical characterisation; one from samples S1 and S2 and two diodes from sample three. These are labelled S1D10, S2D12, S3D7 and S3D10. Figure 7.1 shows a schematic of the GaN material.

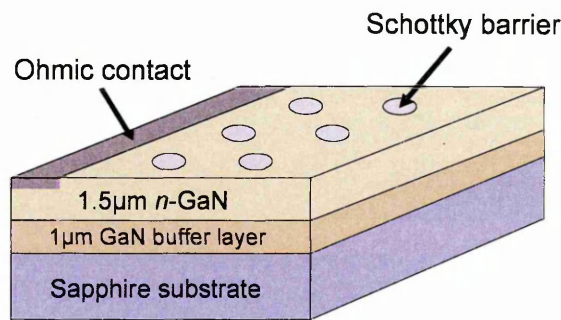


Figure 7.1: Schematic of the GaN layers grown on a sapphire substrate. The Si-doped layer was etched back to deposit the ohmic contact (Ti/Al/Ni/Au). The Schottky barriers are Au dots with a diameter of 1mm.

The average threading dislocation (TD) density in the active layer is $\sim 4 \times 10^8 \text{ cm}^{-2}$. The pure edge and mixed-type dislocation densities are believed to be in equal concentrations, with a less than 1% screw dislocation density. The main impurities present in the material are considered to be carbon, hydrogen, oxygen and silicon, based on work carried out at Cambridge on samples grown under similar conditions.

7.2 Carrier density and device characteristics

This sections shows typical results of the carrier density (n) as a function of voltage (V) determined through capacitance-voltage (C-V) measurements. Temperature effects on the carrier density are investigated

7.2.1 Carrier concentration

Figure 7.2 shows the carrier density for samples S1D10 and S2D12 at reverse biases of -1 and -2 V, between 60 and 600K. The reverse voltage (and hence depth) dependency of the carrier concentration is significantly different for the two samples studied. In sample S1D10, the variation in carrier concentration values recorded at -1V and -2V is minimal in comparison to S2D12, where the difference is about an order of magnitude. The drop in free carrier density deeper into the sample is an indication that the density of electron traps is increasing away from the surface. It has been previously reported that the trap density in GaN is higher at the material-substrate interface, where the dislocation density is greatest². The difference between $n(-1\text{V})$ and $n(-2\text{V})$ for sample S2D12 in Figure 7.2 is less at 400K than at 300K, indicating that carrier emission

occurs from traps at a depth corresponding to the -2V region above 300K. Furthermore, the carrier concentration recorded at -1V is observed to drop slightly between 400K and 500K for S2D12. In contrast, the value of $n(-2V)$ is greater at 500K than at 400K. This further suggests that the trap density is greater away from the surface and deeper into the bulk.

On the other hand, the carrier density at -1V follows that at -2V closely for sample S1D10. However it will be shown that a similar result to that of S2D12 is observed in S1D10 at larger reverse biases. The comparison between voltage dependencies of n in the two samples cleaved from the same wafer is an indication that the trap density is non-uniform within the material.

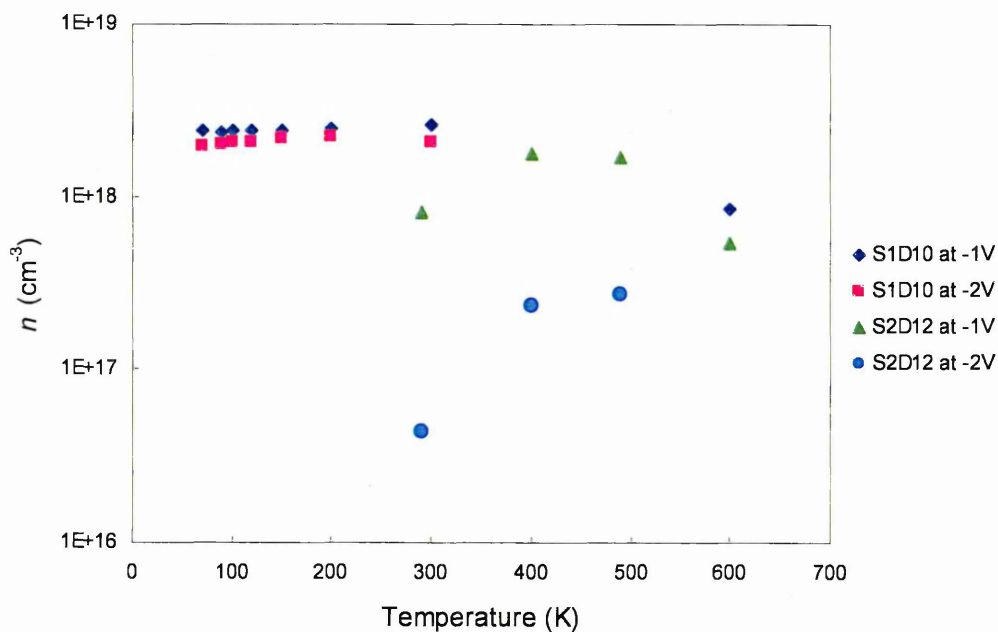


Figure 7.2: Carrier concentration as a function of temperature for samples S1D10 and S2D12 recorded at a reverse bias of -1V and -2V.

Figure 7.3 shows the free carrier density profile for sample S1D10 recorded at 70K, 300K and 600K. It can be seen from Figure 7.3 that a dramatic change in the carrier concentration profile occurs at 600K. There is an overall drop in carrier density, which is most significant deeper into the sample, which is indicative of carrier trapping at elevated temperatures. This effect is associated with the formation of a minority carrier trap above $\sim 560\text{K}$, which will be discussed in section 7.6.

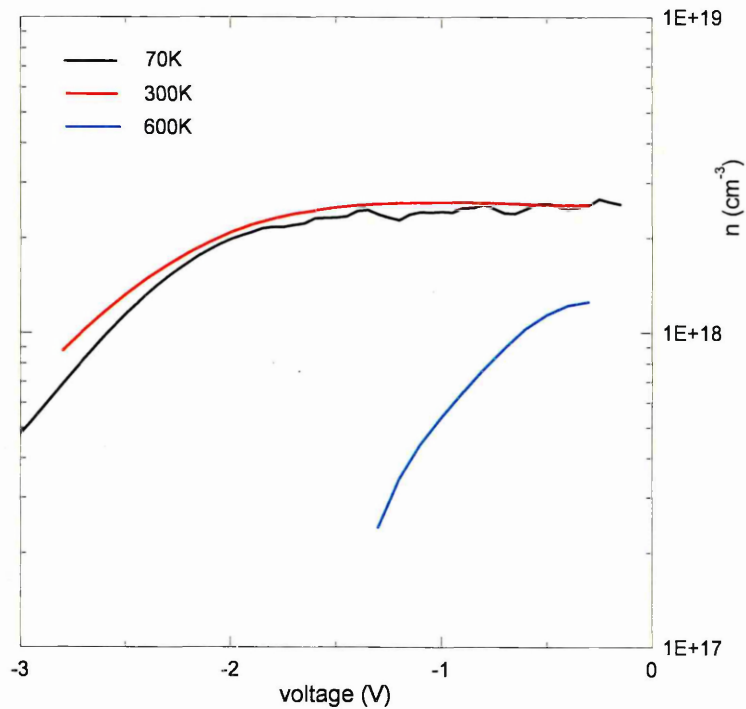


Figure 7.3: Carrier density as a function of voltage for sample S1D10 recorded at 70K (—), 300K (—) and at 600K (—).

The carrier density profiles at 70K and 300K show a sharp drop when the reverse bias exceeds -2V. The differences in carrier concentration as function of voltage are an indication that the distribution of deep level traps is non-uniform. All samples studied display a sharp reduction in the carrier density at reverse biases greater in magnitude than -2 or -3V.

7.2.2 Current-voltage measurements

Figure 7.4 shows the current-voltage (I-V) characteristics for samples S1D10 (60K), S2D12 (300 and 600K) and S3D7 (300K). Figure 7.4 shows that the rectifying capability of diode S2D12 is reduced when the sample is heated to 600K. The reverse breakdown voltage drops by about half a volt from -2V (300K) to -1.5V (600K). This is accompanied by a lower turn-on voltage in the forward direction.

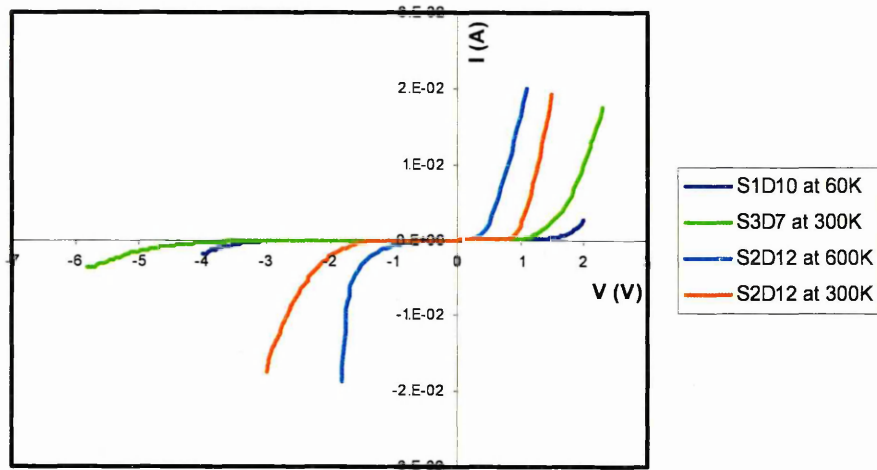


Figure 7.4: Current-voltage characteristics of samples S1D10 (60K), S3D7 (300K) and S2D12 (300K and 600K).

Figure 7.5 displays I-V characteristics recorded between 210K and 380K at increments of 10K for Sample S1D10. The temperature has been allowed to settle to within 0.1K at each new temperature. At each temperature, the corresponding value of current has been recorded at voltages of -5V, -3V, -1V, 1V and 2V.

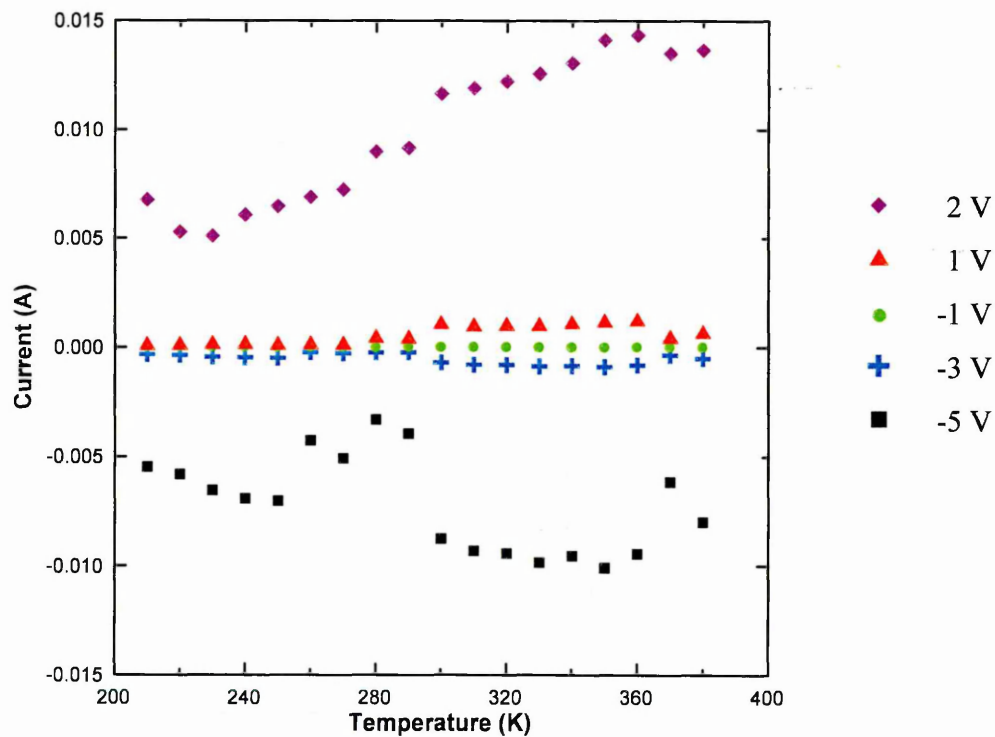


Figure 7.5: Current, I , at biases of -5, -3, -1, 1 and 2V between 200 and 380K.

A general trend is visible in Figure 7. 5. For a forward bias voltage of 2V, the diode passes nearly three times more current at 380K than at 210K. The effects are similar for a reverse bias voltage of -5V, although the amount of reverse leakage current only doubles over the same temperature range.

The high temperature reliability of GaN based devices has been investigated by many, including Yoshida *et al.*^{3,4}, who examined the lifetime of devices under constant current injection at elevated temperatures, for 300 – 1010 hours. It was found that the devices, field-effect and bipolar-junction transistors examined, did not display any degradation in performance. However, Figures 7.4 and 7.5 indicate that reverse bias leakage current increases at elevated temperatures in the material studied.

Although the samples used for this study have been cleaved from the same wafer, the high frequency characteristics differ between the samples. The leakage currents could be a result of the processing methods, such as poor Schottky barrier formation, as well as due to dislocations and defects. Hsu *et al.*¹ have associated reverse bias leakage currents in GaN with the dislocations present in the material by comparing current maps to topographic images and transmission electron microscopy results.

The following sections discuss the deep levels detected by DLTS and Laplace DLTS in the gallium nitride samples examined in this work.

7.3 Deep level transient spectroscopy of gallium nitride

Figure 7.6 displays the deep level transient spectrum of sample S1D10 from 100 to 600K, at a rate window of 200s^{-1} , which is representative of all samples studied. A -2V quiescent reverse bias (V_R) was applied and the fill pulse magnitude (V_P) was 0V. The fill pulse duration (t_p) was 1ms.

The DLTS spectrum is typical of *n*-GaN reported by other groups, although no universal numbering scheme exists and relevant levels are labelled differently in the literature (e.g. references 5 and 6). Properties of the deep levels reported in the literature are discussed in more detail in Chapter 5.

On initial inspection, the peak shapes are characteristic of extended defect related emission due to the broad nature of the spectrum between ~100 and 500K. Such broad spectra are indicative of close separation in temperature between emissions. However, the peak shape is not enough to determine extended defect related emission. This is

because numerous point defects may be situated physically far apart from each other, with similar energy separations from the conduction band edge.

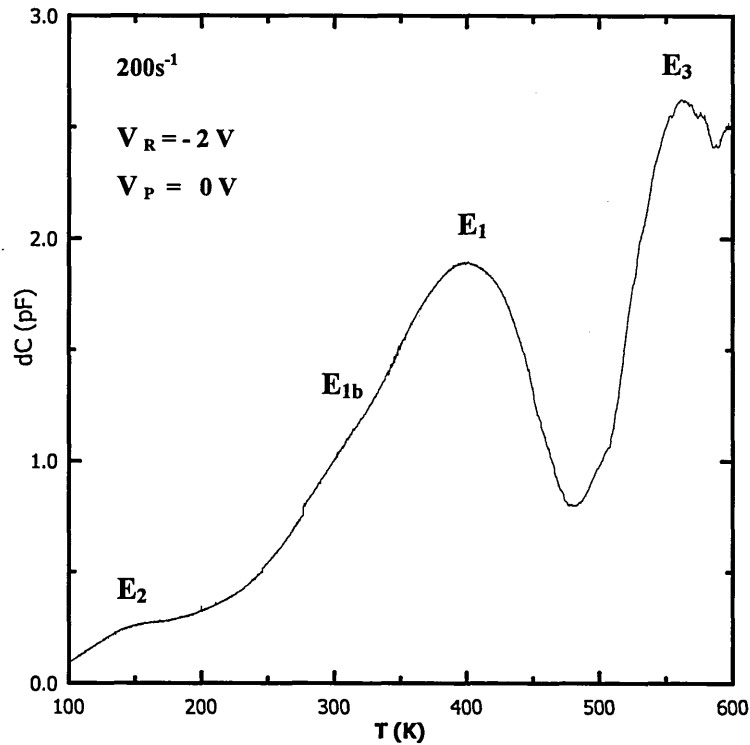


Figure 7.6: DLTS spectrum of sample S1D10 from 100 to 600K at a rate window of 200s^{-1} , with a quiescent reverse bias of -2V, fill pulse amplitude of 0V and a fill pulse duration of 1ms.

DLTS and Laplace DLTS results are presented in the following sections to examine the capture and emission properties of the deep levels displayed in Figure 7.6 and to distinguish between point and extended defect related emission.

When the sample was cooled down in order to select another rate window, the diode no longer appeared to support the same level of capacitance at the reverse bias used for the measurement. The next spectrum taken immediately afterwards is shown in Figure 7.7. The peak labelled E_1 (Figure 7.6) completely disappears and a large negative peak due to minority carrier emission is visible. Further investigation into this level is provided in section 7.7. Sections 7.3 to 7.6 only focus on the emission from majority carrier (i.e. electron) traps.

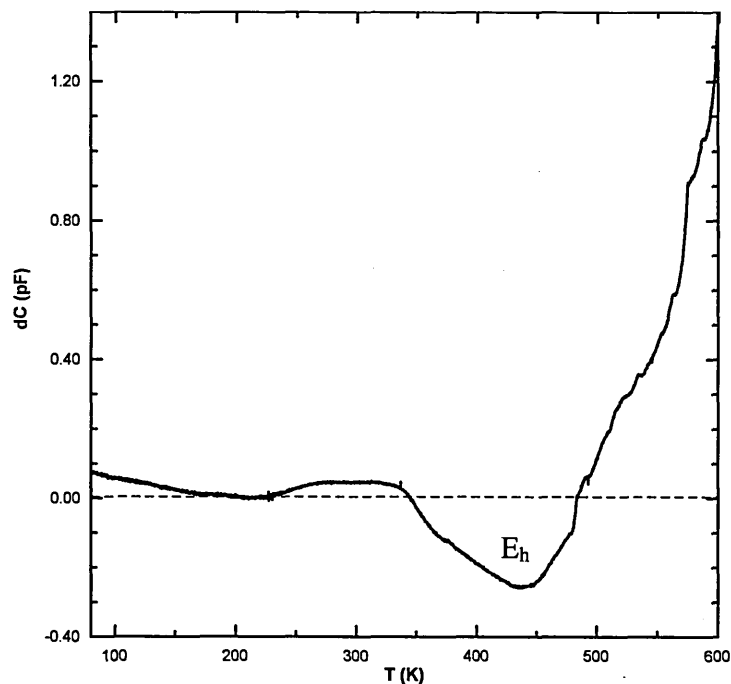


Figure 7. 7: DLTS of sample S1D10 immediately after the spectra shown in Figure 7.6.

Figure 7. 7 actually consists of two spectra, because the software used is limited to a temperature range of about 400K. Further data points cannot be recorded in the spreadsheet, which is limited in the number of columns available. To plot the above two figures, the DLTS measurements have been done in two different settings and therefore the peak heights shown are only an indication and not a true value. The results presented here will be discussed in more detail in the following sections.

7.4 Shallow levels

Figure 7.8 (a) shows the DLTS results obtained for sample S1D10 in the temperature range 60 to 170K, with a quiescent reverse bias of -2V. The fill pulse magnitude was -0.5V, with a duration of 10 ms. This level is not shown in Figure 7.6, as it was observed at a lower temperature after the DLTS spectra displayed a shift in temperature, which will be discussed in later sections. The shallow level in Figure 7. 8 is labelled as E_4 . The activation energy of the level is derived to be 65 meV from the Arrhenius plot displayed in Figure 7.8 (b). The trap density derived from the DLTS plot is $N_T \approx 3 \times 10^{15} \text{ cm}^{-3}$. The trap concentration obtained indicates that below about 100K, the centre traps $\sim 0.01\%$ of the free carrier density that is available at room temperature.

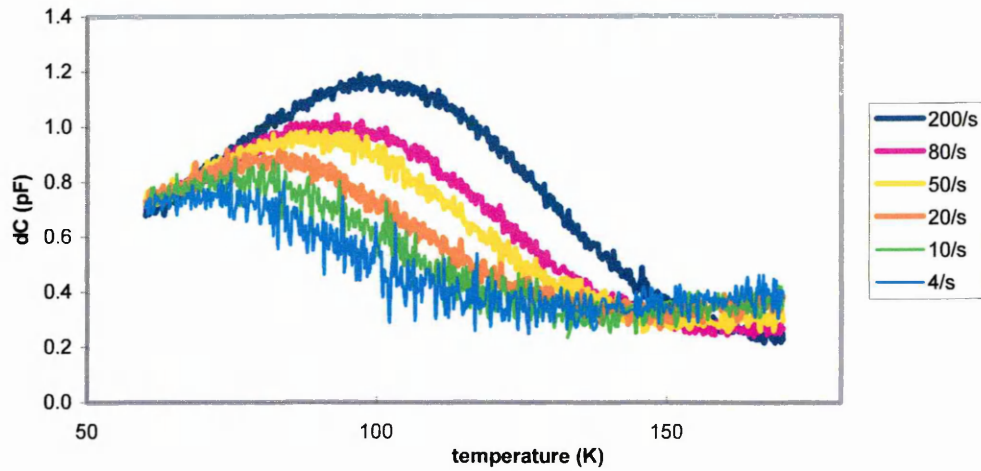


Figure 7.8 (a): DLTS of Sample SID10 between 60 and 170K, showing emission from a shallow level, E_4 . The reverse bias was -2V and the fill pulse voltage was -0.5V lasting 10ms.

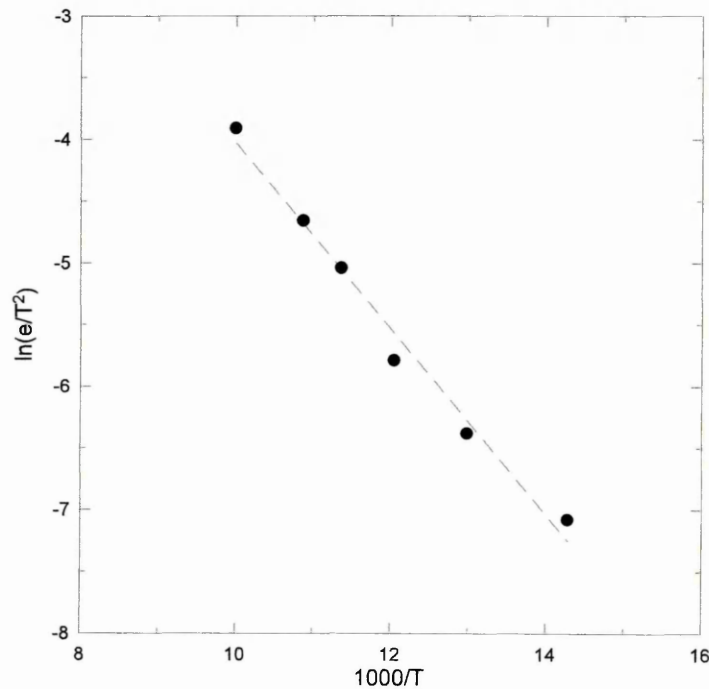


Figure 7.8 (b): Arrhenius plot of level E_4 using DLTS data displayed in Figure 7.8 (a).

An activation energy of 64meV was previously reported by Look *et al.*⁷ by Hall effect measurements in 0.7-1MeV electron irradiated GaN grown on sapphire. The authors associated this level with the nitrogen vacancy, V_N . However, it was mentioned in Chapter 4 that the *n*-type conductivity in GaN can be accounted for by the concentration of oxygen and silicon atoms, which exceed that of the V_N . Theoretical work suggests that the gallium vacancy, as opposed to the nitrogen vacancy is the dominant native defect in *n*-type GaN^{8,9}. Therefore, level E_4 is unlikely to be due to the nitrogen vacancy.

Figure 7.9 displays the Laplace DLTS results for the same sample, taken at 90K, with filling pulse durations of 500 μ s, 5ms and 50ms. The data show two dominant emission rates and an additional emission is detected upon increasing the fill pulse duration to 50 ms. The emission rate of the peak on the left displays a small increase when the fill pulse duration is increased from 0.5 to 5 ms. However, a further tenfold increase in the filling pulse duration to 50 ms does not result in faster emissions. Dislocation related emission is likely to exhibit an increase in emission rate as a result of a further tenfold increase the fill pulse duration^{10,11}. This suggests that the level responsible for this emission may be a point defect, which saturates quickly. This is supported by the almost equal magnitudes of the 0.5 and 50 ms peaks. The smaller magnitude of the 5 ms peak is most likely due to a noisy signal and not a true representation of the process.

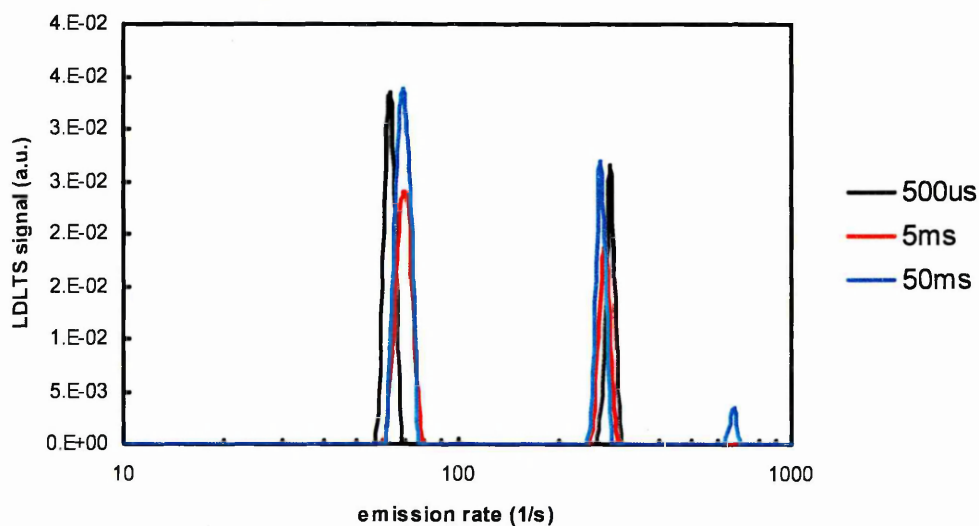


Figure 7.9: LDLS of sample S1D10 at 90K, using fill pulse durations of 500 μ s (—), 5ms (—) and 50ms (—).

The activation energies for these levels have also been found using Laplace DLTS by incrementing the temperature in steps of 2K and allowing the temperature to settle to within 0.01K prior to each measurement. The filling pulse length used was 10ms, which provided three peaks for analysis, similar to the LDLS scan obtained using a fill pulse duration of 50 ms.

The emission rates of the peaks at the specific temperatures have been recorded and used to derive the activation energy of the levels concerned. The Arrhenius plots of the three emissions are shown in Figure 7.10. The resulting activation energies obtained are 39meV, 30meV and 17meV. The activation energy obtained through DLTS is about twice the values obtained through LDLS. The error bars in DLTS are typically

± 50 meV and the activation energies reported through LDLTS are within these error bars.

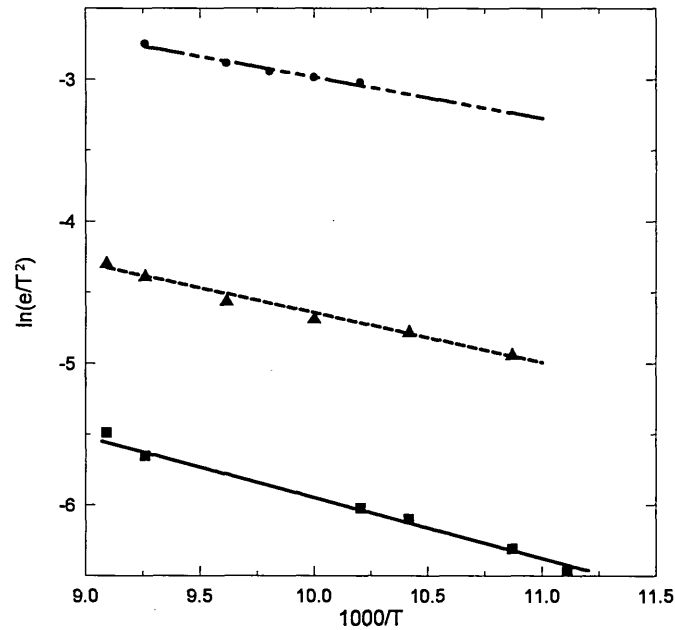


Figure 7.10: Arrhenius plots to obtain the activation energies from emission rates detected by LDLTS at 90K of sample S1D10.

The DLTS peaks in Figure 7. 8 are representative of a point defect, judging by their symmetry. However, they are broader than expected for an ideal point defect, which may explain the multiple emissions observed in the LDLTS spectra. No significant shift is observed in the LDLTS peaks with increasing filling pulse duration. The DLTS and Laplace DLTS results indicate that the level E_4 may be due to shallow donors in the material.

Activation energies of $\sim 27 - 30$ meV for the Si donor have been quoted in the literature^{12,13,14}. The values of ~ 17 meV and $\sim 32 - 37$ meV for the silicon and oxygen donors, respectively have been quoted by Götz¹⁵. The Arrhenius plots in Figure 7.10 appear to have significantly different intercept values on the $\ln(e/T^2)$ axis indicating differences in the capture cross-section (σ_n) prefactors. However, it must be noted that the intercept value is not a reliable indication of σ_n . Based on Laplace DLTS results, the Arrhenius plots in Figure 7.10 and the values reported in literature¹²⁻¹⁵, it is probable that the activation energies obtained are due to different impurities. The 39 meV may be related to the oxygen donor at a nitrogen site. The 30 and 17 meV could be due to the Si donor at a gallium site (Si_{Ga}). The differences in the Si donor activation energies may be due to nearest neighbours or the strain field of the dislocations. It is also probable that certain donor atoms may be in the vicinity of deep level traps which do not empty in this temperature range. Hence, the activation energy of 17 meV may be as a result of

local band-bending near dislocations. This model is supported by the Laplace DLTS result in Figure 7.10. The peak on the left displays a slight increase in emission rate when the fill pulse duration is increased to 5 or 50 ms from 0.5ms. No further increase in emission rate with longer fill pulses is indicative of a point defect, as there are no nearby *empty* traps to fill at this temperature.

In summary, the level at $E_C - 65$ meV detected by DLTS was shown to be made up of two emission rates using Laplace DLTS. Activation energies of 39, 30 and 17 meV were obtained using LDLTS. These levels are indicative of point defect related emission and are likely to be due to the Si_{Ga} and O_N donor levels.

7.5 Deep levels

7.5.1 Level E_1

The broad emission around room temperature is labelled E_1 and is displayed in Figure 7.6. The position of the level E_1 within the GaN bandgap is found to be 624meV and 503meV below the conduction band at filling pulses of 1ms and 50ms respectively. The Arrhenius plot is displayed in

Figure 7.11 and a difference in the gradients for the 1ms and 50ms pulse lines is clearly visible. The trap concentrations are $\sim 6 \times 10^{15} \text{ cm}^{-3}$ and $\sim 1.1 \times 10^{16} \text{ cm}^{-3}$ for the 1ms and 50ms filling pulse scans respectively, at a rate window of 200s^{-1} .

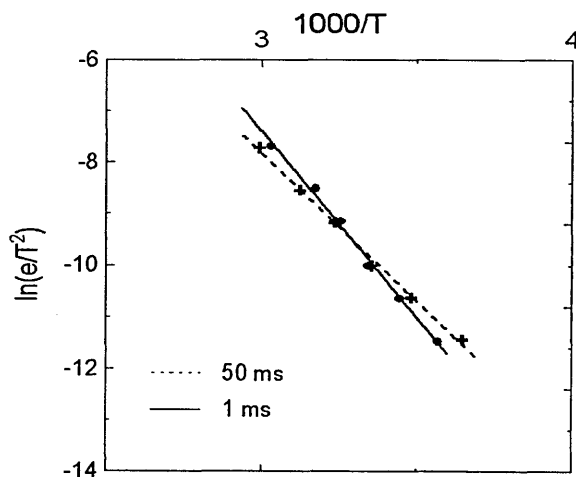


Figure 7.11: Arrhenius plots of level E_1 with fill pulse durations of 50ms and 1ms.

Figure 7.12 shows the DLTS scan of level E_1 from 300K to 400K with filling pulse durations of 500 μ s, 5ms and 50ms. The scans indicate that a tenfold increase in filling

pulse from 500 μ s to 5ms has a minimal effect on the peak position in temperature. However, a further tenfold increase to 50ms results in a noticeable shift towards a lower temperature, which could be representative of emission from a band of states, such as at a dislocation core. Increasing the filling pulse to 50ms from 5ms induces a much larger increase in the DLTS peak height, indicating that long fill pulses are required to saturate the defect states.

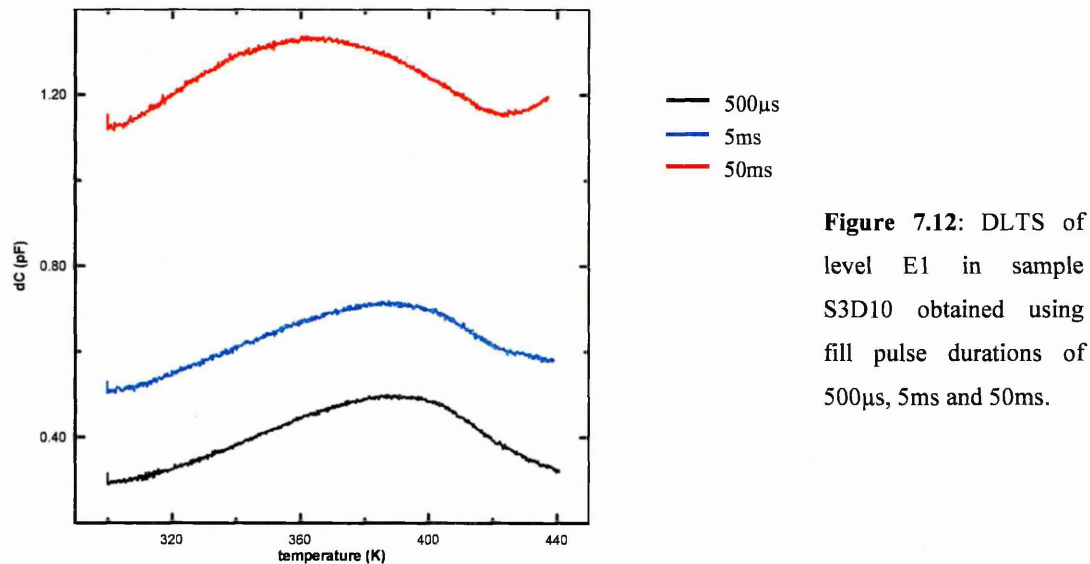


Figure 7.12: DLTS of level E1 in sample S3D10 obtained using fill pulse durations of 500 μ s, 5ms and 50ms.

Figure 7.13 shows the DLTS spectra of sample S1D10 from 100 to 380K. The reverse bias in this measurement was -3V, with a fill pulse amplitude of -1V, in order not to detect surface related states. The DLTS measurement was repeated using 1 and 50 ms fill pulse durations. A large increase in the peak height is observed, which is equivalent to an increase in trap concentration, as mentioned previously. Furthermore, all levels detected appear to shift closer to the conduction band, which is apparent from the shift towards lower temperature of all peaks. This is characteristic of extended defects, where local band-bending exists due to the *band of states* present in the bandgap. Electrical properties of extended defects were discussed in Chapter 5.

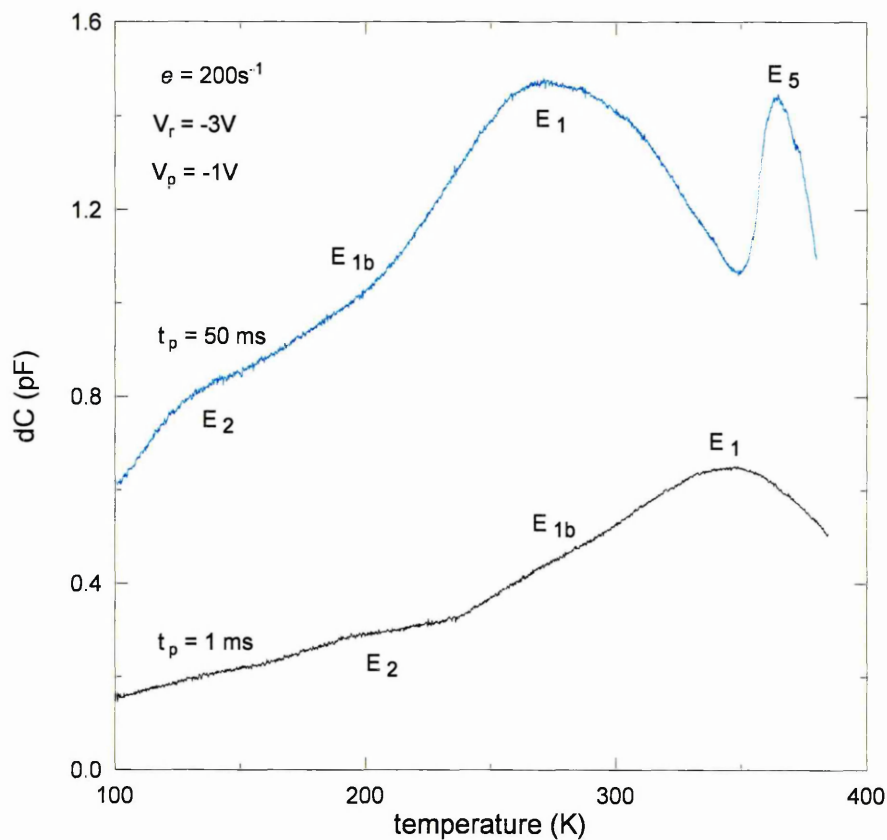


Figure 7.13: DLTS of sample S1D10 with fill pulses of 1 ms (black) and 50 ms (blue).

An additional peak, labelled E_5 , is detected upon increasing the fill pulse duration to 50ms. The longer fill pulse duration of 50 ms has resulted in comparable trap concentrations between E_1 and E_5 . The peak shape of the E_5 level is indicative of a point defect. If this level was due to a band of states, line broadening would occur on the lower temperature side of the peak. From Figure 7.13 alone, it is not possible to determine whether or not this level is affected by the repulsive forces of nearby levels, because the peak position is not visible with a fill pulse duration of 1 ms. The measurements were terminated at 380K because of the limited rows available for data entry. However, previous and subsequent DLTS scans did not reveal a peak in the 400-500K temperature range.

Closer inspection of level E_1 reveals a change in the peak shape when the fill pulse length is extended from 1 to 50ms. In contrast to the stacking fault sample investigated in chapter 6, this level exhibits much less line broadening on the lower temperature side of the peak. Therefore, there is a possibility that level E_1 is made up of more than one level. The different levels giving rise to the E_1 level could arise from a defect which exists at more than one site in the bulk. It is likely that the emissions emanate from defects in the vicinity of dislocations due to the large fill pulse dependency observed.

Room temperature (i.e. 300K) emission in sample S1D10 has been investigated by Laplace DLTS and the results are displayed in Figure 7.14 . The biasing parameters were the same as for the DLTS spectra shown in Figure 7.13, apart from the fill pulse durations. In Figure 7.14, the fill pulse durations used were 0.1, 1 and 10 ms. The emissions due to the 0.1 and 1ms are not clearly visible due to the large peak heights of the emissions from a 10 ms fill pulse length. The LDLTS spectra from 0.1 and 1ms fill pulse lengths are plotted separately in Figure 7. 15. However, Figure 7.14 has been included to show the effect of a tenfold increase from 1 to 10 ms in the filling pulse duration. Four dominant peaks are observed in Figure 7.14 and 7.15. The spectra clearly show a large increase in peak height and a shift towards higher emission rates as the filling pulse is increased to 10ms from 1ms.

A 1ms fill pulse at 300K should detect emissions relating to the E_{1b} and E_1 levels. The higher emission rates are likely to correspond to the E_{1b} level, whereas the lower emission rates may possibly relate to levels E_1 and E_5 .

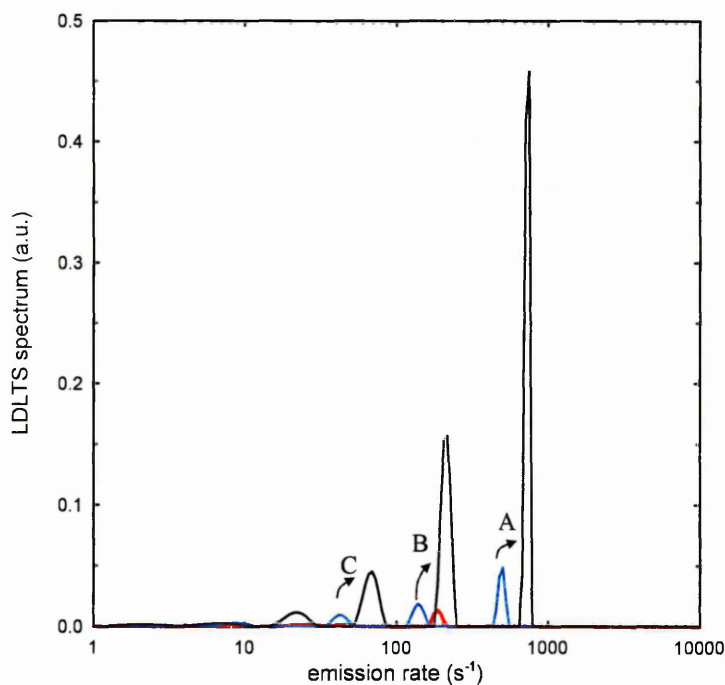


Figure 7.14: LDLTS of sample S1D10 at 300K, with fill pulse durations of 100 μ s (---), 1ms (—) and 10ms (—).

The spectra show a large increase in peak height as the filling pulse is increased to 10ms. Furthermore, an increase in emission rate for the 10ms fill pulse spectrum is evident, which indicates the presence of extended defects. Figure 7. 15 shows the LDLTS spectra for the 0.1 and 1 ms fill pulse experiments. It is likely that the 200s⁻¹ emission due to the 0.1ms fill pulse shifts to the 500s⁻¹ emission as a result of a tenfold increase in the fill pulse length. This inference is based on the behaviour of the emission

rates displayed in Figure 7.14: The 500s^{-1} emission due to the 1ms fill pulse (labelled A) shifts to $\sim 800\text{s}^{-1}$ and displays a significant increase in peak height when the fill pulse duration is extended to 10 ms. If the same behaviour were to be modelled to the change in emission rates due to the 0.1 and 1 ms fill pulses, then it is possible that the emission rates do increase as a result of longer fill pulse durations.

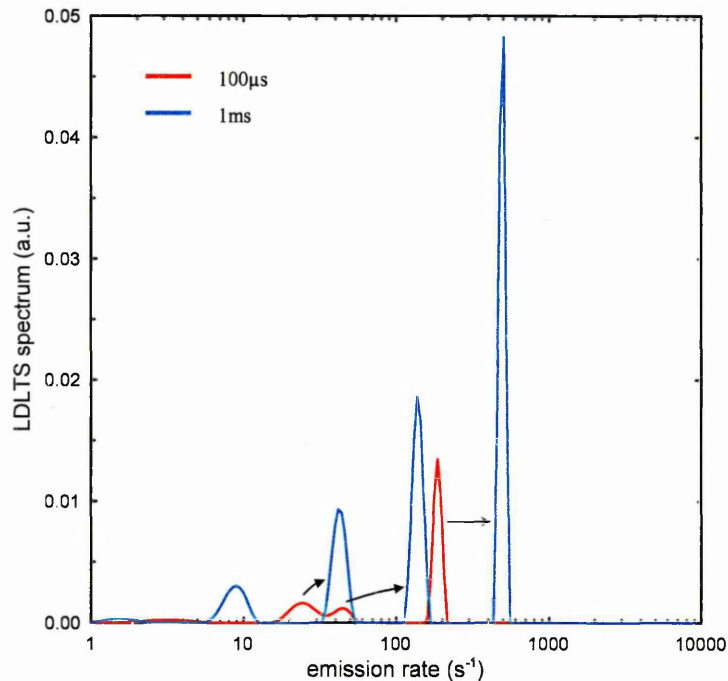


Figure 7. 15: This figure is equivalent to Figure 7.14, but only the spectra resulting from the $100\mu\text{s}$ (—) and 1ms (—) fill pulse durations are displayed.

Emission from extended defects is highly probable, judging by the fill pulse behaviour of the DLTS spectra in Figure 7.13. The broad spectra ($\sim 100 - 400\text{K}$) suggest that numerous emissions are spaced closely in temperature. A range of activation energies for levels E_1 and E_5 have been reported previously in the literature, as discussed in Chapter 5. This further suggests that the emission rates detected by Laplace DLTS should display fill pulse dependency characteristic of extended defects.

In order to investigate the behaviour of level E_5 , Laplace DLTS measurements have been carried out at 354K , which corresponds to the maximum of the 50ms DLTS spectrum in Figure 7.13. The emissions have been split into sets and labelled A, B, C, D, E and F. There are two additional levels in comparison to the LDLS results in Figure 7.14. These additional emissions are likely to be sets A and B, which arise from levels deeper in the bandgap and display and emit at a slower rate at this temperature. At 354K , the set of emissions labelled F are likely to arise from levels which display maxima at a lower temperature than E_5 in Figure 7.13, possibly E_1 . Fill pulse dependency has been observed for levels emitting at 200s^{-1} in both the DLTS and

Laplace DLTS results in Figures 7.13 and 7.14-15. Therefore, the fill pulse dependency observed for set F in Figure 7.16 is likely to arise from dislocation related levels.

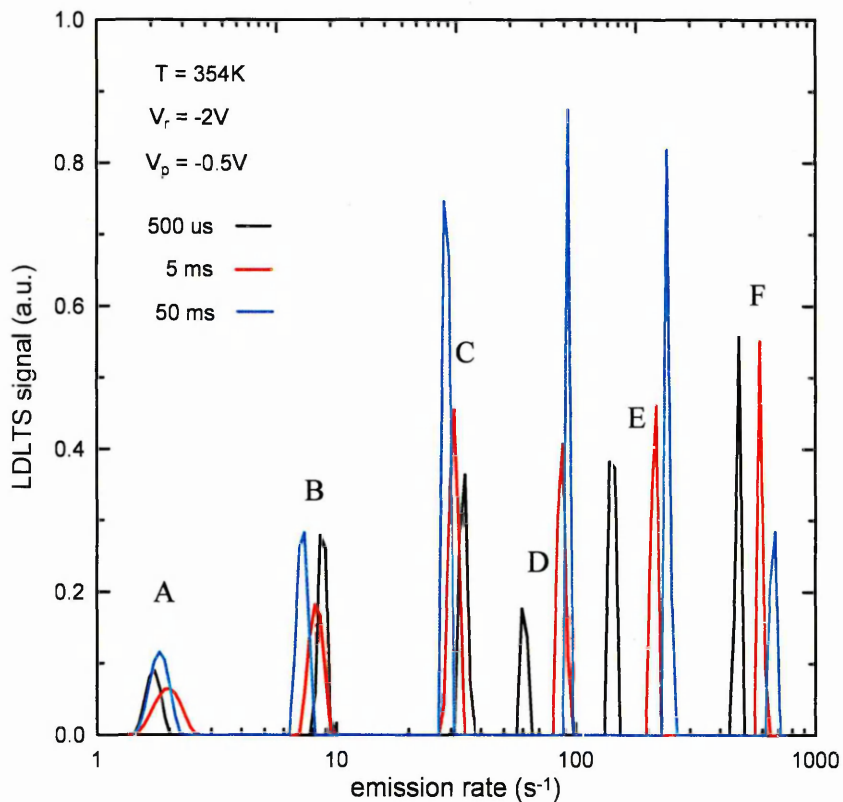


Figure 7.16: LDLTS of sample S3D7 recorded at 354K.

The emission set C does not exhibit fill pulse dependency and indicates the presence of point defects or small complexes. The emission from set C suggests that no local band-bending exists for this level. Sets D and E show the largest peak heights and coincide with the emission rates that are likely to arise from level E₅. However, the DLTS spectra in the 300-500K temperature range is very broad and other levels could exist in this temperature range. It must be noted that the dislocation density in the material is $\sim 4 \times 10^8 \text{ cm}^{-3}$, which corresponds to ~ 31000 emergence points directly under each Schottky diode. Such a structure is expected to have an effect on the position of impurities within the lattice and could lead to small separations in temperature of the emissions from levels.

Emission sets D and E display a fill pulse dependency at shorter fill pulses. A shift is observed when the fill pulse length is extended to 5 ms from 0.5 ms. However, a further tenfold increase to 50 ms has minimal effect on the emission rates. This behaviour is indicative of a point defect which is in the vicinity of extended defects, as it saturates at a much lower fill pulse than would be expected for large clusters or impurities at a

dislocation core. Therefore, the emission sets C, D and E could be due to point defects which exist at different lattice sites.

Trap profiling

The trap concentration of level E_1 has been measured as a function of depth into the sample and the results are displayed in Figure 7.17. As described in Chapter 4, the relevant DLTS measurements must be carried out at the right biasing conditions in order to probe a specific depth. The results indicate that this defect is more abundant towards the surface than in the bulk, with almost a linear drop in trap concentration with depth. It must be noted that a DLTS signal deep into the sample is much weaker than the surface. This is because a linear increase in reverse bias does not correspond to a linear change in depth probed. In other words, a smaller filling pulse is required to probe the region 0.062-0.068 μm under the surface than to probe 0.038-0.044 μm of material. Therefore, the carriers deeper in the material effectively experience a smaller potential difference to accelerate them to the surface. On the other hand, a reduction in trap concentration with depth of level E_1 has been reported by another group¹⁶.

A potential concern that arises when analysing the trap concentration as a function of depth, is the Debye length. This is discussed in Chapter 4. The Debye length for this material has been calculated to be $\sim 5.2 \times 10^{-12}$ m, using equation 4.5. This is ~ 100 times smaller than the lattice spacing and almost three orders of magnitude smaller than the depth probed during the measurement. Therefore, effects of the quasi-neutral region can, in this case, be ignored.

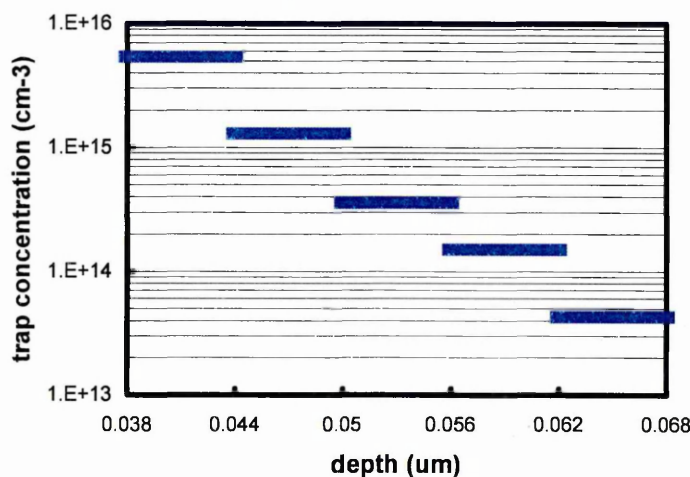


Figure 7.17: Trap concentration vs. depth results for level E_1 .

Laplace DLTS measurements have been carried out in the same regions as in the above trap concentration versus depth measurement. The LDLTS measurements have been recorded at 320K using the same biasing parameters, with fill pulse durations of 1 and 50ms. Figure 7.18 shows the LDLTS spectra in the 44 to 38 nm region below the surface, recorded using fill pulse durations of 1 and 50 ms. Seven emission rates are present, of which the four dominant peaks appear on the 40 to 800 s^{-1} region of the emission rate axis. Comparing the LDLTS results with the DLTS spectra recorded using a fill pulse duration of 50 ms (Figure 7.13), it is possible to conclude that the dominant emission in the LDLTS spectra may be due to E_1 . This is because judging by the peak position of the E_1 level at a rate window of $200s^{-1}$ of the 50 ms spectrum, it is most likely that the peak position corresponding to the $800s^{-1}$ scan would appear around 300-320K.

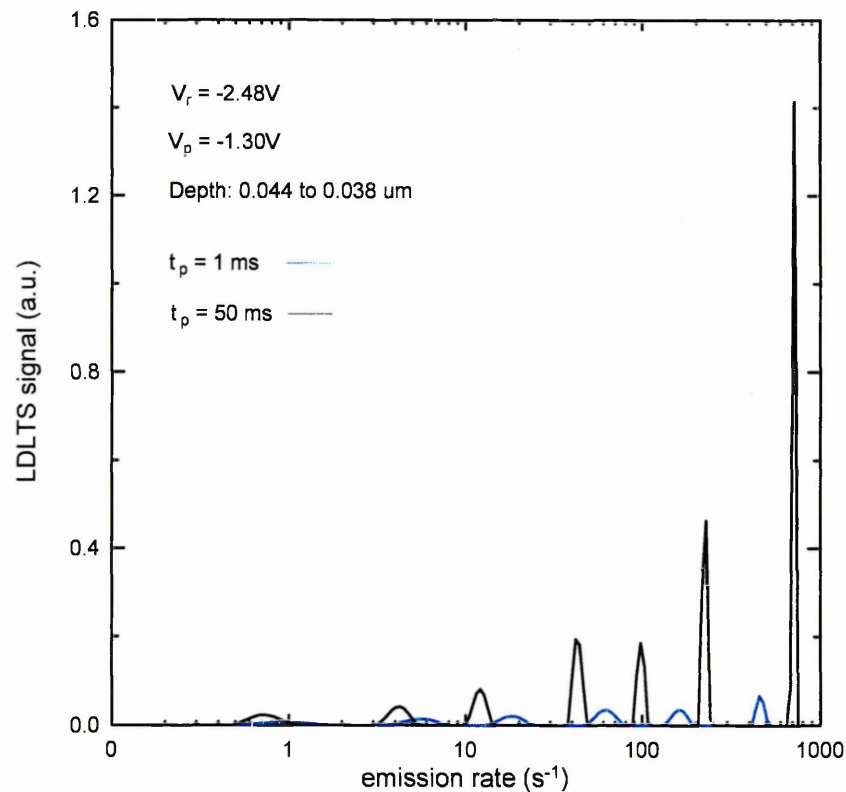


Figure 7.18: LDLTS of sample S3D7 recorded at 320K with biasing parameters corresponding to the region 38 to 44 nm below the surface.

All Laplace DLTS peaks are observed to shift towards higher emission rates when the fill pulse duration is increased to 50ms from 1ms. This is an indication that the levels observed in this region of the sample (38 to 44 nm) are in a region of local band-bending as a result of electrostatic repulsion between band-like states in the bandgap.

The slow emission rate ($<1\text{s}^{-1}$) may arise from near midgap states, such as level E_3 in Figure 7.6, which are likely to emit at a much slower rate at 320K.

Figure 7.19 shows the LDLTS spectra at the same temperature (320K), but in the region of 44 to 50 nm below the surface. In this region, there are also seven emission rates relating to the 50ms fill pulse duration. However, a 1ms fill pulse only results in six emission rates. Furthermore, an emission is detected at 40s^{-1} which does not shift with an increase in fill pulse length.

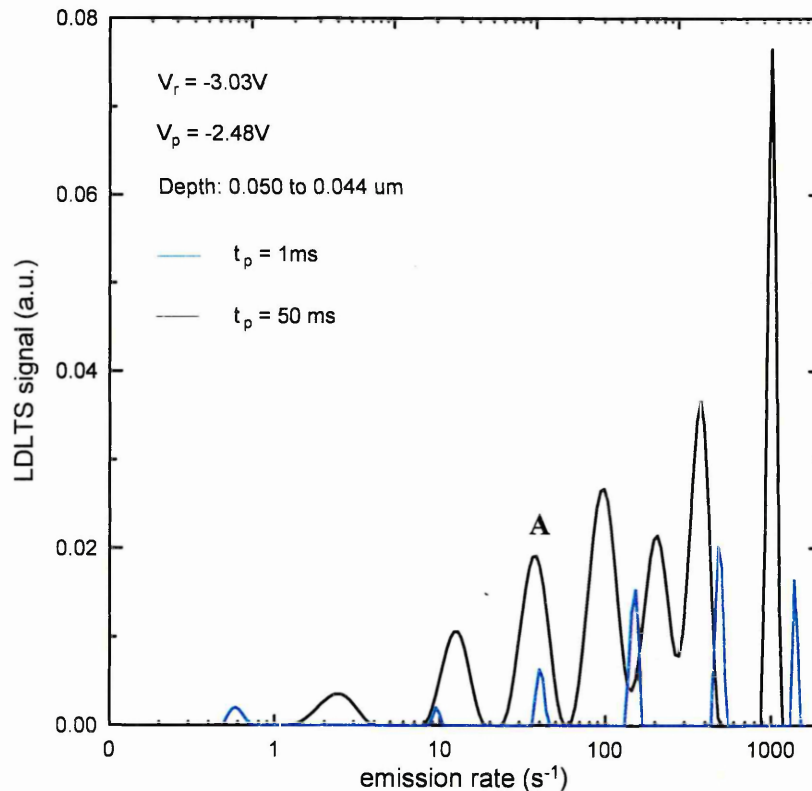


Figure 7.19: LDLTS of sample S3D7 recorded at 320K with biasing parameters corresponding to the region 44 to 50 nm below the surface.

In Figure 7.20, the data corresponding to the 50ms fill pulse lengths from Figure 7.18 and Figure 7.19 are displayed in the same graph to investigate the bias dependency of the emission rates. The results show that six out of the seven emission rates do not shift towards higher emission rates. It must be noted that the potential difference between the reverse bias and the fill pulse used to probe the 38 to 44 nm region is about twice the potential difference for the 44 to 50nm region.

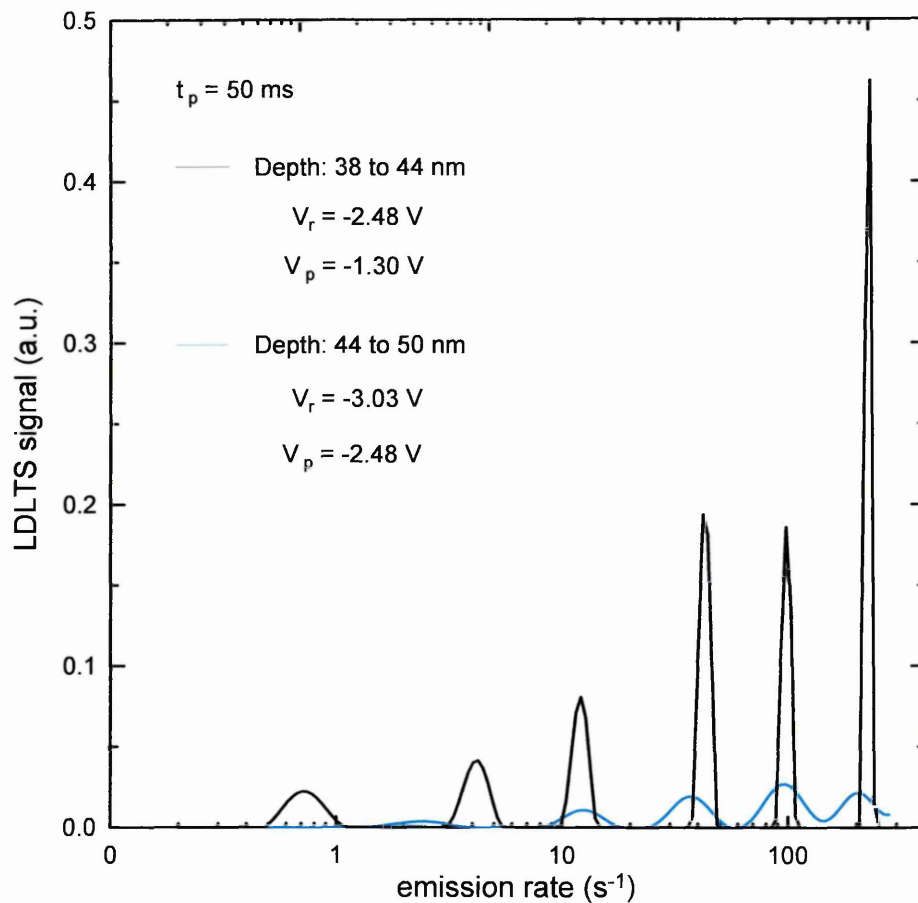


Figure 7.20: LDLTS spectra for the 38 to 44, and the 44 to 50 nm regions below the surface obtained using a fill pulse duration of 50 ms.

The bias dependency of the E_1 level was investigated by DLTS at a rate window of 50s^{-1} . The resulting spectra for sample S3D10 are displayed in Figure 7.21. The reverse bias amplitude and the fill pulse duration used in both scans was -2V and 1ms , respectively. The fill pulse magnitudes used were 0 and 1V . A shift towards lower temperature is observed when the fill pulse magnitude is increased to 1V . This is indicative of barrier lowering.

The E_1 peak narrows on the high temperature side as a result of an increase in fill pulse and a slight separation between E_1 and E_5 is now visible. However, the shoulder on the low temperature side of E_1 , which is labelled as E_{1b} in Figure 7.6, becomes less apparent when the fill pulse magnitude is increased. Furthermore, it does not appear to exhibit a significant shift in peak position. The exact peak positions of the E_{1b} level are not visible and therefore it is not possible to conclude for certain that the E_{1b} level is not bias dependent.

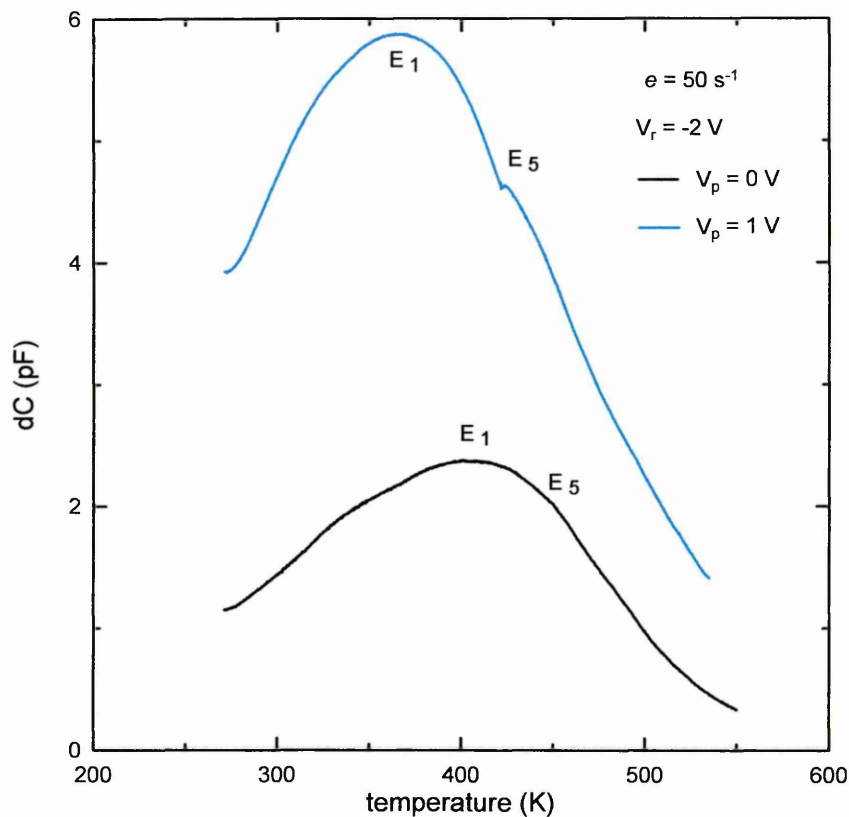


Figure 7. 21: DLTS of sample S3D10 between 270 and 550K with fill pulse magnitudes of 0V (black) and 1V (blue).

The results suggest that the bias dependency of the levels is sensitive to the region of material probed. This may be explained by considering that the electrostatic repulsion in a wider area is greater than for a small area, which could be enhanced by applying a forward bias pulse.

7.5.2 Level E₂ (100 – 200K)

The activation energy of level E₂, was obtained through DLTS with a filling pulse duration of 50ms and 10ms. The resulting Arrhenius plots are displayed in Figure 7.22. The derived activation energies are 350meV and 250meV for filling pulse durations of 10ms (—) and 50ms (- -) respectively. The trap concentration, N_T, was $\sim 8 \times 10^{14} \text{ cm}^{-3}$. A level at $E_C - 0.24 \text{ eV}$ was associated with screw dislocations by Soh *et al.*¹⁷, as the concentration of this level was observed to be minimal in samples with low screw dislocation densities. The density of screw dislocations in the samples studied in this work is less than 1%. If the level observed by Soh *et al.* is due to the same defect giving rise to the level E₂ in this work, then this could provide an explanation to the small amplitude of this level in the DLTS results.

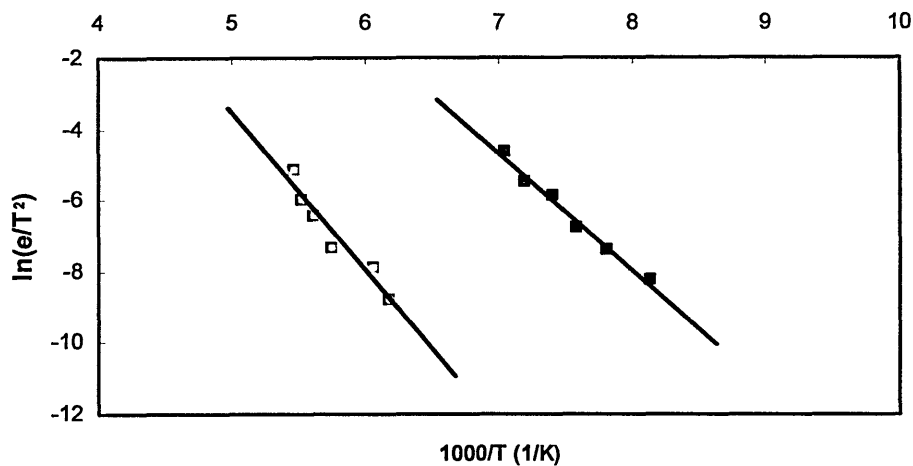


Figure 7.22: Arrhenius plots of level E₂ with fill pulse durations of 10ms (red squares) and 50ms (blue squares).

The decrease in activation energy due to an increase in filling pulse duration suggests that the level E₂ is most likely an extended defect or due to point defects which have segregated to the dislocation cores. However, the peak shape is not clear from DLTS scans such as in Figure 7.6, because E₂ is joined to the broad E₁ peak. To provide further insight into the emission behaviour of this level, Laplace DLTS data was collected using different filling pulse durations. The quiescent reverse bias was -2V and the filling pulse voltage was -0.5V to ensure that surface states do not participate in the emission process. The LDLTS data are displayed in Figure 7.23. The first noticeable result is that two distinct emissions are present. Most importantly, however, it can be seen that a defect state is present, emitting at $\sim 2s^{-1}$, whose emission rate is not affected by the increase in filling pulse duration. This finding suggests that another defect is also present, sufficiently further away from surrounding defect structure, as not to be affected by the Coulomb interaction. The defect resulting in the slower emission of less than $1s^{-1}$ displays a large increase in emission rate with filling pulse duration, especially for 50ms. This emission is likely to arise from an impurity or defect in the strain field of the dislocations, or impurities that have segregated to the dislocation cores.

It is not clear as to why the emission rates observed are much slower than usual at this temperature. The emission rates less than $1s^{-1}$ are more likely to be due to levels exhibiting maxima at higher temperatures on the DLTS spectra at a rate window of $200s^{-1}$. The small amplitudes of the peaks in comparison to other LDLTS results shown could be explained by considering that the DLTS peak height at this temperature is also considerably less when compared to emissions in the 300K region.

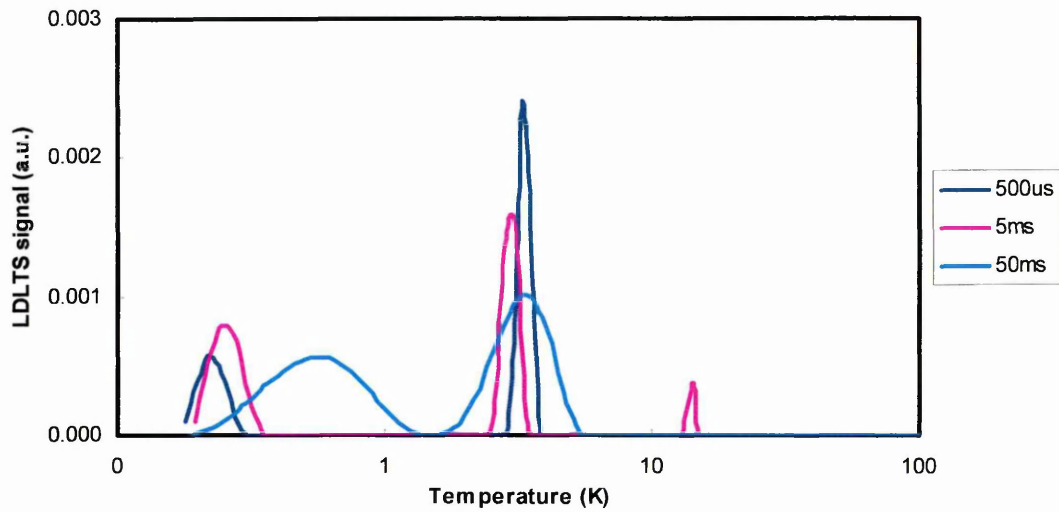


Figure 7.23: LDLTS of sample S2D12 at 150K.

The slow emission rates observed suggest that the dominating part of the non-exponential transients are in the region of $t \gg \tau$. This could occur due to slow rising transients, which may not have reached their quiescent values although the maximum number of samples has been selected for the measurements. Slow rising transients which do not reach equilibrium, even after a long sampling time, are an indication that a background emission is present possibly due to defects in the dislocation strain field. It must be noted that at such high dislocation densities, most lattice sites are expected to be affected by the dislocation strain fields.

7.5.3 Near-midgap states

The activation energy of the level E_3 (500 – 600K in Figure 7.6) could not be obtained through DLTS due to limitations in the software. The maximum allowable temperature setting in the Trapview software is 600K. When the higher rate window of 200s^{-1} is employed, the peak temperature is above 600K. Additionally, at those temperatures, lower rate windows of 10s^{-1} and 4s^{-1} appeared extremely noisy and it was not possible to determine the peak position in temperature. Instead, Laplace DLTS was used to obtain the activation energy of this level by incrementing the temperature in steps of 2K and allowing the temperature to settle to within 0.01K prior to commencing the measurement. The resulting Arrhenius plot is shown in Figure 7. 24 for sample S3D10. The derived activation energy is $E_3 = E_C - 1.46\text{ eV}$.

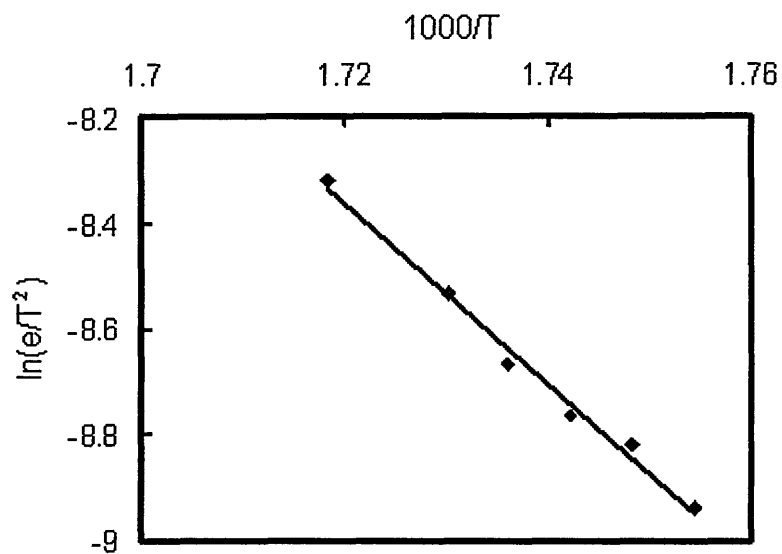


Figure 7. 24: Arrhenius plot of level E_3 obtained through Laplace DLTS.

It must be noted that the value obtained is subject to some speculation due to the behaviour of the LDLTS spectrum. Only one level behaved as expected and shifted in the right direction with increments in temperature. Ideally all levels present should provide data to derive an activation energy, however this was not observed in this instance. This does not mean that the levels observed through LDLTS are a false representation, but rather that the material is complex due to the 31000 end points as stated previously. The interaction between neighbouring states must be taken into account when evaluating such spectra.

The Laplace DLTS fill pulse tests of level E_3 are displayed in

Figure 7. 25. At this temperature range, the emission rate at the deep level should be greater than the capture rate. The Coulomb forces from surrounding states should not be strong enough to influence the emission from other neighbouring states. Therefore, it is likely that the emission at this temperature is point defect like, as observed from the LDLTS results in

Figure 7. 25.

It is also possible that the defects with a level near midgap are not physically located at the dislocation core, but are isolated point defects. However, the emission rate at $\sim 200\text{s}^{-1}$, corresponding to the spectrum of the 0.5 ms fill pulse, does display an increase to $\sim 300\text{s}^{-1}$ when longer fill pulses of 5 and 50 ms are used. This particular emission rate does not exhibit a further shift towards higher emission rates when the fill pulse length is increased from 5 to 50ms. This could indicate the presence of a level which is not at the dislocation core, but is physically close to neighbouring states. This is because the

emission from dislocation cores would be expected to display a further increase in emission rate with longer fill pulses. Such behaviour of the LDLTS spectra was presented in Figure 7.14.

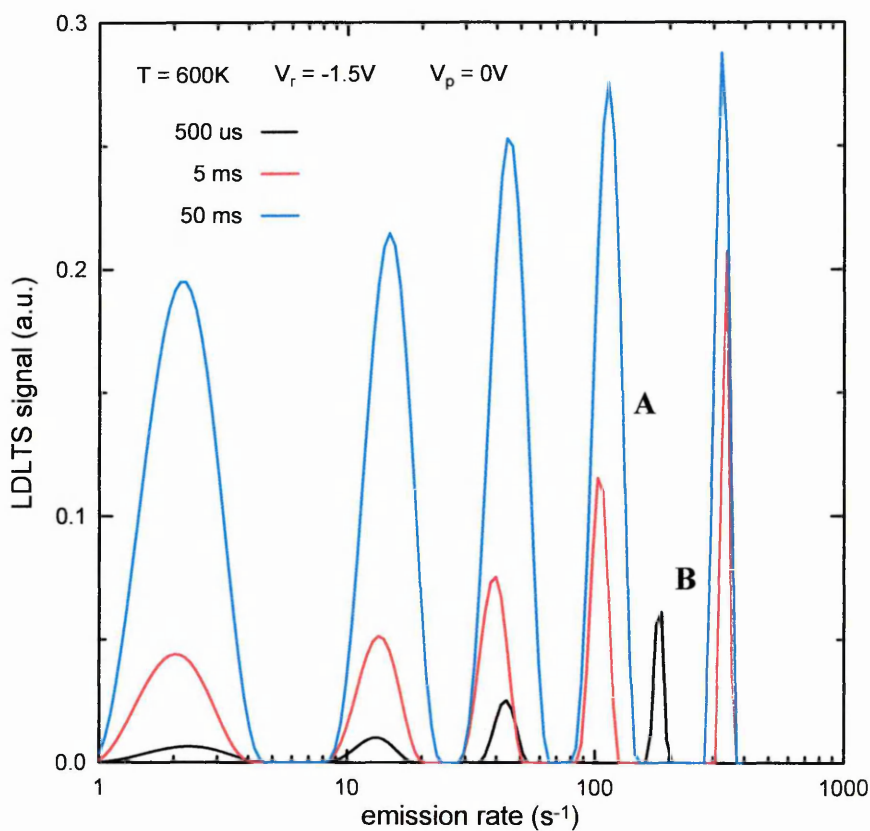


Figure 7. 25: LDLTS spectra of sample S3D10 at 600K with fill pulse durations of 0.5 ms (—), 5 ms (—) and 50 ms (—).

Figure 7.26 displays the LDLTS spectra at 600K for sample S2D12, using the same biasing parameters which were used in

Figure 7. 25. The spectra for this sample are more complex and the emission rate axis has been split to display the results more clearly. On initial inspection the behaviour of the LDLTS spectra with fill pulse appears to differ from that observed in

Figure 7. 25. Firstly, the emission rates appear to shift when longer fill pulse durations are applied. It must be recalled that the axis in Figure 7.26 is split and the shifts observed in the lower graph (0 to 12s^{-1}) are minimal (~ 1 emission per second). Furthermore, closer observation reveals that the set A and B emissions in Figures 7.25 and 7.26 are very similar in their behaviour with fill pulse duration. Only emissions due to the 5 and 50ms fill pulse lengths are observed for sets A in both Figure 7.25 and 7.26, which display a slight increase in emission rate with fill pulse duration. For sets B in

both figures, the increase in emission rates from the 0.5 to 5ms fill pulse is greater than for the 5 to 50ms.

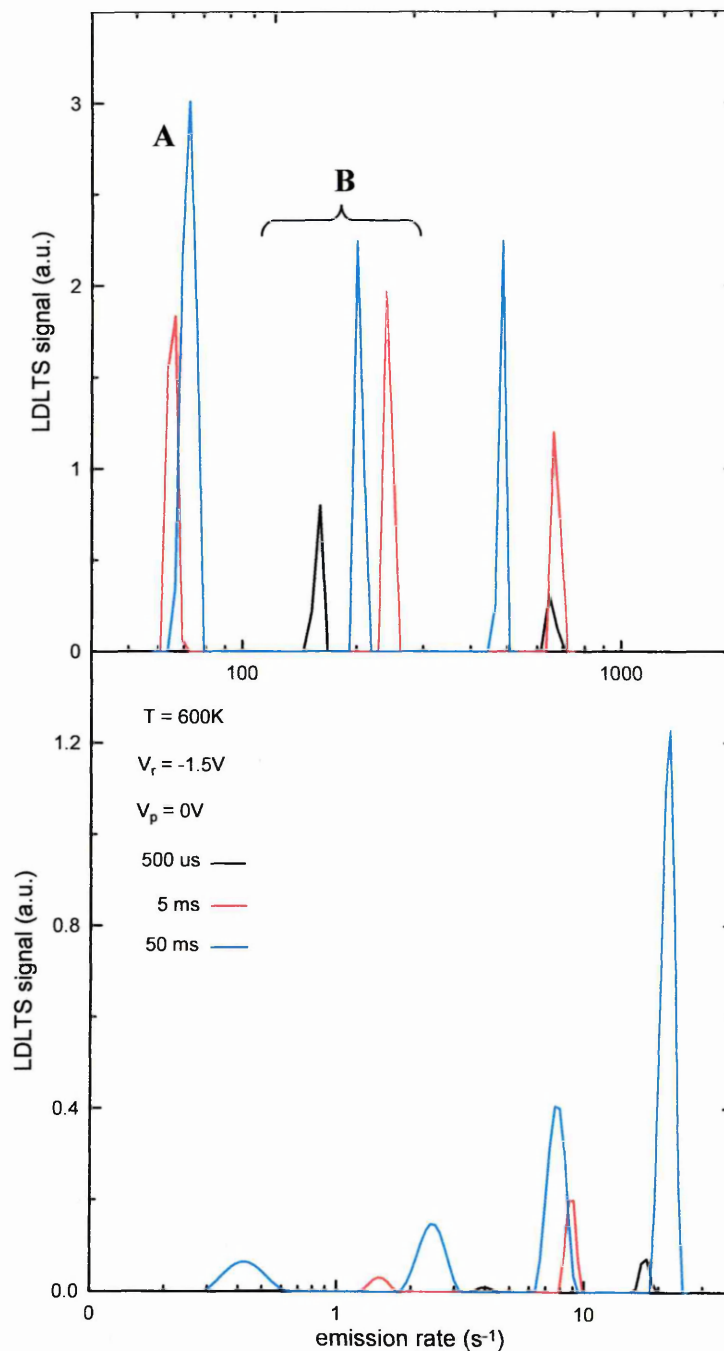


Figure 7. 26: LDLTS spectra of sample S2D12 at 600K with fill pulse durations of 0.5 ms (—), 5 ms (—) and 50 ms (—). Other biasing parameters are the same as for the LDLTS data presented in Figure 7.25.

The similarity observed for sets A and B in Figures 7.25 and 7.26 could indicate that these emissions arise from the same defect in diodes S2D12 and S3D10. The differences observed in the lower emission rates could suggest that defect distribution relating to the near-midgap emissions is non-uniform. It is unlikely that emissions in samples S2D12 and S3D10 are due to different impurities, because the samples have

been cleaved from the same wafer. Therefore, the differences are likely to be due to the effects of the dislocation strain fields.

7.6 Minority carrier emission

In Section 7.3, the formation of a minority carrier trap as a result of subjecting the sample to elevated temperatures was mentioned. This section will discuss the formation of this level and its characteristics in more detail. The presence of a minority carrier level in n -GaN that lies ~ 0.7 - 0.9 eV above the valence band was discussed in Chapter 5. Figure 7.27 shows the DLTS spectra of sample S2D1 with levels E_1 , E_{1b} and E_2 (initial) and the scan recorded immediately after the sample was taken up to 600K (post thermal stress). The scan shown in blue was performed less than one hour later and is significantly different. It shows a large negative-going peak, E_h , which is indicative of a minority carrier trap. In the following sections the term *post thermal stress* will generally be used to indicate that the sample was taken up to near 600K and cooled to room temperature from the E_h level. The term *initial*, or before thermal stress, will be used to indicate the condition of the sample where only majority carrier peaks (E_1 , E_2 and E_3) are present, as shown in Figure 7.6, unless otherwise stated.

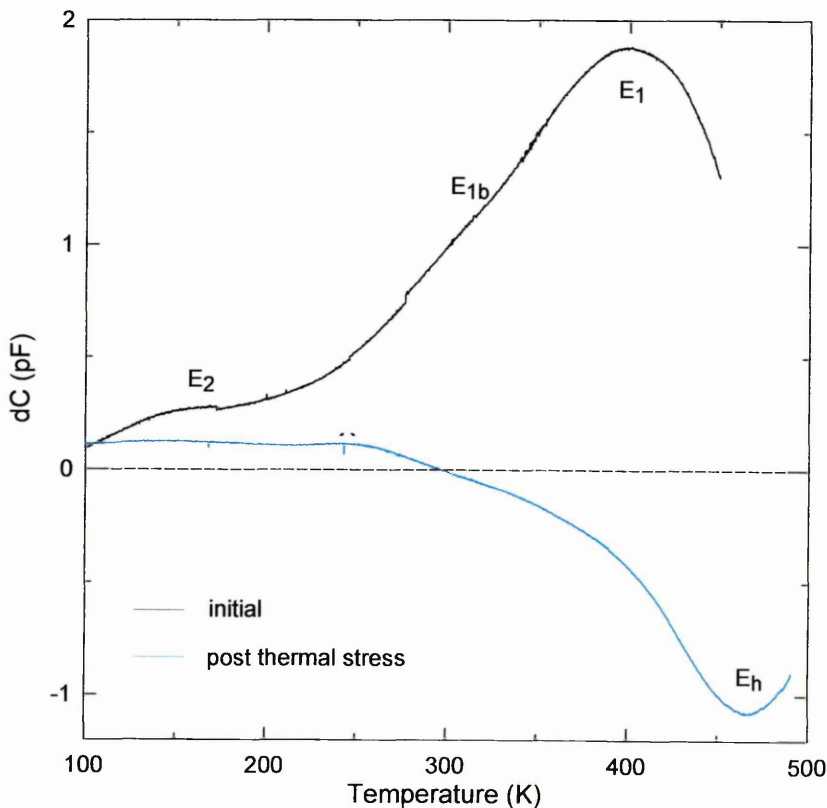


Figure 7.27: DLTS of sample S2D12 before (—) and after (—) thermal stress.

In both the initial and post thermal stress measurements in Figure 7.27, the quiescent reverse bias was set to -2V, and the fill pulse amplitude was -0.5V, with a duration of 1ms. In some cases, the DLTS scans of the minority carrier level have been terminated once the peak position was obtained. This was done in order to minimise the amount of thermal stress that the samples were subjected to.

It is apparent from Figure 7.27 that both E_1 and E_{1b} disappear due to the formation of the E_h level. Furthermore, the amplitude of level E_2 also appears to decrease. There are two possible explanations for this behaviour. The DLTS signal is the consequence of a capacitance transient, which is sampled in time. The capacitance transient, in turn, is determined by the time-dependent trap occupancy. If the energy separations of the minority and majority carrier traps from the valence and conduction bands are comparable, then emission of holes and electrons will occur simultaneously at both traps at a given temperature. Therefore, if the DLTS spectrum displays a negative peak due to a minority carrier level, then hole capture (i.e. electron emission from the hole trap to the valence band) and hole emission must exceed the electron equivalent. Applying this model to Figure 7.27 would indicate that the amplitude of E_2 may decrease as a result of hole emission. It must be noted that minority (hole) carriers do not normally exist in Schottky diodes. However, these materials are of poor crystalline quality and hole leakage currents could be a possibility.

The second possibility that should be considered is the passivation of the electron traps by a mobile impurity. It has been shown by Hierro *et al.* that the DLTS signal of level E_1 can be reduced to almost zero by hydrogenation in an H-plasma for 30min¹⁸. Upon hydrogenation, the trap concentration of level E_1 is reported to reduce to less than 10^{13} cm^{-3} from an initial concentration of $4.1 \times 10^{14} \text{ cm}^{-3}$. Furthermore, the bias dependency of level E_1 amplitude has been investigated by Wu *et al.*¹⁹, which the authors associate with hydrogen. This will be discussed in more detail later in the chapter.

The trap concentration, N_T , of level E_1 was measured to be $\sim 6 \times 10^{15} \text{ cm}^{-3}$ for a fill pulse duration of 1 ms. The trap concentration of E_h was found to be $\sim 9 \times 10^{15} \text{ cm}^{-3}$ with the same biasing conditions. This value is larger than obtained for E_1 , even though the peak of E_1 is greater in magnitude than that of E_h . This is because N_T is derived using the carrier concentration and capacitance values at the quiescent reverse bias at 300K. The appearance of the minority carrier peak due to thermal stress resulted in a change in the carrier concentration profile of the samples studied. A significant difference in the C-V measurements was observed after the sample was heated to 600K and subsequently

cooled to room temperature. This is discussed in section 7.6.1. In order to ensure that the carrier concentration and quiescent capacitance values are representative of the sample when calculating the trap concentration, C-V data have been obtained at 300K prior to each new DLTS experiment.

Figure 7.28 displays the profiles of the minority carrier peaks in the three other samples S1D10, S3D7 and S3D10. In sample S3D10, a double peak is apparent. This may be due to different lattice positions in the vicinity of the dislocation core and will be discussed later in this chapter. If the sample is allowed to rest (i.e. not used for electrical measurements), the spectrum recovers to the original scan as shown in black, in Figure 7.27. The period of recovery has been observed to be different for each sample, but is typically between a couple of days and up to a week. It is difficult to measure this time period, because any thermal stress or biasing will have a direct effect on the time of recovery. The hole level observed is a *metastable* level. Therefore, it is difficult to compare the levels to each other. However, the behaviour of the minority carrier trap with varying fill pulse durations can be investigated in order to obtain information about the capture properties of this level.

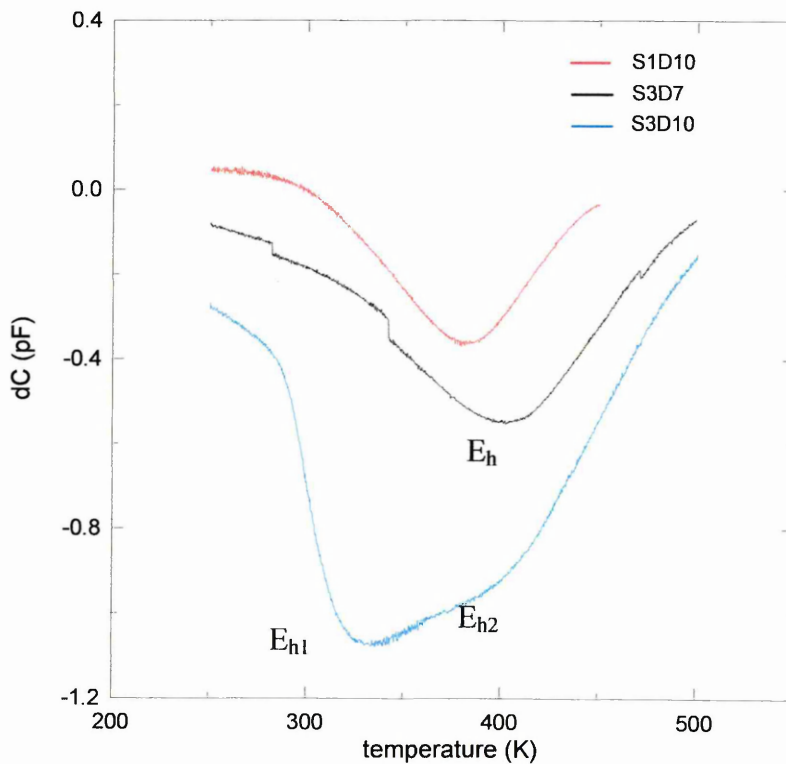


Figure 7.28: DLTS scans of samples S1D10 (—), S3D7 (—) and S3D10 (—), showing the peak due to minority carrier emission as a result of thermal stress.

It was stated in Chapter 5 that the minority carrier emission in *n*-GaN has frequently been associated with the gallium vacancy and its complexes with oxygen. Optical DLTS

measurements so far have reported this level without having to subject the sample to any thermal stress. This suggests that the defect concerned is inherently present in the sample. However, in our work, this level is not observed without having to subject the material to thermal stress. It was previously shown by Auret *et al.* that minority carrier levels in Si Schottky diodes can be detected by DLTS when forward bias fill pulses are applied²⁰. In samples which have not undergone any thermal stress, DLTS measurements were carried out with a forward bias pulse to investigate whether the level could be activated. The results did not indicate the presence of minority carrier emission.

The formation of the E_h level was found to have implications for the trap concentration of the E_1 level after the sample has been allowed to recover to the original scan. Figure 7.29 shows the initial DLTS spectra of sample S3D7 and the scan after the sample was allowed to recover after thermal stress. The term *initial* refers to the first DLTS scan recorded of a sample, or the one after a period of recovery where only majority carrier peaks are observed.

The peak shape of the initial scan in sample S3D7 is different than observed for S1D10, which suggests that the initial concentration of traps relating to E_5 were greater in S3D7.

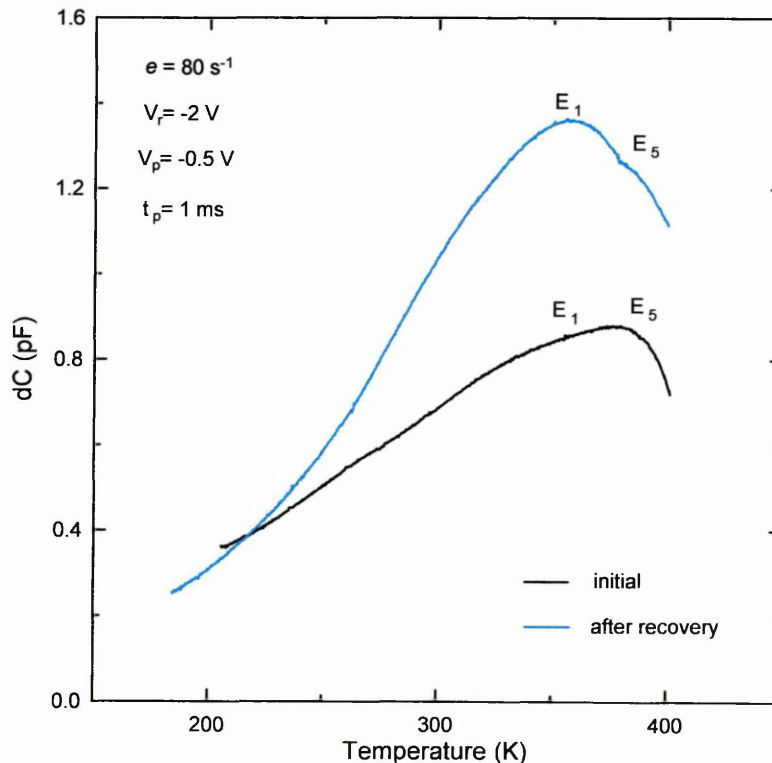


Figure 7.29: DLTS scan of sample S3D7 showing levels E_1 and E_5 before thermal stress (—) and after recovery (—). The term ‘recovery’ is described in the text.

Table 7.1 shows the trap concentration of level E_1 obtained from an initial DLTS scan (i.e. not subjected to any thermal stress) and from a scan of the same sample which has been left to recover for a period of three weeks, following thermal stress.

<i>Thermal history</i>	<i>Approximate trap concentration (cm⁻³)</i>
None (initial scan)	5×10^{15}
3 week recovery after thermal stress	7×10^{15}

Table 7.1: Trap concentration of E_1 obtained from an initial scan and after a period of recovery subsequent to the formation of the E_h level.

The trap concentration of E_1 recovers to above the initial value once it is allowed to rest following the formation of the E_h level. This suggests that the E_1 level was initially passivated by an impurity, which has dissociated from the E_1 level and possibly formed a complex with another defect or impurity.

7.6.1 Changes to carrier density

The first time the sample was cooled back to 300K from 600K in order to start the scan using another rate window pair, the measurement could not be carried out using the previous biasing conditions. A reverse bias of -1.5V or larger resulted in significant capacitance loss and high leakage currents due to the formation of the E_h level and associated changes in device characteristics, detected by C-V and I-V measurements. Figure 7.30 shows the change in carrier concentration before and after the sample was taken up to 600K. The 'initial' scan (blue) is obtained from the first ever C-V plot carried out on this particular sample. The dotted black line shows the drop in carrier concentration when the sample was taken up to 600K and cooled down to 300K. The carrier concentrations in the samples were found never to fully recover after several weeks. This also has consequences for the volume of material being probed for a given set of biasing conditions. Figure 7.31 shows the depth into the material as a function of applied reverse bias. Again, the blue line is obtained from the first C-V plot and the dotted black line was recorded after heating the sample up to 600K and cooling down to 300K. The solid black line represents a 'recovered' plot, which is taken after the sample is allowed to rest for some time and the DLTS spectrum recovers to the original state. It can be seen that at a reverse bias of -3V, the depth into the material is almost doubled when compared to the initial line. These changes were true for all samples.

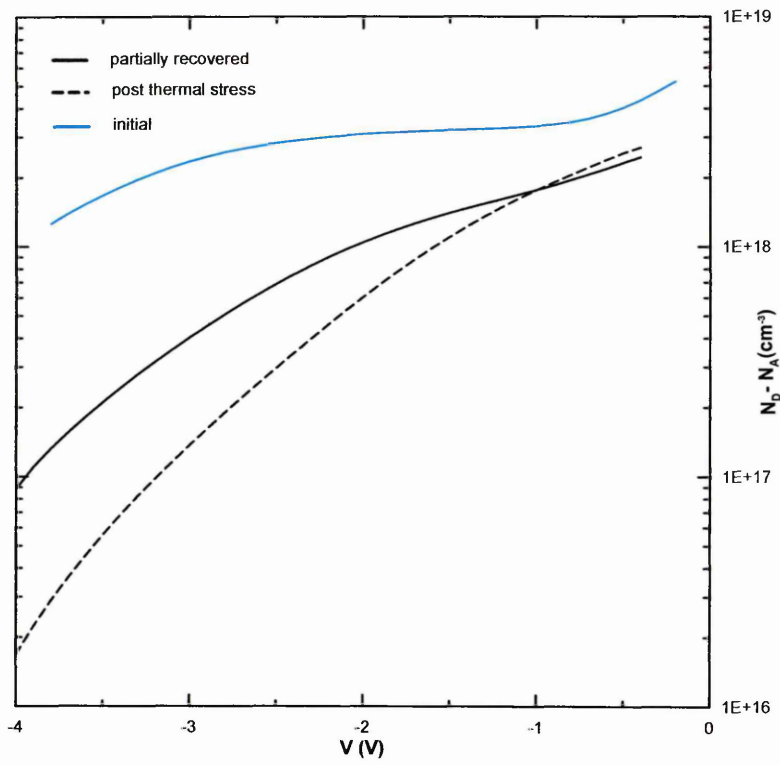


Figure 7.30: Carrier concentration as a function of voltage before (—) and immediately after (---) thermal stress. The solid black line is recorded after the DLTS spectra recover to that shown in Figure 7.6. All measurements were taken at 300K.

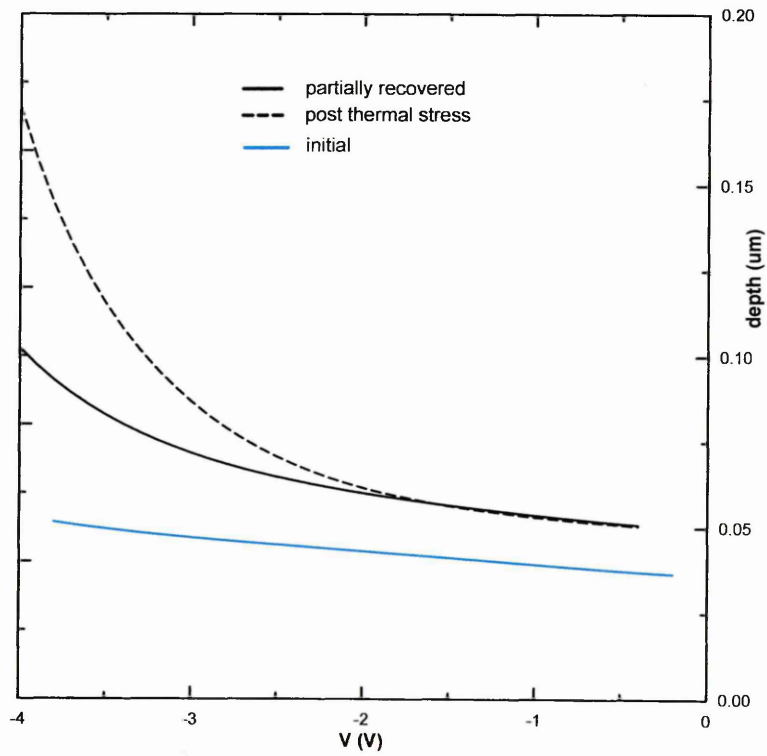


Figure 7.31: Depth as a function of voltage before (—) and immediately after (---) thermal stress and after partial recovery.

Figure 7.32 presents the current-voltage (I-V) characteristics before and after the sample was heated to 600K and subsequently cooled to room temperature. The I-V characteristics after a period of recovery are also shown. It is apparent that the change in reverse bias characteristics is far more significant in comparison to the change in forward bias characteristics. A $\sim 0.7V$ reduction in the turn-on voltage is visible due to thermal stress, which increases marginally towards its original value after a recovery period. The considerable increase in the reverse leakage current due to thermal stress is an indication of barrier height lowering. The reverse leakage currents were found not to decrease back to the initial value after a recovery period.

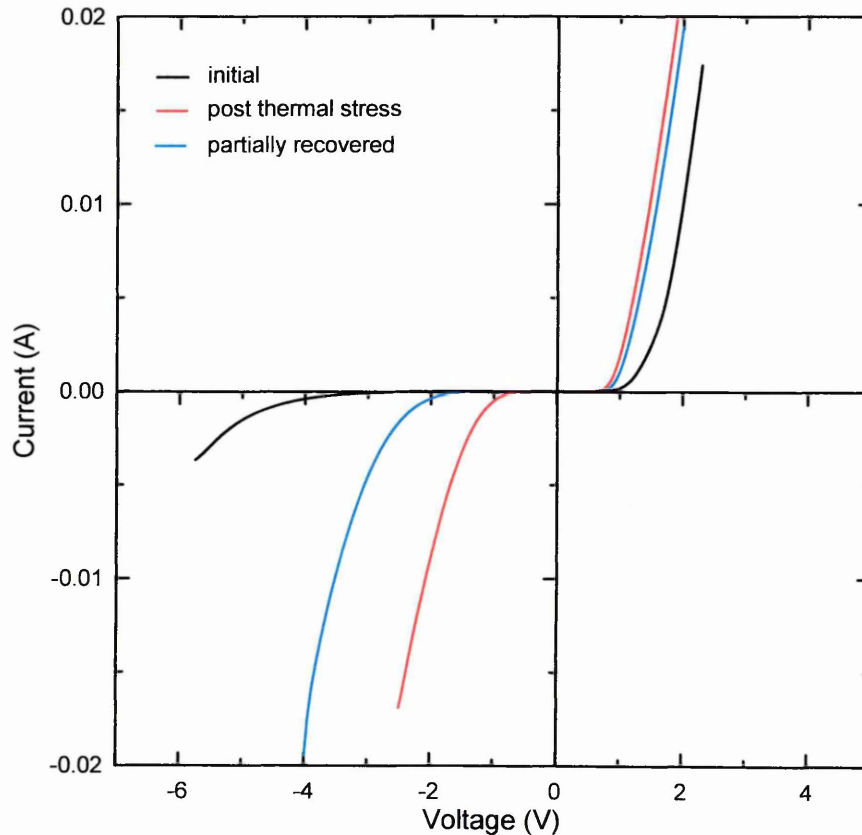


Figure 7.32: I-V characteristics of sample S3D7 at 300K before (—) and after (—) thermal stress. The scan in blue shows the I-V characteristics of the same sample after recovery, where the DLTS scan displayed emission due to majority carrier levels.

Trap concentration as a function of depth into the material could not be measured for the hole trap, because it was not possible to measure the capacitance at the required biasing conditions. All post-thermal stress DLTS and LDLTS measurements had to be recorded with smaller reverse bias settings ($-1.5V$ or smaller, depending on the sample).

7.6.2 Formation temperature of E_h

In order to find out the approximate temperature at which the level E_h forms, the maximum DLTS measurement temperature was incremented in steps of 20 or 30K. At each end point, the temperature was allowed to settle for 20min. The sample was then cooled back to 300K in order to start a new scan with a higher end point in temperature. The subsequent DLTS scan would show whether the minority carrier level had formed. The first measurement end point was 450K, because Laplace DLTS measurements were previously carried out at this temperature, with no apparent changes to device characteristics. This indicated that the temperature of formation is most likely above 450K. The results are shown in Figure 7.33 and reveal a gradual decrease in peak height, and hence active trap concentration, of level E_1 as the end temperature is increased. In the last scan, labelled *m6*, the level E_h is visible and suggests that it is due to thermal stress encountered as a result of the scan labelled *m5*, during which the sample has been taken up to 540K and allowed to settle for 20min. As the previous scan *m4*, with an end point of 520K, does not indicate the presence of the E_h level, it may be concluded that the minority carrier level is activated at a temperature between 520K and 540K.

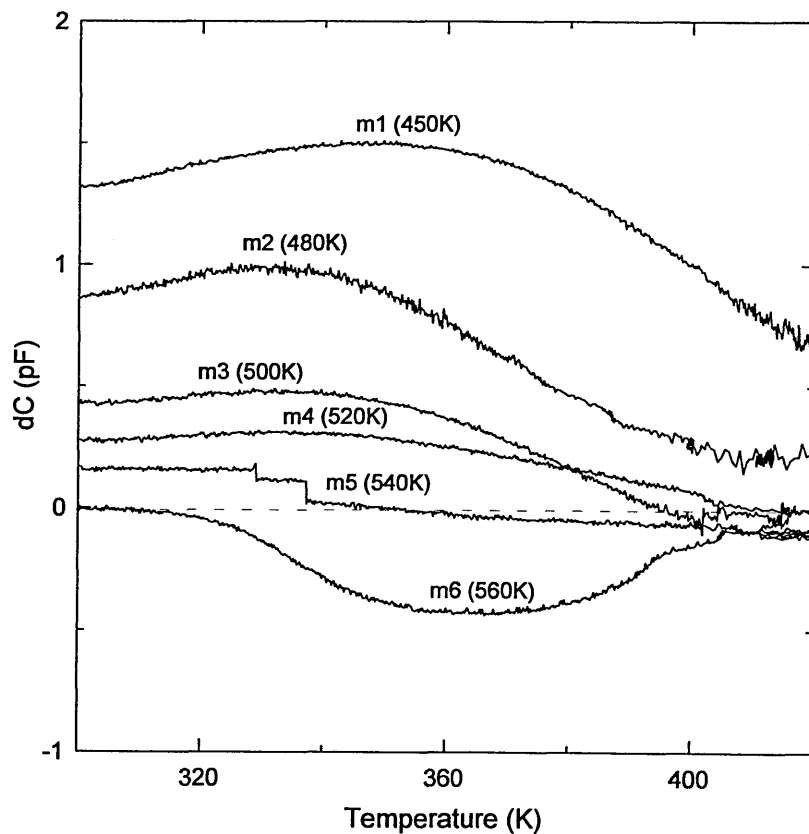


Figure 7.33: DLTS spectra of sample S3D7. The end temperature has been incremented by 20 – 30K for each scan to determine the formation temperature of the E_h level. The sample has been allowed to settle for 20 min at each new end temperature. The dotted line indicates the zero line on the dC axis.

Using the end temperature of each scan as an annealing temperature together with the resulting maximum amplitude of the subsequent DLTS spectrum, an Arrhenius plot was constructed to obtain the formation energy of the minority carrier level. The resulting Arrhenius plot is shown in Figure 7.34. The formation energy of the E_h level is derived to be 550 meV.

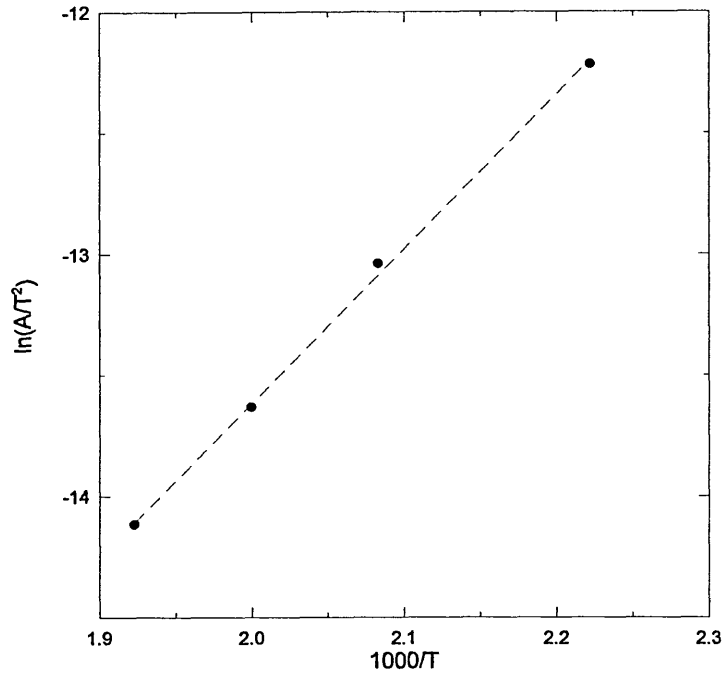


Figure 7.34: Arrhenius plot of level E_h constructed using the DLTS peak height as a function of annealing temperature.

Table 7.2 lists the measured trap concentrations for the subsequent DLTS scans recorded after the sample was cooled back to 300K, following a 20 min settling period at the end temperature of the previous DLTS measurement.

<i>Measurement end temperature (K)</i>	<i>Approximate trap concentration of level E_1 in subsequent scan (cm^{-3})</i>	<i>Approximate trap concentration of level E_h (cm^{-3})</i>
<i>First scan</i>	8×10^{15}	-
450	5×10^{15}	-
480	5×10^{14}	-
500	2×10^{14}	-
520	6×10^{13}	-
540	-	1×10^{14}

Table 7.2: Trap concentration of E_1 obtained in the scan following the 20min 'anneal' at the end temperature of the previous measurement.

7.6.3 Bias dependency

Investigations indicate that the acceptor level does not form if the sample is cooled from 600K to room temperature with the application of a constant reverse bias for the duration of the cooling period. For convenience, this method will be referred to as reverse biased cooling (RBC). In the case that the sample is cooled without any bias applied, it will be referred to as zero biased cooling (ZBC). The results of sample S3D7 are shown in Figure 7.35.

The initial scan (black line) is the DLTS spectrum without any prior intentional thermal stress applied to the sample, where the E_h level is not present. Once this scan was complete, the sample was allowed to settle at 600K for 20min. The sample was then cooled to 270K with a reverse bias of -2V applied throughout the period of cooling. The DLTS measurement was then repeated with the same biasing conditions as the initial scan. This scan is shown in the blue line. Not only is the minority carrier emission not present, but the RBC increases the peak height of the level E_1 .

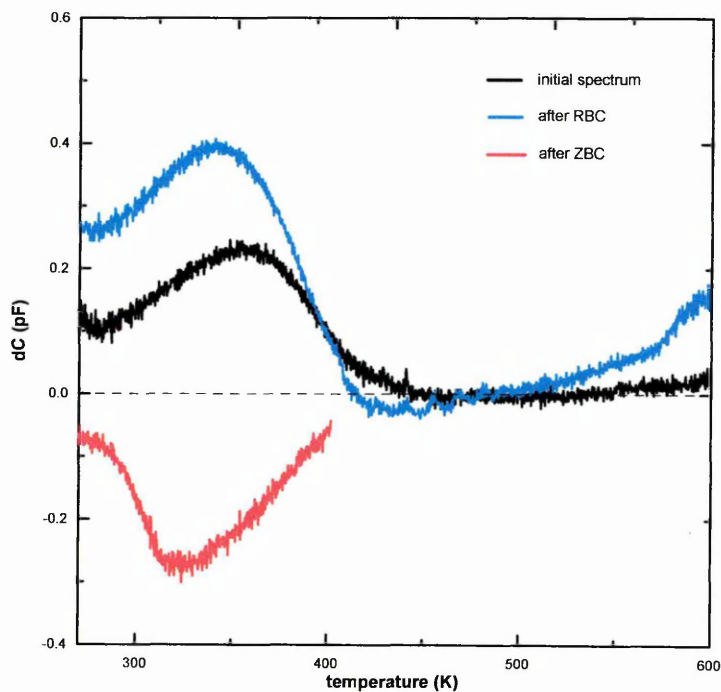


Figure 7.35: Effect of reverse bias cooling (RBC) and zero bias cooling (ZBC) on levels E_1 and E_h .

Level E_1 was previously reported by Wu *et al.*¹⁹ to be bias-dependant and the increase in peak height with reverse bias annealing was associated with the dissociation of a mobile impurity (most likely H^{\cdot}), which otherwise forms a complex with the defect giving rise to the E_1 level.

After the scan (shown in blue) was completed, the sample was again allowed to settle at 600K for 20 min. The sample was then cooled down to 270K again, but this time with no bias applied (zero biased cooling, or ZBC). In the subsequent DLTS measurement (shown in red) the minority carrier emission is clearly visible. This scan was terminated at 400K, as it was only designed to investigate the bias-dependence of the level E_h .

7.6.4 Effect of thermal stress on deep level stability

Level E_1/E_5

Figure 7.33 may pose the question as to whether the minority carrier level would also form if the sample was to be annealed for long enough at a lower temperature. LDLTS measurements were carried out on numerous occasions between 400K and 500K on samples when the minority carrier level was not present (either recovered or not yet formed). Although subsequent DLTS measurements did reveal a slight change in the height of level E_1 , results did not indicate a presence of a minority carrier trap. However, it would be reasonable to conclude that the temperature of formation of the hole trap could be somewhat lower than 540K, given enough time.

Following LDLTS measurements at elevated temperatures lasting one day, a shift to lower temperature of the DLTS spectrum was observed. During LDLTS, the sample is kept at a constant temperature for each new temperature, in addition to the time required for the temperature to settle to within 0.01K. This is usually 30 minutes to ensure accurate results. The settling time is especially important when investigating materials containing extended defects, because emissions are generally closely spaced in temperature. Typically, at least six data points are required for a reliable Arrhenius plot. This corresponds to a total annealing time of about 6 hours, because LDLTS measurements usually last for about 40 minutes. The duration of the measurement depends strongly on the noise and how quickly the transient returns to the quiescent value. It was found that a reverse bias of -3V for DLTS (or LDLTS) measurements was no longer possible due to capacitance loss. The DLTS spectra of the majority carrier levels after the 'anneal' step, due to prolonged LDLTS measurements at elevated temperatures is displayed in blue in Figure 7.36.

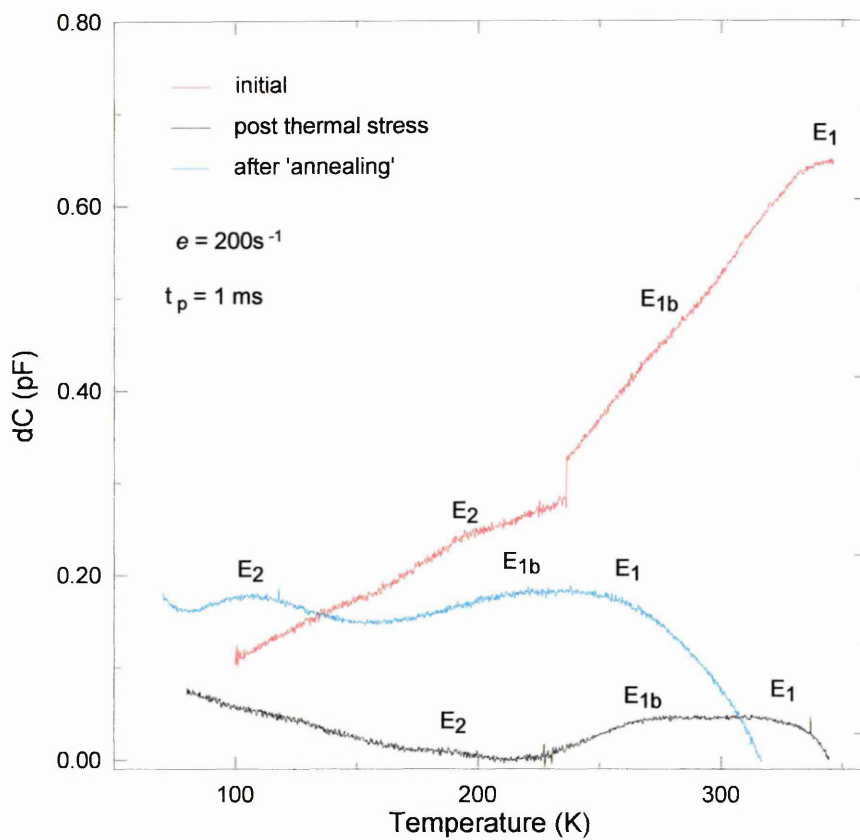


Figure 7.36: DLTS spectra of sample S1D10 before (—) and after (—) thermal stress. A scan (—) following the annealing effect of LDLTS measurements is also shown.

The red scan in Figure 7.36 shows the initial DLTS scan of sample S1D10. A glitch in the scan is visible around 240K, which is possibly due to noise and will be ignored in this instance. The black scan is taken after the sample has been heated to 600K and cooled down without any intentional annealing. Both the red and black scans have been obtained with a reverse bias of -3V and a fill pulse amplitude of -1V, with a duration of 1ms. The broad peak which originally dominated the scan above 240K is significantly reduced in amplitude. Furthermore, the peak heights of E_1 and E_{1b} are now comparable as a result of thermal stress. However, it cannot be determined for certain whether the level E_1 is still present in the 'post thermal stress' scan (black). The peak point of the level labelled as E_1 is about 50K to the left on the temperature axis of where it was originally.

A significant shift in the spectra is observed following the annealing affect of the Laplace DLTS measurements which have been recorded in the 400 – 500K temperature region and also at 600K. Additionally, a rise in the DLTS peak height suggests an increase in trap concentration. The shift in spectra could arise from slight shifts in the lattice positions of the defects or impurities, as a result of further annealing.

Level E_h

In sample S3D10, the E_h level displayed a ‘double peak’ and these have been labelled E_{h1} and E_{h2} in Figure 7.37. The level present in the other samples studied is most likely E_{h2} , judging by the peak point in temperature. However, it cannot be said for certain which level is the one detected in the other samples, because the spectra all display a shift as a result of further thermal stress. Figure 7.37 shows the effect of annealing at 600K without bias (zero bias annealing, or ZBA). The black line shows the initial DLTS spectra, which has been obtained subsequent to heating the sample to 600K and cooling back to 300K, without intentional annealing. The blue and the red lines display the E_{h1} and E_{h2} peaks as a result of 30 min and 1hr ZBA at 600K. All three scans have been recorded on the same day and with the same biasing conditions.

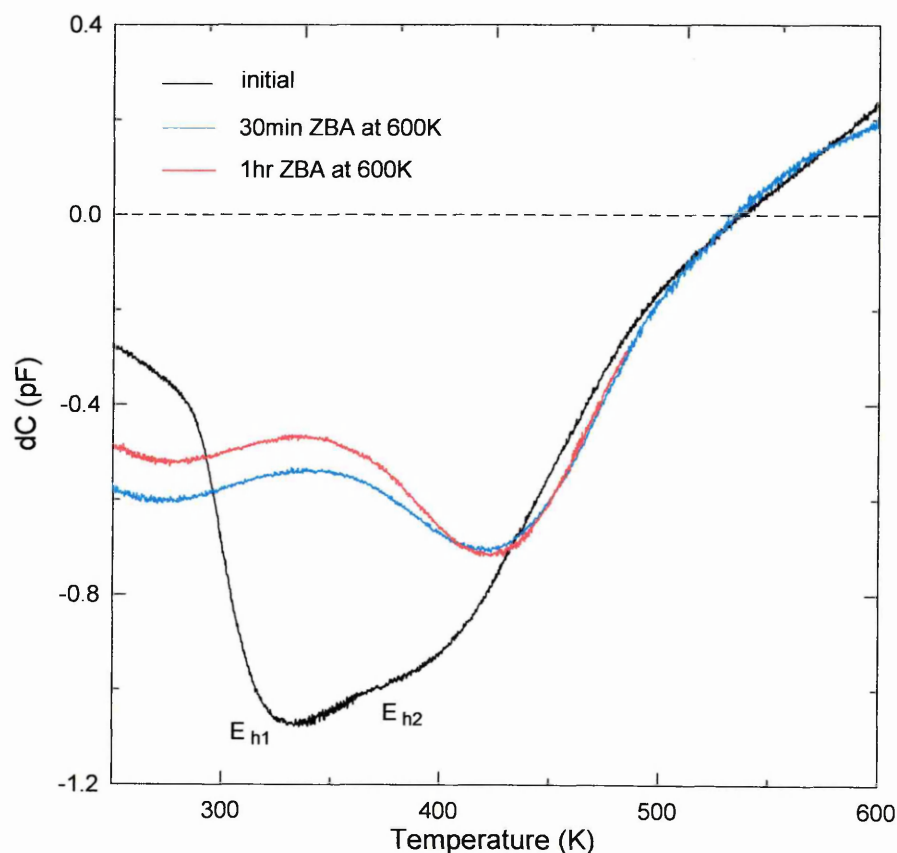


Figure 7.37: DLTS of sample S3D10 at a rate window of 50s^{-1} , showing effects of zero-bias annealing at 600K for 30min (—) and 1 hour (—). The initial scan is shown in black. The reverse bias was -1.5V. The fill pulse amplitude was 0V, with a duration of 1 ms.

It is apparent from Figure 7.37 that E_{h1} peak position shifts to a lower temperature, whereas the peak position of E_{h2} shifts to a higher temperature due to annealing at 600K. This suggests that the level E_{h1} moves closer to the valence band, whereas level E_{h2} moves deeper into the bandgap. This effect is illustrated in Figure 7.38.

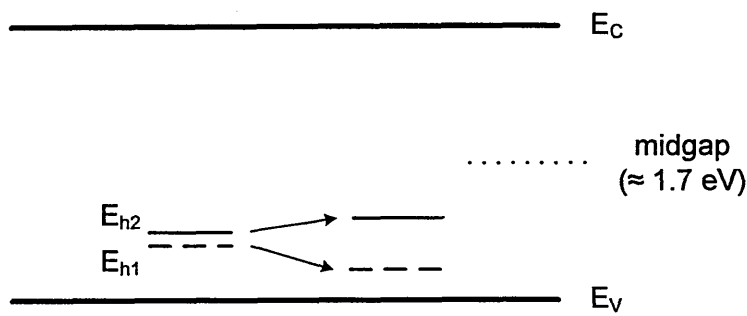


Figure 7.38: The effect of ZBA on the E_{h1} and E_{h2} levels in the GaN bandgap.

The gallium vacancy were found to become mobile at 500-600K by Saarinen *et al.*, who have carried out positron annihilation studies on electron irradiated GaN²¹. Furthermore, the calculated activation energies of $V_{Ga}-(O_N)_x$ complexes in GaN (where $x = 1, 2$ or 3) are reported to be different depending on whether they exist in the bulk or at dislocation sites²². These findings suggest that the shift of levels observed in Figure 7.37 could be due to the formation or movement of $V_{Ga} - (O_N)_x$ complexes. It must be noted that most DLTS measurements of GaN in the literature have been below 500K. Another group who employ a high temperature cryostat have reported the detection of a negative transient¹⁶. However, the maximum temperature of measurement observed in this reference is about 570K and no annealing at elevated temperatures has been mentioned. The authors do not report the formation of a minority carrier trap, which suggests that the formation of E_h level either requires annealing at temperatures above 560K, or higher temperatures of 600K without an annealing step.

Table 7. 3 shows the change in trap concentrations of E_{h1} and E_{h2} as a result of the ZBA anneal at 600K.

Thermal history	Approximate trap concentration (cm^{-3})	
	E_{h1}	E_{h2}
Post thermal stress (no additional annealing)	7×10^{16}	4×10^{16}
30 min ZBA	2×10^{14}	2.4×10^{14}
1 hr ZBA	1.9×10^{14}	2.4×10^{14}

Table 7. 3: Trap concentrations of E_{h1} and E_{h2} upon zero biased annealing for 30min and 1hr at 600K

The drop in the trap concentrations derived from the scan after the initial thermal stress step to those after the ZBA steps appear to be very high in comparison to the change in the DLTS peak heights. This is due to the change in carrier concentration and the

quiescent capacitance at the reverse bias used for the DLTS measurements. The effects of the ZBA at 600K on the carrier density are shown in Figure 7.39.

It is apparent that an additional 1hr anneal at 600K has no further effect on the trap concentration of E_{h2} and the peak positions of both levels. However, the carrier concentration profiles in Figure 7.39 show an additional drop in the carrier density as a result of a further 1 hr anneal.

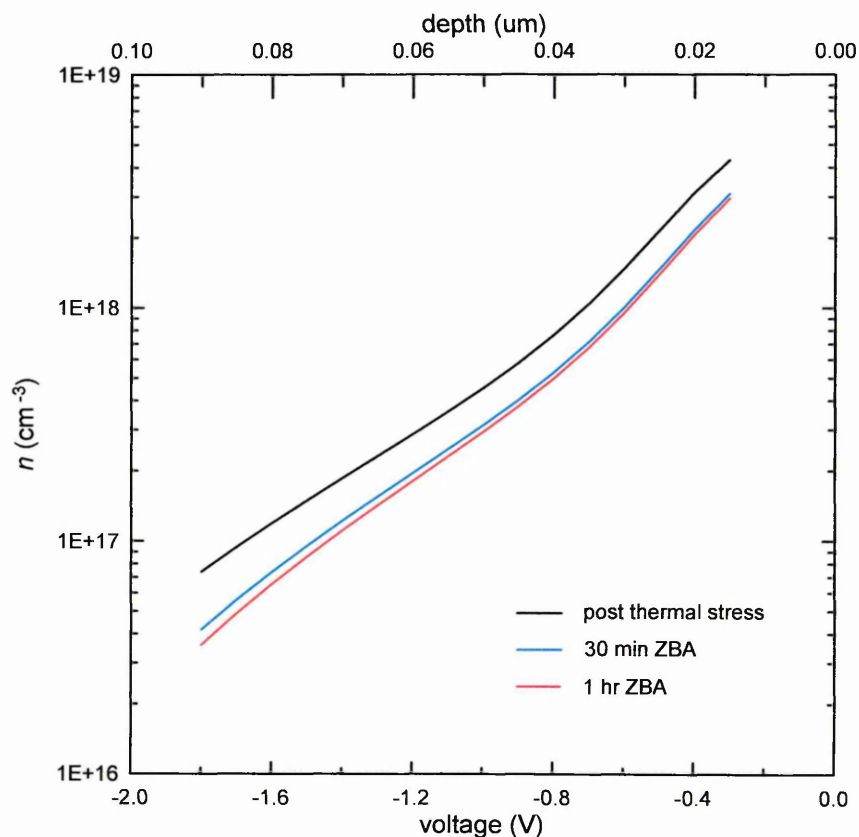


Figure 7.39: Effects of ZBA at 600K on carrier concentration. The black line shows the carrier concentration profile after the initial thermal stress. The data has been recorded at 300K.

It is unclear as to why the peak height of the E_{h1} level decreases due to an anneal at zero bias. The double peak consisting of E_{h1} and E_{h2} was also initially present in sample S3D7. It must be noted that S3D7 and S3D10 are different diodes situated on the same sample. The peak height of E_{h1} level was observed to decrease in magnitude after the reverse bias and zero bias cooling (RBC and ZBC) experiments described in section 7.6.3. This is illustrated in Figure 7.40. The *initial* scan refers to the scan that was recorded after the first thermal stress step (i.e. the first time the sample was heated to 600K and cooled down without bias). The scan in blue was recorded some time after the ZBC and RBC experiments, where the E_{h1} peak only appears as a slight shoulder to the left of E_{h2} . During the RBC and ZBC experiments, the sample was allowed to settle at 600K for 20 minutes, without any applied bias. This effect is similar to the zero bias

annealing experiments described above. However, it is noteworthy that the E_{h1} level is still present after a 30 min anneal for diode S3D10, whereas a 20 min anneal is long enough to anneal out the E_{h1} level detected in diode S3D7. This suggests that the defect concentration and distribution of the defect giving rise to E_{h1} is not homogeneous in the material, because both diodes tested are on the same sample.

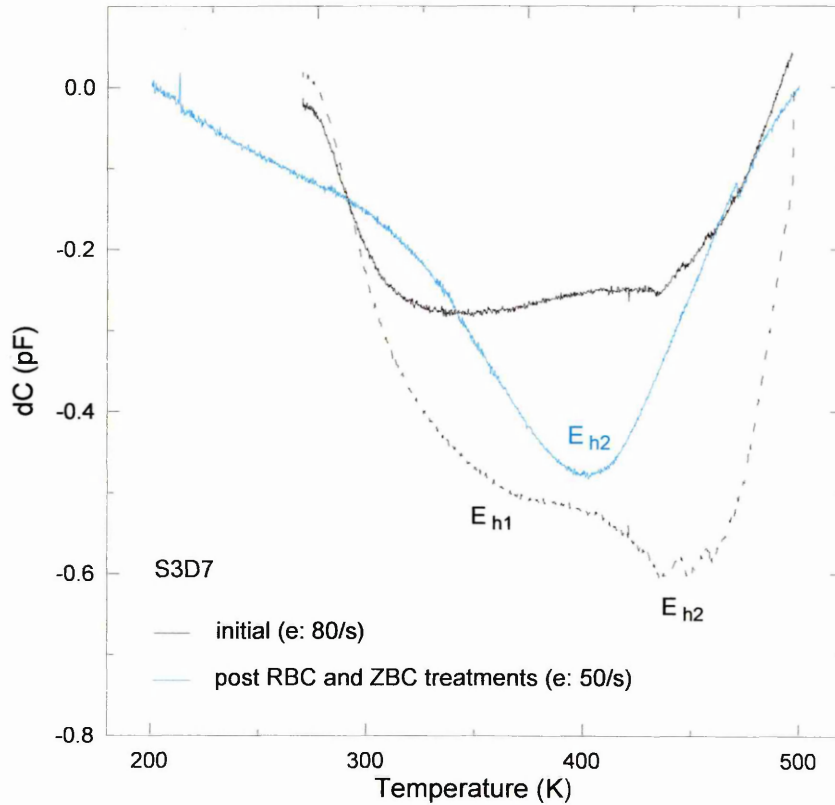


Figure 7.40: DLTS spectra of sample S3D7 showing the initial double peaks present at rate windows of 80s^{-1} (—) and 200s^{-1} (- - -). The scan after the RBC and ZBC treatments is also shown (—).

7.6.5 Fill pulse dependency

Fill pulse tests have been carried out on sample S3D10 by Laplace DLTS at 350K which are displayed in Figure 7.41. This temperature has been chosen in order to detect emissions due to both the E_{h1} and E_{h2} levels immediately after the ZBA treatments. The DLTS scans in Figure 7.37 have been recorded using a rate window of 50s^{-1} . At the measurement temperature of 354K for the LD LTS scans, the set of emissions labelled A are likely to be due to level E_{h2} . This is because the peak position of E_{h2} at a rate window of 50s^{-1} in Figure 7.37 appears at a higher temperature of $\sim 430\text{K}$. This suggests that at 354K, the emission rate is likely to be close to or less than 50s^{-1} . Similarly, the emission set B is most likely to arise from level E_{h1} , because at 354K, the emissions from E_{h1} are likely to be occurring at a faster rate.

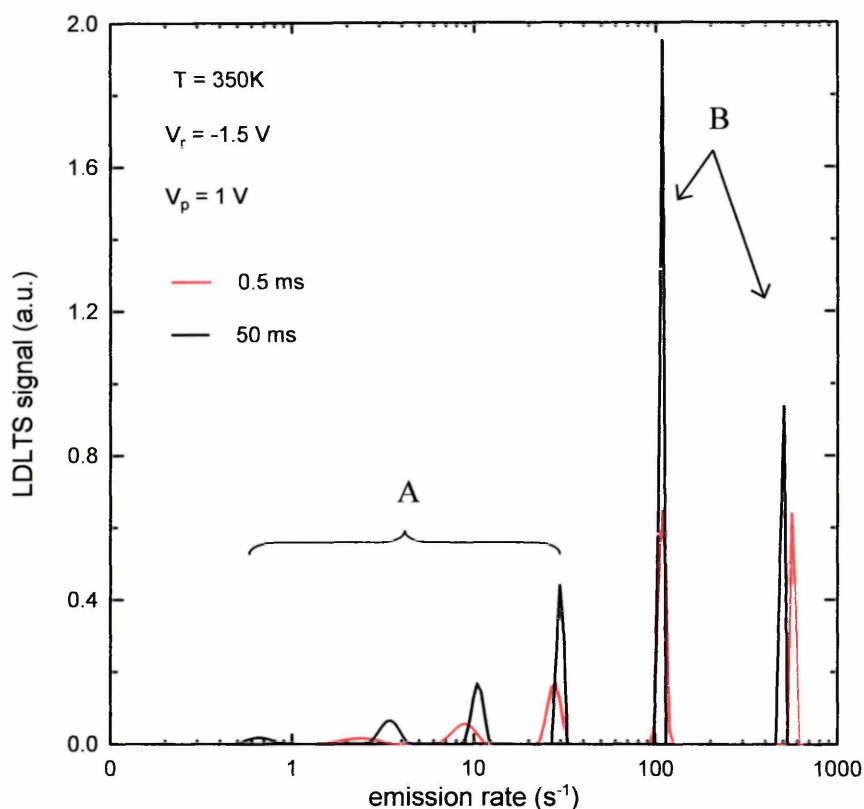


Figure 7. 41: Laplace DLTS of sample S3D10 at 350K, recorded immediately after the ZBA experiments at 600K.

It can be seen from Figure 7.41 that the set A emissions all shift towards a faster rate when the fill pulse is increased from 0.5 to 50ms. However, it must be noted that the shifts observed are in the order of 1 emission per second. Therefore, it is not possible to conclude for certain that the set A emission rates exhibit fill pulse dependency. The slow emission rates of set A could arise from the level E_{h2} . This is because the maxima of E_{h2} occurs at a higher temperature, which suggests that this level should emit at a slower rate at 350K. For set B, the $100s^{-1}$ emission rate does not display fill pulse dependency, which is indicative of a point defect related emission. On the other hand, the $\sim 500s^{-1}$ emission due to a fill pulse duration of 0.5ms shifts to a lower emission rate with an extended fill pulse length. A possible reason for this will be discussed in section 7.7.3.

Laplace DLTS measurements were also carried out on diode S3D7 at 360K. This particular diode is on the same sample (sample 3) as S3D10. The spectra were recorded using fill pulse durations of 0.01, 0.1 and 1ms. The results are displayed on a split axis in Figure 7. 42. The fill pulse dependency of the emission rates occurring under $200s^{-1}$ are very similar to those displayed in Figure 7.41 for diode S3D10. Again, a small shift towards faster emission rates is observed with increasing fill pulse duration for the three emission rates under below $100s^{-1}$. Also, the emission at $\sim 100s^{-1}$ is the only emission rate which does not exhibit fill pulse dependency, as was the case for diode S3D10 in

Figure 7.41. Furthermore, the emission rates between 100 and 1000s⁻¹ appear to emit slower as the fill pulse is increased. The difference between LDLTS results from diodes S3D10 and S3D7 is that two additional emission rates are observed for diode S3D7. This may be due to the higher measurement temperature for diode S3D7, or due to some differences in the strain fields of the dislocations.

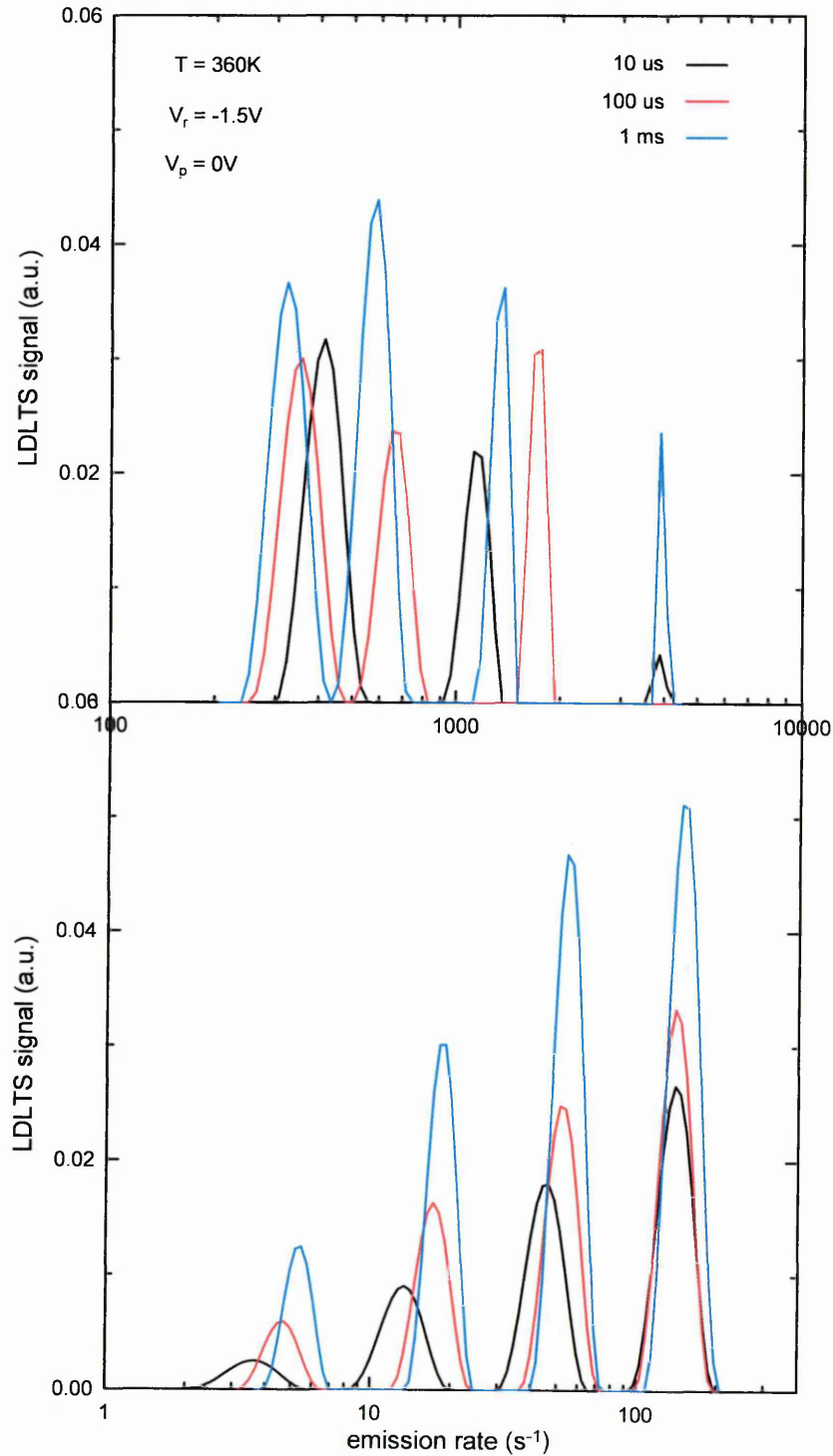


Figure 7. 42: Laplace DLTS of the E_h level in sample S3D7 at 360K.

Figure 7.43 presents the DLTS spectra of sample S1D10, which have been recorded using fill pulse durations of 1 and 50 ms. The reverse bias used for both experiments was -2.5V, with a fill pulse amplitude of -0.5V. The peak shape of the E_h level displays a high level of symmetry and is indicative of a point defect. However, the fill pulse dependency of the level is intriguing. Increasing the fill pulse duration to 50ms results in a shift of the E_h peak to $\sim 395\text{K}$ from 380K, which is not typical of point or extended defects. For emission arising from the vicinity of extended defects, the peak position is likely to shift towards lower temperatures due to local band-bending as a result of Coulombic repulsion between closely-spaced levels in the bandgap. The shift to a higher temperature in this case is more likely to be due to the modification of the capacitance transient as a result of the electron emission from level E_5 .

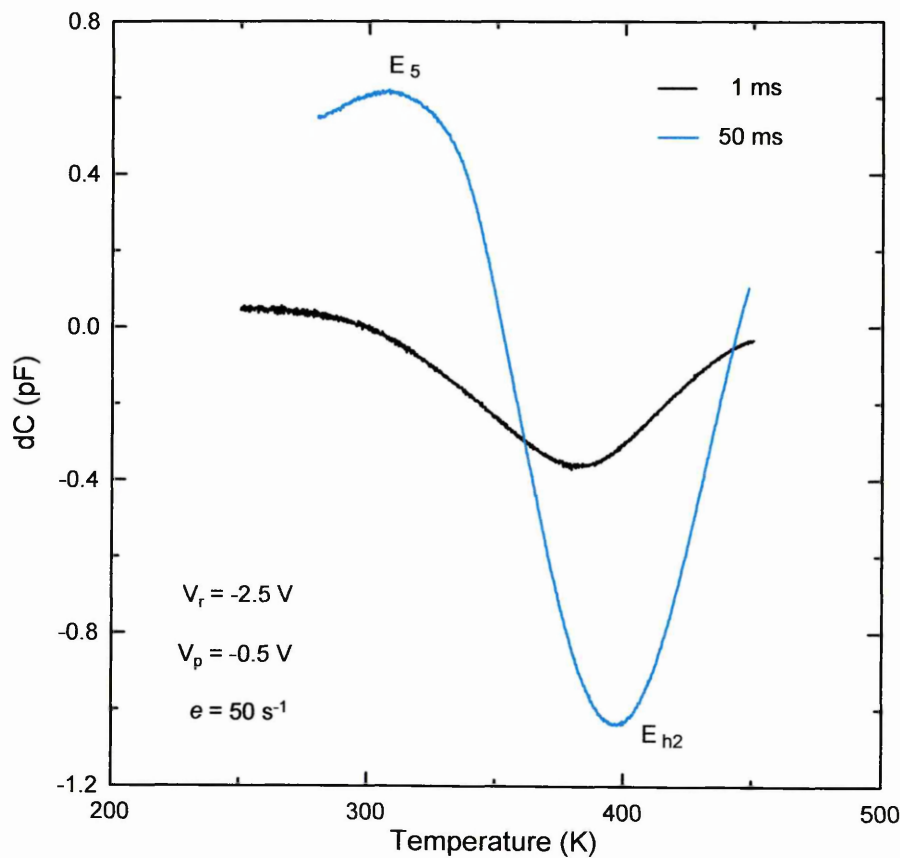


Figure 7.43: DLTS spectra of sample S1D10 at a rate window of 50s^{-1} , showing the fill pulse dependency of the E_h level. Fill pulse durations of 1 (—) and 50 (—) ms were used. All other biasing parameters were kept constant.

It can be seen in Figure 7.43 that a 50ms fill pulse results in a positive value of the DLTS signal in the temperature range of $\sim 300 - 350\text{K}$, which appears to be negative when using a 1ms fill pulse.

The positive peak resulting from the 50ms fill pulse in Figure 7.43 is labelled as level E_5 . It is not possible to be absolutely certain about the nature of the peak from the DLTS spectrum in the above figure. However, based on the peak position of levels E_1 and E_5 in the 50ms fill pulse spectra in Figure 7.13, E_5 appears to be the most likely contender for the positive peak in Figure 7.41. It must be noted that the spectra in Figure 7.13 are obtained using a rate window of 200s^{-1} , which suggests that the peak position of E_1 at a rate window of 50s^{-1} would appear at a lower temperature than shown in Figure 7.13. The detection of a majority carrier level by applying a longer fill pulse further supports the concept that electron emission and capture occur simultaneously. Therefore, thermal stress is likely to result in a greater electron capture rate (or hole emission rate) at E_h than electron emission at electron traps in the upper half of the bandgap. This may explain the decrease in the E_1 level with increasing annealing temperature, as shown in Figure 7.33. It is probable that the peak height of E_1 decreases due to the increase in peak height of the E_h level.

The fill pulse dependency of the E_{h1} and E_{h2} peak positions were also investigated for sample S3D10. DLTS spectra at a rate window of 50s^{-1} have been recorded using fill pulse durations of 1, 25 and 50 ms. All other parameters were kept the same and the results are displayed in Figure 7.44. The peak positions of level E_{h1} are found to be $\sim 330\text{K}$, 325K and 340K with fill pulse durations of 1, 25 and 50 ms, respectively.

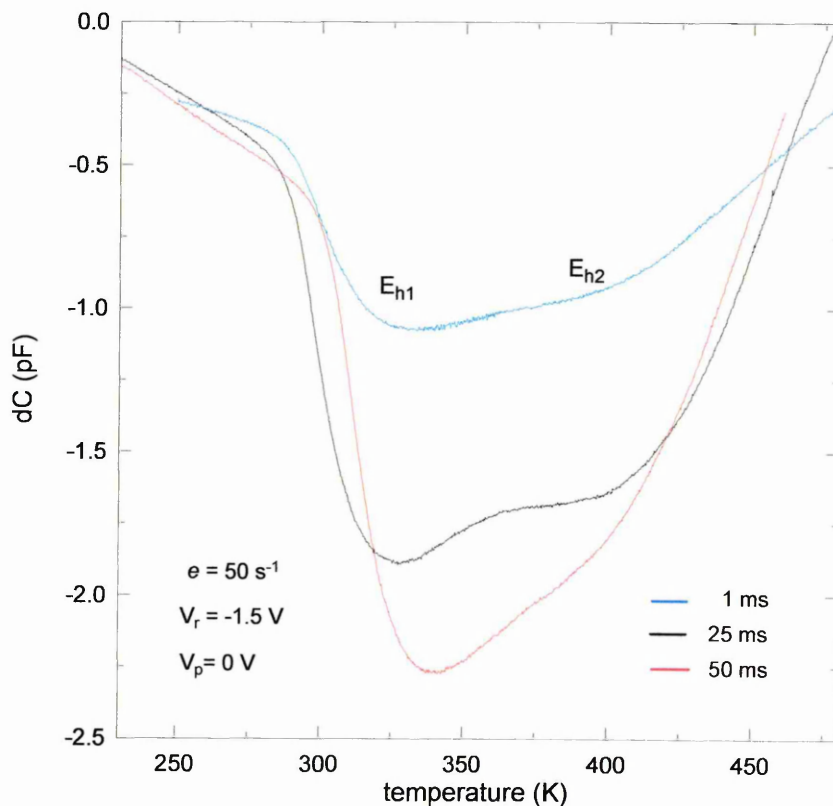


Figure 7. 44: DLTS of sample S3D10 recorded using fill pulse durations of 1 (—), 25 (—) and 50 (—) ms.

The peak position temperatures suggest that there is no definite dependency of the E_{h1} level on fill pulse. The shifts observed in temperature could be due to the ambiguous interaction of simultaneous electron capture and emission processes at a given temperature. This, combined with the temperature hysteresis in subsequent DLTS measurements could account for the differences observed in the peak positions. It is not possible to determine the peak position of the E_{h2} peak at a fill pulse duration of 50 ms. However, the peak shapes with fill pulse lengths of 1 and 25 ms suggest that the peak position does not shift to a lower temperature when the fill pulse is increased to 25 ms. These findings indicate that both E_{h1} and E_{h2} levels exhibit isolated point defect behaviour.

Unlike S1D10, the E_5 level is not detected in sample S3D10 when the fill pulse duration is extended to 50 ms. This could indicate that the trap concentration of E_5 is not homogeneous within the material.

The fill pulse dependency of the E_h level in S1D10 (Figure 7.43) was investigated using Laplace DLTS. The spectra obtained using fill pulse durations of 0.5, 5 and 10 ms are displayed in Figure 7.45. It is apparent that S1D10 exhibits fewer emissions than S3D7 and S3D10, for which the DLTS spectra displayed two levels, E_{h1} and E_{h2} .

All peak heights, excluding the emission labelled D, do not increase when the fill pulse duration is extended to 10ms from 5ms. Furthermore, none of the emissions exhibit fill pulse dependency. These results are a strong indication that the hole trap detected has a point defect nature.

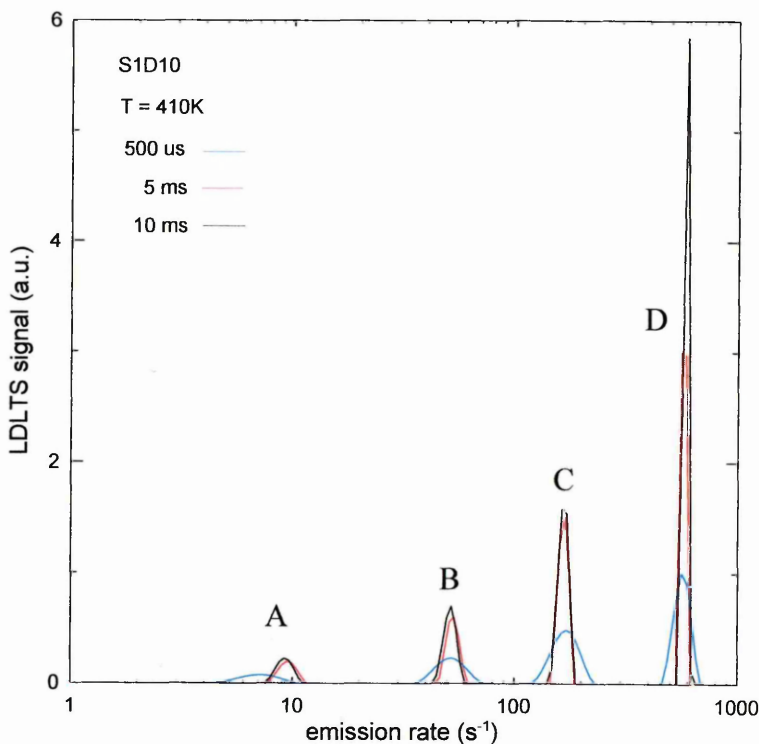


Figure 7.45: Laplace DLTS of S1D10 at 410K with fill pulse durations of 0.5 (—), 5 (—) and 10 (—) ms.

However, it was found that the fill pulse dependency of the E_{h1} and E_{h2} levels can be modified when a much longer fill pulse of 100 ms is applied. This is shown in Figure 7.44. The sets of spectra labelled A, B and C in the $<100s^{-1}$ region display a shift to higher emission rates when the fill pulse is increased to 100ms. A model to explain such a dependency on fill pulse length is described in section 7.7.4.

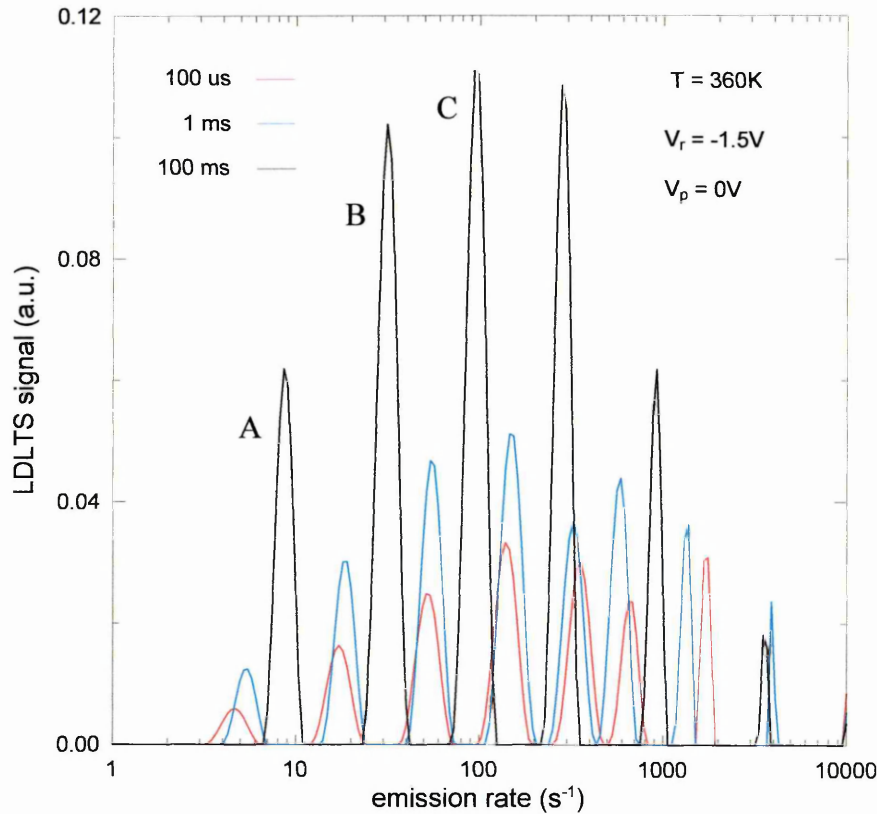


Figure 7.46: Laplace DLTS of sample S3D7 at 360K with fill pulse durations of 0.1 (—), 1 (—) and 100 (—) ms.

The decrease of the higher emission rates with extended fill pulse durations in Figure 7.46 was also evidenced in Figures 7.41 and 7.42. A model is proposed in section 7.7.3 to provide an explanation for this outcome.

7.6.6 Activation energy measurements of the E_h level

The activation energy measurements for the E_h level were problematic due to the additional thermal stress encountered after each scan. The situation is made more complex due to the simultaneous electron emission occurring from deep electron traps. Therefore, the activation energy values derived are an indication of the behaviour of the E_h level under thermal stress. Figure 7.47 shows the Arrhenius plots obtained for S3D7

before additional thermal stress and also for S3D7 and S2D12 after the E_h level was observed to shift, after further stress.

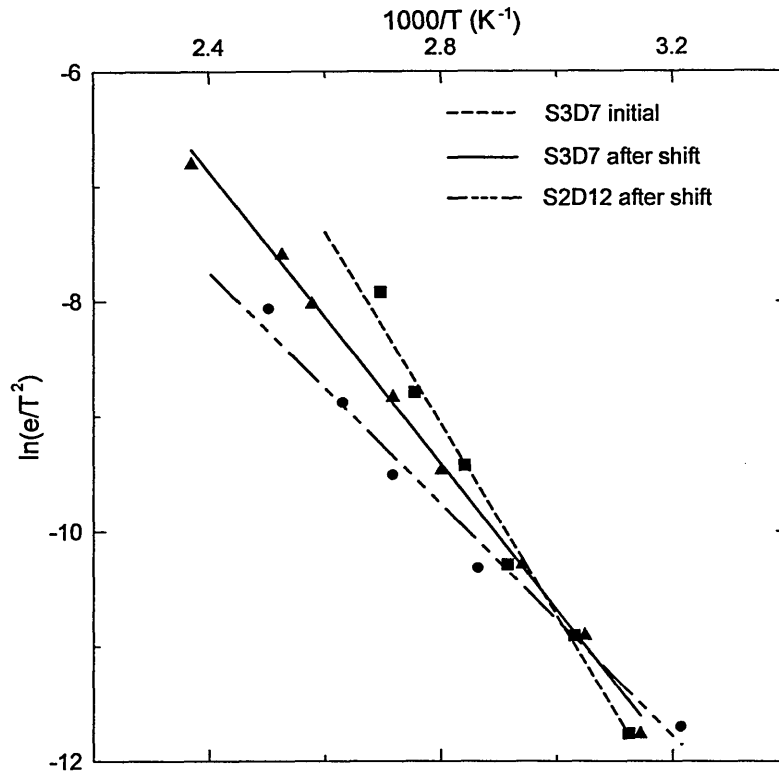


Figure 7.47: Arrhenius plots of the E_h level before and after a shift of the peak position to a lower temperature.

The activation energy values derived from the Arrhenius plots in Figure 7.47 are displayed in Table 7.4.

Sample and condition	Activation energy, $E_T - E_v$ (meV)
S3D7 initial	708
S3D7 after shift of peak position	553
S2D12 after shift of peak position	435

Table 7.4: Activation energies of the E_h peak in S3D7 before, and in S3D7 and S2D12 after a shift in peak position to lower temperatures.

The term *initial* for S3D7 refers to peak position of the E_{h2} level, which remained after the E_{h1} level was reduced, as shown in Figure 7.40. However, the peak position of the E_h level in sample S3D7 moved to a lower temperature as a result of further unintentional thermal stress due to DLTS and Laplace DLTS measurements at elevated temperatures. The E_h level in S2D12 was not measured before the peak position was observed to move to a lower temperature.

It must be noted that the activation energy values obtained after thermal stress are inconsequential. This is because the level observed in this work is metastable and the peak temperatures are highly sensitive to temperature cycling. The sample is repeatedly heated and cooled during DLTS measurements in order to record other sets of rate windows for the construction of an Arrhenius plot. Such additional thermal stress has an effect on the peak positions of subsequent DLTS spectra. The level is observed to be inherent in GaN grown by most methods [REF], but when measured using the Schottky diodes in this study, it is a metastable level.

7.7 Discussion

It is evident from the results presented in this chapter that the deep level emission from defects in the samples studied is a complex process. The high dislocation density ($\sim 4 \times 10^8 \text{ cm}^{-3}$) corresponding to ~ 31000 end points under each Schottky diode should be noted. Although threading edge dislocations in GaN are not expected to have deep levels in the bandgap, the electrical activity associated with dislocations in GaN has been attributed to impurities trapped in the strain field of dislocations²³. It was discussed in Chapter 2, section 2.3 that impurities at the strain field of dislocations may have a distribution of activation energies, which may result in multiple emissions²⁴. Therefore, it is highly probable that the numerous emissions observed in the Laplace DLTS spectra are due to effects of the dislocation strain fields on positions of the impurity levels within the bandgap.

The following sections summarise the deep levels detected in the *n*-GaN samples studied. This is followed by a detailed discussion of the effect of thermal stress on the deep levels, focusing on the minority carrier level observed.

7.7.1 Electron traps and dislocation related emission

A broad emission between ~ 100 - 450 K was detected in the DLTS scan shown in Figure 7.6. Only the peak positions of E_1 is clearly visible in the spectrum. Both levels E_1 and E_2 have been associated with extended defects in the literature due to their fill pulse dependent activation energies, as discussed in Chapter 4. The levels displayed similar behaviour with fill pulse in the DLTS experiments, where reductions in the activation energies were detected. This was associated with local band bending due to Coulomb interaction between nearby states with the application of longer fill pulses. However, the Laplace DLTS results clearly show both point defect and extended defect related

emission, where some emission rates do not increase when the fill pulse duration is increased. Furthermore, an increase in the fill pulse length from 1 to 50ms in the DLTS experiment showed the presence of a peak, E_5 . The peak shape of E_5 is characteristic of point defect related emission, which was undetected when a fill pulse of 1ms was applied. This suggests that the E_5 level could be detected by a 50ms fill pulse because it does not exhibit fill pulse dependency and thus does not shift to lower temperature. This is confirmed by Laplace DLTS results (Figure 7.16), which show that the emission rates recorded at 354K are most likely to arise from the E_5 level and do not exhibit fill pulse dependency. The level E_5 is likely to be due to a point defect.

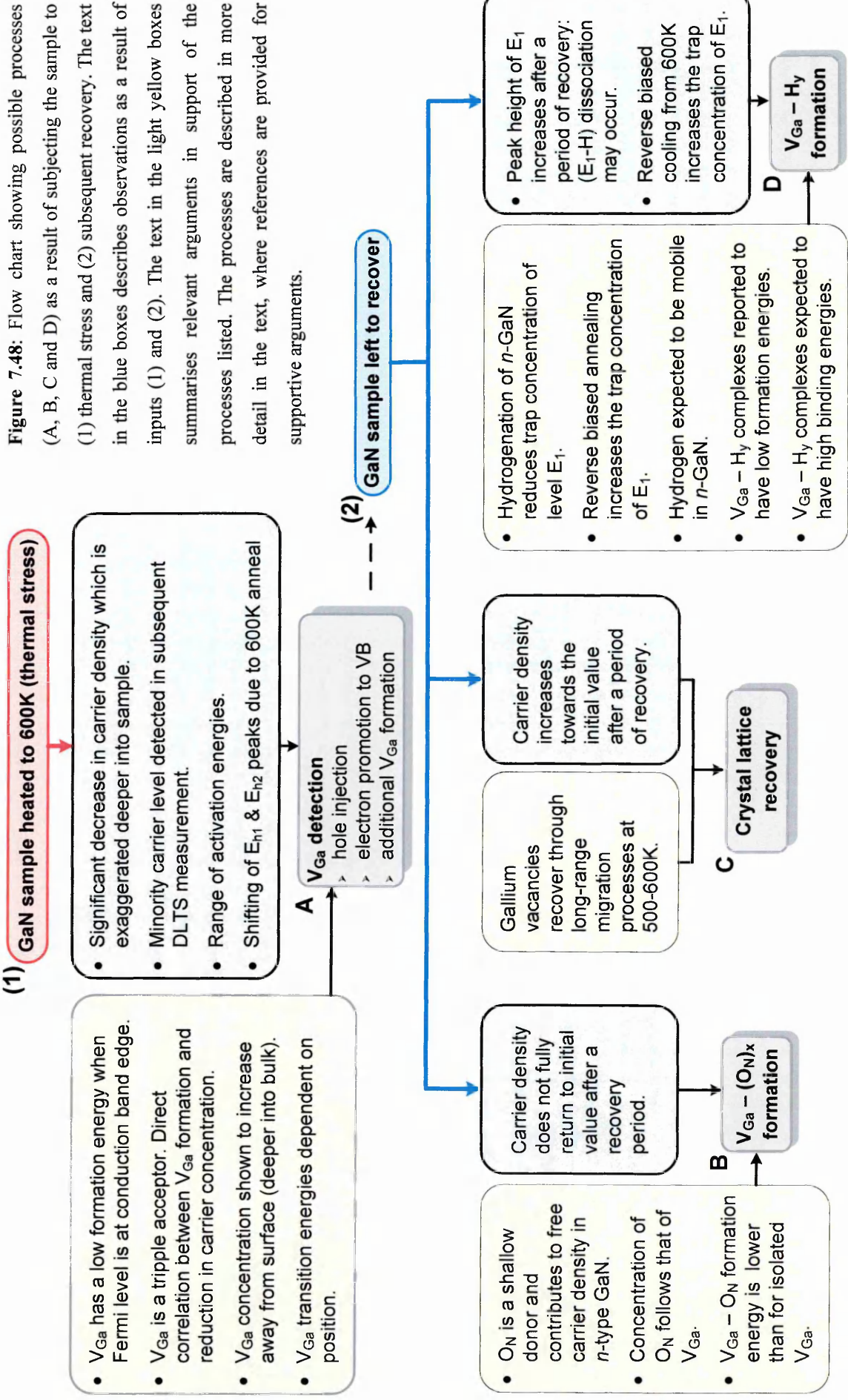
A near-midgap state, E_3 at $\sim E_C - 1.46$ eV, was detected using Laplace DLTS, which exhibits point defect related emission. This type of capture behaviour could be due to several reasons, two of which are considered here. Point defects with near midgap energy levels could be randomly distributed in the bulk. In this case, the multiple Laplace DLTS emissions detected could be a result of different amounts of strain at different bulk positions. Secondly, the point defect related emission could be due to the emission rate at this temperature being far greater than the capture rate.

7.7.2 Minority carrier emission

Results in section 7.6 describe the appearance of a metastable hole trap, E_h , which can be induced by thermal stress. The E_h level is clearly observed after an anneal at 560K. In this section, possible reasons for the appearance of the E_h level will be provided with discussions based on relevant results reported in the literature. Figure 7.48 is a flowchart listing results observed due to (1) heating the sample to 600K and (2) allowing the sample to recover for a period up to 3 weeks. The results observed are listed in the light blue boxes. These are reasoned against results provided in the literature, which are listed in light yellow boxes. By comparing the results in this work against those reported in literature, processes labelled A, B, C and D have been deduced to provide possible explanations for the results observed. However, DLTS and Laplace DLTS alone cannot confirm their validity. The flowchart is discussed in more detail below.

The following processes examine the possibilities of hole injection from the metal to the semiconductor, electron excitation to the valence band and *additional* gallium vacancy formation due to thermal stress. It is acknowledged that the last process would be unlikely at 600K, but it is nevertheless discussed, for completeness.

Figure 7.48: Flow chart showing possible processes (A, B, C and D) as a result of subjecting the sample to (1) thermal stress and (2) subsequent recovery. The text in the blue boxes describes observations as a result of inputs (1) and (2). The text in the light yellow boxes summarises relevant arguments in support of the processes listed. The processes are described in more detail in the text, where references are provided for supportive arguments.



Process A: Gallium vacancy detection

As discussed in chapter 5, the minority carrier level detected by DLTS in p^+n junction diodes, and by optical DLTS and MCTS in Schottky diodes, as reported in the literature, was associated with the gallium vacancy. These findings suggest that the gallium vacancies and their complexes are inherently present in n -GaN. The results in section 7.6 show that if the sample is heated to 600K and cooled down to room temperature, the subsequent DLTS scan shows a minority carrier peak (E_h). This is accompanied by a significant modification of diode characteristics: The carrier concentration is observed to decrease and this effect was observed to be deeper into the bulk (away from the surface), as shown in Figures 7.30 and 7.31. The discussion below examines possible reasons for the formation of the E_h level in the DLTS spectrum.

A-1: Hole injection

If the height of a Schottky barrier formed on an n -type semiconductor is greater than half the bandgap, the region of the semiconductor adjacent to the metal becomes p -type and contains a high density of holes²⁵. The barrier height can be derived using C - V data, by plotting C^{-2} against V . The intercept on the V axis, V_I , can be used to obtain the value of the barrier height, ϕ_b using the following relationship:

$$\phi_b = V_I + \xi + \frac{k T}{q} \quad 7.1$$

where ξ is the separation between the Fermi level and the conduction band edge²⁵. Using the above relationship, the value of ϕ_b was derived to be ~ 4.8 eV before the sample was heated to 600K and ~ 4.5 eV after thermal stress. The C - V measurements were recorded at 300K. This method is not accurate, because it assumes that the carrier concentration is uniform within the sample. The carrier concentration is non-uniform in our samples (as determined by C - V measurements) and although only values up to -1.5 V were selected to maximise linearity, values of $\sim 4.5 - 4.8$ eV are greater than the bandgap. This is not possible, because it suggests that the metal and semiconductor are not in contact, in which case the Fermi levels would not coincide.

Another method of measuring the barrier height is by using the current density values as a function of temperature at $V = 2$ V (Figure 7.5). A plot of $\ln(I/T^2)$ against $1/T$ should result in a straight line with a slope equal to $-q\phi_0/k$, where ϕ_0 is the barrier height at zero bias²⁵. The data did not result in a linear fit and using a small section of the data gives a barrier height of 0.038eV. Experimental barrier heights on GaN reported in the literature

are typically less than $1.5 \text{ eV}^{26,27,28}$, which would result in minimal minority carrier injection. However, it was reported by Maffei *et al.*²⁹ that a 10min anneal at 600°C under ultra-high vacuum enhanced the barrier height by 0.35 eV , suggesting that barrier height modification at higher temperatures is highly probable. Furthermore, the I-V characteristics of samples studied in this work show that the reverse bias leakage currents are significantly increased after thermal stress, as displayed in Figure 7.32.

A-2: Electron promotion to valence band

An additional contribution to the number of holes participating in the deep level emission and capture at level E_h could be the electrons in the valence band. At elevated temperatures of 600K , the electrons in the valence band are likely to be promoted to the E_h level. This inference is based on the amount of energy provided to the electrons at temperatures above 400K . For example, the activation energy of the E_3 level was measured to be $\sim 1.46 \text{ eV}$. This is the change in enthalpy associated with exciting an electron from the defect level to the conduction band. By considering that the energy separation between the valence band edge and the E_h level is less than $(E_C - E_3)$, it is possible to conclude that electrons may be excited from the valence band to the E_h level. This would create a population of holes in the valence band, which can contribute to the capture and emission processes at the E_h level. This process could occur in conjunction with the hole injection process discussed above.

A-3: Additional gallium vacancy formation

The hole injection and electron promotion models do not account for the decrease in carrier density, which matches the reported depth profile of V_{Ga} . They also do not explain the decrease in the trap concentration and shift in peak position of the E_{h1} level with zero bias annealing. Therefore, the possibility of *additional* gallium vacancies will be considered. However, it is acknowledged that vacancy formation is often produced by high energy electron irradiation. Although the formation of additional gallium vacancies is unlikely at a temperature of 600K , it will be considered for completeness.

Theoretical calculations agree that the gallium vacancy should have a low formation energy in GaN when the material is heavily *n*-type, with the Fermi level close to the conduction band edge and that it should exist as a triple acceptor $(V_{\text{Ga}}^{3-})^{30,31}$. Additionally, an increase in the gallium vacancy concentration was shown by positron annihilation studies to result in a comparable reduction in free carrier density³², which agrees with the work presented in this thesis. Furthermore, it was shown that the depth profile of gallium vacancies follows that of the dislocation density and was found to be

more abundant towards the material-substrate interface³³. The changes observed in the carrier density profiles after thermal stress strongly indicate that additional carrier trapping centres are being formed. The significant reduction of the carrier concentration deeper into the bulk matches the reported depth profile of gallium vacancies. The samples prepared for this work have not undergone an anneal step during the growth process. This may have an effect on the crystal lattice stability under elevated temperatures.

The absence of the E_h level due to reverse bias cooling could be explained by considering that carriers are depleted from the space-charge region and hence are not given the opportunity to be trapped by the E_h level. Gallium vacancies created by electron irradiation at room temperature were reported to become mobile at 500-600K²¹. Providing that gallium vacancies have formed, they could become mobile and drift much deeper into the sample under reverse bias conditions, as they will be repelled by the negative potential at the surface and attracted to the positive potential at the Ohmic contact. The DLTS measurements performed will not show this effect. This is because the region probed during typical DLTS measurements is $\sim 0.05 \mu\text{m}$, when the E_h level is not detected. Therefore, the resulting DLTS spectra are likely to present a majority carrier peak.

Process B: Gallium vacancy – oxygen complexes

It is suggested that enhanced carrier concentration in n -type GaN and carrier compensation in p -type GaN can be associated with oxygen at a nitrogen site, O_N ³⁴. The level of the O_N defect has been found to be close to the conduction band and the defect is assumed to be a shallow donor³⁵. At room temperature and above, the oxygen donor is assumed to be ionised and to exist as O_N^+ in the bulk. Additional formation of gallium vacancies as suggested above will create triple acceptors in the material, V_{Ga}^{3-} . Therefore, the formation of $V_{Ga} - (O_N)_x$ defects is highly probable, where x can be 1, 2 or 3, as discussed in chapter 4.

This is supported by theoretical and experimental work. Firstly, the theoretical formation energy of $V_{Ga} - (O_N)_x$ is found to be lower than for the isolated V_{Ga} , as reported by Elsner *et al.*²². SIMS measurements have revealed that the oxygen concentration increases towards the substrate-material interface^{36,37,38}, suggesting that the depth profile of gallium vacancies are comparable to that of oxygen in the bulk. Furthermore, native vacancies (those formed during growth) were found to be stable up to 1300 – 1500K, in contrast to those formed by electron irradiation²¹. This indicates

that Ga vacancies form stable compounds with other impurities or defects in the material²¹.

Results in this work show that the carrier concentration does not return to its original values after a period of recovery, after which only majority carrier emission from deep levels is detected in the DLTS spectra. This could be explained by considering the possibility of additional gallium vacancy (V_{Ga}^{3-}) formation due to thermal stress, which can trap up to three electrons. Such a defect would then form stable complexes with the abundant ionised oxygen donors, which may provide an explanation for the considerable and non-reversible reduction in the carrier density.

Process C: Crystal lattice recovery

When the sample is allowed to recover for a period of several days to 3 weeks, the initial DLTS scan showing majority carrier emission is recovered and the minority carrier level is no longer present. Additionally, the carrier concentration increases towards the original value, although it does not fully return to the initial value. It was discussed above that gallium vacancies formed by electron irradiation at room temperature were found to become mobile and recover at 500 – 600K, as reported by Saarinen *et al.*²¹. The *partial* recovery of the free carrier density (Figures 7.30 and 7.31) may indicate that the crystal lattice recovers gradually.

Process D: The V_{Ga} and the H^-

A negative peak is not detected in the DLTS scan if the sample is cooled from 600K with a reverse bias applied. This could be explained as follows: During the heating process and at 600K, the emission rate at deep levels is expected to be greater than the capture rate. This means that during the heating process, the gallium vacancy is not able to capture an electron, because the emission process is dominant at higher temperatures. During the cooling period under reverse bias, the electrons are removed from the space charge region and are not captured by the gallium vacancy, which is a triple acceptor (V_{Ga}^{3-}). During the cooling phase under reverse bias, the vacancies recover in long-range migration processes as suggested by Saarinen *et al.*²¹, without having captured an electron.

Hydrogenation of *n*-GaN was shown to reduce the trap concentration of the E_1 level by three orders of magnitude¹⁸. Furthermore, the increase in trap concentration of the E_1 level as a result of cooling with an applied reverse bias is similar to the result reported by Wu *et al.*^{19,39}. The peak height of the E_1 level was reported to increase as a result of reverse bias annealing at 370K. The authors suggest the presence of a mobile impurity,

most likely H^- , which passivates the E_1 level. Upon reverse bias annealing, H^- is suggested to drift away from the defect giving rise to the E_1 level. Recent theoretical calculations showed H^- should be readily mobile in wurtzite GaN⁴⁰.

The results reported by Wu *et al.* are similar to what is observed in our samples: The trap concentration of the E_1 level was observed to increase due to two processes, namely reverse bias cooling, but also after a recovery period (i.e. once the sample is heated to form the E_h level and subsequently allowed to rest). Therefore, it is highly probable that H^- dissociates from the E_1 defect at elevated temperatures.

However, to explain the increase in the concentration of the E_1 level after a period of recovery, it must be assumed that H^- is complexing with another defect or impurity. This is because the formation of the E_h level does not involve reverse bias cooling or annealing, hence the H^- impurity is unlikely to drift away from the space charge region. Therefore, the formation of the $V_{Ga} - H_y$ complex (where y can be 1, 2, or 3) should be considered (process D, Figure 7.48). The formation energies of $V_{Ga} - H_n$ (where $n = 1, 2$ or 3) are reported to be in the range $\sim 1.3 - 1.5$ eV⁴¹ for heavily n -type GaN and calculated to have large binding energies⁴¹.

7.7.3 Capture properties of the E_h level

The negative charge associated with dislocations was discussed in chapter 4. This has been reported by numerous techniques, including electron holography⁴². The depth profile of vacancy type defects detected through positron annihilation studies were shown to follow the depth profile of dislocations and that of oxygen in the material³³. Furthermore, theoretical work suggests that gallium vacancies and their complexes with oxygen exist primarily at dislocations, with formation and transition energies dependent on their positions in the vicinity of dislocation cores²². The above suggests that the E_h level should display extended defect related emission, with local band bending due to Coulomb repulsion from neighbouring states. However, such behaviour was not reported in the literature for the E_h level. Hierro *et al.*⁴³ reported that the capture properties of the E_h level showed fill pulse dependency, but DLTS spectra with different fill pulses did not represent emission from dislocation cores. This is based on the model formulated by Schröter and is discussed in Chapter 5. Emission from dislocation cores is signified by line broadening on the lower temperature side, overlapping of the spectra on the high temperature side and a clear shift of the peak position to lower temperatures. Additionally, Muret *et al.*⁴⁴ report point defect related emission, based on a measured single time constant, as opposed to multiple time constant typically observed for

extended defect related emission. In this work, the Laplace DLTS results suggest that the emission is point defect related. However, extended defect related emission could be detected if the fill pulse duration was set to 100ms, which is extremely long. The following model is proposed to explain the point defect related emission which is suggested to arise from the vicinity of extended defects.

It was discussed in chapter 3 that the cores and strain fields of dislocations act as trapping sites for impurities and defects. It was shown in this work and in the literature that the electron levels E_1 , E_2 and E_5 displayed extended defect related emission. However, the probability of impurities occupying a site at dislocation cores is governed by Fermi-Dirac statistics, as discussed in Chapter 3, section 3.1.2 and described by equation 3.2. Therefore, it is highly unlikely for gallium vacancies to segregate to one area of a dislocation and for electron traps to segregate to another. Instead, a mixed structure of minority carrier and majority carrier traps is likely to exist at dislocation cores. Figure 7.49 shows a random arrangement of electron and hole traps at the core of a threading edge dislocation.

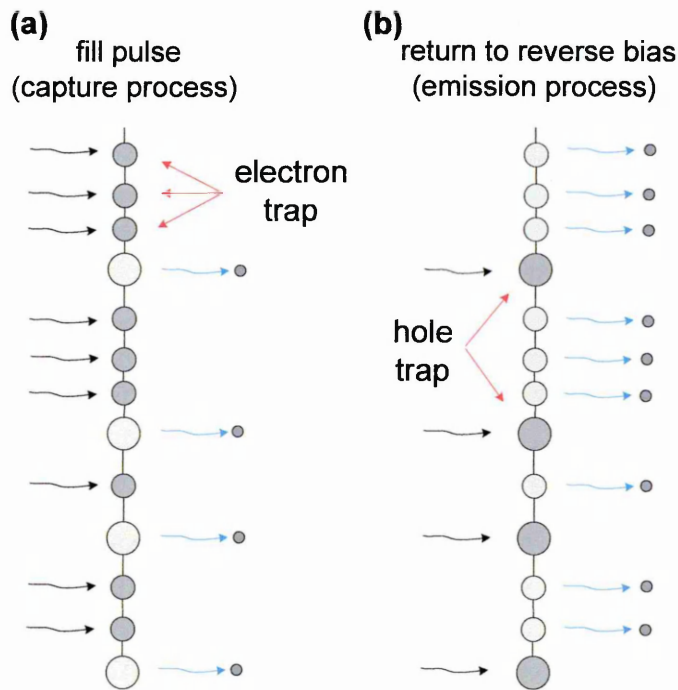


Figure 7.49: Random arrangement of electron and hole traps at a threading edge dislocation. Process (a) represents the fill pulse and (b) represents the return to quiescent reverse bias during a typical DLTS or Laplace DLTS experiment. The small circles at the dislocation cores represent electron traps and the larger circles represent hole traps. The smaller filled circles represent emitted electrons. Hole traps emit electrons during the filling pulse.

During the fill pulse, electron traps will capture, and hole traps will emit, electrons. Similarly, deep electron traps will emit their electrons during the return to quiescent reverse bias and hole traps will capture electrons. This is because a hole trap will capture holes from the valence band during the fill pulse, which is equivalent to emitting an electron to the valence band. The capture and emission processes during the DLTS and Laplace DLTS measurements are summarised in Table 7. 5.

	<i>During fill pulse</i>	<i>During reverse bias</i>	<i>Capacitance transient</i>
Electron trap	Electron capture from VB	Electron emission to CB	positive
Hole trap	Hole capture from VB (<i>electron emission to VB</i>)	Hole emission to VB (<i>electron capture from VB</i>)	negative

Table 7. 5: Capture and emission at electron and hole traps during the reverse bias phase and the fill pulse in a typical DLTS or Laplace DLTS experiment.

During the fill pulse dependency experiment using Laplace DLTS, emission from extended defects is signified by an increase in the emission rate with longer fill pulse durations. In the case of the E_h level, the hole emission rate should increase when longer fill pulses are applied. However, Figure 7.49(b) suggests that the Coulomb interaction between nearest states may be weakened due to a random arrangement of electron and hole traps. The hole emission rate may even decrease as a result of a longer fill pulse. This is because hole emission is equivalent to electron capture, which will be suppressed at $t = 0$ of the capacitance transient, because the neighbouring electron traps are still occupied at $t = 0$. This is likely to result in a barrier for electron capture at the beginning of the electron emission from electron traps. This is observed for emission rates above 100s^{-1} in Figures 7.41, 7.42 and more clearly in 7.46. The slower emission rates are not affected, because at $t \gg 0$, the majority of electron traps are likely to have emitted their electrons and thus electron capture (hole emission) is not hindered.

Similar results were reported by Muret *et al.*⁴⁴ regarding the capture properties of the E_h level. The authors investigated the recombination behaviour of the level using minority carrier transient spectroscopy (MCTS) by applying a light pulse followed by a filling pulse as in a DLTS experiment. The results showed that hole emission (i.e. electron capture from the valence band) is suppressed when sufficiently long fill pulses are applied following the light pulse⁴⁴.

The model in Figure 7.49 also explains the dramatic increase in emission rates between 1 and 100s^{-1} in the LDLTS results in Figure 7.46, when the fill pulse is extended to 100ms. At such long fill pulse durations, the emission rates from electron traps also increases, as evidenced by Laplace DLTS experiments on the E_{1b} , E_1 and E_5 levels (section 7.5.1). This means that the rate of electron capture from the valence band will increase for $t \gg 0$. This is because as t increases, the electron emission from electron traps results in a more positive charge surrounding the hole traps. This is likely to

induce local band bending and increase the hole emission rate (and hence the electron capture rate from the valence band).

7.7.4 Dependency of emission on the trap position in the lattice

The E_h level displays a range of activation energies and is found to be unstable as a result of additional thermal stress, such as annealing at 600K or prolonged Laplace DLTS measurements at elevated temperatures.

Theoretical studies by Elsner *et al.* suggest that the formation and transition energies of the V_{Ga} and $V_{Ga} - (O_N)_x$ complexes are dependent on the position of the defect²². This is because different positions in the vicinity of the dislocation core are associated with different levels of tensile and compressive strains. The effect of such strains on the bandgap was discussed in Chapter 2, section 2.3 and is repeated in Figure 7.50.

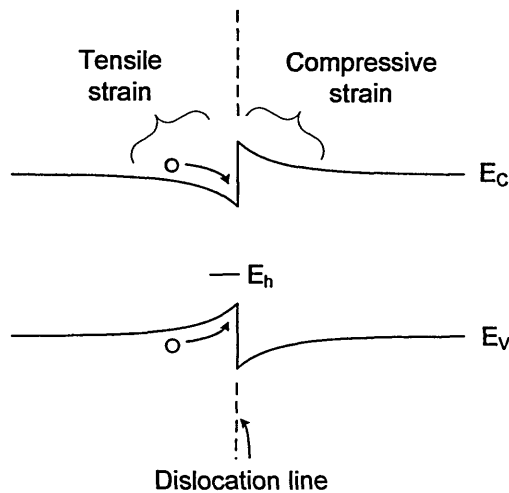


Figure 7.50: Effects on the bandgap at the dislocation line due to the tensile strain immediately below the extra half plane of atoms and compressive strain at the dislocation line.

It can be seen from Figure 7.50 that deep defects existing at the dislocation line are more likely to behave as recombination centres due to the accumulation of electrons and holes at the conduction and valence bands, respectively. Therefore, it follows that the level within the bandgap of a defect located at the dislocation line will be dependent on the level of strain. The structure reported by Elsner *et al.* showing the different positions at the dislocation is repeated in Figure 7.51. It can be seen that position 2 has the highest amount of strain. Therefore, the transition energies associated with a defect at this position are likely to be low.

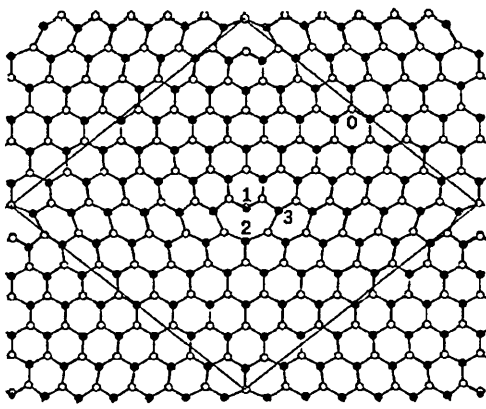


Figure 7.51: Different positions at an edge dislocation in a wurtzite supercell. The dislocations line (core) is labelled as position 1. Two additional positions, 2 and 3, are in the strain field of the dislocation. Position 0 represents a bulklike position, where the strain field of the dislocation is minimal in comparison to the core. After Elsner *et al.*²².

Table 7.6 shows the levels of the vacancy-oxygen complexes above the valence band edge, at various positions shown in Figure 7.51, as presented previously in Chapter 4.

Position	$E(V_{\text{Ga}})^{2-/3-}$	$E(V_{\text{Ga}}\text{-O}_N)^{1-/2-}$	$E(V_{\text{Ga}}\text{-O}_{2N})^{0/-}$	$E(V_{\text{Ga}}\text{-O}_{3N})^{+/-0}$
0 (bulk)	1.4	1.0	0.7	0.9
1 (core)	0.8	1.0	0.7	0.4
2	0.4	0.3	0.6	0.8
3	0.8	1.4	1.0	0.9

Table 7.6: The theoretical energy levels of V_{Ga} and $V_{\text{Ga}} - (\text{O}_N)_x$ complexes at various positions in the vicinity of a dislocation core, as reported by Elsner *et al.*²².

The values in Table 7.6 suggest that the level of the V_{Ga} and $(V_{\text{Ga}} - \text{O}_N)_x$ defects above the valence band edge are dependent on their positions at the dislocation. The defects are expected to exhibit a range of activation energies depending on their positions. This could explain the shifts in the DLTS spectra and the different activation energies observed as a result of additional thermal stress. The shifts in the spectra were most evident as a result of a 30min and 1hr anneal at 600K, as reported in section 7.6.4. It is probable that slight variations in the positions of the acceptor type defects could result in a change in the bandgap position of the defect, as indicated by Figure 7.50.

The multiple emission rates observed in the Laplace DLTS experiments for the E_h level could be due to the different lattice positions of the vacancy type defects. Furthermore, different numbers of oxygen atoms at the $V_{\text{Ga}} - (\text{O}_N)_x$ complexes could arise in distinct emission rates.

7.8 Summary

This chapter has presented DLTS and Laplace DLTS results from *n*-type GaN grown on sapphire by MOCVD. Shallow donor levels were reported at $\sim E_C - 65$ meV using DLTS. Further examination by LDLTS revealed three emission rates at a fill pulse of 10ms, which were used to derive activation energies of 17, 30 and 39 meV. Based on the results reported in the literature, these levels are likely to be associated with the Si_{Ga} and the O_{N} donor levels.

Two electron traps E_1 and E_2 were found to have fill pulse dependent activation energies, suggesting that these defects are located in the vicinity of, or at, dislocation cores. The fill pulse dependent emission rates detected by Laplace DLTS measurements at the peak temperature of E_1 support the notion that emission from the E_1 level is dislocation related. The trap concentration of this level is found to decrease deeper into the material.

Another electron trap, E_5 , was detected at longer fill pulses of 50ms in the DLTS spectra. The peak shape of this level suggests that it is point defect related. Laplace DLTS measurements confirm this, as most emission rates recorded at the peak temperature of E_5 displayed little, or no fill pulse dependency.

A near-midgap state was found, with a level at $\sim E_C - 1.46$ eV and the Laplace DLTS measurements for this level show no obvious fill pulse dependency, which is indicative of randomly distributed point defects. However, it is also possible that these defects exist at dislocation cores. At temperatures approaching 600K, other neighbouring levels such as E_1 and E_2 , will have emitted their electrons and hence the capture at E_3 will not be affected by the Coulomb potential of nearby states.

A minority carrier level, E_h , was detected after the sample was heated to near 600K and cooled back down to room temperature or below. The formation of this level corresponded with a decrease in the carrier concentration, which was found to be more significant deeper into the bulk. The DLTS spectrum recovered to the original, showing only electron levels, if the sample was allowed to rest for a sample-specific period. The gallium vacancy and its complexes with oxygen donor(s) are the strongest contenders for this level, based on the available literature. The formation of the minority carrier level is most likely due to the barrier modification at elevated temperatures and the creation of a hole population in the valence band due to electrons being excited to the E_h level.

7.9 References

- ¹ J. W. P. Hsu, M. J. Manfra, D. V. Lang, S. Richter, S. N. G. Chu, A. M. Sergent, R. N. Leiman, L. N. Pfeiffer, R. J. Molnar, *Appl. Phys. Lett.* **78**, 1685 (2001).
- ² A. Y. Polyakov, N. B. Smirnov, A. V. Govorkov, Z-Q Fang, D. C. Look, S. S. Park, J. H. Han, *J. Appl. Phys.* **92**, 5241 (2002).
- ³ S. Yoshida, J. Suzuki, *Proc. of the Symp. MRS Fall Meeting W4.8* (1999).
- ⁴ S. Yoshida, J. Suzuki, *J. Appl. Phys.* **85**, 7931 (1999).
- ⁵ W. Götz, N. M. Johnson, H. Amano, I. Akasaki, *Appl. Phys. Lett.* **65**, 463 (1994).
- ⁶ M. Asghar, P. Muret, B. Beaumont, P. Gibart, *Mat. Sci. Eng. B* **113**, 248 (2004).
- ⁷ D. C. Look, D. C. Reynolds, J. W. Hemsley, J. R. Sizelove, R. L. Jones, R. J. Molnar, *Phys. Rev. Lett.* **79**, 2273 (1997).
- ⁸ J. Neugebauer, C. G. Van de Walle, *Phys. Rev. B* **50**, 8067 (1994).
- ⁹ A. F. Wright, U. Grossner, *Appl. Phys. Lett* **73**, 2751 (1998).
- ¹⁰ J. H. Evans-Freeman, D. Emiroglu, K. D. Vernon-Parry, *Mat. Sci. Eng B* **114**, 307 (2004).
- ¹¹ J. H. Evans-Freeman, D. Emiroglu, K. D. Vernon-Parry, J. D. Murphy, P.R. Wilshaw, *J. Phys.: Condens. Matter* **17**, 2219 (2005).
- ¹² P. Hacke, A. Maekawa, N. Koide, K. Hiramatsu, N. Sawaki, *Jpn. J. Appl. Phys.* **33**, 6443 (1994).
- ¹³ D. K. Gaskill, A. E. Wickenden, K. Doverspike, B. Tadayon, L. B. Rowland, *J. Electron. Mater.* **24**, 1525 (1995).
- ¹⁴ M. A. Reshchikov, H. Morkoç, *J. Appl. Phys.* **97**, 061301-1 (2005).
- ¹⁵ W. Götz, N. M. Johnson, C. Chen, H. Liu, C. Kuo, W. Imler, *Appl. Phys. Lett.* **68**, 3144 (1996).
- ¹⁶ P. Muret, A. Philippe, E. Monroy, E. Muñoz, B. Beaumont, F. Omnès, P. Gibart, *Mat. Sci. Eng. B* **82**, 91 (2001).
- ¹⁷ C. Soh, S. Chua, H. Lim, D. Chi, W. Liu, S. Tripathy, *J. Phys.: Condens. Matter* **16**, 6305 (2004).
- ¹⁸ A. Hierro, S. A. Ringel, M. Hansen, J. S. Speck, U. K. Mishra, S. P. DenBaars, *Appl. Phys. Lett.* **77**, 1499 (2000).
- ¹⁹ L. Wu, W. E. Meyer, F. D. Auret, M. Hayes, *Physica B* **340**, 475 (2003).

- ²⁰ F. D. Auret and M. Nel, *J. Appl. Phys.* **61**, 2546 (1987).
- ²¹ K. Saarinen, T. Suski, I. Grzegory, D. C. Look, *Phys. Rev. B* **64**, 233201 (2001).
- ²² J. Elsner, R. Jones, M. I. Heggie, P. K. Stitch, M. Haugk, Th. Frauenheim, S. Öberg, P. R. Briddon, *Phys. Rev. B* **58**, 12571 (1998).
- ²³ R. Jones, J. Elsner, M. Haugk, R. Gutierrez, Th. Frauenheim, M. I. Heggie, S. Öberg, P. R. Briddon, *Phys. Stat. Sol. (a)* **171**, 167 (1999).
- ²⁴ L. Dobaczewski, A. R. Peaker, K. Bonde Nielsen, *J. Appl. Phys.* **96**, 4689 (2004).
- ²⁵ E. H. Rhoderick, R. H. Williams, *Metal-Semiconductor Contacts*, Clarendon Press, Oxford (1988).
- ²⁶ L. D. Bell, R. P. Smith, B. T. McDermott, E. R. Gertner, R. Pittman, R. L. Pierson, G. J. Sullivan, *J. Vac. Sci. Technol.* **16**(4), 2286 (1998).
- ²⁷ C. I. Wu and A. Kahn, *J. Vac. Sci. Technol.* **16**(4), 2218(1998).
- ²⁸ T. G. G. Maffeis, M. C. Simmonds, S. A. Clark, F. Peiro, P. Haines, P. J. Parbrook, *J. Appl. Phys.* **92**, 3179 (2002).
- ²⁹ T. G. G. Maffeis, M. C. Simmonds, S. A. Clark, F. Peiro, P. Haines, P. J. Parbrook, *J. Phys. D* **33**, L115 (2000).
- ³⁰ T. Mattila and R. M. Nieminen, *Phys. Rev. B* **55**, 9571 (1997).
- ³¹ S. Limpijumnong, C. G. Van de Walle, *Phys. Rev. B* **69**, 035207 (2004).
- ³² K. Saarinen, P. Seppälä, J. Oila, P. Hautojärvi, C. Corbel, O. Briot, R. L. Aulombard, *Appl. Phys. Lett.* **73**, 3253 (1998).
- ³³ J. Oila, J. Kivioja, V. Ranki, K. Saarinen, D. C. Look, R. J. Molnar, S. S. Park, S. K. Lee, J. Y. Han, *Appl. Phys. Lett.* **82**, 3433 (2003).
- ³⁴ M. A. Reshchikov, H. Morkoç, *J. Appl. Phys.* **97**, 061301-1 (2005).
- ³⁵ B-C. Chung, M. Gershenson, *J. Appl. Phys.* **72**, 651 (1992).
- ³⁶ D. Meister, M. Böhm, M. Topf, W. Kriegseis, W. Burkhardt, I. Dirnstorfer, S. Rösel, B. Farangis, B. K. Meyer, A. Hoffmann, H. Siegle, C. Thomsen, J. Christen, F. Bertram, *J. Appl. Phys.* **88**, 1811 (2000).
- ³⁷ G. Popovici, W. Kim, A. Botchkarev, H. Tang, J. Solomon, H. Morkoç, *Mat. Res. Soc. Symp. Proc.* **468**, 3 (1997).
- ³⁸ D. C. Look, C. E. Stutz, R. J. Molnar, K. Saarinen, Z. Liliental-Weber, *Sol. State Commun.* **117**, 571 (2001).

-
- ³⁹ L. Wu, W. E. Meyer, F. D. Auret, *Phys. Stat. Sol. (a)* **10**, 2277 (2004).
- ⁴⁰ A. F. Wright, *Phys. Rev. B* **60**, R5101 (1999).
- ⁴¹ C. G. Van de Walle, *Phys. Rev. B* **56**, R10020 (1997).
- ⁴² D. Cherns, C. G. Jiao, *Phys. Rev. Lett.* **87**, 205504-1 (2001).
- ⁴³ A. Hierro, M. Hansen, J. J. Boeckl, L. Zhao, J. S. Speck, U. K. Mishra, S. P. DenBaars, S. A. Ringel, *Phys. Stat. Sol. (b)* **228**, 937 (2001).
- ⁴⁴ P. Muret, A. Philippe, E. Monroy, E. Muñoz, B. Beaumont, F. Omnès, P. Gibart, J. *Appl. Phys.* **91**, 2998 (2002).

Chapter 8

Conclusions and future work

In this work, silicon (Si) and gallium nitride (GaN) containing extended defects were characterised using deep level transient spectroscopy (DLTS) and Laplace DLTS (LDLTS). The results on silicon and gallium nitride are presented in Chapters 6 and 7, respectively. In this chapter, the conclusions based on the results presented are outlined and suggestions for future work are provided. The final section of this chapter includes a discussion on the application of Laplace DLTS to extended defects. A general conclusion regarding the application of Laplace DLTS to extended defects is discussed.

8.1 Silicon

In the silicon samples containing oxygen induced stacking faults, fill pulse dependent activation energy of the dominant peak SF1 was evidenced by DLTS. Further investigation using Laplace DLTS revealed multiple emission rates, for which fill pulse dependency was observed. This is believed to be the first time that the effect of local band bending at dislocations on emissions from extended defect levels is witnessed by Laplace DLTS.

Improving mechanical hardness of silicon by means of dislocation locking by oxygen was shown to have possible implications on device performance, if they are in the vicinity of device active regions. A dominant deep level has been detected at ~ 200 meV, which appears to move closer to the valence band (~ 100 meV) upon repeated heating and cooling of the sample. The peak height of the level has displayed a strong dependence on the annealing time and hence the amount of oxygen at the dislocation core. Furthermore, Laplace DLTS results indicate that the emission from this level is dependent on the fill pulse duration. Such a dependency is generally associated with the presence of extended defects due to the Coulomb interaction of nearby states resulting in local band bending.

The application of Laplace DLTS at 225K showed that emission rates are present which do not exhibit fill pulse dependency. Such emissions could arise due to point defects

which are sufficiently farther away from dislocation cores and thus are unaffected by neighbouring occupied states.

8.1.1 Future work

It was mentioned in Chapter 6 that the capture cross-section of the oxygen-related level in the silicon samples containing O-locked dislocations could not be obtained due to the time resolution of the pulse generator in the capacitance meter. However, it would be beneficial to carry out capture cross section measurements to gain further understanding regarding the charge state of the level. This is because the activation energy of the level was found to be unusually high at such low temperatures.

Thermal double donors in silicon are common unless they are annealed out at higher temperatures. It is undoubtedly clear that the level observed is not a donor level. This is because the DLTS peak for a donor level in *p*-type silicon would be negative. In contrast, the O-related level observed in our samples is a positive peak. However, samples like the ones studied could be formed by using a higher annealing temperature, such as 600K to confirm the stability of the O-related level. The disappearance of this level with the use of a higher annealing temperature during the oxygen segregation phase would be a favourable result for the silicon industry.

Silicon has an indirect bandgap and the luminescence from silicon should not be efficient. However, it has been shown that photoluminescence (PL) studies of dislocations in silicon lead to the D1, D2, D3 and D4 lines in the 0.8 to 1 eV range^{1,2,3}. The D1 line was reported to arise from clean and oxygen decorated dislocations⁴ and oxygen implantation of Si was shown to give rise to two PL bands at 0.85 and 0.78 eV⁵. It would be of significance to investigate the PL, if any, from the samples containing oxygen-locked dislocations studied in this work. The intensity of the PL lines relating to oxygen should increase with increasing unlocking stress and hence the amount of oxygen at the dislocation cores.

8.2 Gallium nitride

The electrical characterisation of deep levels in hexagonal *n*-type gallium nitride (*n*-GaN) grown by metal organic chemical vapour deposition (MOCVD) has revealed six electron traps and a metastable hole trap. The electron levels include shallow donor levels, two dislocation related levels (E_1 and E_2), a point defect level (E_5) and a near midgap state (E_3). The shallow donor level was initially detected by DLTS

measurements, giving a donor level of $E_C - 65\text{meV}$. Laplace DLTS measurements revealed three emission rates for fill pulse durations above 10ms. The variation in emission rate with increments in temperature resulted in activation energies of 17, 30 and 39 meV below the conduction band edge. These results are comparable to shallow levels reported in the literature and were associated with the silicon donor at a gallium site (Si_{Ga}) and the oxygen donor at a nitrogen site (O_{N}). The dislocation strain fields are likely result in different activation energies for the same defect.

The level E_1 is the most common level reported in wurtzite n -GaN. In this work, the level E_1 is found to exhibit fill pulse dependent activation energies, suggesting that the emission is dislocation related. This is confirmed by Laplace DLTS measurements, which reveal multiple fill pulse dependent emission rates. The trap concentration of level E_1 decreases away from the surface and deeper into the bulk. The activation energy of level E_2 was also found to vary with the fill pulse duration used in the DLTS measurements and is also likely to arise from dislocation related states. Such levels could be associated with impurities that have segregated to dislocation cores. At high dislocation densities in the order of 10^8cm^{-2} , most lattice sites are likely to be affected by the dislocation strain fields.

A level at $E_C - 1.46\text{ eV}$ was found by Laplace DLTS measurements. The LDLTS spectra displayed numerous emission rates, with no clear dependence on fill pulse duration. This behaviour is typically associated with point defects. However, the results cannot be used to conclude that the defects giving rise to near midgap emissions are randomly distributed point defects. This is because near 600K, the electron emission rate will exceed electron capture rate for neighbouring defects, such as E_1 and E_2 . Therefore, surrounding defects are likely to be empty at this temperature and will not give rise to a long range Coulomb potential to influence the capture kinetics at deeper levels, such as E_3 .

A hole trap, E_h , was observed in the DLTS spectrum if the sample was heated to near-600K and cooled down. The formation of this level is associated with a significant decrease in carrier concentration. Both the DLTS and Laplace DLTS results indicate that the E_h level is likely to be due to a point defect. A minority carrier level was previously reported in the literature in n -GaN Schottky studied by optical DLTS and p^+n junction diodes, suggesting that it is inherently present in the material grown by most methods. Therefore, the detection of the minority carrier level in this work may be due to an enhanced hole population in the valence band upon thermal stress. Comparison with the available theoretical and experimental results in literature suggests

that the minority carrier level is likely to be due to the gallium vacancy and its complexes with oxygen donors, $(V_{\text{Ga}} - O_{\text{N}})_x$.

The complex nature of the Laplace DLTS of the electron and hole levels is likely to be due to the dislocation strain fields. It is suggested that acceptor and donor type defects may be randomly distributed along the threading edge dislocations.

8.2.1 Future work

Based on the literature, it would be reasonable to conclude that the gallium vacancies and associated complexes are inherently present in *n*-type gallium nitride. Therefore, it can be suggested that a certain number of such defects are present in the samples studied in this work. To ensure that this inference is correct, it is important that a characterisation technique is selected, which is more sensitive to minority carriers. One such technique is minority carrier transient spectroscopy (MCTS), which excites minority carriers by shining monochromatic light through a semi-transparent Schottky barrier diode and measuring deep level emission using DLTS.

In order to investigate fully the effects of thermal stress on the concentration of minority carrier traps, MCTS should be applied to the SBD before and after thermal stress. If thermal stress does increase the minority trap concentration, then this would become evident in the MCTS measurements.

Defect-induced electronic states in the gallium nitride bandgap lead to a broadband emission with a line width of ~ 1 eV, which is centred at 2.2 – 2.3 eV and located in the yellow part of the spectrum. This is commonly referred to as the *yellow luminescence band* (YL) and has been associated with a transition from a shallow donor to a deep acceptor^{6,7}. Positron annihilation studies by Saarinen *et al.* have revealed a strong correlation between V_{Ga} density in the GaN samples and the intensity of the yellow luminescence in *n*-type GaN grown by MOCVD. It has been suggested that the deep acceptor participating in the YL is the gallium vacancy (V_{Ga}) and/or its complexes with oxygen, $\{V_{\text{Ga}} - (O_{\text{N}})_x\}$. It would be beneficial to investigate the effect of thermal stress on the YL in *n*-GaN samples.

Theoretical calculations have suggested that the formation energy of V_{Ga} is low (high) when the Fermi level is close to the conduction band (valence band), as discussed in Chapter 3. The Fermi level in unintentionally doped samples should be significantly lower than samples which have been doped intentionally with silicon. The unintentionally doped samples could be subjected to similar thermal stresses as reported in chapter 7 to investigate whether the minority carrier level would still form when the

Fermi level is closer to midgap. Furthermore, any differences in the general DLTS spectra between doped and undoped samples may aid in determining the nature of the electron levels detected.

It would be far more accurate to measure the activation energy of the E_h , E_{h1} and E_{h2} levels with optical experiments, such as optical DLTS (O-DLTS) or MCTS. This is because the resulting capacitance transient would not be affected by the presence of majority carrier (electron) emission. It has been discussed in chapter 7 that the detection of the minority carrier trap is likely to be a result of electron capture (from the valence band) at deep levels exceeding electron emission at a given time and temperature. Furthermore, the initial scans in chapter 7 have shown that majority carrier emission does exist at the same temperature range as the minority carrier emission after thermal stress. Therefore, it is possible that the negative capacitance transient representing minority carrier emission is not a true representation of the electron capture process. This principle can be explained in more detail when the nature of the DLTS signal is considered. It was mentioned in chapter 4, section 4.3, that the maximum DLTS signal, δC_{\max} , occurs at the maximum time constant of emission, $\tau_{e(\max)}$. This relationship determines the difference between the capacitance value of the transient, which is sampled at two points in time, $C(t_1)$ and $C(t_2)$. If both electron capture and emission are taking place, then the capacitance transient is a result of both processes and not due to electron capture alone. Therefore, the value of δC_{\max} obtained from the transient will not occur at the maximum time constant of the electron capture (minority carrier emission). Instead, the value of $\tau_{e(\max)}$ obtained will be made up of two processes, electron capture and emission.

8.3 Laplace DLTS and extended defects

The results obtained using Laplace DLTS on *n*-type GaN and *p*-type Si were invaluable to understanding the behaviour of deep levels in the bandgap. It was shown using LDLTS that the broad peaks typically observed are not only due to extended defects and certain emissions are present which are not affected by long range Coulomb interactions. It must be noted that broad peaks in DLTS are typically due to numerous emissions. This information is lost if DLTS alone is used.

In GaN, the decrease of higher emission rates with increasing fill pulse was observed when examining the E_h level. This was used to construct a possible model of the defect structure to explain the point defect related emission, which was thought to arise from

threading edge dislocation cores. This would not have been possible using DLTS alone. Furthermore, the minority carrier level, E_h , appears to be a simple point defect, when examined by DLTS measurements. However, Laplace DLTS measurements showed that multiple emissions are present at a given temperature.

Laplace DLTS is typically not applied to extended defects, because of the complex emission and capture relationships due to the local band bending at closely spaced levels in the bandgap. However, it was shown in this work that it is precisely this band edge modification which makes Laplace DLTS highly beneficial in characterising emission and capture at extended defects. This is believed to be the first time that Laplace DLTS was used extensively to investigate capture properties at extended defects and to distinguish between point and extended defect related emission. Extensive computer models have been developed by many, including Schröter, to simulate the capture and emission at extended defects based on DLTS. Research has gained invaluable information through such modelling. Similar simulations should be developed for the behaviour of Laplace DLTS spectra of extended defects with variations in the fill pulse durations. Such models, when confirmed experimentally would add further information to the current understanding of extended defect related emission. Firstly, with the use of Laplace DLTS, it is possible to view the transient in full. This is in contrast to conventional DLTS, where the transient is only sampled at two intervals in time. Secondly, the transients in DLTS measurements are often noisy, which is worsened at slower rate windows. However, in Laplace, it is possible to record several thousand transients, resulting in a typical signal to noise ratio of >1000 . Admittedly, the capacitance transient is the essence of a deep level measurement.

8.4 References

- ¹ N. A. Drozdov, A. A. Patrin, V. D. Tkachev, *Phys. Stat. Sol. (b)* **83**, K137 (1977).
- ² M. Suezawa, K. Sumino, *Phys. Stat. Sol. (a)* **78**, 639 (1983).
- ³ R. Sauer, J. Weber, J. Stolz, E. R. Weber, K. H. Küsters, H. Alexander, *Appl. Phys. A* **36**, 1 (1985).
- ⁴ S. Pizzini, M. Acciarri, E. Leoni and A. Le Donne, *Phys. Stat. Sol. (b)* **222**, 141 (2000).
- ⁵ A. J. Kenyon, E. A. Steinman, C. W. Pitt, D. E. Hole, V. I. Vdovin, *J. Phys.: Condens. Matter* **15**, S2843 (2003).
- ⁶ E. Calleja, F. Sánchez, D. Basak, M. A. Sánchez-García, E. Muñoz, I. Izpura, F. Calle, J. M. G. Tijero, J. L. Sánchez-Rojas, B. Beaumont, P. Lorenzini, P. Gibart, *Phys. Rev B* **55**, 4689 (1997).
- ⁷ I. Shalish, L. Kronik, G. Segal, Y. Rosenwaks, Y. Shapira, U. Tisch, J. Salzman, *Phys. Rev B* **59**, 9748 (1999).